THOMAS SUREN

SINGLE-MOLECULE STUDY OF THE GLUCOCORTICOID RECEPTOR LIGAND BINDING DOMAIN

CONFORMATIONAL DYNAMICS OF HORMONE BINDING AND CHAPERONE INTERACTION

DISSERTATION AT THE PHYSICS DEPARTMENT E22
TECHNISCHE UNIVERSITÄT MÜNCHEN

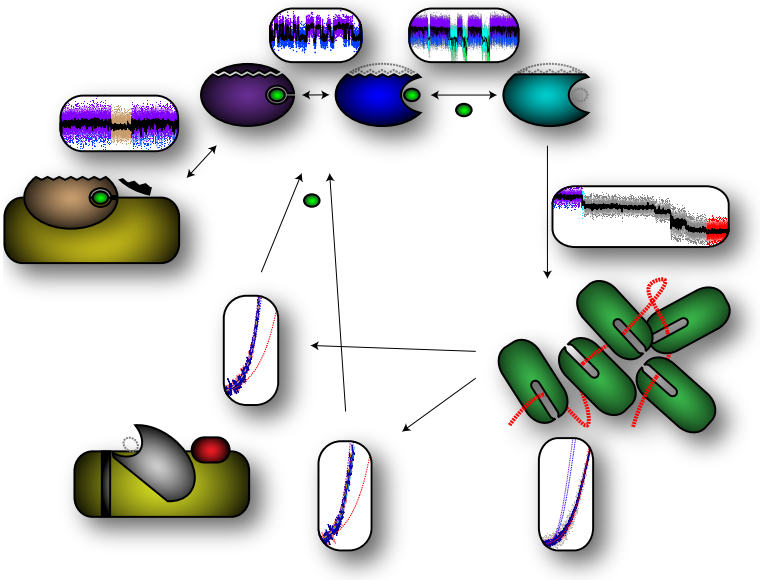

TECHNISCHE UNIVERSITÄT MÜNCHEN
PHYSICS DEPARTMENT E22

SINGLE-MOLECULE STUDY OF THE GLUCOCORTICOID RECEPTOR LIGAND BINDING DOMAIN

CONFORMATIONAL DYNAMICS OF HORMONE BINDING AND CHAPERONE INTERACTION

THOMAS SUREN

Vollständiger Abdruck der von der Fakultät für Physik der Technischen Universität München zur Erlangung des akademischen Grades eines

Doktors der Naturwissenschaften (Dr. rer. nat.)

genehmigten Dissertation.

Vorsitzender:	Prof. Dr. Martin Zacharias
Prüfer der Dissertation:	1. Prof. Dr. Matthias Rief
	2. Prof. Dr. Andreas Bausch

Die Dissertation wurde am 02. Juli 2018 bei der Technischen Universität München eingereicht und durch die Fakultät für Physik am 17. Juli 2018 angenommen.

Die Menschen haben keine Ahnung, wie man schon denken kann; wenn man sie neu denken lehren könnte, würden sie auch anders leben.

— Robert Musil

ABSTRACT

The Glucocorticoid Receptor (GR) is a critical signaling protein playing a role in many serious diseases, however many details of its function are still unresolved. GR is of additional interest as it also constitutes a model system for studying how chaperones function, assisting one fifth of all proteins in eukaryotes. In this work, state-of-the-art techniques were developed to provide detailed insights into chaperone-assisted receptor function, through the manipulation and observation of single protein molecules in real time.

GR is a ligand-induced transcription factor, regulating numerous genes, and thus, is involved in immune and inflammatory disorders such as asthma, leukemia, and depression. Via its Ligand Binding Domain (LBD), GR binds the steroid hormone cortisol. Studies of the GR-LBD have been hampered by its instability and a strong tendency to aggregate. GR is regulated allosterically. Hence, knowledge about its conformational dynamics is critical to understand the GR-LBD function entirely. *In-vivo*, GR it is tightly regulated by the molecular chaperones Hsp70 and Hsp90. Despite its importance, little is known about GR-LBD folding, its ligand-binding pathway, or the reason for its aggregation and chaperone-dependence.

In this study, single-molecule force-spectroscopy with optical tweezers was used to unravel the pathway of folding and hormone binding of GR-LBD. An N-terminal *lid* structure was identified whose dynamics were tightly coupled to hormone binding. The lid dynamics could be used as a mechanical readout to monitor whether the hormone is bound. Novel measurement and analysis techniques revealed the influence of misfolding on the folding kinetics. Despite a rough folding energy landscape, the apo-GR-LBD folds readily without the need for chaperones and hormone-independent, exhibiting unexpectedly high stability of 41 k_BT. A possible cause for aggregation is the *lid* that remains unstable until a hormone binds. Then it closes, adding 12 k_BT of energy, which drastically increases hormone affinity.

Knowing the GR behavior the effect of chaperones was monitored using a custom-designed microfluidic system. After hormone dissociation, Hsp70 entirely GR-LBD and blocks any refolding attempt. Hsp90 then promotes a stable, binding competent GR-LBD state. The data reconstruct the maturation of a functional GR-LBD-Hsp90 complex casting new light on the regulatory role of Hsp90.

These measurements open detailed insights into the activation of signaling proteins and their tight regulation by chaperones. These are significant milestones in the quest to unravel the basic principles of these vital biochemical processes.

ZUSAMMENFASSUNG

Der Glucocorticoid-Rezeptor (GR) ist ein Signalprotein, der bei vielen schweren Erkrankungen eine Rolle spielt. Viele Details seiner Funktionsweise sind unklar. Er ist zusätzlich als Modellsystem von Bedeutung für die Funktionsweise von Chaperonen, die etwa ein Fünftel aller Proteine in Eukaryoten in deren Funktion unterstützen. Es wurden modernste Methoden weiterentwickelt, um Details der chaperongestützten Rezeptor Funktionsweise zu erforschen, indem einzelne Protein Moleküle in Echtzeit manipuliert und beobachtet wurden.

Der GR ist ein hormoninduzierter Transkriptionsfaktor, der bei Immunerkrankungen und Entzündungen, wie Asthma, Leukämie und Depression involviert ist. Mit seiner Ligandenbindungsdomäne (LBD) bindet der GR das Steroidhormon Cortisol. Studien der GR-LBD sind erschwert durch deren Instabilität und Aggregationstendenz. Die GR-LBD funktioniert durch kleinste Strukturänderungen. Daher ist es unumgänglich, diese Dynamiken zu begreifen, um die Funktionsweise der GR-LBD vollständig zu verstehen. *In-vivo* ist der GR abhängig von Hsp70/90. Trotz der zentralen Rolle der GR-LBD, ist kaum etwas über deren Faltung, den Ablauf der Hormonbindung und die Ursache für dessen Aggregation und Chaperonabhängigkeit bekannt.

In dieser Studie wurde Einzelmolekül Kraftspektroskopie mit einer optischen Pinzette angewandt, um den Ablauf von Faltung und Hormon-Bindung der GR-LBD zu erforschen. Eine *Hebel* Struktur wurde am N-terminus entdeckt, deren Dynamik an die Hormonbindung gekoppelt ist. Daher konnte sie als mechanische Anzeige der Bindung genutzt werden. Neuste Mess- und Analysemethoden legten den Einfluss von Fehlfaltung auf die Faltungskinetik offen. Trotz einer rauen Faltungs-Energielandschaft faltet die apo-GR-LBD ohne die Hilfe von Chaperonen und Hormon-unabhängig. Sie zeigte eine unerwartet hohe Stabilität von 41 k_BT. Eine mögliche Aggregationsursache hingegen ist der *Hebel*, der bis zur Hormon-Bindung instabil bleibt. Dann fügt er sich mit 12 k_BT an die restliche Struktur, wodurch die Hormon-Affinität drastisch erhöht wird.

Das Verständnis des natürlichen GR Verhaltens wurde genutzt, um mit einem spezifisch gestalteten Mikrofluidik System die Funktion von Chaperonen in Aktion zu beobachten. Nach der Dissoziation des Hormons wird die GR-LBD durch Hsp70 komplett entfaltet und an jeglicher Rückfaltung gehindert. Hsp90 führt daraufhin die GR-LBD in einen stabilen, bindungsfähigen Zustand über. Diese Messungen rekonstruieren die Entstehung eines funktionalen GR-LBD-Hsp90 Komplexes und werfen neues Licht auf die regulatorische Rolle von Hsp90.

ACKNOWLEDGMENTS

MY SUPERVISOR This work would not have been possible without Prof. *Matthias Rief*. He built up a lab in which cutting-edge science can be performed and guided me with great ideas and valuable feedback. Furthermore, he allowed an amazingly comfortable working environment.

Matthias, ich bin dankbar, dass deine Tür stets offen stand und für deine Fähigkeit, die Dinge auf das Wesentliche zu reduzieren.

MY COLLABORATORS I would like to acknowledge *Patrick Mößmer* and *Ulrike Majdic* for direct contributions to the success of this work and our collaborators *Johannes Buchner* and *Daniel Rutz* for providing the essential proteins and sharing their knowledge about them.

MY LABMATES I appreciate that I could use all the extensive resources built up over generations of hard working meticulous students. I want to thank *Fabi Ziegler*, *Alex Mehlich*, *Jo Stigler*, *Lorenz Rognoni* and *Benni Pelz* for introducing me to all these techniques.

Ulrich Merkel, *Kasia Tych*, and *Andreas Weißl* helped to maintain the optical traps in great shape and assisted me in technical questions. A particular thank-you goes to *Marco Grison* for advice and support in various situations, for bringing people together, and being a precious friend throughout the whole time.

Спасибо Саша, ты привнес неповторимые и офигенные впечатления с самого начала моего научного путешествия!

For sharing their knowledge and fruitful discussions, I want to acknowledge *Gabriel Zoldak*, *Anja Schlierf*, *Daniela Bauer*, *Soumit Mandal*, *Markus, Jahn* and *Philip Wortmann*, and especially *Ziad Ganim* as a valuable source of scientific inspiration.

For assistance in the lab, I highly valued the help of *Gabriele Chmel*, *Karin Vogt*, *Monica Rusp*, and *Rudi Lehrhuber*. For guiding me in the depths of bureaucracy, I thank *Elke Fehlsenfeld*, *Nicole Mittermüller*, and *Anne Ploss*

I want to thank all the members of the E22 and E27 chair for creating a unique and really joyful atmosphere to work in.

MY FRIENDS This thesis is only readable due to the joint effort of *Leo Rossetti*, *Chris Battle*, *Stefan Müller*, Иван Исаков, *Ibrahim Kara* and especially Kasia, who spent great effort improving the whole style.

Dirk, muchísimas gracias por todos los incentivos i la inspiración.

For supporting me during the loneliness of writing, I want to thank *Dirk Christoph*, *Mahmut Kara*, and my flatmates at the *Villa Schandfleck*.

Mahmut ez ji dil sipas dikim ji bo ku tu hevalek yekane ye û ji bo kû tu herdêm dixwazî vê Cihanê biki cîyek basdir. Destê te sax be!

MY FAMILIY My sincerest gratitude goes to the persons I could always count on in any situation; my mother *Marianne*, my sister *Lena* and my father *Dr. Klaus Suren*, to whom I basically owe, who I am today. *Vielen Dank, dass ihr für mich da seid, ich hab euch lieb!*

CONTENTS

LIST OF FIGURES

LIST OF TABLES

ACRONYMS

SMFS	Single-Molecule Force-Spectroscopy
NA	Numerical Apperture
AOD	Acousto-Optic Deflector
PSD	Position Sensitive Detector
GR	Glucocorticoid Receptor
LBD	Ligand Binding Domain
DEX	Dexamethasone
WLC	Worm-Like Chain
HMM	Hidden Markov Model
F-DEX	Fluorescein-labeled Dexamethasone
HSP	Heat Shock Protein
Hsp70	Heat shock protein 70
Hsp90	Heat shock protein 90
Hsp40	Heat shock protein 40
HOP	Hsp70/Hsp90 Organizing Protein

ATP	Adenosine Triphosphate
ADP	Adenosine Diphosphate
CCS	Complete Chaperone System
TIF2	Transcriptional Intermediary Factor 2
HDX	Hydrogen Deuterium Exchange
MS	Mass Spectrometry
AF1	Activation Function 1
AF2	Activation Function 2
NR	Nuclear Receptor
TRF	Transcriptional Regulatory Factor
SHR	Steroid Hormone Receptor
GC	Glucocorticoid
GRE	Glucocorticoid Response Element
TPR	Tetratricopeptide Repeat

Part I

INTRODUCTION

1 INTRODUCTION

This chapter provides background information about the biological systems investigated in this thesis. It illustrates both the importance and the complexity of the involved processes, highlighting the need for a detailed investigation. A general introduction about proteins is given in Section 1.1, followed by a review of current knowledge about the Glucocorticoid Receptor (GR) in Section 1.2. Section 1.3 describes the connection of the GR with other essential proteins and finally, the scope and outline of this work are presented in Section 1.4.

1.1 PROTEINS, HORMONE RECEPTORS AND CHAPERONES

Proteins are large biomolecules, which can be regarded as nano-machines serving many vital processes in living cells. They participate in virtually all cellular functions within organisms such as metabolism, transportation of molecules, signal transduction, DNA replication and mechanical stabilization. Thus, understanding the mechanisms of how proteins work is fundamental for understanding life at the molecular level.

PROTEINS Protein molecules consist of linear chains, built of a sequence of amino acids, which are covalently bound together. They have an amino terminus (N-terminus) and a carboxyl-terminus (C-terminus). These protein sequences are coded on our genome and translated by the ribosome. After leaving the ribosome, the polypeptide folds into a complex 3D structure, defined by the interaction properties of the amino acid residues constituting the chain. For instance, hydrophobic residues tend to be buried in the core of the protein while polar residues form the surface in contact with the surrounding solution. This process of reliable folding of the chain into its predefined structure still remains poorly understood in many aspects. [51, 126, 271].

A linear chain of amino acid residues is also called a polypeptide. There are 20 different amino acids.

There are roughly 20000 proteins encoded by the human genome [99]. It is the 3D structure, including its potential conformations and interaction sites that determines a protein's function. A chief characteristic of proteins is their ability to bind other molecules specifically. Some proteins act as molecular motors[1], binding to and walking on "biomolecular roads" by changing their conformation upon binding and consumption of small ATP molecules as "fuel" [206]. Enzymes are

1 https://www.youtube.com/watch?v=uWsFS8vbMEg

proteins specifically binding substrates to catalyze chemical reactions [56]. Many proteins are involved in the process of signal transduction. They feature a highly specific binding pocket to bind individual signal substances, which activates them, to enable their interaction with other proteins along the signaling pathway.

NUCLEAR RECEPTORS A particular class of signaling proteins that are responsible for sensing hormones and other molecules, such as vitamins or sterols, are Nuclear Receptors (NRs). They act as Transcriptional Regulatory Factors (TRFs) [165]. In response to ligand binding, they undergo conformational changes to bind to DNA and regulate the expression of specific genes, thereby controlling the development, homeostasis, and metabolism of the organism. Many of the regulated genes are associated with various diseases, which is why approximately 13% of all drugs approved by the U.S. Food and Drug Administration (FDA) target NRs [166]. Thus far, 48 NRs have been identified in humans [23].

Substances that form a complex with a biomolecule are usually called ligands.

A subclass of the Nuclear Receptor superfamily are Steroid Hormone Receptors (SHRs) that consists of 5 members, classified by their ligand:

- (ER) Estrogen receptor (Sex hormones: Extrogen)
- (PR) Progesterone receptor (Sex hormones: Progesterone)
- (AR) Androgen receptor (Sex hormones: Testosterone)
- (MR) Mineralcorticoid receptor (Aldosterone)
- (GR) Glucocorticoid receptor (Cortisol)

SHRs reside in the cytosol and get transferred into the nucleus upon hormone binding to interact with the transcriptional machinery [253]. that means they first interact with other proteins involved in the process of nuclear import.

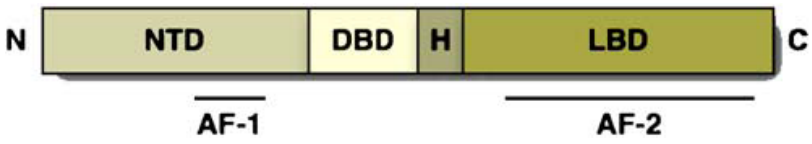

Figure 1.1: General schematic of steroid receptor functional domains. Adapted from [90].

Co-regulators are proteins that interact with transcription factors to either activate or repress the transcription of specific genes [81].

They all share a common structure [118] as displayed in Figure 1.1. The regulatory N-terminal domain (NTD) is the most variable in sequence between the different receptors, except for a region rich in negatively charged acidic amino acids [90] known as Activation Function 1 (AF1). AF1 has been shown to interact directly with the basal transcriptional machinery and other co-regulator proteins participating

in transcriptional regulation [43, 96, 121]. Close to the AF1 region is the centrally located, highly conserved, DNA binding domain (DBD), containing two zinc fingers that control binding to specific genes [65] via direct electrostatic interactions [129]. The DBD is followed by a conformationally flexible hinge region (HR) that controls the movement of the receptor to the nucleus [241]. The ligand binding domain (LBD), which is moderately conserved in sequence but highly conserved in structure between NRs is located at the C-terminal end.

In addition to its role in ligand recognition, the LBD of NRs is also the primary interaction site for sophisticated regulation by chaperones [97] and co-regulatory proteins [244]. The latter bind to Activation Function 2 (AF2), which undergoes a hormone-dependent conformational change to switch between co-activator or co-repressor binding [173].

In this work, the Ligand Binding Domain (LBD) of the Glucocorticoid Receptor (GR) was examined. The structural similarity of NRs implicates a common mechanism of function. Thus there is hope that knowledge gained about one receptor can be transferred to the whole group.

CHAPERONES An essential type of proteins are molecular chaperones. They support a vast variety of other proteins in fulfilling their functions [31]. Complex chaperone machines help proteins to reach their native conformation, support complex assembly, target damaged proteins to degradation and disaggregate protein aggregates [86, 114, 199, 247, 252]. Failure of these processes is the cause of fatal diseases like cancer, cystic fibrosis, and neurodegenerative disorders like Alzheimer's disease [16, 155, 186, 264]. Hence, chaperones often ensure quality control for the proteome of the cell.

Often, different chaperones work together to maintain proper function of their clients.

The primary molecular chaperones were discovered due to their elevated expression in response to high temperatures, the so-called heat shock response. Heat Shock Proteins (HSPs) are among the most highly expressed cellular proteins across all species [42]. They are well-conserved and account for 1 – 2% of all cellular proteins in most cells. Their most prominent representatives are Hsp70 and Hsp90. These chaperones were estimated to assist the folding of more than 10 – 20% of all proteins in eukaryotic cells [134]. An overview of the different chaperone mechanisms is given in [135]. A closer view on chaperone interaction with the Glucocorticoid Receptor (GR) that was under investigation in this work, is presented in Section 6.1.

The number refers to their molecular mass.

1.2 THE GLUCOCORTICOID RECEPTOR (GR)

This section describes the physiological pathway of the Glucocorticoid Receptor (GR). It demonstrates the importance of the protein for

the whole organism, its involvement in an intricate protein machinery and limitations of previous investigations.

The HPA axis is the primary neuroendocrine system that controls reactions to stress and regulates many body processes, including digestion, the immune system, mood and emotions, sexuality, and energy balance.

THE CLINICAL RELEVANCE OF GLUCOCORTICOIDS The natural glucocorticoid in humans is cortisol, a cholesterol-derived hormone secreted by the adrenal glands [105]. The synthesis and release of the hormone are under dynamic daily and longer term regulation by the hypothalamic-pituitary-adrenal (HPA) axis [22].

Approximately 20% of the genes expressed in human leukocytes are regulated positively or negatively by Glucocorticoids (GCs) [73]. GCs are involved in almost every cellular, molecular and physiological network of the organism and play a central role in critical biological processes, such as development, reproduction, metabolism, immune and inflammatory reactions, as well as central nervous system and cardiovascular functions [73, 256]. Physiological amounts of GCs are also essential for normal renal tubular function and consequently for water and electrolyte homeostasis.

GC signaling is nearly ubiquitously prevalent in the diverse organ systems (Figure 1.2). So it is not surprising that GCs are among the most prescribed drugs worldwide for the treatment of various immune and inflammatory disorders [244]. Their function is linked to a vast variety of diseases such as diabetes [100], rheumatoid arthritis [119], allergic rhinitis [19], asthma [105], leukemia [187] and depression [40, 182] (Figure 1.2).

In clinical applications mostly synthetic GCs are used due to their higher potency and specificity. The synthetic glucocorticoid Dexamethasone (DEX) used mainly in this work, is thought to be 25 times more efficient than cortisol [132] and does not bind to other receptor resulting in reduced adverse effects.

1.2.1 *The physiology of glucocorticoid signaling*

The physiological aspects of GC signaling have been recently reviewed with the focus on precision and plasticity [253], genomics [197], regulation [244], signaling pathways [105] and trafficking [243]. In the following, some of these aspects will be summarized.

GC BINDING TO THEIR INTRACELLULAR RECEPTOR After its synthesis in the adrenal cortex, cortisol is delivered to target tissues by transport proteins [23]. GCs function mostly by binding to their intracellular receptor. The 777-amino-acid-containing Glucocorticoid Receptor (GR) is a ligand-induced transcription factor that is part of the sizeable Nuclear Receptor (NR) super-family [253]. GR isoforms are expressed in nearly all vertebrate cells and tissue types [161] (Figure 1.2) and regulate numerous genes involved in various biological processes [90]. They are most prevalent in hepatic, nervous system,

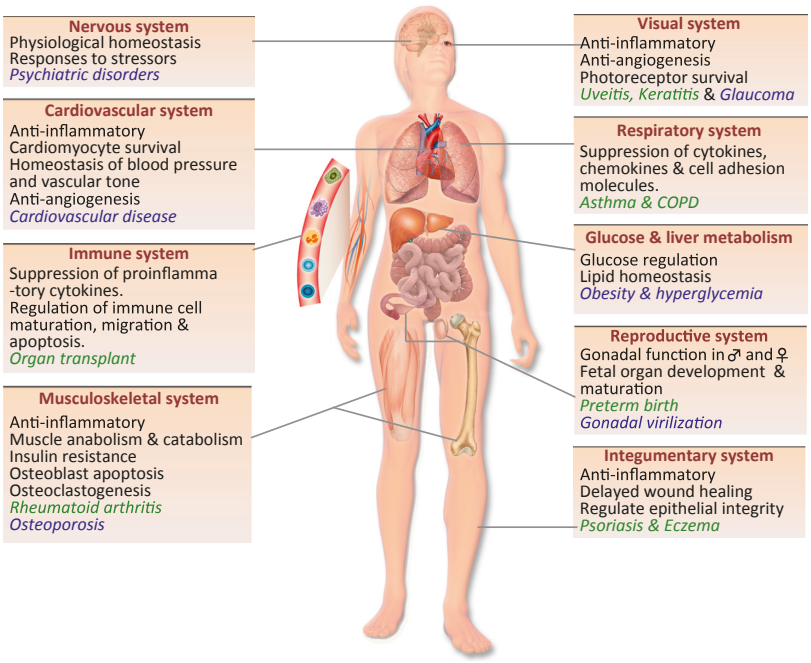

Figure 1.2: This schematic represents the roles of glucocorticoids in primary organ systems of the human body (black text), beneficial roles of glucocorticoids in the clinic (green text), and adverse outcomes in patients with elevated glucocorticoid levels (blue text). Adapted from [105].

and muscular tissues [18]. GCs can diffuse freely through the cell membrane due to their small size and lipophilic nature, and bind to the LBD of the GR.

The GR operates in a versatile manner, leading to diverse outcomes that are precisely determined by the given context of cell type and physiological state (recently reviewed by Sacta *et al.* [197]). Therefore, it is not surprising that its action involves an intricate interplay with co-regulator and chaperone proteins.

The ligand-unbound receptor is thought to reside in the cytoplasm, directly bound to Heat shock protein 90 (Hsp90). Hsp90 mediates the interaction with a multimeric chaperone complex, consisting of p23, immunophilins and other regulating proteins [39, 174, 178, 179]. This complex assists in GR maturation, prevents its degradation and promotes high-affinity hormone binding while inactivating other receptor activities, such as nuclear localization and DNA binding [253]. Upon hormone binding, the GR undergoes a conformational change that triggers its translocation to the nucleus [105] and the formation of either receptor homodimers or heterodimers with related NRs in the nucleus [202]. What this conformational change looks like remains unclear.

More details about the chaperone complex will be given in Section 6.1.

NUCLEAR IMPORT The conformational changes provoked by GC binding activate multiple functional domains, including nuclear-localization sequences within the hinge and LBD regions [253].

It has generally been believed that ligand binding to GR induces release from the Hsp90 chaperone complex, in a temperature-dependent manner, consequently exposing the nuclear localization sites before moving to the nucleus [48, 243]. However, recent studies suggest that the chaperone partners are needed in aiding transport and cytoplasmic-nuclear shuttling of GR [59, 71] and also participate in the transcriptional complex [68].

A coherent model of GR nuclear transport remains elusive, but an overview of the current model was reviewed by Vandevyver *et al.* [243]

GENE TRANSCRIPTION INSIDE THE NUCLEUS Inside the nucleus, assisted by interactions with different co-regulators, the GR either up- or down-regulates transcription of individual genes. Accessory proteins or co-activators, such as steroid receptor co-activator-1 (SRC-1) and Transcriptional Intermediary Factor 2 (TIF2), are essential for the transcription functions of the GR, many of which exhibit chromatin-modifying activities [23, 41, 93, 224]. More than 200 such co-regulators for nuclear receptors have been described, highlighting the versatility of GR interactions.

Transactivation or transrepression of genes is done either by direct binding of a GR homodimer to Glucocorticoid Response Elements (GREs), by cooperation with other TRFs or by interference with parallel signal transduction pathways [1, 46, 140, 149, 200].

For example, suppression of inflammation in disease such as asthma and chronic obstructive pulmonary disease happens by GR tethering with pro-inflammatory TRFs such as nuclear factor-κB (NF-κB) or activator protein-1 (AP-1) [74, 138, 161, 203].

Additionally to the nuclear transcription mechanism that usually takes a few hours, GCs have also been reported to exert non-genomic effects within minutes, for instance directly by membrane-bound or cytoplasmic GRs [14, 32, 105].

OPEN RESEARCH QUESTIONS To fulfill its function, the GR is embedded in an intricate regulatory network. The details of the underlying interactions are still far from being understood.

- What are conformational changes leading to the different GR activities?
- How are these changes transmitted to the chaperone complex to perform its different roles?
- How does the GR accomplish mediation of all the different interactions?

Answers for these questions call for a detailed understanding the underlying mechanisms on the molecular level. The LBD as the primary interaction site for ligand, chaperone and co-regulator binding is of crucial interest.

1.2.2 *The GR-Ligand Binding Domain (GR-LBD)*

The structure and function of the GR-Ligand Binding Domain (LBD) was reviewed in great detail by Bledsoe *et al.* [23], including a description of ligand recognition and an exhaustive list of mutations and their functional consequences.

In general, it is clear that the GR-LBD is a remarkably adaptable and flexible structure that enables the receptor to bind a broad range of ligands and perform a diverse array of signaling activities. Signal transduction, gene transcription, and transrepression are all regulated by ligand binding to the GR-LBD. Most of the actions are affected by the ligand-induced plasticity of the LBD. It ultimately dictates the various protein-protein and protein-DNA interactions [137].

As the different NRs show a strikingly similar three-dimensional structure [25, 147], knowledge about the GR-LBD function is hopefully universal for all NRs.

STRUCTURE OF THE LBD Structural investigations of GR-LBD have long been hindered by problems in solubilizing it. Using a stabilized variant F602S, a DEX-bound structure in complex with the co-activator TIF2 could be solved [24].

NR LBDs primarily consist of 11 to 12 helices, which are stacked together into a three-layer bundle (Figure 1.3A). Overall the DEX-bound GR-LBD comprises 11 α-helices and 4 β-strands forming two short β-sheets. Note that specific structural features change depending on the bound ligand. Arranged in an anti-parallel manner, the primary N-terminal helices 1 and 3 (blue) form one side of the bundle while helices 7 (light green) and 10 (orange) form the other. Between these two outer layers are helices 4, 5, 8 and 9 (cyan, green, yellow and orange respectively) that for the most part form the top portion of the domain and leave a cavity in the lower half of the protein. This cavity provides the space for the lipophilic ligand [23], in this case, DEX (white/red in sphere representation). The β-hairpin between helix 5 and 6 (green) forms the front portion of the ligand pocket.

The C-terminal helix 12 (red), known as the Activation Function 2 (AF2) helix, is thought to cover the ligand binding pocket and, as in other NRs, is believed to play a central role as a molecular switch that modulates the functional response to ligand binding [209, 259]. The extended β-strand following helix 12 appeared to be essential for stability as removal leads to a compromised receptor that was fount to be unable to bind a ligand [266].

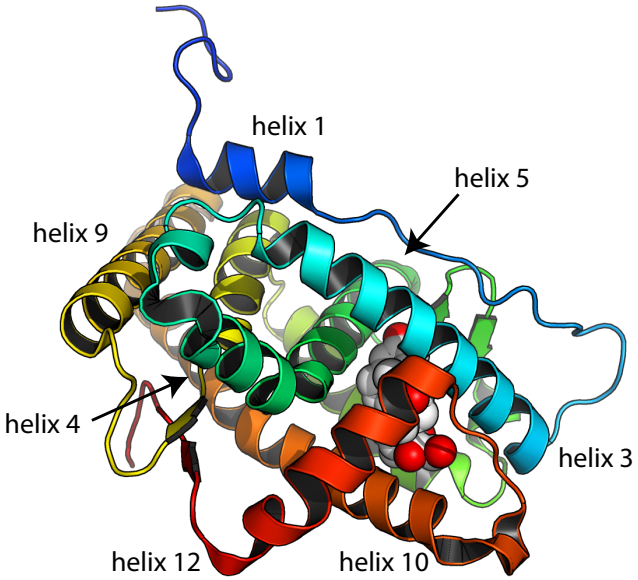

Figure 1.3: Structure of DEX-bound GR-LBD F602S (pdb:1m2z[24]) in cartoon style. Amino acid residues are colored using the rainbow scale from the N-terminal (blue) to the C-terminal (red) end. DEX is displayed as spheres and colored in white with red oxygen atoms.

Meanwhile, further structures with different ligands and co-regulatory peptides have emerged [69, 87, 109, 209, 254], demonstrating the flexibility of the LBD. However, the hormone-unbound apo-GR-LBD is not amenable to structural investigation and is therefore thought to be weakly folded and dynamic [15].

LIGAND BINDING The SHRs GR, MR, PR, and AR evolved from a common ancestor. They share high similarity in structure and sequence of their LBDs. Still, crucial architectural differences yield strict ligand selectivity [236].

The first crystal structure of the GR-LBD complexed with a ligand Dexamethasone (DEX) presented an intricate network of polar and hydrophobic interactions, which account for ligand selectivity. Each polar atom of DEX directly interacts with the GR-LBD [24]. Detailed information about the direct interactions between DEX and the GR-LBD residues can be found in [23]. Despite this strong binding specificity, the binding pocket in the GR-LBD is still extraordinarily adaptable and can accommodate a diverse set of ligands by slight rearrangements. DEX occupies only about 2/3 of the ligand binding pocket [24], similarly to the endogenous ligand cortisol [87].

Different LBD structures bound to various GR ligands exhibit extensive structural malleability within the LBD [109]. The binding of a range of potential ligands could confer different allosteric changes that account for ligand-specific alterations in regulatory outcomes.

By looking at structures of NRs bound to agonist ligands, it was assumed that the AF2 helix 12 forms the lid of the ligand binding pocket [23]. Direct interaction of AF2 residues with the ligand stabilizes its conformation [24]. In antagonist-bound structures the helix is displaced, removing this direct interaction [109]. This structural plasticity enables small molecule ligands to modulate the function of the GR.

An agonist is a type of ligand that binds to and activates the receptor to induce a biochemical response, whereas an antagonist blocks this response by binding to the same receptor.

To gain insight into the dynamics of hormone binding, Hydrogen Deuterium Exchange (HDX)-Mass Spectrometry (MS) was used [69], but the details of the conformational dynamics triggered by these interactions have remained elusive. Studies investigating the detailed conformational changes of SHRs associated with ligand binding and release are sparse [76].

The dynamic process, through which the hormone enters the binding pocket that is embedded inside the GR-LBD structure remains an open question; such as the conformation of the hormone-unbound receptor.

CO-REGULATORY PROTEIN BINDING As mentioned before, co-regulatory proteins that bind to the LBD in response to hormone binding are necessary for the gene transcription function of the GR in the nucleus. These large, multi-functional proteins can be viewed as readers of GR-mediated signaling. The co-regulators convert the integrated, signal-driven allosteric transitions at distinct receptor surfaces into context-specific transcription-regulating actions.

Structural analysis has shown that these co-regulators interact with the regulatory AF2 domain of GR-LBD [244] that is minimally comprised of helices 3, 4 and 12 [250]. These co-regulators associate with the ligand-bound GR mainly through a highly conserved short, leucine-rich, amphipathic α–helix, known as an LXXLL (L=leucine; X=any amino acid) or NR box motif [45, 88, 239]. Interestingly helix 1 also contains a LXXLL motif at the end, but interaction with its own AF2 has not been under investigation.

Figure 1.4A shows a structure of GR-LBD with bound antagonist (Mifepristone) and the NR box peptide of nuclear receptor co-repressor (NCoR, red). It illustrates how helix 12 is repositioned by antagonist binding, thus forming the binding site for the co-repressor. In comparison the agonist (DEX)-bound structure with the co-activator TIF2 peptide (light blue) is displayed (Figure 1.4B). The interaction with agonist ligand, such as DEX, aids in stabilizing helix 12 in a position so that it forms a shallow hydrophobic groove between helices 3, 4 and 12, serving as the AF2 [23].

The used peptide fragments represent only the GR-LBD binding site of whole the co-regulatory proteins.

These results illustrate the adaptability of the GR-LBD, again highlighting the demand for detailed insights on the molecular level to unravel all of its functional mechanisms. They demonstrate, how ligand binding can couple to the interaction with regulatory proteins,

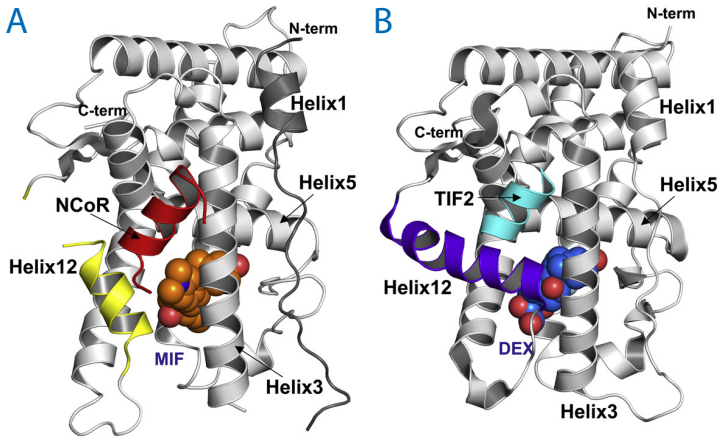

Figure 1.4: (A) Structure of Mifepristone (orange)-bound GR-LBD (pdb: 3h52[209]) associated with co-repressor NCoR peptide (red). (B) DEX (blue)-bound GR-LBD structure (PDB:1M2Z[23]) associated with co-activator TIF2 peptide (light blue). Adapted from [209].

presenting helix 12 as a central structural feature. The dynamics of these interactions and how they influence the stability and conformational dynamics of the LBD – and consequently the interaction with other proteins – still needs to be investigated.

The molecular chaperone Hsp90 will be introduced in more detail in Section 1.3.1.

CHAPERONE INTERACTION SITE Most of the surface for the interaction with the molecular chaperone Hsp90 has been mapped to the GR-LBD and a small region of the hinge located N-terminal to the LBD [97]. A number of studies have tried to define a specific region in the GR-LBD for interaction with Hsp90, which turned out to be challenging [108]. A reason might be that some of the residues taking part in the interaction require partial of local unfolding of the GR-LBD [44].

The LBD is thought to bind Hsp90 both as folding intermediate but also in its folded, native state [128, 185]. For the latter case, a structure of the complex was modeled, inferring an Hsp90 interaction surface of the GR-LBD.

So despite the central role of the Hsp90 complex for GR function, most details of the interaction remain elusive.

- What is the structure of the GR-LBD-Hsp90 complex?
- Are there different conformations?
- In which conformation does the GR-LBD interact with Hsp90?
- How does it influence stability and hormone binding?

To answer these and the questions mentioned above, a comprehensive understanding of the GR-LBD is of essential importance. This understanding should include the hormone-bound and -unbound GR-LBD structure, conformations, and dynamics.

1.2.3 *The labile nature of GR*

Several examples of partial purification from recombinant sources have noted the problematic nature of the GR [4, 33, 164]. One presumed reason for these challenges is the GR dependence on Hsp90 (see Section 1.3.2).

Also, the expression, purification, and biophysical characterization of only the GR-LBD have proven to be problematic due to the putatively low intrinsic stability and poor solubility [23, 215]. SHR LBDs, in general, are inherently unstable and extensive mutagenesis was required to enhance expression and crystallization [253]. For the GR-LBD one particular mutation, F602S – that was also used in this work – drastically increased its expression levels and made crystallization possible [24].

This mutation was found by sequence alignment with other NRs [23].

However, without bound hormone, the GR-LBD displayed a volatile nature, exhibiting unfolding and aggregation already at comparably low temperatures (10°C) even despite stabilizing mutations [113, 117, 128]. Hence, it was not amenable to structural investigations [69]. Folding studies using ensemble methods have been problematic due to solubility issues and refolding into its native configuration could not be achieved [139].

This strong tendency to aggregate in ensemble studies highlights the need for a new experimental approach to study GR-LBD properties and function.

1.3 THE GR AS A CLIENT TO STUDY CHAPERONE FUNCTION

Another interesting aspect of the GR is its strong regulation by the molecular chaperones Hsp70 and Hsp90 [243]. This chaperone dependence suggests that the GR and particularly the LBD, the primary interaction site for the chaperone machinery [97], may exhibit pronounced folding defects. This view is supported by the unstable nature of the GR-LBD discussed in Section 1.2.3.

As mentioned before, in their apo-form, SHRs are found in abundant protein complexes, the primary components of which are Hsp90 and its co-chaperones. Also, the unstable GR-LBD resides in the cytosol exclusively in complex with chaperones [113, 128, 176].

The importance of the complex chaperone machinery for the GR and many other signaling pathways is still far from being understood. One vital element to further elucidate the contribution of this machinery is to understand its mechanisms from the perspective of a client protein.

1.3.1 *The molecular chaperone Hsp90*

Heat shock protein 90 (Hsp90) is one of the most abundant and conserved molecular chaperones and a critical regulator of proteostasis under both physiological and stress conditions, essential in eukaryotic cells [210]. Hsp90 is required for the folding, maturation, activation and degradation of many hundreds of structurally and sequentially unrelated client proteins [185]. This fact makes Hsp90 a central modulator of essential processes ranging from stress regulation and protein folding to DNA repair, development, immune response, neuronal signaling and many others [58]. The Picard laboratory[2] maintains an extensive list of Hsp90 interactors. Due to the importance of Hsp90 in the regulation of many cellular proteins, it has become a promising drug target for the treatment of several diseases, which include cancer and neurodegenerative disorders as Alzheimer's and Parkinson's disease [130].

HSP90 AND CANCER Owing to the stressed environment in cancer cells, they often show highly elevated expression levels of Hsp90 [155]. Many oncogenic proteins, necessary for proliferation of cancer cells as tyrosine kinase Src and the tumor suppressor protein p53 are chaperoned by Hsp90 [255]. Oncogenic proteins are often mutated and consequently more dependent on chaperoning, which is why deactivating the Hsp90 machinery is more critical for cancer cells. Many Hsp90 related treatments are already in clinical trials [155].

There is an online database of current clinical trials of Hsp90 inhibitors at www.cancer.gov.

Hsp90 plays a central role in the function of the human body. Hence, it is not surprising that it is of particularly high scientific interest.

CURRENT KNOWLEDGE ABOUT HSP90 CONFORMATIONS A lot has been learned in recent years about Hsp90 structure, conformational dynamics and regulation by co-chaperones recently reviewed by Schopf *et al.* [210] and Radli and Rüdiger [185]. In recent Single-Molecule Force-Spectroscopy (SMFS) experiments the folding and assembly of Hsp90 was studied in-depth [102]. This kind of investigation has proven capable of unraveling details of conformational dynamics in great detail.

The use of SMFS techniques will be discussed in more detail in Section 2.1.

Hsp90 proteins function as dimers, where each monomer consists of three functional domains [3] and weighs roughly 90 kDa. They undergo substantial conformational changes between N-terminally unbound (open) and dimerized (closed) states [54, 218]. These conformations are associated with nucleotide binding and hydrolysis, both of which are required for chaperone function [163, 167]. Despite this, Adenosine Triphosphate (ATP) turnover has been measured to be slow [95]. More than 20 co-chaperones were discovered to inter-

A 90 kDa protein is rather abundant, compared to the average size of roughly 50 kDa in eukaryotes [116].

2 https://www.picard.ch/downloads

act with Hsp90, many of which stabilizing distinct conformations or recruiting clients [184, 192].

Hsp90 is an abundant, complex protein, exhibiting a variety of different conformations. More details about the current view on Hsp90 structure and the chaperone cycle related to GR interaction will also be given in Section 6.1.2.

CHAPERONING OF CLIENTS Comparably little is known about the mechanism how Hsp90 interacts and chaperones its substrates [106]. What makes Hsp90 unique in a way is that in contrast to other chaperones it is more selective in its clients as it interacts with proteins in a mostly folded state [103]. The diverse types of proteins supported by Hsp90 range from kinases, transcription factors, ligases to telomerases [154, 177, 234] with kinases and SHRs being the most extensively studied clients. A central function of Hsp90 is to shield hydrophobic residues that become temporarily exposed during initial folding or damage of existing proteins [112, 199, 257].

Hsp90 binding sites are usually extended over 50-170 residues [107, 128, 245]. Hsp90 is thought to bind its clients via a large number of low-energy contacts, which allows dynamic, transient interactions [107]. There are very few atomic structures of Hsp90 complexes [245].

The various clients of Hsp90 do not show structural similarity, and no universal binding motif could be identified. The only feature that the clients seem to have in common is their propensity to be unstable. Reproducing client dependencies discovered *in-vivo* has been challenging due to client instability. An example of an Hsp90 interaction with a stringent client successfully reconstructed *in-vitro* is the GR-LBD [113, 128].

Despite its high physiological relevance, the mechanism by which Hsp90 activates and matures clients is far from being understood. How the ATP-ase cycle couples to the chaperone cycle and for what reason ATP is consumed remain enigmatic. Also, what a client-Hsp90 conformation looks like is unclear, not to mention the dynamic pathway of complex association.

So on the one side, the actions of Hsp90 appear to be sophisticated to leave many questions unanswered. However, due to the involvement of the Hsp90 chaperone system in such a diversity of processes, there is hope that its function relies on some basic principles which allow for versatile support in protein function. Therefore, understanding the mechanisms of interaction with one client can help to elucidate many other vital processes.

1.3.2 *The GR strictly depends on Hsp90* in-vivo

SHRs represent the most stringent Hsp90 client proteins [234], as their maturation strictly depends on the interaction with Hsp90 [30].

Several studies have shown that Hsp90 is required for GR-LBD and many other signaling proteins, to bind ligand and become active *in-vivo* [26, 57, 174, 180, 188, 201, 243]. Hsp90 binds to the GR-LBD with low micromolar affinity [128]. Therefore, it is not surprising that the GR pathway is the most studied example of Hsp90 regulation [177].

It has been proposed that Hsp90 is required for proper folding of the GR and opening of the ligand binding pocket to allow ligand association [148, 156, 181], but also for the intracellular transport of SHRs, the regulation of their nuclear mobility, their recycling and for the regulation of their transcriptional output.

SHRs have served as model systems for illuminating the composition of the Hsp90 machinery [179]. The Glucocorticoid and progesterone receptors in particular, have been a rich source for identifying components, functional interrelationships, and complex pathways in the molecular chaperone machinery [39]. In this way also the requirement and role of many co-chaperones for activation could be discovered [5, 38, 177, 181, 219, 221] and many details of Hsp90-client interaction revealed [106, 176, 185, 196, 210].

Hence, SHRs remain the best-characterized examples of cytoplasmic and nuclear proteins relying on molecular chaperones for folding, stabilization, or functional modulation.

Nevertheless, many details of and reasons for the chaperone interaction, especially the question of what happens to the client upon chaperone interaction remain elusive.

1.4 OUTLINE

So far, much has been learned about the physiological pathway of the GR, its structure and interaction partners, but the details of its conformational dynamics in correlation with hormone binding and chaperone interaction remain unclear.

In particular, the pathway of hormone binding into the binding pocket of the GR, which is deeply buried inside the protein structure, has remained enigmatic. Whether the protein folds around a hormone-bound core or undergoes major structural rearrangements from a folded open to a bound closed structure is therefore still unresolved.

The strong chaperone dependence suggests that the GR-LBD, in particular, may exhibit pronounced folding defects. But even the simple question of whether chaperones are necessary for proper folding of apo-GR-LBD *in-vitro* is unanswered, as the strong tendency to aggregate hampers folding studies in bulk experiments.

In this study, single-molecule optical tweezers experiments were used to monitor the conformational dynamics of folding, hormone binding and chaperone interaction of the GR-LBD and thus to investigate its folding capability, stability, and reason for chaperone interaction.

Basic questions were:

- Is an isolated GR-LBD molecule capable of reversible folding?
- What is the apo-structure of the GR-LBD?
- What is the pathway for hormone binding and
- how does it influence conformation and stability of the protein?
- How do chaperones interact with the GR-LBD?

OUTLINE In Chapter 2 I introduce and describe the Single-Molecule Force-Spectroscopy (SMFS) experimental setup used in this work. It also contains a description of new methods I developed and a microfluidics setup I redesigned and implemented. Chapter 3 describes the theory and methods employed to analyze the measured data. The next three chapters summarize the results. In Chapter 4 I describe the receptor's native conformational dynamics associated with hormone binding, whereas Chapter 5 focuses on folding and stability of the GR-LBD and its intermediate states. The action performed by the Hsp70 and Hsp90 chaperone system on the receptor is presented in Chapter 6. Finally, I summarize the results and propose further experiments in Chapter 7. The appendix contains additional results (Appendix A), detailed protocols (Appendix B) and supplemental figures (Appendix C).

Part II

EXPERIMENTAL APPROACH, THEORY AND METHODS

2

EXPERIMENTAL SETUP

2.1 SINGLE-MOLECULE FORCE-SPECTROSCOPY (SMFS)

Proteins and in particular protein complexes are dynamic structures [91, 262]. Their functional pathways are often determined by transient interactions and subtle conformational changes on the nanometer scale [124, 131, 170].

Structural and functional analysis of proteins at the atomic level has been revolutionized by high-resolution X-ray crystallography [217], nuclear magnetic resonance (NMR) spectroscopy [231], cryo-electron microscopy (cryo-EM) [152] and small-angle X-ray scattering (SAXS) [142]. These methods provide atomic-resolution or near-atomic-resolution snapshots of protein conformations [91]. They however lack the detailed kinetic information to reconstruct the complete functional trajectory. Additional technical limitations include the need for either homogeneous protein crystals or small soluble proteins [262].

Dynamic processes such as protein folding, complex assembly and ligand binding have been studied by classical biophysical ensemble measurements. These use fluorescence, circular dichroism, absorbance and other ways to detect overall properties of protein states yielding average kinetic characteristics of protein ensembles [91]. Yet, subtle structural rearrangements, distributions of heterogeneous configurations and meta-stable transition states remain hard to capture using these techniques. For instance, unstable conformations of proteins requiring the help of chaperones are problematic to investigate in particular, due to their tendency to aggregate in ensembles [128].

Single-molecule techniques have evolved to uncover the fine details of protein conformational dynamics associated with their functional pathway [49, 143]. These measurements allow to precisely follow the conformational trajectories of single-molecules during ligand-binding, interaction with other proteins and unfolding. These observations reveal also transient intermediate states and complex kinetic pathways related to the proteins function [262]. They bring to life a dream that biochemists have had for many years — watching a single protein molecule functioning in real time. While in a typical structure-function relation study, proteins are changed by mutagenesis and its functional effect is probed via biochemical means, single-molecule spectroscopy gave a whole new meaning to the "structure-function relation" by observing the real-time conformational dynamics of individual biological macromolecules while functioning [153, 263].

Summarized under the term Single-Molecule Force-Spectroscopy (SMFS) are new tools that directly apply forces on single molecules and measure their mechanical response [98, 158]. These methods are unique in their ability to actively manipulate single proteins. This ability makes them a particularly versatile technique, as the investigated protein can be promoted into certain states to precisely address specific questions about its function.

Optical tweezers are a SMFS technique that is suitable to measure low forces with high resolution in space, time and force and will be described in the next sections.

2.2 SMFS USING OPTICAL TWEEZERS

The potential formed by these laser beams, in which the particles are kept, is also called an optical trap.

The working principle of optical tweezers is based on the ability of a strongly focused laser beam to trap micron-sized particles. This principle was first demonstrated by A. Ashkin in 1970 [7, 9] and later used for trapping single cells, viruses and bacteria [10, 11]. To investigate single molecules, they can be tethered to a micron-sized bead, which is held by an optical trap. Measuring the deflection of the laser beam due to displacement of the bead from the trap center, the force response of the molecules can be measured. With this method, a variety of topics could be addressed, like elastic properties of DNA [222, 248], mechanics of RNA polymerase [249], the mechanism of molecular motors [28, 34] and the folding of single proteins [36].

The next generation of optical tweezers, which was also used for this work, uses a combination of two optical traps. The molecule of interest is tethered between two beads, each confined in an optical trap produced by the same laser as described in the following sections (2.3 and 2.4). This method significantly reduces noise and drift by mechanically decoupling the measurement from the rest of the system. By using the differential signal of both beads the signal is further improved as it eliminates any perturbations in the laser beam path acting on both traps [144]. In that way remarkable force resolutions on a sub-piconewton scale can be achieved allowing the investigation of complex protein folding networks [227], ultrafast kinetics of tiny biomolecules [270] and subnanometre enzyme mechanics [170].

2.3 THE OPTICAL TWEEZERS SETUP

TRAPPING A PARTICLE IN A FOCUSED LASER BEAM. To illustrate and understand how a small particle can get trapped in a focused laser beam one can use simple geometric ray optics [8]. Light is refracted by an object with different refractive index than the surrounding medium. This changes the momentum of the refracted photons, which in turn results in a force pulling the particle. Because of the gaussian profile of the laser beam, there are more photons refracted

from the center, thus the sphere is pulled towards the center (*gradient force*) [233]. As the light is also reflected backwards, in a straight laser beam the particle would get pushed along the beam (*scattering force*). Using a strongly focused beam creates also a backwards gradient force and enables a stable 3D potential minimum. This can be realized by a lens with high Numerical Apperture (NA) such as an objective. A descriptive view on the optical forces can be gained by playing with one of the many web applets such as on the DiLeonardo Lab homepage[1].

An optic ray description is only correct in a regime, where particles are significantly larger than the wavelength ($\lambda \ll d$, called *Mie regime*). The trap works also in other regimes ($\lambda \gtrsim d$), but the mathematical treatment is more complex [159, 233, 237].

THE OPTICAL TWEEZERS SETUP USED IN THIS WORK To create and manipulate such optical traps, different custom-built, high-resolution dual-trap optical tweezers setup with back-focal plane detection designed by B. Pelz was used. A schematic overview of the setup design is shown in Figure 2.1. The setup has been described in detail before [85, 169].

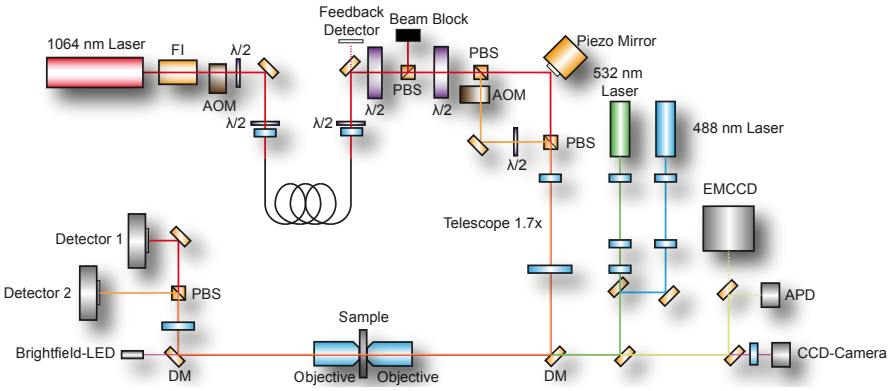

Figure 2.1: Optical tweezers design (adapted from [169]). The trapping laser light is shown in red and orange, fluorescence excitation at 532 nm in green and 488nm in blue. Light green represents the emitted fluorescence light. If not labeled otherwise, orange rectangles correspond to mirrors and blue rectangles to lenses. FI: Faraday isolator, AOM: Acousto optical modulator, PBS: Polarizing beam splitter cube, DM: Dichroic mirror, APD: Avalanche photodiode

To summarize: A TEM_{00} mode (yielding a Gaussian intensity profile) of a Nd:YVO_4 solid state laser with a wavelength of $\lambda = 1064\,\text{nm}$ is used. It is split into its two polarization components forming two beams that create two independent traps in the sample chamber. The laser intensity of the two beams can be adjusted separately by motorized $\lambda/2$-plates. One of the beams can be steered by a piezo mirror stage to move the trap.

1 http://glass.phys.uniroma1.it/dileonardo/content/apps/trapforces.php

For historical reasons the trap created by this second beam will still be called the fixed trap.

For some of the experiments a similar setup was used, designed by U. Merkel. The main difference for this setup is that the second beam additionally passes through an Acousto-Optic Deflector (AOD). that allows shifting the position of the second trap on a 10 µs-time-scale.

The beams are recombined and expanded by a telescope to overfill the back aperture of a high-numerical-aperture objective (NA = 1.27) that creates the optical traps in the sample chamber. In this work spherical silica beads with a diameter of 1 µm and a refraction index of 1.47 were trapped. The light, forward scattered by the beads was collimated by an identical objective and monitored on two separate Position Sensitive Detectors (PSDs). By projecting the back-focal-plane of the collimator onto the PSDs, the relative displacement of the bead center from the trap-center (further called deflection x) was measured.

THE TRAPPING POTENTIAL The trapping potential in the x-y-plane perpendicular to the beam direction can be considered Gaussian. For small deflection (here up to $x \approx 100\,\text{nm}$) the potential can be approximated by a parabola. that means the restoring force F is proportional to the deflection ($F = k_T \cdot x$). The trap stiffness k_T can be changed by adjusting the laser intensity and calibrated for each trap [238]. The error of this calibration is assumed to be about 10%. Here values between 0.2 pN/nm and 0.3 pN/nm were used.

Data were acquired at a sampling frequency of 150 kHz, downsampled and stored at 30 kHz. The measured deflection signals of the two traps were corrected for crosstalk [13] and the sum of the signals multiplied by the effective trap stiffness of both traps $k_{eff} = (k_{T1}^{-1} + k_{T2}^{-1})^{-1}$ to yield the force signal.

2.4 THE DUMBBELL ASSAY

To exert and measure the force on a protein with optical tweezers, the molecule of interest needs to be tethered between two beads that are trapped in the two laser beams as illustrated in Figure 2.2. This is called the dumbbell configuration.

The principles of this assay were described before [35]. The detailed assembly protocol and protein sequence are given in Appendix B. To summarize, cystein residues were introduced at the protein termini, which could then get covalently linked to maleimide modifications on short oligo-nucleotides (34 bp). These can then hybridize to a complementary single-stranded overhang of 180 nm-long dsDNA linkers that carry either a digoxygenin or biotin modification on the other end.

This linker-protein-linker construct was incubated with anti-digoxygenin functionalized beads. These beads were added to the sample chamber together with streptavidin functionalized beads. By mov-

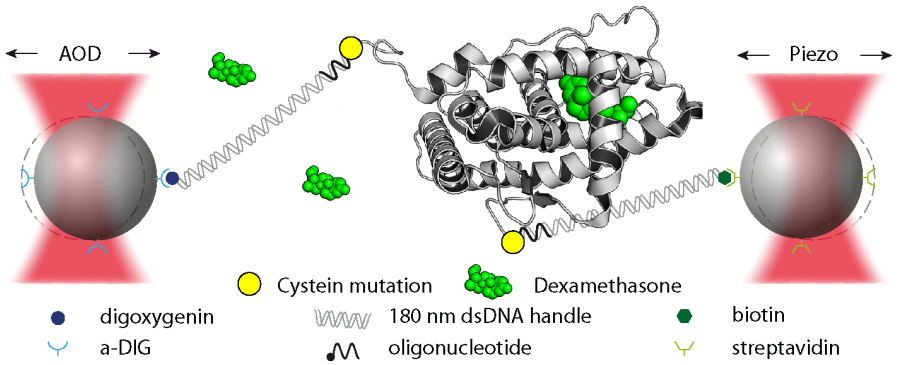

Figure 2.2: Schematic of the dumbbell assay used to exert and measure force on single proteins. DEX-bound GR-LBD (pdb structure: 1*M*2*Z*) is linked to dsDNA linkers via mutated cystein residues binding to maleimide-modified oligonucleotides. These linkers tether the protein to 1 µm sized silica beads via antibody interaction. The beads held and moved by the infra-red optical traps.

ing the sample chamber in the optical tweezers setup, two different types of beads were trapped. One of the two bead types was fluorescently labeled. So they could be distinguished on the EMCCD camera when turning on the 532 nm laser (shown in Figure 2.1). The dumbbell was finally formed by bringing the beads in close proximity to each other.

DETECTING FOLDING AND UNFOLDING EVENTS The transition of a folded structure tethered between two beads into an unfolded polypeptide increases the extension of this construct as illustrated by Figure 2.3. If, and only if a force is applied on the construct, the increase in extension leads to a relaxation of the trapped beads towards the laser foci. The concomitant decrease in force and increase in extension can be measured as described in Section 2.3.

The length at maximum physically possible extension of a polypeptide is also called its contour length.

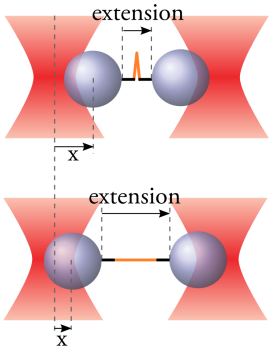

Figure 2.3: Measuring unfolding events with optical traps. The deflection x of the beads from the laser trap centers changes upon a changing extension of the protein structure (orange). Not drawn to scale. Adapted from [83].

The constant parameters in the setup during folding events are the trap distance d and the force bias that is defined as the force experienced by the completely folded protein structure at a given trap distance.

From the measured force F, the extension of the tether e can be calculated as described in Section 3.1.

2.5 BIOCHEMICAL METHODS

The details of biochemical preparation, protein constructs, chaperones, peptides and used buffer conditions are described in Appendix B.

2.6 MEASUREMENT MODES

To answer specific questions about the characteristics of a protein, different measurement modes can be used. They differ in the pattern of the trap distance variation over time and can serve to actively probe and investigate certain conditions of the protein. Keeping the trap distance temporarily constant at different positions reveals equilibrium properties of the investigated molecule, whereas fast changes of applied force can drive the protein out of equilibrium, broadening the range of accessible information.

Observing the change in kinetic properties at different forces can reveal additional information about the underlying folding pathways.

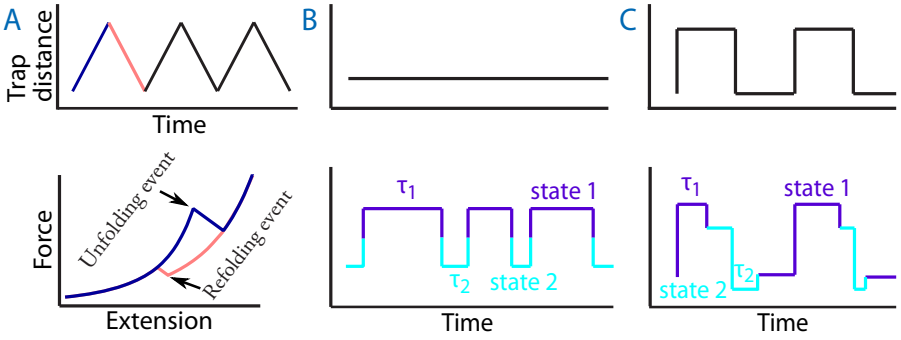

Figure 2.4: Visualization of different trap driving pattern. The time axis of (B) and (C) are equal for trap distance and force trace. (A) Trap distance for consecutive stretch-and-relax cycles (above). The force vs. extension curve measured during increase (blue) and decrease (pink) were usually overlaid for analysis (below). (B) In passive-mode, the trap distance is held constant (above) while observing fluctuations of a protein structure between a folded (high force, purple) and unfolded (low force, cyan) state (below). (C) During a force-jump assay, the trap distance is quickly switched between high and low forces (above) triggering unfolding (purple to blue) and refolding (cyan to purple) transitions (below).

2.6.1 *Stretch-and-relax cycles*

The stretch-and-relax cycles were used to initially determine the unfolding pattern of the protein, to identify the force range of unfolding and folding transitions and to examine its ability to refold (Figure 2.4A).

The distinct unfolding pattern of a native protein is also called its fingerprint as it can identifies its native structure.
This driving pattern is sometimes also called force-ramp pattern.

To this end, the optical traps are moved apart until the protein completely unfolds (blue part). Afterwards the trap distance is reduced again to allow the protein to refold (pink part). For the analysis of these experiments, the force F was plotted against the tether extension e (Figure 2.4A lower panel). The contour length gains ΔL associated with unfolding and refolding events can be determined as described in Section 3.1.

Comparing the total contour length gain of the complete unfolding with the number of amino acids in the protein structure serves as evidence that the protein was completely folded. The force vs. extension traces could also be used to determine non-equilibrium unfolding rates using a method proposed by Oberbarnscheidt *et al.* [162].

At the beginning or at the end of each experiment, stretch-and-relax cycles were performed to verify that the tethered construct was the native protein and to determine the elastic properties of the tether. The latter is needed for the calculation of free energy stored in the system (compare Section 3.3), since each tether slightly varies in its properties.

USED PARAMETERS A constant relative trap velocity of 500 nm/s was used if not stated otherwise. Force vs. extension traces displayed in this work were usually smoothed by a running average of 21 points for pulling with 500 nm/s and of 201 for pulling with 50 nm/s.

2.6.2 *Passive-mode*

Passive-mode measurements are mainly used to monitor equilibrium fluctuations between different folding intermediate states and to extract their free energy differences, transition rates and contour length gains (Figure 2.4B).

The traps are held at a constant distance, applying a certain force bias to shift the equilibrium from folded to more unfolded states. Thus, depending on the applied force bias, fluctuations between all folding intermediate states can be observed. Note that while keeping the trap distance constant the force changes when the protein changes its conformation and thus the extension of the tether.

The force bias *is defined as the force experienced by the completely folded protein at a certain trap distance.*

Hence, while keeping the force bias constant, each folding intermediate state experiences slightly different forces.

The measured forces were transformed into contour length as described in Section 3.1, using the elastic properties determined by the

stretch-and-relax cycles before or after the passive-mode experiments Section 2.6.1. The free energies of folding intermediate states were calculated as described in Section 3.4.1 and kinetic parameters were extracted as described in Section 3.4.

USED PARAMETERS If not mentioned otherwise the 30 kHz data was smoothed by a running average of 101 points (displayed as black lines).

2.6.3 *Force-jump*

Passive-mode experiments are well suited if under certain conditions all necessary transitions occur on an accessible timescale. If the observed kinetics involve very slow transitions, it may take a long time to observe the required amount of events at equilibrium.

This can be also an issue if the transition of interest is fast, but the back reaction is slow. For example as unfolding is very slow at low forces, measuring refolding events in passive-mode would take a long time and vice versa. To overcome this limitation, the force-jump method can be used, in which the forces on the protein are continuously altered between low and high loads, similar to chemical double-mixing techniques [150, 213, 268](Figure 2.4C).

During the high force phase, the protein was driven to unfold while it could refold during the low force phase. Low and high force phases were analyzed separately as described in Section 3.5.

The AOD was used to rapidly switch between a shorter and longer trap distance on a 10 µs-time-scale [84]. This sudden switch of trap distance is necessary to ensure the following transition to be probed under well-defined conditions.

This method additionally allows to measure folding kinetics at very low or even zero-force that cannot be observed directly in single-molecule mechanical experiments since a measurable signal depends on application of load. In 2012 this method was applied for the first time using an optical trap to measure the folding rates of Spectrin repeats in the low force regime ($0 - 5\,\mathrm{pN}$) (unpublished data), demonstrating the agreement of zero-force rates with ensemble measurements [214] and validating the model of rate extrapolation as described in Section 3.4.2.

The extrapolation of rates from experiments under force is under ongoing debate.

APPLICATION IN THIS WORK In this work the method was applied in two slightly different ways:

1. To measure hormone-binding kinetics to a folded state at zero-force.

2. To investigate the force-dependent refolding kinetics from the completely unfolded state near zero force.

The applications differed in the force applied during the high force level. The protein was either promoted into an unbound but folded, or into a completely unfolded state. Also different frequencies of switching between the force levels were applied to account for the different kinetics and to optimize the amount of events per time. As the protein investigated in this work also showed an increased probability to get damaged irreversibly in the unfolded state, the assay was performed in a way to minimize the time for the protein to be unfolded.

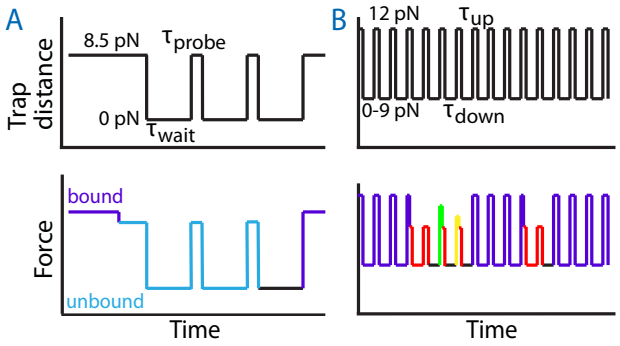

Figure 2.5: Two different applications of force-jumps. The upper parts describe the control of trap distance. The lower parts illustrate the measured force. (A) Slow variation between zero- and high force phase to promote unbinding without unfolding. (B) Automated switching between low and high force to promote complete unfolding and refolding.

USE OF FORCE-JUMPS TO MEASURE HORMONE BINDING As described in Chapter 4, the protein investigated in this work exhibited slow ligand dissociation rates at zero-force which could be drastically increased upon application of force (Section 4.4).

To investigate the rebinding rate to a folded protein at zero-force, a force bias of around 8.5 pN was applied to promote hormone dissociation but avoid unfolding of the protein Figure 2.5A. After the dissociation was observed, the force-jump pattern was started manually.

The force-jump pattern included the repeated reduction of force to 0 pN for a defined time τ_{wait} with subsequent increase to the original force for a short time $\tau_{probe} = 200$ ms to test whether hormone was bound. $\tau_{probe} \ll \tau_{wait}$ was chosen to avoid eventual binding during the high force phase. Binding during the high force phase were excluded from the analysis of the zero-force binding rate.

Choosing too long τ_{wait} would result in binding events for most attempts, which leads to increased statistical error. A shorter τ_{wait} increases the probability of binding during the high force phase rather than at zero-force. A longer τ_{wait} also gives the system more time to equilibrate at zero-force, which is good to account for slow processes.

Here, τ_{wait} was chosen to yield an expected chance of rebinding of about 50%, assuming the same rebinding rate as that measured under force.

USE OF FORCE-JUMPS TO MEASURE REFOLDING To investigate the refolding at low forces, an automated continuous switching was applied between a high force level, for $\tau_{up} = 30\,\text{ms}$ and a low force level for $\tau_{down} = 200\,\text{ms}$. The high force bias of 12 pN was chosen such that the protein was stable in its native state, but an unbound or partially folded protein would be reliably unfolded in each high force phase. Refolding could be excluded during the high force phase. Hence, the signal observed during the high force phase reports on the extent to which refolding had occurred during the preceding low force phase. The force bias during the low force phase F_{ref} was varied between 0 and 9 pN.

τ_{up} was chosen in a way to minimize the time the protein spends in the unfolded state, but long enough to completely unfold partially folded protein states. τ_{up} was also long enough to detect the distinct kinetics of the native state, once reached.

τ_{down} was chosen to be short enough to have the time resolution for the refolding kinetics involved in the measured force range. At the same time it was chosen to be long enough to promote refolding and avoid unnecessary long time of the protein spending in the unfolded state at the high force level.

2.7 ADDITIONAL ASSAYS

CHAPERONE INTERACTION AT ZERO-FORCE To probe the interaction of the Hsp70 system with the DEX-unbound GR-LBD at zero-force, the protein was incubated overnight at 30 nM DEX and about 1−3 h before the experiment with 6 µM of Hsp70 and 600 nM Heat shock protein 40 (Hsp40). Afterwards a protein-DNA tether was formed between the beads and the first force vs. extension trace was analyzed.

RECOVERY TIME AFTER CHAPERONE INTERACTION AT ZERO-FORCE To measure the recovery time after the chaperone-induced unfolding – $\tau_{recover}$ –, the force on the GR-LBD was reduced and it was kept at zero-force in presence of the various chaperone systems in solution. To get a read-out for the protein state, every 6 s, a stretch-and-relax cycle was performed to check to what extent the protein had refolded.

$\tau_{recover}$ was analyzed as the total time after the complete unfolding of GR-LBD until the first occurrence of its native *open-closed* fluctuations during the stretch-and-relax cycles.

The fact that the waiting time at zero-force was interrupted by the stretch-and-relax cycles which possibly influenced the dissociation of

chaperones was neglected here. In case of the stretches with no detectable structure the force does not put any significant energy bias on the system. In most of the other cases, the observed transitions during the stretching appeared to be reversible equilibrium transitions, indicating that the protein state remained unchanged after the relaxation of force.

2.8 MICROFLUIDICS FOR THE OPTICAL TWEEZERS SETUP

To make the optical tweezers setup more versatile and to address further complex questions in particular linked to protein-protein interactions, a microfluidics system was integrated during this work.

The main idea of using microfluidics in combination with optical tweezers is to change the environment of the protein under investigation in real time. This adds one more dimension to the possibilities of manipulating the protein and directly observing its reaction.

The rapid change of protein environment during the measurement is achieved by using a flow cell with different streams of various solutions. By moving the flow cell relatively to the optical traps, the protein can be transferred from one stream to another.

ADVANCES THROUGH MICROFLUIDICS A general advantage of the ability to switch solution conditions during the investigation of a protein is to directly observe and compare the effects induced by the presence of different salt conditions, or interaction partners back-to-back for the very same molecule. This rules out any interference with the observed effect caused by heterogeneity of the combined protein-DNA-bead-trap system. It also allows to ensure that the protein is in a functional state before the probed interaction. In addition, also the reversibility of certain interactions can be probed. By bringing the protein back to the standard conditions, the native functionality of the protein can be tested after an interaction. The controlled timing of switching conditions for interaction also allows to better evaluate the association and dissociation rates, in particular if more than one molecule interacts.

In more complex cases, for example if several different proteins interact with the tethered protein, questions about the sequence of interactions and thus the pathway of complex formation can be addressed. A possible question is: Do chaperone 1 and 2 have to pre-assemble before interacting with the protein or does chaperone 2 also bind to the protein-chaperone 1 complex?

The microfluidics setup also opens the opportunity to directly test interactions of the protein in different states. The tethered protein can be first promoted into a certain state before being exposed to interaction partners. On the other way a complex that is formed in

the absence of a ligand in solution could be afterwards tested for the ability to bind the ligand after complex formation.

These and further ideas allow many new questions to be addressed at the single-molecule level, in particular when it comes to multi-component protein-protein interactions.

2.8.1 *Microfluidics system by Lumicks*

To introduce a laminar flow into the sample chamber (compare Section 2.3), a commercially available microfluidics system (Figure 2.6A) was purchased from Lumicks[2] and customized for integration into the used optical tweezers setup. This system works by creating a controlled pressure on the content of 5 syringes which are connected via valves and silica tubes to the inlets of a monolithic glass flow cell. Adjusting the pressure controls the flow velocity inside the flow cell.

COMPONENTS OF THE SYSTEM The components of the microfluidics are displayed in Figure 2.6B and C. A pressure chamber (2) was connected to three air pressure systems (with different Δp) via three separately computer controlled valves (1). One was connected to a system with $\Delta p \approx 3\,\text{atm}$ for application of high flow, one to a system with $\Delta p \approx 0.2\,\text{atm}$ to fine tune low pressure differences and one to the surrounding atmospheric air ($\Delta p = 0\,\text{atm}$) to vent pressure. The pressure in the chamber was measured by a sensor (3). By quickly controlled opening and closing of the valves for fractions of seconds, the pressure in the chamber could be adjusted with a precision of $\Delta p = 0.01\,\text{atm}$.

The pressure is transmitted to 5 syringes (1 ml) containing the different solutions (4). The syringes were connected to valves (5) via short PEEK tubes with an inner diameter of 0.25 mm. The valves allowed to control each stream individually (on and off). The valves were connected to the microfluidic chip via silica tubes (6 in Figure 2.6C) with an inner diameter of 0.15 mm and a length of about 10 cm.

INTEGRATION INTO THE CURRENT SETUP A custom holder (7 in Figure 2.6C and D) was designed and created to mount the microfluidic chip (8) in the same way as the original holder (Figure 2.6A) but to exactly fit into the current setup by replacing the standard sample chamber holder (9) in front of the objectives. In this way the flow cell was positioned such that all relevant regions are accessible by the foci of the objectives in all three dimensions.

Figure 2.6B and C show the installation of the microfluidics system located above the back objective of the optical tweezers setup. The system was installed such that the standard sample chamber holder

2 https://lumicks.com/u-flux-laminar-flow-microfluidics/

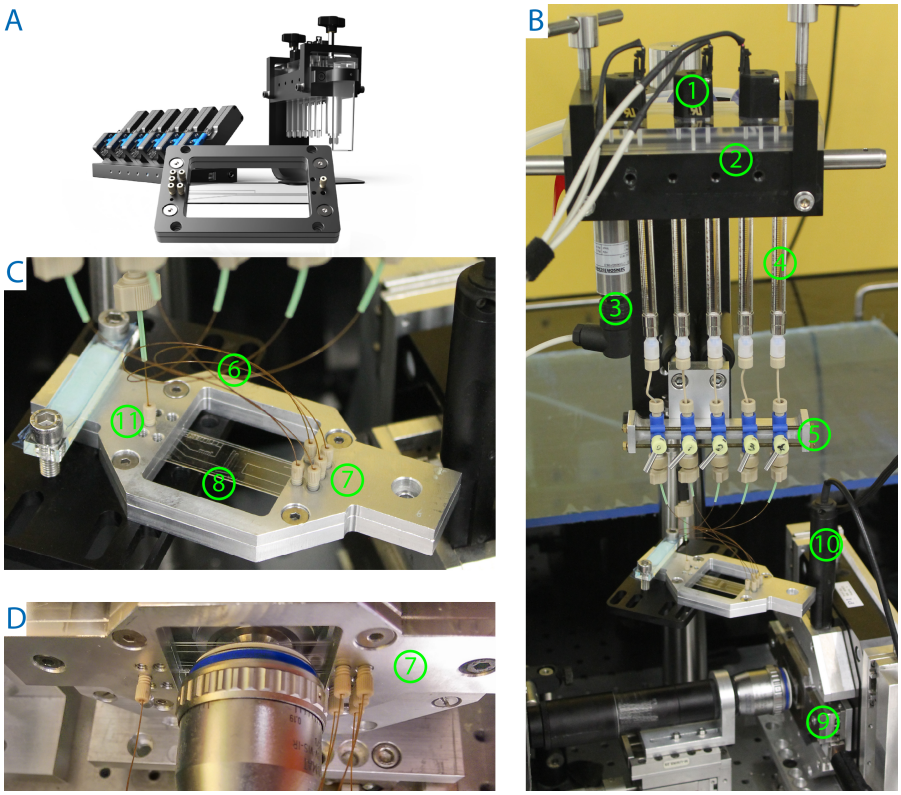

Figure 2.6: Microfluidics system. (A) Product image (c) Lumicks. (B) Custom implementation for optional usage at the optical tweezers setup. (1) computer controlled valves for (2) pressure chamber (3) pressure sensor (4) syringes (5) valves (9) holder for standard sample chamber (10) computer controlled stepper motor. (C) Focus on microfluidic chip. (6) Silica tubes (7) custom chip holder with inlets. (D) Microfluidic chip installed between the optical tweezers objectives.

(9) could be optionally replaced by the flow cell holder (7). It could be moved up and down and rotated in order to move and install the flow cell holder between the optical tweezers objectives (as in Figure 2.6D). The tubes were kept as short as possible to avoid dead volume, settling of beads in the tubes and diffusion of oxygen.

To move the optical traps and thus the protein relative to the flow cell, two stepper motors (10) were used to move the flow cell independently in x- and y-direction relatively to the optical traps.

As gravitation already produced quite high flow velocities, the outlet from the flow cell (11) was connected to a long, thin FEP tube, producing high flow resistance to inhibit gravitational flow (not displayed). For cleaning procedures the outlet was switched to a shorter tube.

2.8.2 *Design of microfluidic chip*

Figure 2.7: (A) First design of microfluidic chip. The five different channels (purple) are connected to the inlet holes (shaded circles). They are then combined and connected to the outlet hole. (B) Etching geometry of microfluidic chip channels and inlet holes.

The first design of the monolithic microfluidic flow cells produced by Lumicks is displayed in Figure 2.7A. They had a size of 60 × 15 mm and an overall thickness of 445 µm and were made of D263 optical quality glass. A cross section through the flow cell is displayed in Figure 2.7B. The channels were wet etched into the lower 270 µm thick part with an etching radius of 100 µm. that left 170 µm of glass underneath the channels, which resembled the thickness of the glass slides used for the standard sample chambers. The inlets (shaded circles in Figure 2.7A) were powder blasted holes in the upper 175 µm part of the flow cell. The 5 different flow channels entered from the left and were connected to an outlet as a combined main channel.

Note that due to the etching, the channels will have round edges on one side.

CAPTURING BEADS IN THE FLOW CELL The chip was placed in a landscape orientation. Channels 0 and 1 (as in Figure 2.7A) were used to continuously flush in the two different types of beads as illustrated in Figure 2.8. The beads were captured in front of the channels entering from the left side. The two optical traps were created left and right of each other. The first bead could be kept in the right trap while moving to the upper channel and capturing the second bead in

the left trap. Hence, a second bead falling into the right trap could be avoided.

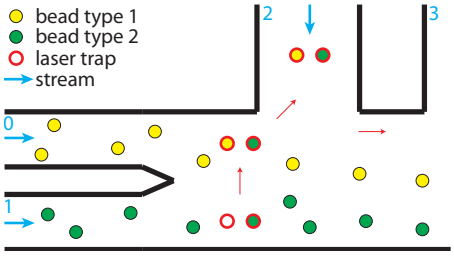

Figure 2.8: Method to capture beads an transfer them into the measurement channel in the microfluidic flow cell. The red arrows indicate the process of capturing one bead type after the other and the movement into the measurement channels.

After catching the beads, they were transfered into channel 2, and subsequently 3 and 4, for the measurement. The measurements were performed under constant flow. Entering the channels ensured well-defined solution conditions. To avoid an asymmetric influence on the force measurement due to the flow dragging on the beads a stream perpendicular to the distance between the beads was desirable during the measurements.

As the silica tubes sometimes get clogged to different extent, the parallel streams in the main channel would not reliably exhibit the same width.

ISSUES WITH THE OLD FLOW CELL LAYOUT The first layout of the channel geometry on the microfluidic chip had several issues. First of all, the distance of the separate channels entering into the main channel were too far from each other to be reached with the optical traps due to confinement created by the objectives (9 mm maximal distance, compare Figure 2.7A).

It turned out that a certain minimal flow was required for the bead channels (0 and 1 in Figure 2.7A), otherwise the amount of beads reaching the main channel continuously reduced as they possibly started to settle earlier in the channel. The settling of beads started at flow velocities roughly below 400 µm/s. The flow in the measurement channels (2,3,4 in Figure 2.7A) on the other hand is required to be rather low, to influence the force measurement as little as possible. In the first layout all channels had the same width of 500 µm resulting in similar flow velocities in all channels.

According to Stokes' law, a flow of 100 µm/s produces a frictional force of $F_d \approx 1$ pN on a 1 µm sized sphere in an aqueous solution.

NEW FLOW CELL LAYOUT To avoid the named issues, a new flow cell layout was designed. It was aimed to feature lower flow velocities in the measurement channels (coming from the top) compared to the flow in the bead channels (coming from the left). Additionally there should be no stream entering from the main channel into the measurement channels. To optimize the geometry of the layout the flow was simulated using COMSOL Multiphysics. A simulation of the streams in the final design is displayed in Figure 2.9.

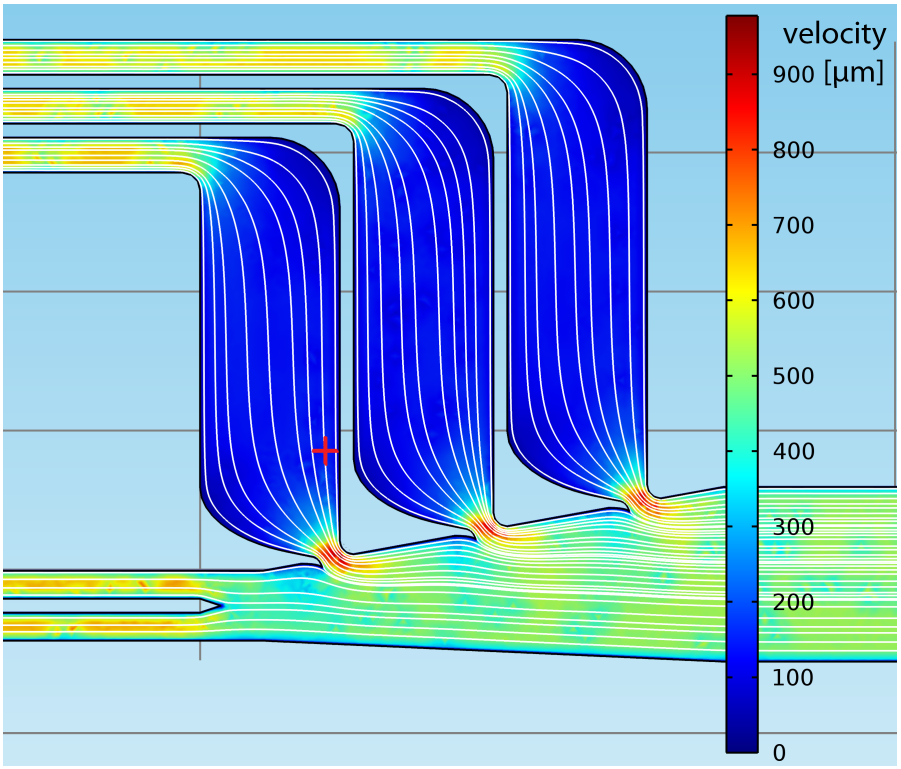

Figure 2.9: Simulation of streams for the design of a new flow cell. Flow velocities are displayed using the rainbow color scale. White streamlines display the velocity field. The red cross marks a designated measurement position.

The same pressure difference Δp was simulated for all inlets and adjusted to yield a flow velocity of 400 µm/s in front of the bead channels. The flow velocity at the measurement position (red cross in Figure 2.9) yielded around 150 µm/s.

The measurement channels narrow down to create higher flow velocities at the transition to the main channel. This avoids stream from the main channel to enter into the measurement channels even if unequal clogging of the silica tubes leads to lower pressure in the side channels. Thus well-defined measurement conditions were maintained.

Another feature of this layout are the streamlined edges to avoid accumulation of dirt as has been found for the old design.

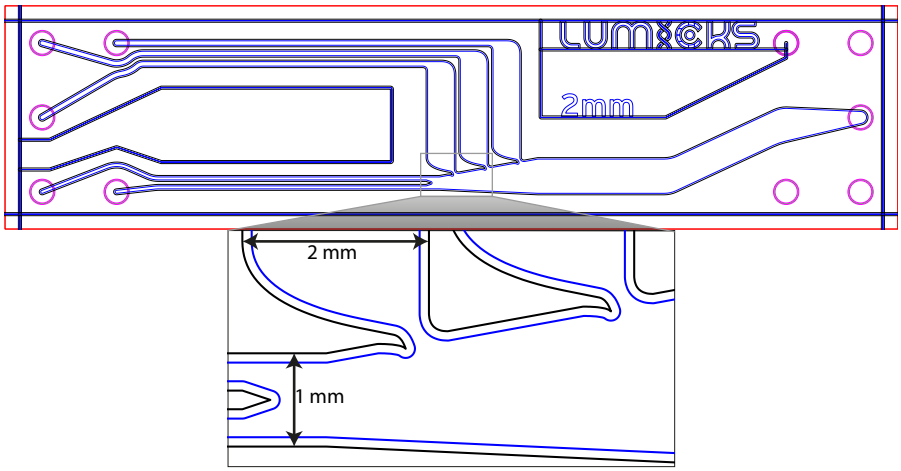

Figure 2.10: Etching mask for the new flow cell layout. Outer etching mask is displayed with black lines. Blue lines display the inner etching radius. Inlets and outlets are displayed in pink. As zoom into the measurement region is shown below.

The etching mask for the final layout is given in Figure 2.10. The etching creates round edges with a radius of 100 µm, as displayed in Figure 2.7B. These edges define an inner mask for the etching (blue lines). The channels exhibit a flat surface only inside the inner mask. The narrow parts were designed such that the measurement channels could be entered by the optical traps without crossing the round edges of the channels.

2.8.3 *Measurement procedure*

To clean the system before each experiment, it was flushed one time with 1 ml pure ethanol (EtOH), two times with 1 ml doubly distilled water (ddH2O) and one time with 300 µl buffer solution applying the maximum pressure ($\Delta p = 3$ atm). After the measurement the whole system was again cleaned with ddH2O and then kept in EtOH.

All measurement buffer solutions had to be filtered properly with 20 nm pore size except beads and oxygen scavenger system. For each channel 300 µl solution were used, which lasted for up to 3 h depending on the adjusted flow speed.

After cleaning, the measurement solutions were flushed in with $\Delta p = 0.5$ atm. Flushing in the protein covered beads using drastically higher or lower pressure resulted in more proteins exhibiting non native behavior. For the measurements a continuous flow of ≈ 150 µm/s in the measurement channels was used. Therefore a pressure of $\Delta p \approx 0.03$ atm was applied using the high resistance outlet. The flow velocities were checked by video analysis of beads released after the measurement.

The trajectories between the measurement and bead trapping positions were programmed to control the motors accordingly.

PRACTICAL CONSIDERATIONS The preparation of the measurement requires slightly more effort than that using a normal sample chamber. This is mainly due to additional filtering of the components and the need of cleaning the system before usage. Also higher amounts of the components have to be used (about 6-fold for each channel).

On the other hand, a major advantage is that no other beads can fall into the traps while measuring. Some components as Magnesium or higher concentration of chaperones and/or peptides can prevent proper tether formation. The microfluidics system always allows tether formation in a standard environment.

3

THEORY AND DATA ANALYSIS

This chapter aims to describe methods for data analysis of optical tweezers measurements and underlying theoretical concepts. This data analysis methodology has been described in great detail in several preceding works [83, 101, 141, 169, 191, 228, 267], thus only its central aspects and newly developed methods will be summarized here.

Section 3.1 describes a way to model the elastic response of a tethered protein upon application of force. An introduction into the concept of energy landscape theory describing protein folding processes is given in Section 3.2. Section 3.3 describes the energy contributions of the whole dumbbell configuration. Section 3.4 explains the analysis of passive-mode experiments, including the extraction of kinetic parameters and free energies. It includes a model for the extrapolation of force-dependent transition rates and the computation of the associated kinetic energy landscape. Section 3.5 describes the analysis of force-jump experiments and an indirect method to determine transition rates. How the kinetic energy landscape was used to extract overall folding rates and to model an off-pathway misfolded state is presented in Section 3.6.

3.1 THE WORM-LIKE CHAIN (WLC) MODEL

The methods in this part describe how to calculate the protein contour length gains of folding and unfolding transitions and to relate them to the protein structure. These are also needed to determine the elastic parameters of the protein tether which is required to compute the required for the consideration of free energy stored in the system (as used Section 3.4.2), in addition to the energy stored in the protein structure itself.

To calculate the elastic properties of the DNA tethering the protein, the force (F) vs. extension (e) curves, measured by stretching the protein tether (as described in Section 2.6.1), were modeled using the extensible Worm-Like Chain (WLC) model [248] given in Equation 3.1.

$$F_{eWLC}(e) = \frac{k_B T}{p_{DNA}} \left(\frac{1}{4} \left(1 - \frac{e}{L_{DNA}} + \frac{F}{K} \right)^{-2} - \frac{1}{4} + \frac{e}{L_{DNA}} - \frac{F}{K} \right), \quad (3.1)$$

where $k_B T$ is the thermal energy, p_{DNA} the DNA persistence length, L_{DNA} the DNA contour length and K the elastic stretch modulus.

The force vs. extension curve for the unfolded protein, which is needed to calculate the protein contour length gains of folding transitions, can be similarly described using the standard Worm-Like Chain (WLC) model [133, 189] given in Equation 3.2.

$$F_{WLC}(e) = \frac{k_B T}{p_{prot}} \left(\frac{1}{4} \left(1 - \frac{e}{L_{prot}} \right)^{-2} - \frac{1}{4} + \frac{e}{L_{prot}} \right), \tag{3.2}$$

with the protein persistence length p_{prot} and the protein contour length L_{prot}. To fit the curve after part of the protein has unfolded, a linear combination of Equation 3.2 and Equation 3.1 was used. A fixed p_{prot} of 0.7 nm was used for all traces in this work.

For given elastic parameters, expression Equation 3.1 and Equation 3.2 can also be used to relate the trap distance to the force bias F and the forces F_i acting on the different states i. Note that the trap distance d is related to the extension e by $e = d - \frac{F}{k_{eff}}$. The trap distance d is by convention given by the actual distance between the laser foci minus the diameter of the beads so that $d = 0$ nm when the beads are in contact.

STRUCTURAL RELATION Increases in protein contour length can also be related to the number of amino acid residues involved in the folding transition. To this end, the average contour length per amino acid ($d_{aa} = 0.365$ nm) and the pulling direction on the remaining folded structure before and after the transition are considered as described in [50].

For compact single domain protein structures, unfolding most likely starts from either the N- or C-terminal end if a terminal-pulling geometry is applied. An unfolding of a part in the middle of the structure would require two independently stable terminal parts.

The errors given for L_{prot} are a combination of SEM, the uncertainties of the elastic parameters (estimated through the variation of the parameters) and a systematic error due to the unknown state of the terminal amino acids (estimated by an error of ± 0.5 nm). For N_{aa_folded} there is an additional uncertainty as it is unclear which amino acids comprise the folding intermediate conformation.

3.2 ENERGY LANDSCAPE THEORY

The folding and unfolding of a protein can be thought of as diffusion in a multidimensional energy landscape [29, 51, 60, 64, 126, 246]. In optical trap measurements a 1D projection of the landscape is measured. The energy along the coordinate of protein contour length is probed.

The probed coordinate is often called the reaction coordinate.

In this view the native state is the global energy minimum. Local minima along the folding pathway define intermediate states. The height of the energy barriers separating the states defines the rates of transition from one state to another [6, 120]. The peak of this energy barrier defines the transition state (TS) (Figure 3.1A).

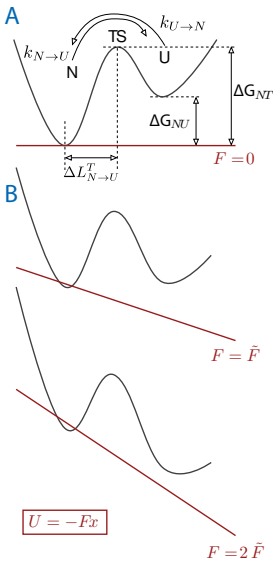

Figure 3.1: Schematic of 1D Energy landscape in an optical trap (A) 1D energy landscape of simplified 2-state system (black line) plotted along the reaction coordinate. Native (N) and unfolded (U) states are separated by the energy barrier of the transition state (TS).(B) Simplified tilting of the energy landscape by an external applied force F (red line).

TRANSITION RATES The crossing of a well-defined single energy barrier can be described as a memoryless Poisson process[1] [29, 126]. that means at each point in time, the system is found in an initial state i, it has the same probability of transitioning into another state f, which leads to an exponential distribution of dwell-times before a transition [63]. In fact, protein folding does not take place on a smooth energy landscape with well-defined single energy barriers between states [63, 64, 91, 126]. In reality the dwell-time distributions become more complex and thus the definition of a single transition rate more problematic [63]. Often times, however, the crossing of the highest energy barrier on the folding pathway is the rate-limiting transition. Thus in most cases the dwell-time distribution before folding events can be well approximated by a single-exponential distribution.

TILTING OF THE ENERGY LANDSCAPE BY EXTERNAL FORCE Figure 3.1B illustrates how an externally applied force to the system tilts the energy landscape so that more extended states like the unfolded

1 https://en.wikipedia.org/wiki/Poisson_point_process

(U) become energetically favored. As described in Section 3.4.1, this shifts the population probability from the folded to the unfolded state.

Since the energy of the transition state (TS) is altered by the applied force, it increases the unfolding rate $k_{N\to U}$ and decreases the folding rate $k_{U\to N}$. The extent to which each rate depends on the force depends on the position of the transition state. This dependence will be discussed in more detail in Section 3.4.2.

3.3 ENERGY CONTRIBUTIONS IN THE DUMBBELL CONFIGURATION

The free energy associated with a certain state $G_i(F_i)$ subjected to the force F_i is the sum of the energy stored in the folded protein conformation G_i^0 and the force-dependent energy stored in the system of beads ($G^{beads}(F_i)$), DNA linker ($G^{DNA}(F_i)$) and elastic peptide of the unfolded protein part ($G_i^{peptide}(F_i)$) [205]:

$$G_i(F_i) = G_i^0 + G^{sys}(F_i) \tag{3.3}$$

$$G^{sys}(F_i) = G^{beads}(F_i) + G^{DNA}(F_i) + G_i^{peptide}(F_i) \tag{3.4}$$

The beads are displaced by the force in the harmonic potential of the traps by $x = \frac{F}{k_{eff}}$. Hence, the free energy stored in the displacement is:

$$G^{beads}(F) = \frac{1}{2} k_{eff}^{-1} F^2, \tag{3.5}$$

with the effective spring constant, calculated from the spring constants of each trap $k_{eff} = k_1^{-1} + k_2^{-1}$.

The free energy stored in the stretched DNA handles can be calculated by integrating Equation 3.1:

$$G^{DNA}(F) = \int_0^{e_{eWLC}(F)} F_{eWLC}(e')de' \tag{3.6}$$

The free energy of the stretched unfolded protein part using Equation 3.2 is

$$G_i^{peptide}(F) = \int_0^{e_{WLC}(F)} F_{WLC}(e')de' \tag{3.7}$$

Thus, the energies stored in the system can be calculated using the elastic properties determined for each molecule by stretch-and-relax cycles.

3.4 ANALYSIS OF PASSIVE-MODE EXPERIMENTS

Force vs. time traces, measured at constant trap distance in passive-mode experiments, reflect trajectories in which the protein changes its total contour length by folding and unfolding [227]. Keeping the trap distance constant, different force levels reflect different folding states with distinct contour lengths.

To calculate energies and transition rates data points from force vs. time traces need to be assigned to certain protein states. As these traces also contain noise from the system, which obscures the transitions, a sophisticated approach is needed for this assignment.

STATE ASSIGNMENT BY HIDDEN MARKOV MODEL ANALYSIS In this work, a Hidden Markov Model (HMM) analysis was used to assign raw data points to discrete folding states (as described in [229]). The traces were discretized into 25 to 100 force bins (depending on trace length and state separation). The number of states and their initial emission probabilities were determined by fitting gaussians to the force histogram of the evaluated trace. A minimal number of states was chosen accounting for all peaks in the force histogram and resulting in a single-exponential lifetime distribution. The emission probabilities were optimized after each iteration of the forward-backward and Baum-Welch algorithm. The transition probability matrix was adjusted manually to result in optimal single-exponential lifetime distributions and kept constant for different molecules at similar trap distance. A single-exponential distribution is a hallmark of lifetimes with an underlying Poisson process and also serves as further evidence for correct state assignments.

More details on the algorithms can be found in [183].

An example of lifetime distributions of the assigned states is given in Figure C.1.

COMPUTATION OF TRANSITION RATES The off-rate k_i^{off} of a state i was calculated by fitting an exponential (Equation 3.8) to a cumulative histogram $p(\tau < t)$ of the lifetimes τ_i.

$$p(t) = \frac{\exp(-kt) - \exp(-k\tau_{min})}{\exp(-k\tau_{max}) - \exp(-k\tau_{min})} \tag{3.8}$$

τ_{min} and τ_{max} are experimental limits for possibly measured lifetimes. τ_{min} reflects the time resolution of the setup and was set to 0.2 ms. τ_{max} was set to 100 s. The rates of hormone binding and dissociation were calculated as the inverse of average dwell-time.

To compute the transition rates from state i to state j, the off-rate of state i was multiplied by the probability p_{ij} to go to state j after

leaving state i. This was determined by counting the number of corresponding transitions in the considered trace.

$$k_{i\to j} = k_i^{off} p_{ij} \tag{3.9}$$

The effect of missed events was neglected in this work. For averaging rates from different experiments the geometric mean was used rather than the arithmetic mean as rates are log-normal distributed.

EXTRACTION OF OVERALL FOLDING RATE To extract an overall rate for folding-&-binding – k_{FB} – for the transition from the completely unfolded to the native, hormone-bound state, the mean first-passage time (MFPT) [175] – τ_{FB} – was extracted from the passive-mode force vs. time traces. To this end, the time between each occurrence of the completely unfolded state and the next occurrence of the native, hormone-bound state were analyzed.

The average of these times was used to calculate the overall transition rate $k_{FB} = \frac{1}{<\tau_{FB}>}$. This method was used instead of an exponential fit of the times, because the overall transition rate does not exhibit perfect does not perfectly resemble a single-exponential behavior due to multiple energy barrier crossing involved in the transition (for discussion see Section 3.6.1).

3.4.1 *Calculation of ΔG from passive-mode traces*

Once the data of a force vs. time trace at a certain trap distance is assigned to different states, the population probabilities P_i of these states can be extracted by summing up the total dwell-time spent in each state.

These probabilities are linked to the free energy differences,

$$\Delta G_{ij}(F_i, F_j) = G_j(F_j) - G_i(F_i),$$

between the states by the Boltzmann distribution (Equation 3.10).

$$\frac{P_j(F_j)}{P_i(F_i)} = \exp\left(-\frac{\Delta G_{ij}(F_i, F_j)}{k_B T}\right) \tag{3.10}$$

with $P_i(F_i)$ being the probability for the system to be in state i subjected to the force F_i.

The free energy differences ΔG^0 for each state were calculated for various traces at different trap distance, hence with different force biases. The agreement of the results at different force bias served as further check for correct elastic parameters and state assignment.

3.4.2 *Extrapolation of force-dependent transition rates*

By changing the applied force bias in passive-mode experiments, the force dependence of the transition rates can be explored in a certain force range. These transition rates can be extrapolated to yield a zero-force rate ($k^{0\,\mathrm{pN}}$). This rate can be compared to other studies done in the absence of force.

The force dependence of the transition rate $k_{i\to j}(F_i)$ from state i to state j arises from the force-dependent energy difference from state i to the transition state $\Delta G_{iT}^{sys}(F_i, F_T) = G_i^{sys}(F_i) - G_T^{sys}(F_T)$ (compare Equation 3.4) [205]:

$$k_{i\to j}(F_i) = k_{i\to j}^{0\,\mathrm{pN}} \cdot \exp\left(-\frac{\Delta G_{iT}^{sys}(F_i, F_T)}{k_B T}\right) \tag{3.11}$$

For given elastic parameters of the system and the contour length of state i, the only independent fitting parameters are the zero-force rate constant $k_{i\to j}^{0\,\mathrm{pN}}$ (yielding vertical offset) and the contour length difference $\Delta L_{i\to j}^{T}$ (changing the slope) from state i to the respective transition state. The latter parameter is the only independent variable of the energy difference $G_{iT}^{sys}(F_i, F_T)$.

The zero-force energy difference between state i and the transition state is contained in

$$k_{i\to j}^{0\,\mathrm{pN}} = k_\omega \exp\left(-\frac{\Delta G_{iT}^{0}}{k_B T}\right), \tag{3.12}$$

where the pre-exponential factor k_ω reflects the reconfiguration time of the protein chain [75, 212, 263].

For the values for $k_{i\to j}^{0\,\mathrm{pN}}$ and $\Delta L_{i\to j}^{T}$ given in Table 5.3, the force-dependent rates were measured and extrapolated for each molecule individually and afterwards a global average of all parameters was computed.

3.4.3 *Calculation of the folding energy landscape*

With knowledge of the free energies of all folding intermediate states and the respective transition states, a 1D folding energy landscape along the coordinate of protein contour length can be computed (compare Section 3.2). This landscape contains all relevant kinetic parameters and illustrates the overall characteristics of the measured folding pathway.

The free energies of the folding intermediate states can be calculated not only via the state probabilities as described in Section 3.4.1,

but also from kinetic parameters. At equilibrium, the Boltzmann equation (Equation 3.10) holds for the transition rates:

$$\frac{P_j(F_j)}{P_i(F_i)} = \frac{k_{i\to j}(F_i)}{k_{j\to i}(F_j)} = \exp\left(-\frac{\Delta G_{ij}(F_i, F_j)}{k_B T}\right) \tag{3.13}$$

The free energies of the transition states can thus be calculated using the relations given in Equation 3.12 and Equation 3.11, assuming a k_ω of 1.2×10^4 /s, consistent with Gebhardt *et al.* [75].

The energy landscape displayed in Figure 5.6 was calculated stepwise from the unfolded state by adding the energy differences calculated using the ratio of transition rates from one state to the next (extrapolated as described in Section 3.4.2).

The forces F_i and F_j of the corresponding states were calculated from the given force bias F using the relations given in Equation 3.1 and Equation 3.2.

The averaged protein contour lengths L_{prot} were used as given in Table 5.1. The contour length of the respective transition states $\Delta L^T_{i\to j}$ – as obtained by the force dependence of the respective transition (see Section 3.4.2) – was added to L_{prot} of the preceding intermediate state.

3.5 ANALYSIS OF FORCE-JUMP EXPERIMENTS

Due to the memoryless property of Poisson processes, the force-jump experiments described in Section 2.6.3 can be analyzed in a similar way as the force vs. time traces from passive-mode experiments.

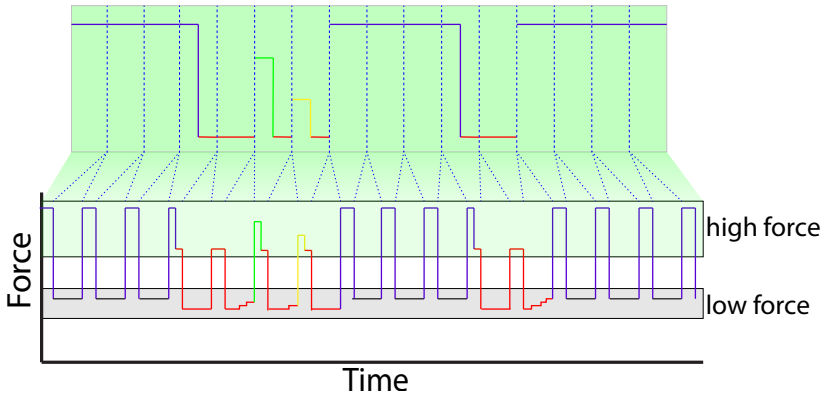

Figure 3.2: Schematic of force-jump trace analysis. The force vs. time trace (lower part) is cut at the force-jump positions (dashed blue lines) and the data during the high force phase (green box) merged (above). This passive-mode-like trace could be classified into folding intermediate states (colors). The data during the low force phases (gray box) is analyzed separately.

To automate the detection of proper refolding, the traces were cut at the positions of the force jumps and the data obtained during the

high force phases were merged (Figure 3.2). Similarly to the passive-mode experiments, the merged high force traces can be analyzed with the HMM algorithm as described in Section 3.4 to classify the states present in the high force phase (upper part). As unfolding of the native state does not occur in the low force phase, its dwell-times can be treated as in passive-mode traces because of the memoryless property of the underlying Poisson process.

Note that, despite the similarity of the merged traces to those obtained in passive-mode experiments, refolding occurs only during the low force phases (at the blue dashed lines). Hence, the signal observed during the high force phase reports the extent to which refolding had occurred during the preceding low force phase.

The hydrodynamic drag on the beads introduced an artifact in the first 70 µs after each jump with the laser traps (for details, see [84]). Hence, the first 9 data points (300 µs) after each jump were ignored.

For the cases in which $F_{ref} \gtrsim 4\,\mathrm{pN}$, the data obtained during the low force phase could be used to follow the refolding trajectory, however a detailed state assignment was not possible due to the limited resolution at low forces. To this end the low force phases that started in the unfolded state (marked in red in gray box) were aligned after the jump to low force and averaged. This yielded an average force contraction trajectory for folding.

3.5.1 *Calculation of rates for hidden transitions*

In some cases, a folding transition cannot be observed directly, e.g. if it is probed at zero-force, where force resolution is lost (as in the force-jump experiments described in Section 2.6.3). An alternative way to compute the transition rate from state i to state j of an underlying Poisson process, is the relation

$$k_{i\to j} = -\frac{1}{\tau_{wait}} \cdot \ln(1 - P_j(\tau_{wait})), \tag{3.14}$$

where P_j is the probability to observe a certain state j after a defined time τ_{wait}, if the system has been prepared in state i.

Note that this is only valid if under the given conditions, there is no transition back from j to i on the timescale of τ_{wait}.

3.5.2 *Analysis of overall folding-&-binding rate k_{FB}*

To calculate the rate $k_{FB}(F_{ref}) = k^{overall}_{unf\curvearrowright closed}(F_{ref})$ of the overall transition from the unfolded to the hormone-bound *closed* state at a certain refolding force bias F_{ref}, the probability of successful transitions in a certain waiting time τ_{wait} at F_{ref} was evaluated.

In other words, the average number of jumps to low force after an unfolding until the next bound state occurred was counted.

Each jump to the lower force that happened while the protein was being in the completely unfolded state was counted as an attempt;

of these that were classified as the *closed* state immediately after the jump back to high force, were counted as a success. The rate k_{FB} could then be calculated as described in Section 3.5.1.

Note that for $F_{ref} \gtrsim 5\,\mathrm{pN}$, unfolding of semi-folded intermediates will occur on the timescale of τ_{wait}. Thus $P_{native}(\tau_{wait})$ will not perfectly follow a single-exponential curve (compare calculations in Section 3.6). Hence, k_{FB} is intrinsically not well-defined and the measured k_{FB} will depend slightly on the choice of τ_{wait}. Therefore it is important to use the same τ_{wait} in the calculations modeling the measured k_{FB} (Section 3.6.1).

3.6 COMPUTATION OF THE STATE PROBABILITY EVOLUTION

An example for such a state population probability evolution can be found in Figure 3.3D.

With knowledge of the transition rates between all intermediate states of a kinetic network, the evolution of all state population probabilities from a given initial state can be calculated numerically.

To this end the probabilities $P_i(t)$ of the protein being in state i after time t were computed iteratively for discrete small time steps Δt in a linear approximation of ΔP_i:

$$P_i(t+\Delta t, F) = P_i(t,F) + \sum_j \left[k_{j\to i}(F_j)\cdot \Delta t \cdot P_j(t,F) - k_{i\to j}(F_i)\cdot \Delta t \cdot P_i(t,F)\right] \tag{3.15}$$

Note that the force bias F is the force acting on the completely folded state at a certain trap distance and F_i are the forces experienced by state i at that trap distance.

The time steps Δt were chosen such that $k_{i\to j}(F_i)\cdot\Delta t \ll 1 \forall i,j$ to ensure the accuracy of the linear approximation. To calculate the evolution for a given force bias F, the transition rates $k_{i\to j}(F_i)$ from state i to state j were picked from the global rate extrapolations as described in Section 3.4.2.

OPTIMIZATION OF TIME STEPS Δt If the transition rates in the kinetic network vary over several orders of magnitude (as in the case of GR-LBD 1×10^{-2} - 1×10^{6} /s, compare Figure 5.5), a static Δt leads to various complications since the timescale of changes in the state probabilities shifts drastically during the system evolution. At the beginning, states with high off-rates are depopulated on a short timescale until their P_i is almost zero and they do not contribute significantly to the system anymore. Then the states with slower off-rates become relevant.

A small Δt, accounting for the fastest transitions in the system, leads to unnecessaryly many iterations for the slow processes, increasing the computation time and numerical error. The latter led to changes in the total probability ($\sum_i P_i \neq 1$) of more than 10% (compare Figure 3.3A).

Thus Δt was optimized after each iteration step by adjusting it to the relevant timescale, using $\Delta t = 1/(1000\cdot\max(k_{i\to j}\cdot P_i))$. This optimization increased the performance of the calculation drastically

while guaranteeing the accuracy of the linear approximation in the relevant regime and reducing the numerical error (compare Figure 3.3B).

On the other hand this dynamic Δt introduced a new numerical error in the population probabilities of nearly depopulated states with fast off-rates (see Figure 3.3C). At the point where P_i of the states with fast off-rates (red+yellow) got small, they started oscillating into negative values due to inaccuracy of the linear approximation of ΔP_i. This effect was suppressed by limiting all P_i to positive values (Figure 3.3D).

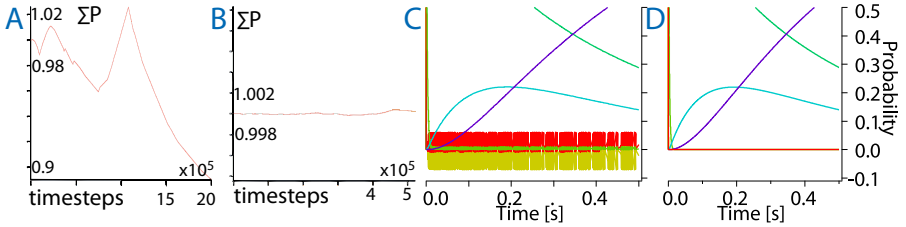

Figure 3.3: Numerical errors in the computation of the state population probability evolution. (A) $\sum_i P_i$ (red curve) for calculation using a static Δt (B) as in (A), but using a Δt, optimized after each iteration. (C) Population probability evolution for different states (with an underlying kinetic network allowing transition from red to yellow to light green to turquois to cyan to purple) highlighting a numerical error for states with fast off-rates (red+yellow) when using the optimized Δt. (D) as in (C) but keeping $P_i(t) > 0 \forall i, t$.

3.6.1 *Calculation of overall rates from state evolution*

From the state population evolution, computed as described in Section 3.6, an overall rate for the transition from an initial state i to a final state f, $k_{i\curvearrowright f}^{overall}$ can be inferred. To this end, the initial parameters for the iteration (Equation 3.15) are set to $P_i(0) = 1, P_j(0) = 0 \forall j \neq i$.

As k_f^{off} was set to zero, $k_{i\curvearrowright f}^{overall}$ reflects a mean first-passage time (MFPT) [175].

By setting the off-rate from the final state to zero $k_f^{off} = 0$ for the numerical calculation, $P_f(t)$ will yield the probability that - starting from state i - after a certain time t, the final state f has been reached at least once. In this case $P_f(t \to \infty)$ will settle to 1. Note that this is different from the probability to actually find the system in state f after time t. If there were backward transitions it would settle to an equilibrium value.

In the case where f is the folded state, at low forces $k_f^{off} \approx 0$ is negligible.

Having computed $P_f(t)$, $k_{i\curvearrowright f}^{overall}$ can be calculated using the relation given in Equation 3.14.

DEVIATION FROM SINGLE-EXPONENTIAL BEHAVIOR If one transition is rate limiting and its timescale is much bigger than those of all other transitions, $P_f(t)$ will follow a single-exponential increase. In energy landscape theory this is the case where one transition en-

ergy barrier is far higher than the others (compare Section 3.2). In the cases where rates between the other intermediate states are not much smaller than the limiting transition rate, $P_f(t)$ does not exactly follow an exponential increase (purple in Figure 3.3D). It exhibits a lag-phase $t_{lag} \approx 50\,\text{ms}$ at the beginning. Thus the $k_{i\curvearrowright f}^{overall}$ calculated will depend slightly on the choice of τ_{wait} in Equation 3.14, which makes it not perfectly well-defined. By neglecting the lag-phase and calculating $k_{i\curvearrowright f}^{overall}$ for a $\tau_{wait} \ll t_{lag}$, the overall transition can be approximated with a single-exponential process.

VALUES USED FOR CALCULATIONS For the overall refolding rate as displayed in Figure 5.7A, a τ_{wait} was used that defines the probability of reaching a certain value $P_f(\tau_{wait}) = (1 - \exp(1))$ (which reflects $\tau_{wait} = \frac{1}{k}$, compare Equation 3.14).

For the calculation of k_{FB} as displayed in Figure 5.10, the binding rate $k_{bind}(DEX)$ at 200 µM DEX was included in the numerical calculation. A fixed $\tau_{wait} = 200\,\text{ms}$ was chosen to resemble the waiting time as used in the force-jump experiments.

The case of DEX unbinding right after successful folding-&-binding could be neglected as it is $< 1.5\,/\text{s}$ in the measured force range, so unbinding rarely occurs within $\tau_{wait} = 200\,\text{ms}$. The effect was also simulated and yielded a difference in rate of $< 10\%$.

3.6.2 *Modeling off-pathway misfolded states*

Computing the state population evolution is a powerful tool to adjust the kinetic network model so that it reflects the measured data. In this work it was also used to find a model reflecting the effect of misfolding on the folding pathway, as the misfolded state could not be identified unambiguously.

An off-pathway state is a dead-end beside the productive folding pathway which possibly slows down folding at low forces [17].

An off-pathway misfolded state branching off the intermediate states was modeled into the existing kinetic network such that it resembles the measured data at high forces, where no misfolding was detected. To this end, an intermediate states i was given the possibility to fold into an off-pathway state with an additional contour length contraction ΔL_{mf} and additional free energy ΔG_{mf}^0. These parameters yield a force-dependent probability $P_{mf}^i(F_i)$ of the intermediate state i being in a misfolded configuration. A fast equilibration of the transition between the intermediate state i and its misfolded configuration was assumed. Thus, $P_{mf}^i(F_i)$ can be calculated using Equation 3.10 and Equation 3.3. A folding of state $i \to j$ into the next productive folding intermediate j is only possible if i was not in the misfolded configuration. All the transition rates originating from this intermediate state i were recalculated using the probability of not being in the off-pathway misfolded state $k_{i\to j}^{mf\text{-}model}(F_i) = \left(1 - P_{mf}^i\right) \cdot k_{i\to j}^{mf\text{-}model}(F_i) \forall j$.

3.6.3 *The refolding contour length evolution*

The state population evolution, described in Section 3.6 can also be used to compute the average contour length evolution from a given initial state i at a certain force bias F. This could be, for example, the average length contraction vs. time of the unfolded state at low forces (dashed lines in Figure 5.11).

To this end, the average force evolution was calculated using the time-dependent average state distribution, multiplied by the forces exhibited by the different states.

$$F_{avg}(t) = \sum_i P_i(t) \cdot F_i \tag{3.16}$$

$F_{avg}(t)$ was then transformed into contour length space by using Equation 3.1 and Equation 3.2. For the calculation of F_i of the misfolding intermediate i, the reduced contour length of the intermediate due to the misfolded configuration was taken into account.

Part III

RESULTS

4

THE PATHWAY OF GR-LBD HORMONE BINDING

The following chapter describes a single-molecule study of the GR-LBD conformational changes associated with binding and unbinding of the hormone Dexamethasone (DEX). The measurements illustrate the observation of binding events to a protein in real-time. The results allow the direct computation of hormone binding kinetics, and also clarify basic principles of GR-LBD function. Furthermore, this knowledge is needed for further investigation of the details of chaperone interactions with the receptor.

In the first section (4.1), the mechanical unfolding pattern of the native GR-LBD is introduced. The measurements demonstrate the ability of GR-LBD to refold into its natively folded conformation under single-molecule conditions. The next sections focus on the kinetics of the GR-LBD, in particular how it fluctuates between the native and a partially unfolded conformation (4.2). The influence of hormone binding on these fluctuations is presented in Section 4.3. Following on from this, the influence of these conformational changes on the dissociation of the hormone is demonstrated in 4.4. Analogous results are presented for Fluorescein-labeled Dexamethasone (F-DEX) (Section 4.5). Section 4.6 addresses the localization of the measured conformational fluctuations in the protein structure. Following a short summary of the hormone binding pathway as measured under force (Section 4.7), the relevance of this pathway in the absence of force is tested. To this end, the conformation of the hormone-unbound state at zero-force is examined (4.8) and the results of a novel mechanical double jump assay to directly measure binding rates in the absence of force are described in Section 4.9. Finally, a kinetic model of conformational states, describing the complete hormone-binding and -dissociation pathway, is given in Section 4.10. This model that also describes the relevant pathway in the absence of force, is discussed and the resulting kinetic properties are compared to values found in the literature.

This distinctive unfolding pattern is also called the fingerprint of the protein.

4.1 MECHANICAL FINGERPRINT OF NATIVE GR-LBD UNFOLDING

To identify the native unfolding pattern of the DEX-bound GR-LBD and test its capability of refolding, stretch-and-relax cycles were performed as described in Section 2.6.1. The trap distance was increased

with a relative trap velocity of 500 nm/s, hence applying an increasing force on the protein.

The blue trace in Figure 4.1 shows a force vs. extension trace during the mechanical stretching of GR-LBD in the presence of DEX. This unfolding pattern occurs reproducibly when stretching a GR-LBD molecule for the first time after formation of the tether. Hence, it can be considered to be the native unfolding pattern of the GR-LBD. The DEX concentration of 200 µM is significantly higher than the reported $K_d \approx 100$ nM [128], consequently the traces show unfolding of hormone-bound GR-LBD.

Unfolding traces of hormone-unbound GR-LBD are presented in Section A.2. A detailed analysis of hormone-unbound GR-LBD folding and unfolding is done using passive-mode measurements, presented in Chapter 5.

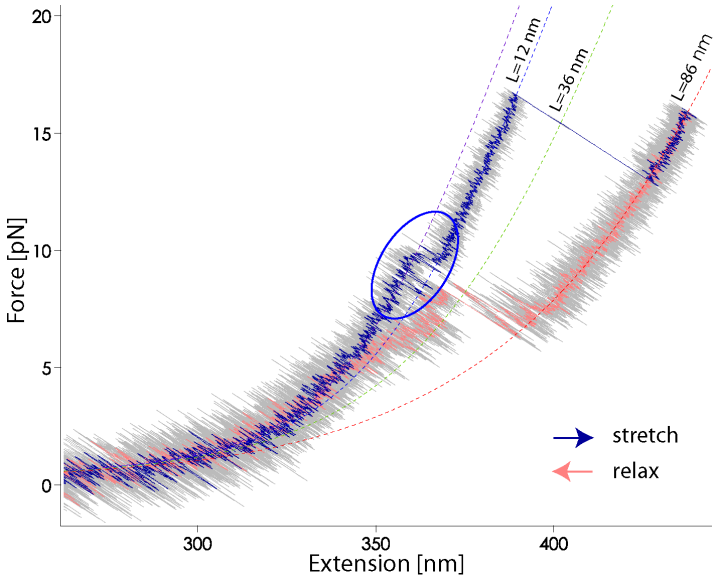

Figure 4.1: Stretch (blue) and relax (pink) cycle in the presence of 200 µM DEX at a constant pulling velocity of 500 nm/s. The data was smoothed using a running average of 21 points. 30 kHz raw data is superimposed in gray. Dashed colored lines show WLC fits for different protein contour lengths.

DESCRIPTION OF THE NATIVE UNFOLDING PATTERN At around 10 pN the protein shows characteristic rapid fluctuations where parts of the structure fold and unfold in equilibrium (blue circle in Figure 4.1). Further increase of the force keeps this part unfolded and finally leads to a clear unfolding transition at around

$$F_{avg}^{boundunf} = 16.3 \pm 1.6\,\text{pN}$$

(as averaged from 112 unfolding traces). A more detailed analysis of the force-dependent DEX-bound unfolding rates, using a method by Oberbarnscheidt *et al.* [162], is given in Section A.1.

The dashed lines in Figure 4.1 shows fits to the parts of the trace between the transitions using the WLC model (described in Section 3.1).

These fits provide the increase in contour length of the protein construct associated with the unfolding transitions. The

$$\Delta L = 12.0 \pm 1.3\,\text{nm}$$

contour length increase of the equilibrium fluctuation corresponds to an unfolding of 33 ± 4 amino acid residues (as described in Section 3.1). For a small single domain protein such a transition usually occurs by the unfolding of amino acids at the N- or the C-terminus. The total contour length gain of $86 \pm 3\,\text{nm}$ corresponds to the ≈ 250 amino acids of the complete GR-LBD, which is further evidence that the traces represent a completely folded GR-LBD.

Zooming into the raw data (gray) of the major unfolding transition reveals another short-lived unfolding intermediate of around 36 nm protein contour length. A more detailed analysis of the kinetic network of folding intermediates using passive-mode experiments presented in Chapter 5.

REFOLDING By decreasing the force on the molecule (i.e., decreasing trap distance), refolding transitions could be observed (pink trace in Figure 4.1). The protein contracts back to the original folded length. Whether the protein has refolded back to its native conformation can be confirmed if a subsequent unfolding trace shows again the fingerprint of the protein. A series of repeated stretch-and-relax cycles is shown in Figure 4.2. The subsequent unfolding traces repeat the pattern, indicating the molecule had refolded to the native state. The kinetics and refolding intermediates are addressed in further detail in Chapter 5.

These results demonstrate that, despite difficulties in measuring it to date, the GR-LBD is capable of proper refolding without the assistance of chaperones under single-molecule conditions.

4.2 THE FLUCTUATIONS OF THE N-TERMINAL *lid*

A characteristic feature of the GR-LBD native unfolding pattern is the fast equilibrium transition occurring at 10 pN (blue circle in Figure 4.1). At this point the protein fluctuates reversibly between the *closed* native and a partially unfolded *open* conformation with the rest of the structure remaining stably folded. The fast and reversible kinetics of this transition are an indicator of its potential physiological relevance. To study the kinetic and energetic properties of this transition in detail, passive-mode measurements were used (as described in Section 2.6.2). The traps were set to a constant distance such that the force bias on the molecule was around 10 pN. Force vs. time traces were recorded while the protein was fluctuating between the two states. An example trace is depicted in Figure 4.3. This assay al-

The physiological relevance of this transition is discussed later in this chapter.

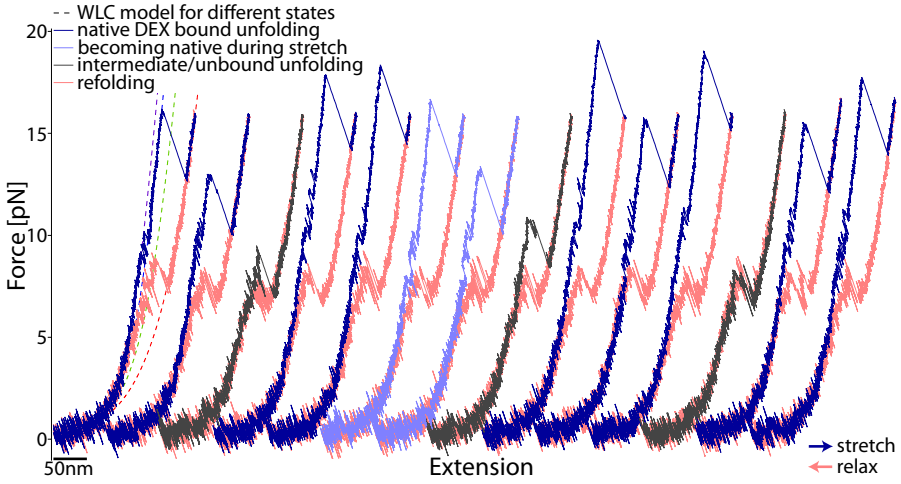

Figure 4.2: Force vs. extension traces showing consecutive unfolding and refolding of GR-LBD by repeated stretch-and-relax cycles with a relative trap velocity of 500 nm/s, DEX concentration of 200 µM and a waiting time between each cycle of 200 ms. For clarity each trace is horizontally shifted chronologically from left to right. Dark blue traces show the native, DEX-bound unfolding pattern. Light blue traces show a transition into the native state during the pull. Brown traces show non-native or unbound unfolding.

lows a detailed kinetic and energetic characterization of the observed equilibrium transition.

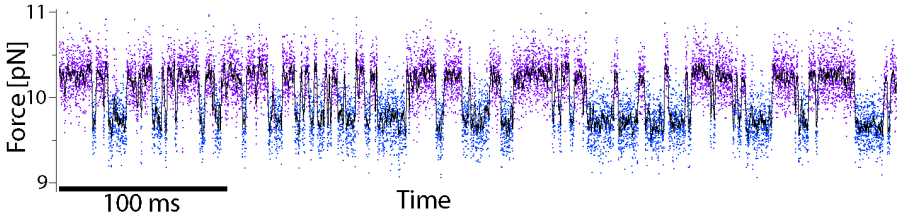

Figure 4.3: Force vs. time trace of the equilibrium transition between the *open* (blue) and *closed* (purple) state while keeping the traps at a constant distance (passive-mode). The data points were colored according to a state assignment by HMM analysis. The black line shows the data smoothed by a running average of 21 points.

Each data point was assigned to the *open* (blue) and *closed* (purple) state by HMM analysis (see Section 3.4 for details). Both states followed single-exponential lifetime distribution. that implied that the fluctuations could be well modeled as a 2-state system. From the lifetime distributions the transition rates $k_{closed \to open}(F_{closed})$ and $k_{open \to closed}(F_{open})$ were calculated. Systematically varying the trap distance and consequently shifting the force bias on the protein, the force-dependent opening and closing rates were computed. A plot of these rates is given in Figure 4.4.

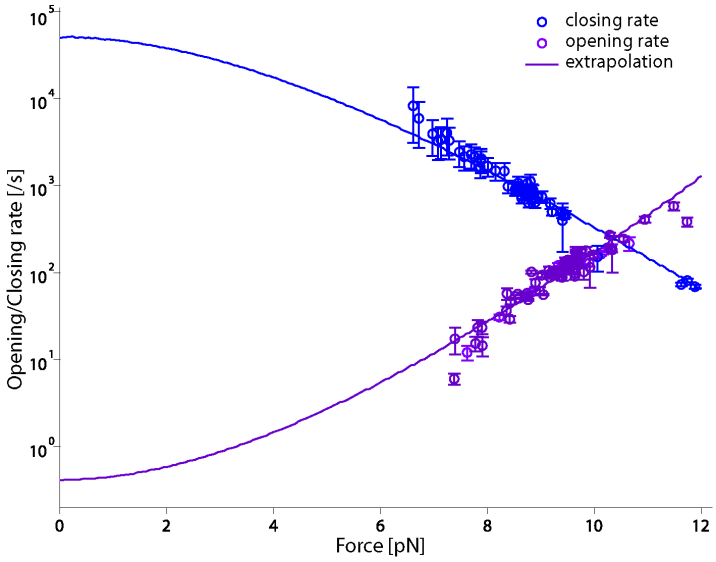

Figure 4.4: Force dependence of opening (purple) and closing (blue) rates measured using passive-mode. The data of 5 different molecules are plotted. Lines are extrapolations using the Berkemeier-Schlierf model described in Section 3.4.2.

The transition rates at zero-force were computed using an extrapolation of the force-dependent rates as described in Section 3.4.2. This extrapolation yields a closing rate of

$$k^{0\,\mathrm{pN}}_{open\to closed} = 4.8 \pm 0.5 \times 10^4\ /\mathrm{s}$$

and an opening rate of

$$k^{0\,\mathrm{pN}}_{closed\to open} = 0.4 \pm 0.1\ /\mathrm{s}$$

at 0 pN. From these rates, it can be concluded that this part – even though it is the weakest part of the protein – binds strongly to the remaining folded part of GR-LBD. It can detach and reattach rapidly under force, without triggering further unfolding. Note that even at zero-force this element detaches on a physiologically relevant timescale.

The binding of a DEX ligand to GR-LBD was reported to take about 5 min *at a* 1 µM *concentration [113].*

In the following this structural part, exhibiting the described native *open-closed* fluctuations with a contour length difference of $\Delta L = 12\,\mathrm{nm}$ will be further called the "*lid*".

The extrapolations in Figure 4.4 also yield the contour length differences from the originating states to the transition state $\Delta L^T_{open\to closed} = 5.6 \pm 0.1\,\mathrm{nm}$ and $\Delta L^T_{closed\to open} = -6.6 \pm 0.5\,\mathrm{nm}$. The fact that these independently fitted values sum up to the full contour length difference between the *open* and *closed* state serves as further validation of the model used.

Computing the ratio of the zero-force rates provides a free energy of

$$\Delta G^0_{lid} = 11.6 \pm 0.3\,\mathrm{k_B T}$$

stored in this structural part. This energy could also be calculated for each passive-mode trace separately without the extrapolation of rates using the method described in Section 3.4.1, This calculation yielding an average of $\Delta G^0_{lid} = 11.3 \pm 0.5\,k_BT$. The excellent agreement of these values further supports the use of the rate extrapolation model. The energy stored in this *lid* structure translates to a probability of finding the *lid* in the *open* state at 0 pN of

$$P^{0\,pN}_{open} = 0.9 \pm 0.4 \times 10^{-5}$$

when DEX is bound.

4.3 A MECHANICAL READOUT FOR HORMONE REBINDING

At constant trap distance same contour length implies the same force is measured.

By monitoring the *lid* fluctuations at a DEX concentration of 6 µM over a longer timescale, a switch in kinetics could be observed, as demonstrated in Figure 4.5. At some point the fluctuations stop and the protein remains in a state with a contour length similar to the *open* state (colored cyan in Figure 4.5) of 13.7 ± 1.3 nm. Even though this state did not have a distinct force signature, an assignment was possible because of its distinct lifetime. From this cyan state further partial unfoldings occur (green).

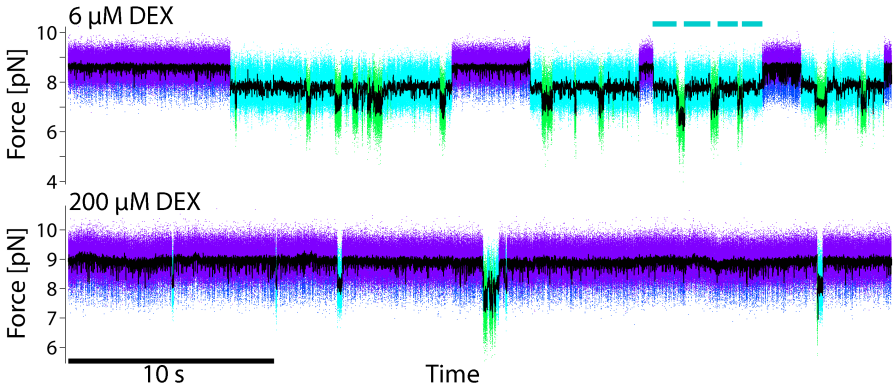

Figure 4.5: Comparison of force vs. time traces at low (6 µM) and high (200 µM) DEX concentrations recorded at constant trap distance (passive-mode). Black lines are data smoothed by a running average of 101 points. Raw data (30 kHz) is colored according to a state assignment using a 4-state HMM analysis. The *lid* fluctuations between the *closed* (purple) and *open* (blue) state are interrupted by DEX-unbound *open-ub* (cyan) phases that partially unfold (green). The cyan bars in the upper trace mark an example of the total dwell-time spent in the *open-ub* state between two bound phases. This is considered one rebinding event in the calculation of the binding rate.

DEPENDENCE ON DEX CONCENTRATION Increasing the DEX concentration in solution resulted in a decreasing dwell-time of the cyan

and green states (compare lower trace of Figure 4.5). This indicates that they reflect hormone-unbound states. To provide evidence for this in a more quantitative manner, the time of the putative unbound phases was measured under systematic variation of hormone concentration in solution. Each interruption between two phases of *open-closed* fluctuations was considered a rebinding event. Under the hypothesis that the hormone binds only to the cyan state but not to the partially unfolded green states, the time for rebinding τ_{rebind} can be extracted by summing up as the total dwell-time spent in the cyan state during a rebinding event. An example for the time of one rebinding event is marked in the upper trace of Figure 4.5. The τ_{rebind} exhibited a single-exponential dwell-time distribution confirming the homogeneity of the state. For each trace the τ_{rebind} of all rebinding events were averaged and the inverse value plotted vs. the DEX concentration in Figure 4.6A. The linear dependence of the measured rate on the hormone concentration is an evidence that the cyan state is an unbound state that binds hormone. The cyan state will hence be called *open-unbound* (*open-ub*). The average of all measured rates normalized by the hormone concentration yielded a binding rate to the *open-ub* state of

$$k_{bind} = 0.033 \pm 0.003\ /\mathrm{s}/\mu\mathrm{M}.$$

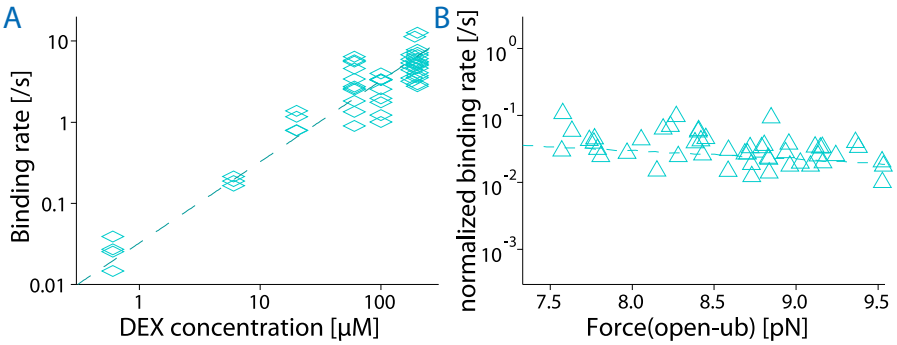

Figure 4.6: (A) Concentration dependence of the DEX binding rate to the *open-ub* (cyan) state. Each diamond represents the average of one trace exhibiting at least 8 rebinding events. 55 traces from 30 molecules were analyzed. The dashed line is a linear fit. (B) Force dependence of the binding rate normalized to $c(DEX) = 1\,\mu\mathrm{M}$. Here the force of the *open-ub* state was measured. The dashed line is an exponential fit.

HORMONE BINDING TO THE *open-ub* STATE To test the assumption that binding leading to the native bound state occurs only while the protein is being in the *open-ub* state and not while being partially unfolded, the force dependence of the binding rate was measured (Figure 4.6A). In this force range the probability of the *open-ub* state

relative to all unbound states varies from nearly 100% at low forces to only 7% for high forces.

The probability of all intermediate states and whether they can bind a hormone is analyzed in detail in Chapter 5.

If binding were to occur also in any of the other partially unfolded states, considering only the time spent in the *open-ub* state would underestimate the time it takes for rebinding. This effect would get more drastic at higher forces, as the relative population of the *open-ub* state decreases. Hence, this would imply that the putative binding rate increases with higher force. This is not the case, which confirms the assumption that binding occurs mainly to the *open-ub* state. The slight increase of the binding rate towards lower forces is possibly a result for the slightly longer contour length of the *open-ub* state compared to the *open* state. In that case the equilibrium gets shifted to the *open-ub* state with increasing force.

The measurements presented in this section illustrate how hormone rebinding can be monitored in real-time by observing the change in stability of the *lid* structure, where closing of the *lid* (transition to the *closed* purple state) is tightly linked to hormone binding.

4.4 HORMONE DISSOCIATION BY *lid* OPENING

The experiments presented in this section were performed in order to determine, how the hormone dissociation kinetics depend on the state of the *lid* structure. Increasing the force bias on the protein the population probability can be shifted from the *closed* to the *open* state (as already demonstrated in Section 4.2). To determine whether the hormone dissociates rather from the *open* or from the *closed* state, the dissociation kinetics were monitored at different population probabilities P_{open} of the *open* state. Figure 4.7 shows the frequency of hormone dissociation in two force vs. time traces with different applied force biases and consequently different values of P_{open}. An increase of the force bias by 1.4 pN already results in a significant increase in population of the *open* (dark blue) state (see zooms into the traces in the lower part of Figure 4.7). Concomitantly, also more *open-ub* states (cyan), i.e. dissociation events can be observed. Already this effect shows qualitatively that DEX dissociates faster from the *open* state.

To quantify this dependence, the dwell-times of the hormone-bound phases (an example is marked by a bar in Figure 4.7) can be analyzed for different values of P_{open}. The inverse average dwell-time in the bound states is the effective dissociation rate k_{diss}^{eff} from the *open*/*closed* state ensemble. A log-log plot of k_{diss}^{eff} vs. P_{open} (Figure 4.8A) shows that these values are directly proportional, indicating that dissociation occurs exclusively from the *open* state under these force conditions. If there was a considerable dissociation from the *closed* state with a rate of $k_{diss}^{closed} \gtrsim 0.1\,/\mathrm{s}$, the effective rate k_{diss}^{eff} would not decrease below, but would instead settle to k_{diss}^{closed} for low P_{open}.

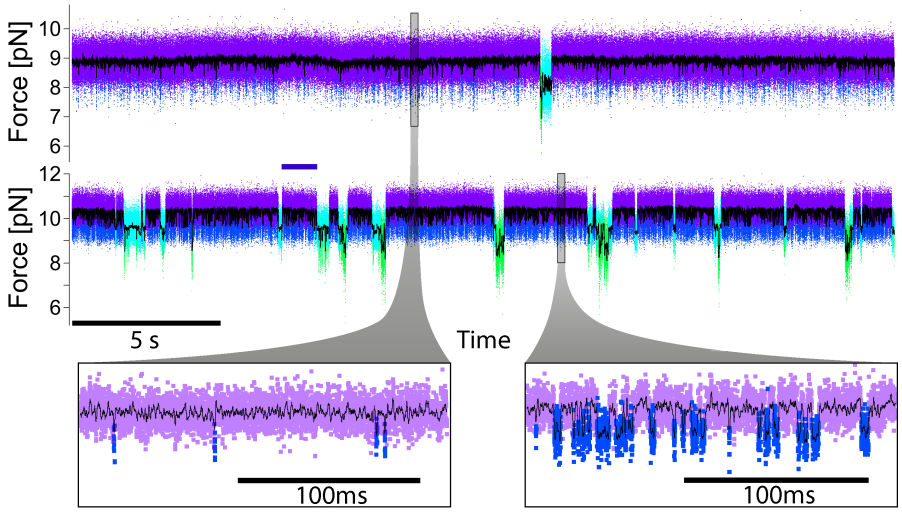

Figure 4.7: Comparison of force vs. time traces under two different force biases (data presentation as in Figure 4.5). The force bias is around 9 pN in the upper trace and around 10.4 pN in the lower trace. The purple bar marks an example for a dwell-time during which DEX is bound and the protein fluctuates between the *open* and *closed* state. The zooms below highlight the different population probabilities of the *open* state at the different forces

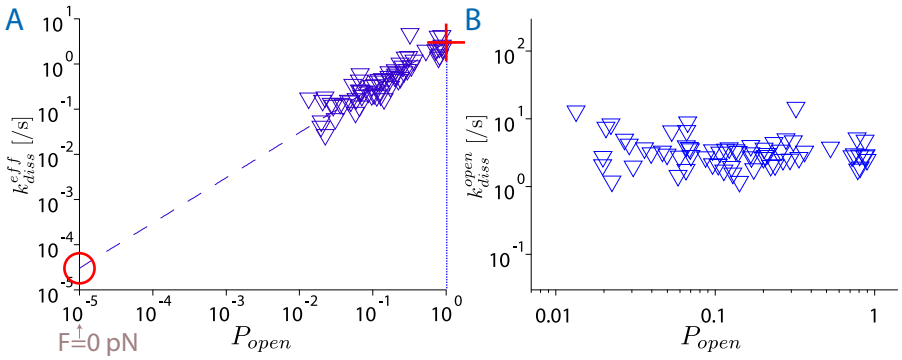

Figure 4.8: (A) Dependence of the effective dissociation rate k_{diss}^{eff} on the population probability of the *lid open* state P_{open} during the DEX-bound phase. The forces of the *open* state varied between 7 and 12 pN. Each triangle represents the average of one trace exhibiting at least 8 rebinding events. 67 traces from 30 molecules were analyzed. The dashed line is a linear fit without offset $y = a \cdot x$. The red cross and circle illustrate the intersection at $P_{open} = 1$ and $P_{open}^{0\,\mathrm{pN}} = 1 \times 10^{-5}$ and mark the dissociation rate from the *open* state k_{diss}^{open} and the extrapolated effective k_{diss}^{eff} at 0 pN, respectively. (B) Plot of the dissociation rate from the *open* state k_{diss}^{open} vs. P_{open}.

DISSOCIATION RATE FROM THE OPEN STATE The red cross in Figure 4.8A marks the k_{diss}^{eff} for $P_{open} = 1$, which is the dissociation rate from the *open* state k_{diss}^{open}. This rate can also be calculated directly ()and independently of P_{open}), by summing up only the dwell-times spent in the *open* state during each hormone-bound phase instead of using the whole dwell-time of the *open*/*closed* fluctuation phase.

Figure 4.8B demonstrates that the k_{diss}^{open} does not show a dependence on P_{open}, which provides further evidence that there is no considerable dissociation from the *closed* state in this force range. The variation of P_{open} in Figure 4.8 reflects a force range from 7 to 12 pN of the *open* state. As the k_{diss}^{open} stays constant at these forces, the dissociation from the *open* state is not triggered by force. This makes sense as the hormone-unbound *open-ub* and the *open* state exhibit very similar contour lengths and consequently the applied force does not favor the unbound state. The average of all unbinding events yields a dissociation rate from the *open* state of

$$k_{diss}^{open} = 3.0 \pm 0.2\ /\mathrm{s}.$$

EFFECTIVE DISSOCIATION RATE AT ZERO-FORCE In the absence of force, the *open* state is only populated with a probability of $P_{open}^{0\,\mathrm{pN}} = 0.9 \pm 0.4 \times 10^{-5}$. Assuming that even at 0 pN, hormone dissociation occurs mainly from the *open* to the *open-ub* state, the effective dissociation rate can be extrapolated to zero-force (red circle in Figure 4.8A) and yields

$$k_{diss}^{eff}(0\,\mathrm{pN}) = 3 \pm 2 \times 10^{-5}\ /\mathrm{s}.$$

This extrapolation is simply obtained by a multiplication of k_{diss}^{open} by the probability $P_{open}^{0\,\mathrm{pN}}$ of the *lid* being open at 0 pN (calculated in Section 4.2).

These measurements also quantify an affinity of the hormone to the *open* state, as well as an effective affinity at 0 pN by dividing k_{diss} by k_{bind}. DEX binds to the *open* (blue) state with

$$K_d^{open-open\text{-}ub} = 93 \pm 13\,\mu\mathrm{M}$$

affinity. The closing of the *lid* decreases the k_{diss}^{eff}, consequently resulting in an effective affinity of

$$K_{d,eff}^{closed-open\text{-}ub} = 0.8 \pm 0.5\,\mathrm{nM}$$

in the absence of force.

VALIDITY OF EXTRAPOLATION Compared to zero-force conditions, P_{open} is increased by more than 3 orders of magnitude in the measured force range, strongly favoring the dissociation from the *open* state. With the measurements presented here it cannot be excluded

that another pathway involving a more compact transition state allows a faster dissociation in the absence of force, where a completely unfolded *lid* is rather unlikely. For example if this pathway would allow an effective dissociation with a rate of $k_{diss}^{eff} \approx 1 \times 10^3$ /s, this would be the dominant pathway at zero-force but negligible in the investigated force range.

To test the assumption of whether unbinding from the *open* state is still relevant at zero-force, the dissociation should be measured directly in the absence of force. The slow kinetics make this process problematic to be assessed by single-molecule studies, but the rates can be compared to ensemble measurements. The unbinding pathway will be further addressed in Section 4.5 and discussed in Section 4.10.

4.5 BINDING OF FLUORESCENTLY LABELED DEXAMETHASONE

Previously hormone binding rates have been mostly previously measured using fluorescence anisotropy assays with Fluorescein-labeled Dexamethasone (F-DEX) [113, 128, 173]. To compare the zero-force binding rates yielded by this mechanical study with ensemble measurements and to study the influence of a fluorescent label on the binding kinetics, the experiments described in Section 4.3 and Section 4.4 were repeated using F-DEX in solution.

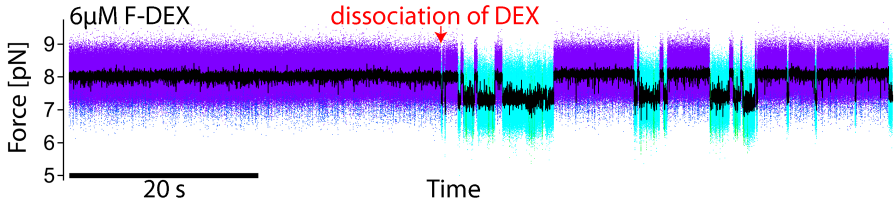

Figure 4.9: Force vs. time trace with 6 µM F-DEX in solution (data presentation analogous to Figure 4.5). As the GR-LBD is stored in a buffer containing DEX and the timescale of dissociation is longer than the preparation of the experiment, there is still a DEX molecule bound until the first unbinding event (red arrow). The residual concentration of DEX is < 1 nM

The GR-LBD was stored in buffer containing saturating amounts of DEX and was diluted into the final solution shortly before the measurement (the protocol is given in Section B.7). The time it takes for a bound DEX to dissociate in the absence of force was measured to be on the timescale of hours (as analyzed in Section 4.4), therefore it was expected that the GR-LBD still had a DEX molecule bound at the beginning of the measurement. Note that the DEX from the storage buffer got highly diluted so the residual concentration in the measurement solution was less than 30 nM, which corresponds to a

binding rate of 1×10^{-3} /s. Hence, the rebinding of DEX could be neglected.

Figure 4.9 shows a force vs. time trace with 6 µM F-DEX in solution analogous to the traces presented in Figure 4.5. In the first 40 s no dissociation event occurs. Note that the force bias of $F_{closed} = 8$ pN in this trace is less than that in the traces shown before (Figure 4.7, 4.5). This agrees also with the decreased amount of partial unfoldings during the unbound (cyan) phases in Figure 4.9. Thus the *lid* is mostly closed ($P_{open} < 0.01$), which slows down the DEX dissociation to $k_{diss}^{eff} < 0.03$ /s. Notably, after the first, slow unbinding event (red arrow in Figure 4.9), rapid unbinding and rebinding events could be observed. This points towards a substitution of the initially bound DEX molecule by F-DEX, which shows significantly faster dissociation and binding kinetics. Fast unbinding occurs already at relatively low forces.

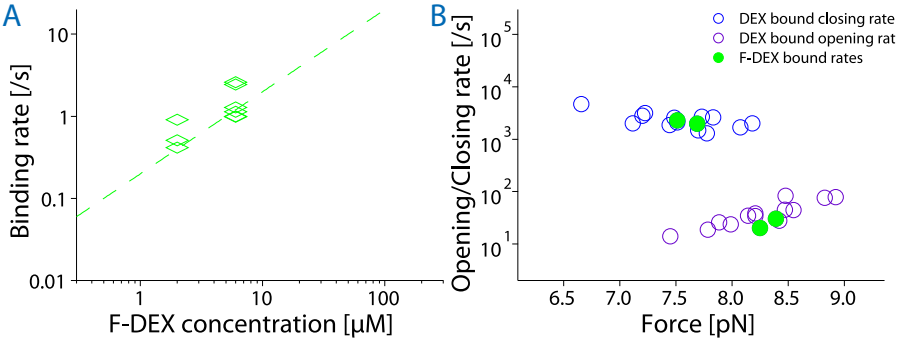

Figure 4.10: (A) Binding rates for two different F-DEX concentrations analogous to Figure 4.6A. 9 traces of 7 different molecules were analyzed. (B) Comparison of *lid* opening and closing rates with bound DEX or F-DEX. The data is taken from two different molecules each of which first had a DEX-bound that was replaced by a F-DEX. The rates were measured before and after the replacement.

The binding rates for F-DEX were analyzed in the same way as before (4.3) for two different F-DEX concentrations (see Figure 4.10A) and yielded an average of

$$k_{bind,F\text{-}DEX} = 0.21 \pm 0.04 \text{ /s/µM},$$

binding to the *open-ub* state. This rate is about 6-fold higher than the binding rate of unlabeled DEX.

Analyzing the dissociation kinetics as before (4.4) but only after the first unbinding event, yielded a dissociation rate from the *open* state of

$$k_{diss,F\text{-}DEX}^{open} = 35 \pm 5 \text{ /s}.$$

This rate is about 10 times higher than the one for unlabeled DEX. The rates are summarized in Table 4.1.

EXTRAPOLATION TO ZERO-FORCE Figure 4.10B shows a comparison of the *lid* fluctuation kinetics of GR-LBD molecules before and after the substitution from DEX to F-DEX-bound. The agreement of both opening and closing rates suggested there is no major influence of the fluorescence label on the stability of the *lid*. Hence, the same $P_{open}^{0\,\mathrm{pN}}$ was used to calculate the effective dissociation rate of F-DEX as before, yielding

$$k_{diss,F\text{-}DEX}^{eff}(0\,\mathrm{pN}) = 3 \pm 2 \times 10^{-4}\,/\mathrm{s},$$

again assuming a dissociation occurring from the *open* to the *open-ub* state. As both $k_{bind,F\text{-}DEX}$ and $k_{diss,F\text{-}DEX}^{eff}$ were measured to be higher than the rates for DEX, F-DEX exhibited a similar affinity of

$$K_{d,F\text{-}DEX}^{eff} = 1.5 \pm 1.0\,\mathrm{nM}.$$

The dissociation constant and the affinity are compared to ensemble measurements in Section 4.7.

The direct measurement of hormone binding with this mechanical study allowed the comparison of binding kinetics for DEX and fluorescently labeled F-DEX. The increase of the binding rate due to the fluorescent label might reflect a first interaction of the hydrophobic label with the protein surface, keeping the hormone closer before it binds into the binding pocket. The faster dissociation rate might be an effect of the label not perfectly fitting into the pocket.

These results are important to note for future bulk fluorescence measurements.

4.6 LOCALIZATION OF THE *lid*

The opening of the *lid* has been shown to be tightly linked to hormone dissociation from the GR-LBD, and therefore is integral to its function. So far, it is not clear on which terminus of the GR-LBD the *lid* is located. The *lid* fluctuations could be explained by an unfolding of 33 amino acids (compare Section 4.1) either on the N-terminal or the C-terminal side (highlighted in purple and blue respectively in Figure 4.11).

Single domain proteins usually start unfolding from one of the termini.

An unfolding of a structural element located within the central part of the structure is very unlikely for such a small single domain protein. It would mean that after the unfolding, a folded structure would have to remain at both ends. This seems to be very unlikely as there are no obvious terminal sub domains in the native fold, such that a separation of the native structure in two parts would not result in compact sub structures. Furthermore, two separate unfolding events with independent rupture forces would have to occur later on the folding pathway, which was not observed.

For hormone binding to the apo-GR-LBD, the C-terminal helix 12 has been widely discussed as an important structural factor since it

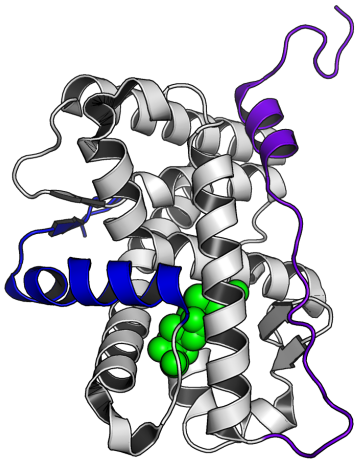

Figure 4.11: Structure of GR-LBD F602S (pdb: 1M2Z [24]). 33 N-terminal amino acids are colored in purple, C-terminal in blue. DEX is colored in green.

has direct interactions with the hormone and was found to be allosterically coupled to hormone binding [23, 69, 173, 209]. These findings would be strong indications that the observed *open-closed* fluctuations represent the C-terminal helix 12.

Three independent approaches were employed in the present work to find out the correct structural interpretation of the *lid*. All three yield the same result. In the following all three approaches are presented as they might be useful for similar questions in other proteins.

4.6.1 *Measuring the stabilizing effect of TIF2 peptide binding*

To investigate the nature of the *lid* fluctuations without modification of the protein, a 14 amino acid fragment – known to bind to the GR-LBD – was utilized. The peptide fragment comprised the GR-LBD binding site of the Transcriptional Intermediary Factor 2 (TIF2) accessory protein. The TIF2 peptide binds to the Activation Function 2 (AF2) region and has been used for crystallization of the GR-LBD (Figure 4.12A) [24]. It interacts directly with helix 12 via hydrogen bond formation, with a conserved glutamate at position 755 [23]. Following the hypothesis that the *lid* comprises helix 12, one would expect a stabilization of the *closed* conformation in the presence of the TIF2 peptide. The K_d for the TIF2 peptide binding has been measured to be about 3 µM [117, 173].

Figure 4.12B shows a comparison of unfolding/refolding traces in the presence (left) and in the absence (right) of 60 µM the TIF2 peptide. Against the expectations of a stabilized *closed* conformation, the *lid open-closed* fluctuations appear to be unaltered. A comparison of the *lid* fluctuation rates measured in passive-mode experiments with

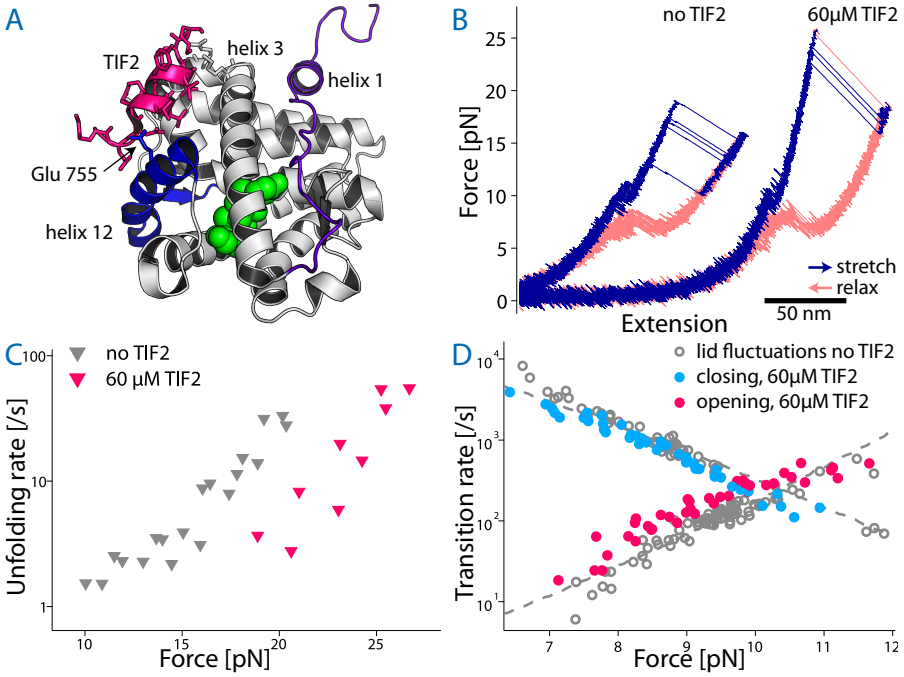

Figure 4.12: (A) PDB structure 1M2Z [24] highlighting the interaction of the TIF2 peptide with helix 12. The N-terminal helix 1 is colored in purple, C-terminal helix 12 is colored in blue and the TIF2 peptide is colored in pink. Amino acids of the TIF2 peptide and GR-LBD residues that are involved in the primary and secondary charge clamp [23] are displayed in stick representation. (B) Comparison of stretch (blue) and relax (orange) cycles using a constant beam velocity of 500 nm/s with and without 60 µM TIF2 peptide. An overlay of 4 traces each are shown. For clarity the TIF2 traces are shifted on the extension axis. (C) Comparison of *lid* opening and closing rates with (colored) and without (gray, compare Figure 4.4) the TIF2 peptide. (D) Comparison of rates for the unfolding event following the *lid* fluctuations with and without the TIF2 peptide in solution.

and without the TIF2 peptide are shown in Figure 4.12C. Instead of a decrease the opening rates rather showed a marginal increase, which implies the stability of the *lid* is even slightly decreased ($\approx 2\,k_BT$ or lower).

A large change was however observed in the further unfolding of the *open* state. A significant shift from an average unfolding force of about 16 pN to 24 pN (Figure 4.12B, compare to Section 4.1) was observed. A method described by Oberbarnscheidt *et al.* [162] was used to calculate the force-dependent unfolding rates (Figure 4.12D). In presence of the TIF2 peptide the unfolding rate of the *open* state at 20 pN decreases roughly by a factor of 10. Assuming that the refolding rate does not change, the zero-force energy difference stabilizing this transition is estimated to be $3 \pm 1\,k_BT$. that indicates the binding of the TIF2 peptide to helix 12 did not stabilize the *closed lid* conformation but rather the next step on the unfolding pathway. This suggests that the *lid* comprises N-terminal helix 1 and further unfolding, proceeding either by unfolding of helix 3 or helix 12 was shifted to higher forces by the stabilizing interaction of the TIF2 peptide.

Additional preliminary data indicate that the binding of the TIF2 peptide also decreased DEX dissociation rate from the *open* state (data not shown), indicating allosteric rearrangements due to this interaction. Such influence has also been measured by Pfaff and Fletterick [173].

4.6.2 *Peptide binding competing with* lid *closing*

In previous force-spectroscopy studies by Grison *et al.* [84], the binding of a peptide to a protein was probed by tethering the peptide with a flexible GGS linker to the protein construct. By applying force to the construct, the reversible detaching and reattaching fluctuations of the tethered peptide, similar to the *lid* fluctuations of the GR-LBD (ref. Section 4.2), could be observed. Adding the same peptide in solution, concentration-dependent lag phases of these fluctuations could be induced, yielding the binding rate of the peptide from solution.

Inspired by these experiments, the idea was reversed for an assay to investigate the nature of the native *lid* fluctuations of the GR-LBD as illustrated by Figure 4.13A. The sequence of 22 amino acids from the N-terminal *lid* was used to synthesize an identical peptide (further called *Npep*) that could be added into solution (sequence is given in Section B.3).

Figure 4.13B shows a force vs. time trace of the native *lid open* (blue) - *closed* (purple) fluctuations in the presence of 10 µM *Npep* and 20 µM DEX in solution. At forces of around 8 pN, the closing of the *lid* proceeds with a rate of $k_{open \to closed} \approx 2 \times 10^3\,/\mathrm{s}$ (compare Figure 4.4). Rebinding of DEX at this concentration happens with a rate of $k_{bind} = 0.7\,/\mathrm{s}$.

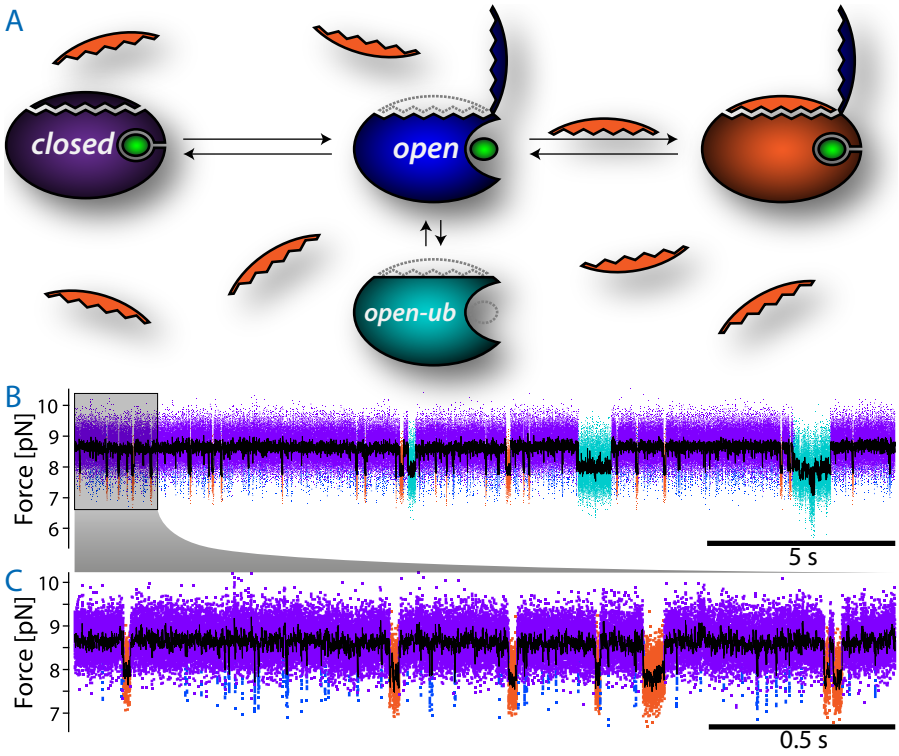

Figure 4.13: (A) Schematic of *lid* sequence peptide binding from solution. The peptide in solution is colored in orange. For clarity, both the peptide in solution and the open N-terminal *lid* are represented as the shape of the folded *lid* even though they are thought to be unfolded. (B) Force vs. time trace at constant trap positions in the presence of 10 µM *Npep* and 20 µM DEX (data presentation as in Figure 4.5). Events of blocked closing by peptide binding from solution are colored in orange. (C) Zoom into (B).

Having the *Npep* in solution, a new state occurred at the contour length of the *open* state (orange). This state exhibited dwell-times that were significantly shorter than the DEX rebinding events (cyan in Figure 4.13B) but significantly longer than the *open* state (blue in Figure 4.13C). This state can be explained by the binding of the *Npep* to the region where the N-terminal *lid* usually binds, consequently inhibiting the closing of the *lid*.

Increasing forces yielded a higher probability of the *open* state, resulting in proportionally more peptide binding events. This highlights the binding of the peptide to the *open* state. An HMM analysis (Section 3.4) of the dwell-times in the orange state yields a dissociation rate of about 40 /s. The binding rate of the *Npep* to the *open* state was calculated to be about 100 /s, reflecting the difference to the DEX dissociation rate of 3 /s. Testing a lower *Npep* concentration of 2 µM, resulted in fewer orange states, yielding on-rates of 20 /s.

As a control, the experiments were repeated, using another peptide, comprising 25 amino acids of the C-terminal sequence of GR-LBD. Even using up to 100 µM of peptide, no detectable difference in the native *lid* fluctuations was observed.

A side result of this investigation was that the company GenScript had massive problems to synthesize and purify the Npep*, highlighting its strong hydrophobicity.*

This result served as further evidence for the observed *open-closed lid* fluctuations relating to the unfolding of the N-terminal helix 1 (purple in Figure 4.11).

These results demonstrate a new versatile method of inferring structural interpretation of unfolding events in optical trap measurements. It is fast and easy to do as no mutations nor preparation of a new construct is needed. Synthesis of peptides is commercially possible and can be usually done in less than 6 days – if there are now technical difficulties – for a length of up to 25 amino acids at a reasonable price.

4.6.3 *Loop mutation in N-terminal helix 1*

Another method of determining whether the *lid* is located at the N- or C-terminus is to genetically insert an unstructured loop at a certain position within the protein construct sequence. By unfolding this modified construct an increase in protein contour length gain of certain folding intermediates can be observed (demonstrated already by Bauer *et al.* [20]).

A flexible stretch of 11 residues (GGSGGSGGSGG) was inserted between the N-terminal helices 1 and 3, more precisely between the serine at position 551 and the valine at position 552 (Figure 4.14A). This construct will be called GR-LBD^{N-loop} (the complete sequence is given in Section B.1). If the *lid* comprises the 33 N-terminal residues (purple in Figure 4.14A), its opening should result in an increase of the contour length gain by about 4 nm [50].

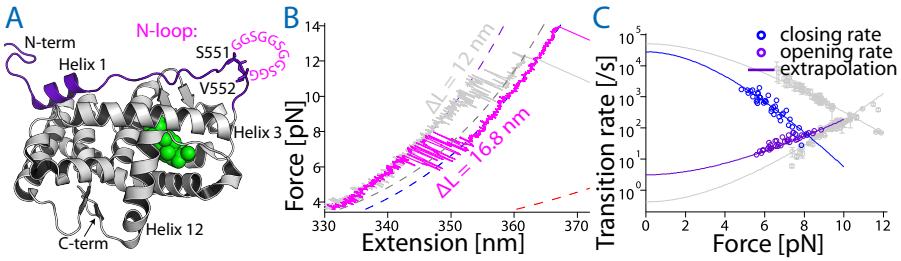

Figure 4.14: Loop insertion construct. (A) Structure of GR-LBD F602S (PDB: 1M2Z). N-terminal 33 amino acid residues are colored in purple. DEX is colored in green. S551 and V552 are highlighted by stick representation. The loop insertion in the GR-LBD^{N-loop} construct is symbolized by pink GGS (B) Comparison of stretching curves obtained from GR-LBD^{N-loop} (pink) and GR-LBD (gray) at 200 µM DEX using a constant pulling velocity of 50 nm/s. Dashed colored lines show WLC fits (compare Figure 4.1)(C) Comparison of force-dependent *lid* closing (blue) and opening (purple) rates of GR-LBD^{N-loop} with the rates measured for GR-LBD (gray, compare Figure 4.4)

A zoom into the *lid* fluctuation region of a force vs. extension trace of GR-LBD^{N-loop} pulled at 50 nm/s is displayed in Figure 4.14B. Indeed, the fluctuations show a significant increase in contour length gain (16.8 ± 1.0 nm vs. 12 nm) (cf. gray trace of GR-LBD).

Passive-mode experiments yielded force-dependent opening and closing kinetics of GR-LBD^{N-loop}, which are plotted in Figure 4.14C. Consistent with the increase in protein contour length, the midpoint forces were shifted to lower values (8 vs. 10 pN). The energy for *lid* closing as obtained by the zero-force rates decreased slightly

$$\Delta G^0_{lid+N-loop} = 9.3 \pm 0.4\, k_B T$$

(vs. 11.6 k_BT). Moreover, GR-LBD^{N-loop} showed similar DEX rebinding kinetics as the GR-LBD with

$$k^{N-loop}_{bind} = 0.05 \pm 0.01\ /s/\mu M$$

(compare Section 4.3), which confirmed the proper functioning of the construct.

4.7 SUMMARY OF HORMONE PATHWAY MEASURED UNDER FORCE

The dissociation pathway as measured at around 10 pN and extrapolated to 0 pN is summarized in Figure 4.15. With no hormone bound, the GR-LBD resides in the *open-ub* state. The *lid*, comprised of the 33 N-terminal amino acid residues is destabilized and unfolded under these forces. Upon binding of DEX the *lid* becomes stabilized by 11.6 k_BT, which induces the transition to a mostly closed conformation. This state in turn inhibits the dissociation of the hormone

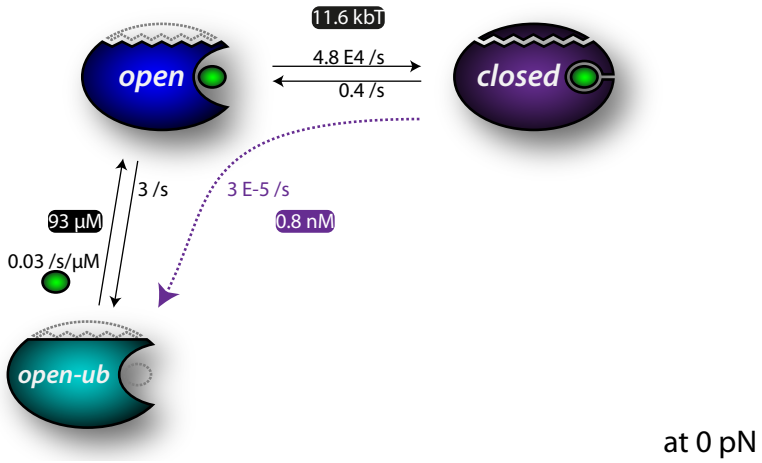

Figure 4.15: State model of DEX binding as measured under force. States colored as shown in data traces before. Unfolded parts are displayed in gray dashed lines. Numbers are rates of the given transition extrapolated to 0 pN. Numbers with colored background are the energy differences or K_d between the neighboring states. The dotted purple line illustrates the effective dissociation from the closed state.

	DEX	F-DEX	LIT. [113]
$k_{bind}[/s/\mu M]$	0.033 ± 0.003	0.21 ± 0.04	
$k_{diss}^{open}[/s]$	3.0 ± 0.2	35 ± 5	
$k_{diss}^{eff}(0\,pN)[/s]$	$3 \pm 2 \times 10^{-5}$	$3 \pm 2 \times 10^{-4}$	5×10^{-4}
$K_{d,eff}^{closed-open\text{-}ub}[nM]$	0.8 ± 0.5	1.5 ± 1.0	150

Table 4.1: Summary of DEX and F-DEX binding and dissociation rates and affinities considering the hormone exchanging only between the *open* and the *open-ub* state. Comparison with values recently measured in ensemble studies using F-DEX and a slightly different GR-LBD variant containing only the F602S mutation [113].

leading to the nM affinity at zero-force. The fluctuations of the *lid* are equilibrated on the timescale of hormone dissociation, implying that it opens and closes many times before the hormone spontaneously dissociates from the *open* state. Hence, the dissociation is limited by the fast closing of the *lid* and the rate scales with the fraction of time spending in the *open* state. Binding of the hormone to the *open-ub* state immediately leads to closing of the *lid* at zero-force.

Table 4.1 provides a summary of the measured and extrapolated binding and dissociation rates and affinities of DEX and F-DEX. The $k_{diss,F\text{-}DEX}^{eff}(0\,pN)$ is in good agreement with dissociation rates for F-DEX recently measured in bulk using fluorescence anisotropy [113, 128]. This would suggest the dissociation pathway that was measured under force resembles the relevant pathway in the absence of force. On

the other hand the extrapolated K_d differs by 2 orders of magnitude, reflecting a drastically faster binding rate measured in the present work. Note also that these ensemble studies used variants of GR-LBD including the F602S mutation but not the C638D mutation, which was also present in the GR-LBD used in the present work. The C638D mutation has previously been observed to have influence on hormone binding kinetics [23, 37, 265].

The following sections present results shedding more light on the conformation of the GR-LBD at zero-force and a more detailed discussion of the binding and dissociation pathway is given in Section 4.10.

4.8 THE STABILITY OF THE *lid* IN THE APO STATE

The apo-conformation is, in general, the inactive and unbound state of a protein.

The experiments provided so far did not answer whether the *open-ub* resembles the apo-conformation of the GR-LBD at zero-force. Consequently, experiments were performed to test whether the N-terminal *lid*, which is unfolded in the *open-ub* state, possibly attaches to the residual folded conformation of the GR-LBD also in the hormone-unbound case at lower forces. Passive-mode (see 2.6.2) measurements at low DEX concentrations were performed. The protein was first kept at around 10 pN until a remaining DEX molecule dissociates and the GR-LBD transitions to the *open-ub* (cyan) state. The force was decreased step-wise, force vs. time traces recorded and analyzed (similarly to Section 4.2). Figure 4.16A depicts such a trace at low forces.

At lower forces the GR-LBD exhibited transitions from the *open-ub* state to a more compact short lived state (colored in pink). This state can be interpreted as the N-terminal *lid* transiently attaching to the residual folded part of the protein. This hormone-unbound, lid attached state will be henceforth referred to as the *apo* state. It is the energetically favored state in the absence of force.

It is not exactly as compact as the *closed* state, but exhibits a protein contour length of 1.7 ± 0.5 nm. With decreasing force the lifetime of this state and the frequency of its occurrence increase exponentially as expected. The force dependence of the attachment and detachment rate of the *lid* are illustrated in Figure 4.16B. The extrapolations in Figure 4.16B yield contour length differences to the transition state of $\Delta L^T_{open\text{-}ub \to apo} = 7.5 \pm 0.5$ nm and $\Delta L^T_{apo \to open\text{-}ub} = -4.0 \pm 0.2$ nm. The fact that these independently fitted values sum up to the contour length difference between the *open-ub* and *apo* state serves as further evidence of the model used. The extrapolation of the transition rates to zero-force yields

$$k^{0\,\mathrm{pN}}_{open\text{-}ub \to apo} = 2.8 \pm 0.9 \times 10^3\ /\mathrm{s}$$

and

$$k^{0\,\mathrm{pN}}_{apo \to open\text{-}ub} = 70 \pm 30\ /\mathrm{s}$$

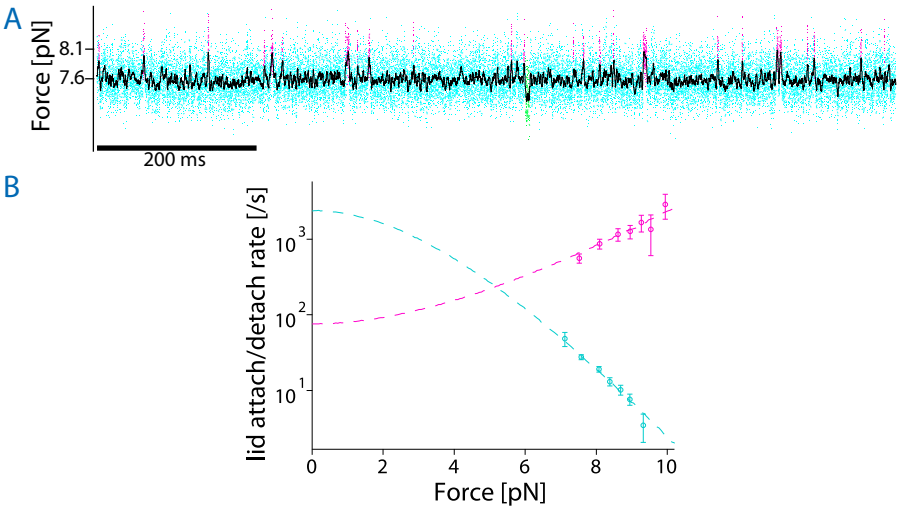

Figure 4.16: *Lid* attaching to the hormone-unbound GR-LBD (*apo* state). (A) Force vs. time trace after hormone dissociation, analogous to Figure 4.5. The cyan state was already classified before as the *open-ub* state. Short excursions to a more compact state are colored in pink (*apo* state). (B) Chevron plot of the transition between *open-ub* and *apo* showing the force dependence of the rate for the terminal *lid* to attach (cyan) and detach (pink) from the residual protein structure. Data of one molecule is shown. The dashed lines are extrapolations by the Berkemeier-Schlierf model described in Section 3.4.2.

(3 different molecules were averaged). From the ratio of these rates, the free energy stored in the attachment of the N-terminal *lid* to the residual protein structure in the hormone-unbound state – $\Delta G^0_{ub\text{-}lid}$ – can be computed:

$$\Delta G^0_{ub\text{-}lid} = 3.7 \pm 0.2\,k_BT$$

This energy can also be calculated for each passive-mode trace separately without the extrapolation of rates with a method described in Section 3.4.1 yielding $\Delta G^0_{ub\text{-}lid} = 4.0 \pm 0.4\,k_BT$.

4.9 HORMONE BINDING AT ZERO-FORCE

From the experiments described in the previous sections it cannot be concluded whether the binding rate measured to the *open-ub* state is the same as in the absence of applied force. The measurements presented in Section 4.8 indicated that the *open-ub* state does not exactly resemble the apo-state at zero-force but a similar state – the *apo* state – in which the N-terminal *lid* interacts with the residual folded protein. The additional energy of this interaction makes this state the most populated at zero-force. In the *apo* state, the binding pocket might be closed, leading to a slower binding rate to this state. To directly test this, a mechanical force-jump assay as generally described in Sec-

tion 2.6.3 was performed, which allows the measurement of binding kinetics at 0 pN.

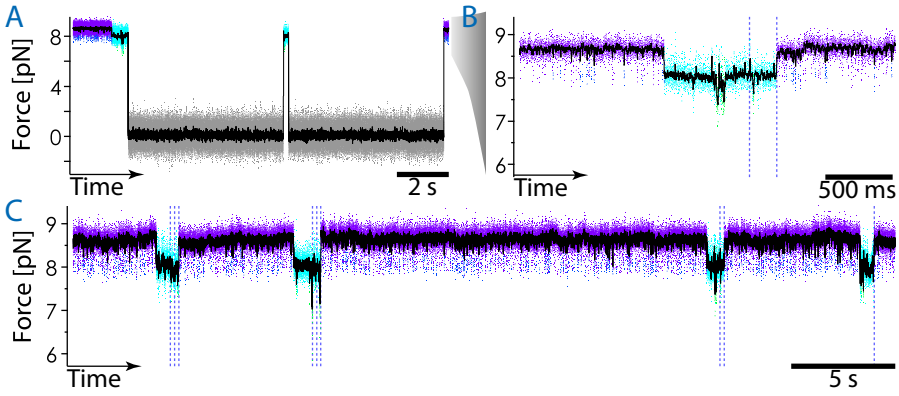

Figure 4.17: Force-jump assay to study rebinding of 6 µM DEX at 0 pN. (A) Force vs. time trace during a force-jump pattern with 6 s waiting time at 0 pN and a high force probing step of 200 ms. The data during the high force phase is colored according their HMM state assignment. At 0 pN the states cannot be distinguished (gray). (B) Merge of the high force data as described in Section 3.5. The blue dashed lines indicate where 6 s of 0 pN data was truncated. (C) Example force vs. time trace showing 4 rebinding events during a force-jump assay after truncation of the low force data

ASSAY PROCEDURE Figure 4.17A illustrates the assay procedure for this particular case. The GR-LBD was promoted into the *open-ub* (cyan) state before the force was reduced. To this end a low force bias of around $F_{probe} = 8.5\,\text{pN}$ was applied, which induced some opening of the *lid*, but did not trigger further unfolding after dissociation of DEX. A low DEX concentration of 6 µM was used to avoid rapid rebinding, and to enable the protein unbound states to equilibrate at zero-force before hormone binding would occur. After dissociation, the force bias was quickly reduced to $\approx 0\,\text{pN}$ for a predefined time of $\tau_{wait} = 6\,\text{s}$. After τ_{wait} the force was programmed to increased again for $\tau_{probe} = 200\,\text{ms}$ to test whether binding had occurred. Observing the *open-ub* state indicated that there was no binding event and the force was reduced again for another attempt. The beginning of *open-closed* fluctuations indicated the binding of DEX (as illustrated in 4.3).

An unbinding at zero-force is very unlikely ($P < 1 \times 10^{-4}$, see Section 4.4).

Figure 4.17B illustrates a trace of such a rebinding event after 2 attempts at 0 pN (The data at the high force level was merged as descriebd in Section 3.5). An example of 4 consecutive rebindings can be found in Figure 4.17C. From the ratio of successful rebinding events and the total number of rebinding attempts (blue dashed lines in Figure 4.17C) $P_{rebind}(\tau_{wait}) = \frac{N_{rebind}}{N_{attempts}}$, the rebinding rate at 0 pN was calculated using Equation 3.14.

BINDING RATES AT ZERO-FORCE Similar traces were recorded using 2 and 6 µM F-DEX. Due to the faster dissociation of F-DEX compared to DEX (see Section 4.5), a slightly lower force could be used. Figure 4.18 shows the binding rates measured at zero-force in comparison to the ones measured under force. Averaging the binding rates yields

$$k_{bind}^{0\,\mathrm{pN}} = 0.021 \pm 0.002\ /\mathrm{s}/\mu\mathrm{M},$$

for DEX which is less than a factor of 2 slower than the rate measured under force (4.3). The value for F-DEX is

$$k_{bind,F\text{-}DEX}^{0\,\mathrm{pN}} = 0.05 \pm 0.02\ /\mathrm{s}/\mu\mathrm{M},$$

which is a factor of 4 slower than the rate measured under force (4.5).

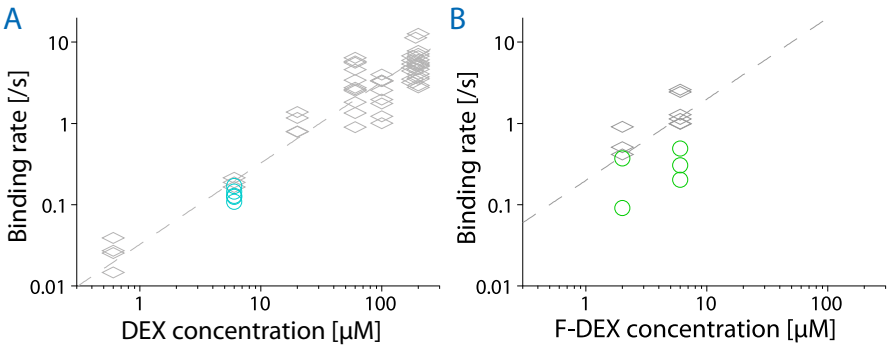

Figure 4.18: Comparison of binding rates measured at 0 pN to the binding rates measured under force (grey diamonds). (A) Binding rates for 2 µM DEX (cyan circles). 5 traces of 3 different molecules were analyzed. τ_{wait} varied from 1 to 6 s. (B) Binding rates for two different F-DEX concentrations (green circles). 5 traces of 4 different molecules were analyzed. τ_{wait} varied from 3 to 6 s.

4.10 SUMMARY AND DISCUSSION

4.10.1 *N-terminal* lid *coupling to hormone binding*

DEX makes direct contacts with the C-terminal AF2 helix 12 (at position L753) and the preceding loop (I747 and F749) [24]. These interactions likely stabilize helix 12 in the active conformation. Crystal structures of antagonist-bound LBD also show major rearrangements of the C-terminal helix 12 [209] and other studies described a coupling between helix 12 and hormone binding [69, 173]. Therefore it was unexpected that the single-molecule measurements demonstrated in the present work identified the N-terminal helix 1 as a new key structural *lid*-like element tightly linked to hormone binding.

Interestingly, Giannoukos *et al.* [79] and Dong *et al.* [55] found the LXXLL motif in residues 532-536 – located in helix 1 – important for

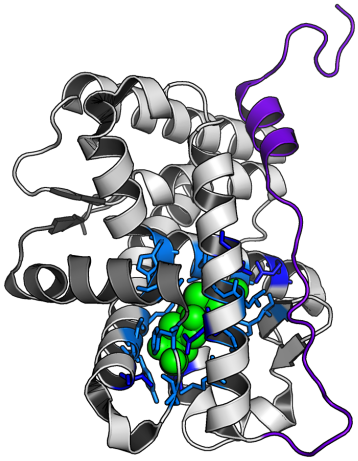

Figure 4.19: Structure of GR-LBD F602S (pdb: 1M2Z [24]). Amino acids exhibiting direct hydrophobic interactions (light blue) or forming hydrogen bonds (blue) with DEX are displayed in stick representation. 33 N-terminal amino acids are colored in purple, C-terminal in gray. DEX is colored in green.

hormone binding *in-vivo*. The data presented here now offers a structural explanation for this finding. The strong coupling of hormone binding and the N-terminal *lid* is particularly surprising since the *lid* has no direct contacts with the hormone [24]. This indicates that not only *lid* closing but also hormone binding is accompanied by a significant allosteric rearrangement. The binding rates ($k_{bind} = 0.03\,/\mathrm{s}/\mu\mathrm{M}$) for binding even to the *open-ub* state are comparably slow for small molecule binding [34, 171], strongly suggesting that major structural rearrangements are necessary for binding the hormone deep inside the protein structure.

In the hormone-unbound conformation, the *lid* is only weakly attached to the rest of the protein. This could be a possible explanation for the strong tendency of the unbound GR-LBD to aggregate under bulk conditions [117, 215]. The difficulties in the synthesis and purification of the N-terminal peptide further support this hypothesis.

A partial unfolding facilitating ligand binding and release was also proposed for the Estrogen Receptor [76], which might be a comparable mechanism to the destabilization of the N-terminal *lid* observed in this study.

4.10.2 *The hormone binding and dissociation pathway*

A model for hormone binding to the *open-ub* state and dissociation from the *open* state was given in Section 4.7. The closing of the *lid* with a free energy of $11.6\,k_BT$ leads to enclosure of the hormone in the binding pocket. This consequently reduces the effective dissociation

rate from the *closed* state drastically at zero-force, leading to the high affinity.

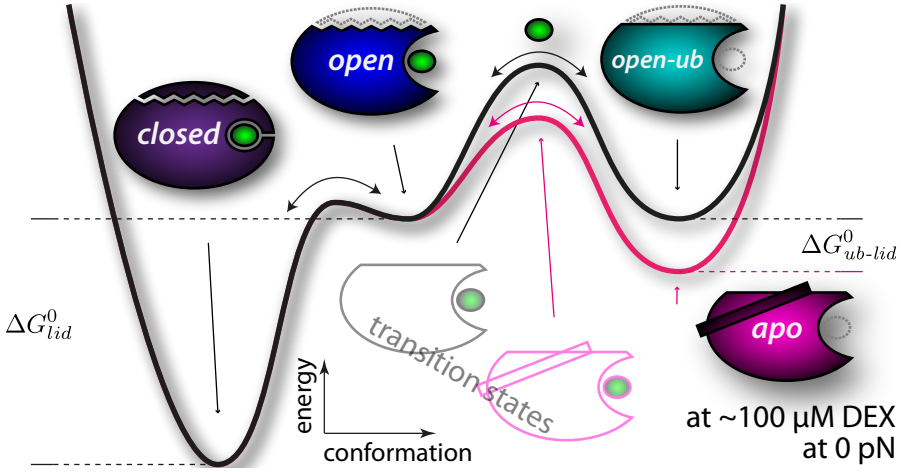

Figure 4.20: Schematic of the energy landscape for hormone binding, illustrating the influence of the *lid*, attaching in the unbound and transition state.

THE *lid* ATTACHING IN THE APO-CONFORMATION The measurements presented in Section 4.8 revealed that the *lid* can also attach to and stabilize the unbound conformation by a free energy of $\Delta G^0_{ub\text{-}lid} = 3.7\,k_BT$. Figure 4.20 illustrates the influence of this stabilization on the hormone binding and dissociation pathway. The rate of DEX binding to the GR-LBD at zero-force was not significantly reduced by this attachment of the *lid* (as demonstrated in Section 4.9). These results suggest a picture in which the *lid* attaches in a different way than in the *closed* state, leaving the binding pocket accessible in the *apo* state, such that the *lid* does not need to detach for the hormone to bind (illustrated by the magenta *apo* state). In other words, the transition state for hormone binding to the *apo* state is stabilized by the same free energy $\Delta G^0_{ub\text{-}lid}$, as illustrated in Figure 4.20.

The simplest way to model this transition state is to suppose that it resembles the transition state between the *open* and the *open-ub* state but with the *lid* attached in the same way as in the *apo* state (as depicted in gray and magenta lines in the lower part of Figure 4.20).

ENERGY CONSERVATION AND THE DISSOCIATION PATHWAY The *apo* state has a lower free energy than the *open-ub* state due to the stabilization by this alternative attachment of the *lid* ($\Delta G^0_{apo} = \Delta G^0_{open\text{-}ub} - \Delta G^0_{ub\text{-}lid}$). Binding of DEX to both states proceeds to the *open* state with a similar rate.

The free energy change must be zero for a closed thermodynamic cycle. Consequently, the difference in free energy upon binding to the

	DEX	F-DEX	LIT. [173]
$k_{bind}^{0\,\mathrm{pN}}[/\mathrm{s}/\mu\mathrm{M}]$	0.021 ± 0.002	0.05 ± 0.02	0.017
$k_{diss}^{open \to apo}[/\mathrm{s}]$	76 ± 30	$300 + 300 - 150$	
$k_{diss,eff}^{closed \to apo}(0\,\mathrm{pN})[/\mathrm{s}]$	$7(+7-4) \times 10^{-4}$	$3(+5-2) \times 10^{-3}$	4.3×10^{-3}
$K_{d,eff}^{closed-apo}[\mathrm{nM}]$	$30(+30-15)$	$60(+60-30)$	250

Table 4.2: Summary of binding rates and affinities for DEX and F-DEX considering all measured GR-LBD conformations. As rates and affinities are log-normal distributed, their errors are asymmetric. The high errors of nearly a factor 2 are due to error propagation of all the rates factoring into these values. Comparison to values measured in ensemble studies using F-DEX and the same GR-LBD variant [173].

apo state – meaning between the *open* and *apo* state – must be smaller than the one between the *open* and *open-ub* state:

$$\left(\Delta G_{apo}^{0} - \Delta G_{open}^{0}\right) = \left(\Delta G_{open\text{-}ub}^{0} - \Delta G_{open}^{0}\right) - \Delta G_{ub\text{-}lid}^{0}$$

Hence,

$$K_{d}^{open-apo} = K_{d}^{open-open\text{-}ub} \cdot \exp\left(\frac{\Delta G_{ub\text{-}lid}^{0}}{k_B T}\right).$$

As the binding rate basically did not change (ratio < 2), this must result in a faster dissociation rate from the *open* to the *apo* state, which is predominant at zero-force:

$$k_{diss}^{open \to apo} = k_{bind}^{0\,\mathrm{pN}} \cdot K_{d}^{open-apo} = 76 \pm 30\ /\mathrm{s} \tag{4.1}$$

This faster dissociation rate can again be understood by the stabilization of the transition state for hormone dissociation by the alternative attachment of the *lid* (as depicted in Figure 4.20).

The low energy barrier between the *open* and the *closed* state – which reflects the fast *lid* closing rate ($k_{open \to closed}^{0\,\mathrm{pN}}$) at zero force – highlights the equilibration of this transition in regard to hormone dissociation. Based on this pathway, an effective dissociation rate – $k_{diss,eff}^{closed \to apo}(0\,\mathrm{pN})$ – and affinity – $K_{d,eff}^{closed-apo}$ – at 0 pN could be calculated for DEX and F-DEX through multiplication of $k_{diss}^{open \to apo}$ by $P_{open}(0\,\mathrm{pN})$ (as discussed in Section 4.4). The model for the complete state network is illustrated in Figure 4.21. All values are summarized in Table 4.2.

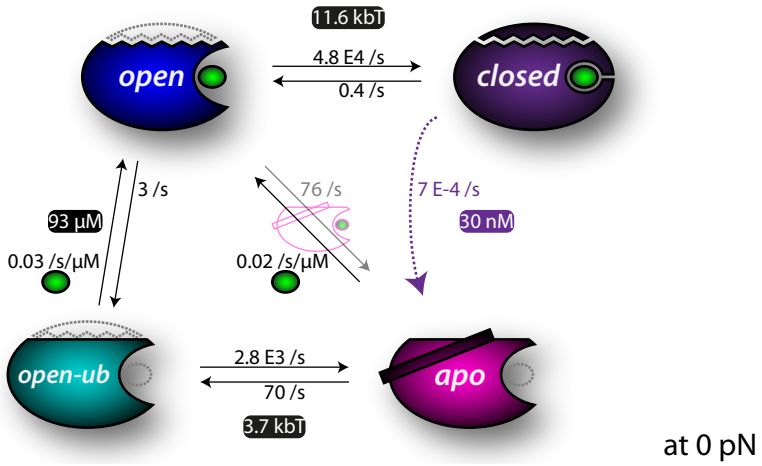

Figure 4.21: State model of DEX binding. States colored as shown in data traces before. Numbers are the rates of the given transition extrapolated to 0 pN. Numbers with colored background are the energy differences or K_d between the neighboring states. Black numbers were measured, the gray number was calculated using Equation 4.1. The dotted purple line illustrates the effective dissociation from the closed state.

ALTERNATIVE *lid* ATTACHMENT IN THE OPEN STATE Could this alternative attachment of the *lid* also stabilize the hormone-bound *open* state and could this theoretically be observed during the *open-closed* fluctuations? Forces of about 8 pN are necessary to shift the equilibrium from the *closed* to the *open* state. These forces would destabilize such a conformation – due to its reduced contour length – to the same extent as the *apo* state. Hence, its population probability vanishes in comparison to the much more stable *closed* state. Therefore it is practically impossible to detect such a conformation. The existence of such a state has no influence on the effective dissociation rate. Its increased population probability in regard to the *open* state at 0 pN would cancel out with an increased energy difference to the transition state for hormone dissociation.

COMPARISON TO VALUES FOUND IN THE LITERATURE The dissociation rate, measured in a previous fluorescence anisotropy study by Pfaff and Fletterick [173], using a variant of GR-LBD with the same mutations F602S and C638D and F-DEX was in good agreement with the $k_{diss,eff}^{closed \rightarrow apo}(0\,\mathrm{pN})$ measured in the present work, supporting the model elaborated in this section.

The binding rate in the ensemble study was measured to be slightly lower, resulting in a slightly higher K_d. This small deviation might be explained by misfolded or binding-incompetent species (ref. to A.5, 5.6, A.4.2), which might influence the apparent GR-LBD concentration used in ensemble measurements. In the present work, only fully functional GR-LBD molecules were analyzed. The dissociation

rate was also determined by fluorescence anisotropy measurements, in the framework of a bachelor thesis by Leif Mummenbrauer [151]. Here exactly the same protein variant as in the trap measurements was used. This study yielded $k_{diss,F\text{-}DEX} = 1.2 \times 10^{-3}\,/\mathrm{s}$, which also agrees with the $k_{diss,eff}^{closed \to apo}(0\,\mathrm{pN})$ for F-DEX within the measurement error.

Different studies with slightly different GR-LBD variants reported similar affinities of DEX and F-DEX in a range between 6 and 250 nM [113, 128, 173, 188].

Usual cortisol levels in an adult human blood serum vary between 140 and 690 nM in the morning and between 0 and 280 nM at night [168]. Dexamethasone (DEX) is thought to be 25 times more efficient than cortisol [132]. This would translate into a high DEX level of roughly 30 nM, supporting a lower value for K_d.

Interestingly, as demonstrated by the DEX binding rates at zero-force, there was no binding cleft that needs to open for hormone binding as often previously assumed in the literature [181].

4.10.3 *Summary*

The results presented in this chapter gave detailed insight into the pathway of hormone binding to the GR-LBD and how it is linked to conformational changes. A state model was elaborated reproducing the rates for hormone binding and dissociation measured in ensemble studies.

The demonstrated mechanical readout allows the direct on-line observation of single binding events and the active modulation of their timescales. The ability to monitor such conformational trajectories gives the perspective of observing changes on the dynamics upon interaction with different ligands, co-factors and chaperones in a direct and real-time manner.

5

FOLDING AND STABILITY OF GR-LBD INTERMEDIATE STATES

The following chapter deals with the folding energy landscape of the GR-LBD. The stability of the bound, unbound and folding intermediate conformations were determined. Questions were: How stable is the GR-LBD without hormone bound? Does the GR-LBD need the presence of hormones or the assistance of chaperones to fold properly? What does the kinetic folding pathway look like? At which point in the folding pathway does the hormone bind? What are the overall refolding kinetics of the GR-LBD? What are the possible reasons that GR-LBD needs to interact with chaperones for proper folding *in-vivo*?

In Section 5.1, measurements of the folding intermediate states of GR-LBD and their contour lengths by passive-mode experiments are presented. Their stabilities and possible hormone interactions are revealed in Section 5.2. Next the force-dependent kinetics and folding energy landscape are explored and extrapolated to zero-force in Section 5.3. Using these results, the force-dependent overall rate of folding is extrapolated in Section 5.4. In Section 5.5 this rate is directly measured for zero and low forces by force-jump experiments and a model is elaborated in Section 5.6 which describes the observed effects. The results and their significance are discussed in Section 5.7.

5.1 THE FOLDING INTERMEDIATE STATES

To investigate the folding intermediate states of the GR-LBD, passive mode experiments were performed by applying higher force biases to drive the protein to the fully unfolded state. Figure 5.1A shows a force vs. time trace in the presence of DEX. The force bias was sufficiently low that refolding into the native state could still be observed. Thus equilibrium fluctuations could be monitored with the GR-LBD populating all folding intermediate states.

The data was analyzed by assigning the data points to different states using HMM analysis (explained in detail in Section 3.4). 6 distinct force levels could be observed in the data traces (histogram next to zoom in Figure 5.1A). Additionally it was known from the lower force data presented in Chapter 4 that the *open* and the *open-ub* state exhibit a similar force but different kinetics. That implies a model with a minimum of 7 states should be applied. Indeed, a

model with 7 on-pathway states described the data well judged by single-exponentiality of the lifetimes in each state (see Figure C.1).

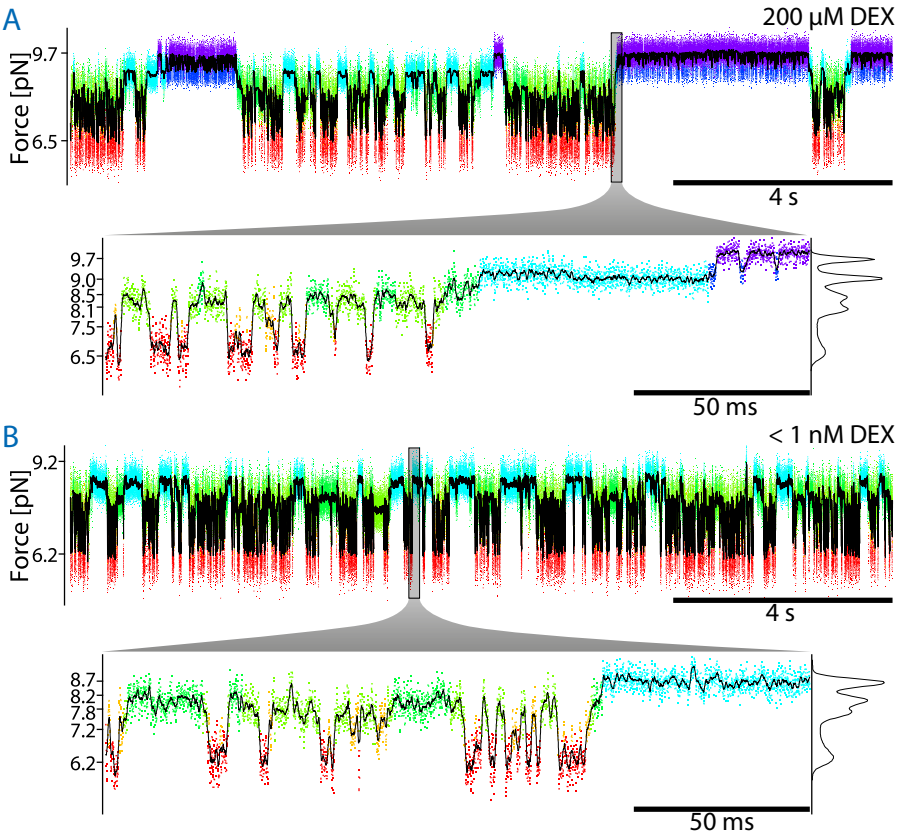

Figure 5.1: Force vs. time traces in passive-mode at forces high enough to completely unfold the GR-LBD at 200 µM DEX (A) and without adding DEX (B) in solution. Residual DEX concentration in the latter case is < 1 nM. Raw data is colored according to a state assignment using HMM analysis based on a 7-state (A) and 5-state (B) on-pathway model. The black line shows the data smoothed. The forces given on the axes are the forces of the *closed* and the *unf* state. A zoom into the data is shown below. Here the forces of all states are given on the axis. Next to the zoom is a histogram of the whole trace force data smoothed by a factor of 31.

The apo *state is not considered in this chapter as it barely appears at elevated forces and does not play a role for the folding energy landscape.*

The trace in Figure 5.1A contains the *closed* (purple), *open* (blue) and *open-ub* (cyan) state as discussed in the previous chapter (Figure 4.5). Already the slight increase in force bias of less than 1 pN to 9.7 pN leads to complete unfoldings starting from the hormone-unbound *open-ub* state. Note that the unfolding rate of the hormone-bound GR-LBD was measured to be about 1 order of magnitude slower than the dissociation rate from the *open* state at these forces (**??**B). This implies, the unfolding observed in these passive-mode traces is mainly preceded by hormone dissociation.

FOLDING INTERMEDIATE STATES The additional states populated at this force bias were labeled Intermediate 1 (*IM1*, green), Interme-

	L_{prot}[nm]	N_{aa_folded}
closed	0.0 ± 0.5	245 ± 9
open	12.0 ± 1.0	212 ± 8
open-ub	13.7 ± 1.0	207 ± 8
IM1	25.6 ± 1.4	172 ± 11
IM2	35.6 ± 1.6	145 ± 10
IM3	51.7 ± 3.1	101 ± 12
unf	86 ± 4	0

Table 5.1: Protein contour length – L_{prot} – of the folding intermediate states and estimates for the number of amino acids contained in the folded portion – N_{aa_folded} – as measured in passive-mode experiments. The length of the *unf* state is taken from force-ramp traces. The errors given for L_{prot} are a combination of SEM, the uncertainties of the elastic parameters and a systematic error due to the unknown state of the terminal amino acids. For N_{aa_folded} there is an additional uncertainty as it is unclear which amino acids comprise the folding intermediate conformation.

diate 2 (*IM2*, lime), Intermediate 3 (*IM3*, yellow) and unfolded (*unf*, red). From the forces exhibited by the different states at a given trap distance, the protein contour length L_{prot} of each state can be calculated using the WLC model as described in Section 3.1. The elastic parameters necessary to describe the DNA linkers had been measured before using stretch and relax cycles as shown in Figure 4.1. From the contour length the number of amino acids contained in the folded portion – N_{aa_folded} – of the intermediate states were estimated and the results are given in Table 5.1, together with the measured L_{prot}.

L_{prot} is the change in contour length due to unfolding of structured protein parts into a poly-peptide chain.

5.2 ΔG AND HORMONE DEPENDENCE OF FOLDING INTERMEDIATES

To investigate the stability of the GR-LBD and its folding intermediate states in the presence of 200 µM DEX, the force-dependent population probabilities were analyzed using the Boltzmann distribution (as explained in Section 3.4.1). This analysis yields quantitative information about the difference in free energy (ΔG^0) among the observed states in the absence of force (given in Table 5.2).

To investigate the influence of DEX on the folding pathway, similar traces were recorded without adding the hormone to the measurement solution. As the GR-LBD was stored in a DEX containing buffer, some residual hormone concentration of < 1 nM was still present during the measurement. Figure 5.1B shows such a trace at vanishing hormone concentration analogous to Figure 5.1A. The pattern and kinetics resemble the traces in the presence of hormones, but lacking

the *open* and *closed* states. Even in the absence of the hormone, the GR-LBD could still fold rapidly (< s) and multiple times from the fully unfolded *unf* to the *open-ub* state.

To characterize the states quantitatively and provide evidence that they are hormone-independent, the free energies at different hormone concentrations were compared as presented in Table 5.2 and Figure 5.2. The folding free energies of all intermediate states up to the *open-ub* state (cyan) did not depend on hormone concentration. This is evidence that the *unf* and *IM1-3* states could not bind hormone at the given concentrations. Any interaction between the hormone and a partially folded intermediate with a higher affinity than $K_d = 200\,\mu M$ would have resulted in a stabilization of this intermediate at $c(DEX) > K_d$.

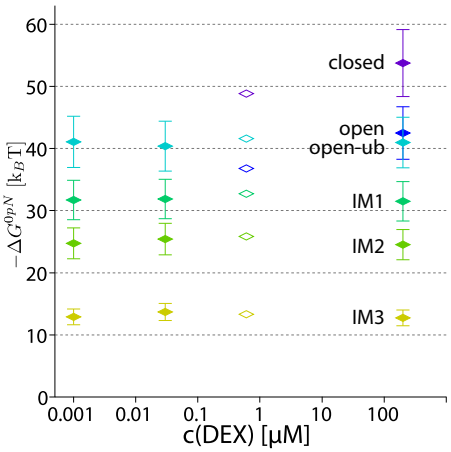

Figure 5.2: Zero-force free energy differences (ΔG^0) of folding intermediate states to the unfolded state for different hormone concentrations. The energies were calculated from the force-dependent occurrence probabilities of the states in passive-mode experiments as explained in Section 3.4.1. The Energy axis is negative so that more stable states appear above less stable ones. Each filled diamond represents an average of at least 10 passive-mode traces from 4 different molecules at varying forces. The given error bars reflect the estimated systematic error of the force calibration. The statistical variation between the experiments is much smaller and can be found in Table 5.2. The empty diamonds are data of one trace at 600 nM illustrating the energy shift of the hormone-bound *open* and *closed* states.

At $c(DEX) = 200\,\mu M$ the *open* state exhibits a similar free energy as the *open-ub* state, as this concentration is about 2-fold above the $K_d^{open-open\text{-}ub}$ (4.4). For the hormone-bound *open* and *closed* states, the stabilization by DEX interaction could be measured even at $c(DEX) < K_d$ as illustrated by the data at $c(DEX) = 600\,nM$ in Figure 5.2. This is due to the fact that the *open* state could be kinetically distinguished from the *open-ub* state since it interacts with the more compact *closed* state. For DEX concentrations < 100 nM the *open* and *closed* state did

A factor of 2 in probability corresponds to a ΔG of $\ln(2) \cdot k_BT = 0.7\,k_BT$ (3.4.1).

$\Delta G^0[k_BT]$	<1 nM DEX	30 nM DEX	200 µM DEX
closed	NA	NA	-53.8 ± 0.5
open	NA	NA	-42.5 ± 0.5
open-ub	-41.1 ± 0.2	-40.4 ± 0.9	-41.0 ± 0.4
IM1	-31.7 ± 0.2	-31.9 ± 0.7	-31.5 ± 0.4
IM2	-24.7 ± 0.2	-25.4 ± 0.5	-24.5 ± 0.3
IM3	-12.9 ± 0.3	-13.7 ± 0.4	-12.7 ± 0.3

Table 5.2: Comparison of free energy differences ΔG^0 of folding intermediate states for different DEX concentrations as displayed in Figure 5.2. The free energy of the the *unf* state was defined as 0. Each value represents an average of at least 10 passive-mode traces from 4 different molecules at varying forces. The error given here reflects the SEM.

not occur on the timescale of the measurement because the binding rate was too slow (4.3).

Surprisingly, even apo-GR-LBD appeared to be a thermodynamically stable protein since even the *open-ub* state exhibits a folding free energy of 41 k_BT. Hormone binding further increases the total stability of the protein (52.8 k_BT at 200 µM DEX).

STATE MODEL OF THE FOLDING PATHWAY A summary of the folding pathway as measured under mechanical load is given in the state model depicted in Figure 5.3.

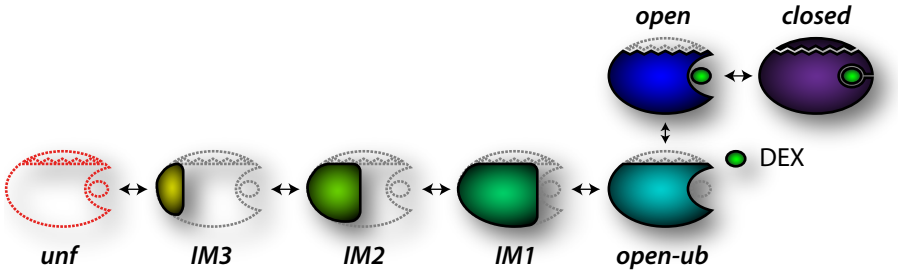

Figure 5.3: Kinetic state model of GR-LBD folding intermediate states, including DEX binding. Coloring as in the state assignment in Figure 5.1. For simplicity, the structure is depicted growing around one nucleus from intermediate to intermediate. However, the exact structural nature remains elusive.

5.3 THE FORCE-DEPENDENT KINETIC FOLDING NETWORK

The force vs. time traces at a constant force bias also allowed for measurement of the transition rates between intermediates. These rates contain information about the free energy of the transition state be-

tween the intermediates, as explained in Section 3.2. Through systematic variation of the force bias on the molecule, the force dependence of the kinetic folding network was explored.

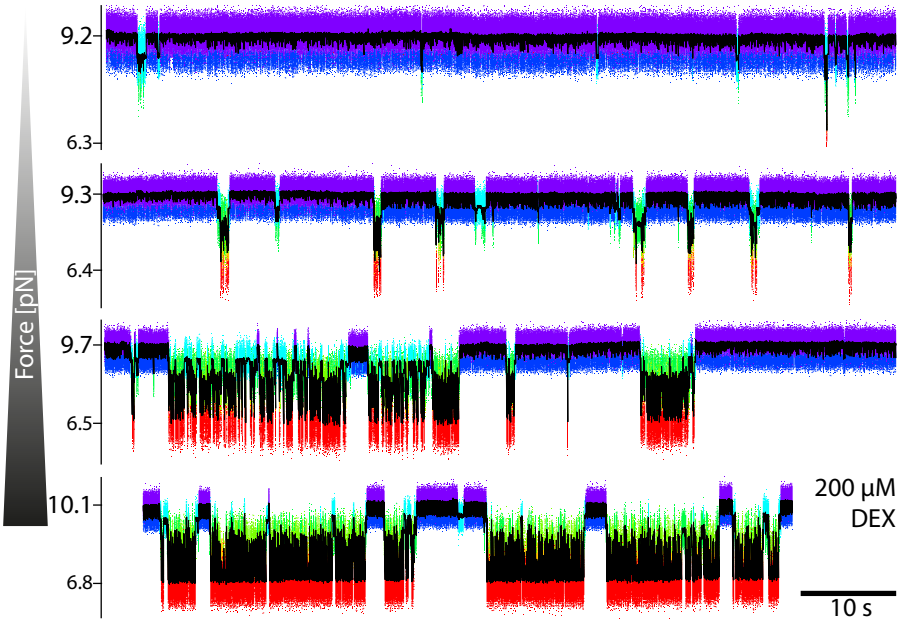

Figure 5.4: Force vs. time traces with 200 µM DEX in solution at 4 different force biases. Presentation analogous to Figure 5.1

Figure 5.4 shows force vs. time traces at 4 different force biases between 9 – 10 pN. Even the slight increase in force bias of less than 1 pN from the upper to the lower trace shifts the equilibrium from predominantly folded to predominantly unfolded states.

Plots such as in Figure 5.5 are also called chevron plots in classical folding studies.

The force dependence of the transition rates between the consecutive intermediate states (as illustrated by the state model in Figure 5.3) is shown in Figure 5.5. As expected, unfolding rates increased and folding rates decreased exponentially with applied force, which is a further evidence of correct state classification at different trap distances. The force dependence was extrapolated using a model described in Section 3.4.2. Note that the curvature of the extrapolation is not a result of the fit but of the predetermined elastic parameters of the DNA linkers and unfolded peptide part. The only free fit parameters were the zero-force transition rate – $k^{0\,\mathrm{pN}}$ – and the contour length difference to the transition state – ΔL^T – Average values for these parameters are given in Table 5.3.

Interestingly, all unfolding transitions exhibited a considerable force dependence. In other words, the transition states appeared to be significantly more extended than the more folded states in contour length (as explained in Section 3.4.2), which is not intuitive for stiff protein structures (compare e.g. to α-actinin [84]). This might be an indication of the flexibility of the conformations.

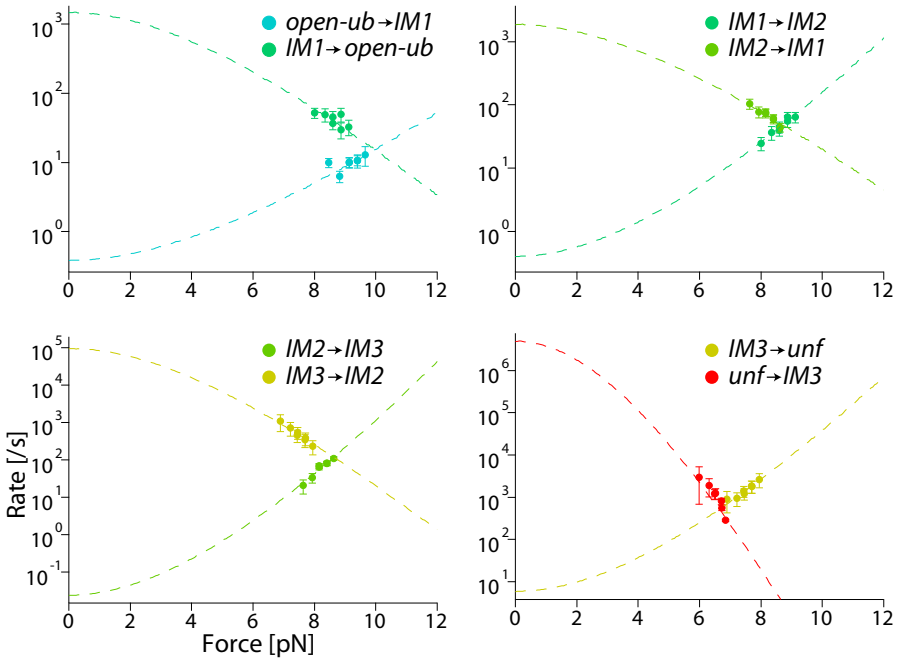

Figure 5.5: Force dependence of transition rates between the folding intermediate states. For clarity only example data measured from 1 molecule is shown. Forces given are as experienced by the initial state. For that reason rate pairs measured at the same trap distance are horizontally shifted towards each other. Dashed lines are extrapolations using a model explained in Section 3.4.2.

	$k^{0\,\mathrm{pN}}[1/\mathrm{s}]$	$\Delta L^T[\mathrm{nm}]$
IM1→open-ub	$2.0 \times 10^{3\pm0.3}$	5.1 ± 0.7
open-ub→IM1	$2.8 \times 10^{-1\pm0.2}$	-6.6 ± 1.6
IM2→IM1	$1.7 \times 10^{3\pm0.2}$	4.9 ± 0.8
IM1→IM2	$1.4 \times 10^{0\pm0.2}$	-5.6 ± 0.4
IM3→IM2	$5.8 \times 10^{4\pm0.6}$	8.5 ± 2.2
IM2→IM3	$3.3 \times 10^{-2\pm0.2}$	-13 ± 1
unf→IM3	$1.4 \times 10^{6\pm0.5}$	16 ± 2
IM3→unf	$1.8 \times 10^{1\pm0.1}$	-8.0 ± 0.3

Table 5.3: Zero-force transition rates and contour length differences for transition states between the folding intermediate states. The values were extrapolated using the model explained in Section 3.4.2. Fitting parameters of 3 experiments were averaged. Negative length values indicate the transition state has a longer contour length than the initial state. The errors for the rates are given in the exponent as they are log-normal distributed.

THE FOLDING ENERGY LANDSCAPE The succession of several stable folding intermediates, observed along the folding pathway of the GR-LBD at the applied forces of around 8 pN, indicate that the folding energy landscape is rough under these conditions. The energy landscape (as described in Section 3.2) for different mechanical force biases was computed from the force-dependent kinetics of the transitions between the intermediates (Figure 5.5). The energy landscape at 9 and 10 pN shows large barriers between the intermediates. However, in the absence of force, the barriers are reduced and folding should proceed rapidly to the native state. The free energy differences calculated from the kinetics at zero-force were in good agreement with the energies calculated in Table 5.2.

The expected overall folding time from unf *to* open-ub *at zero-force is calculated in Section 5.4.*

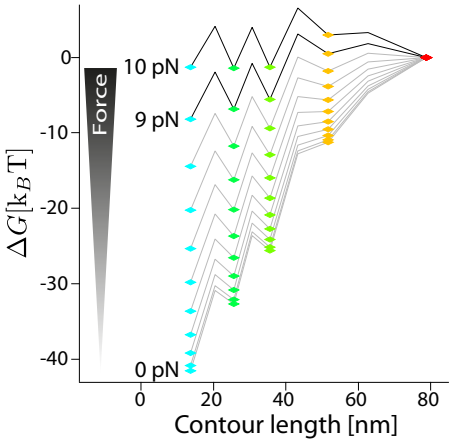

Figure 5.6: Folding energy landscape at different applied force biases. The free energies were calculated using the ratio of extrapolated transition rates as shown in Figure 5.5 and described in Section 3.4.3. Each line represents the landscape at a certain force bias that differ by 1 pN. Black lines illustrate the measured force range, gray lines are calculated from extrapolated rates. Diamonds represent the free energy of the folding intermediate states colored as in the traces before. The peaks of the lines represent the free energy of the transition states.

The kinetics between the folding intermediate states did not show any dependence on hormone concentration. that implies hormone binding to a transition state in the folding pathway could also be excluded, since the stabilization of a transition state by hormone interaction would have increased the corresponding transition rate.

5.4 THE OVERALL FOLDING TIME

Knowledge of the folding energy landscape and the kinetic folding network discussed in Section 5.3, allows the calculation of the overall time it takes for the protein to fold from the *unf* state to the *open-ub* state at different force biases. To this end the time evolution of the state population probabilities was numerically computed using

the transition rates between the intermediates as shown in Figure 5.5, starting with $P_{unf}(t = 0) = 1$. The details of the procedure for computation of this evolution are specified in Section 3.6. From the probability that folding had proceeded from the *unf* to the *open-ub* state after a certain time, the overall folding rate $k^{overall}_{unf \curvearrowright open\text{-}ub}$ was derived as described in Section 3.6.1. Note that $k^{overall}_{unf \curvearrowright open\text{-}ub}$ reflects the rate at which the *open-ub* state is reached for the first time. It does not account for unfolding transitions from *open-ub*.

This time at which a state is reached for the first time is called the mean first-passage time (MFPT) [175].

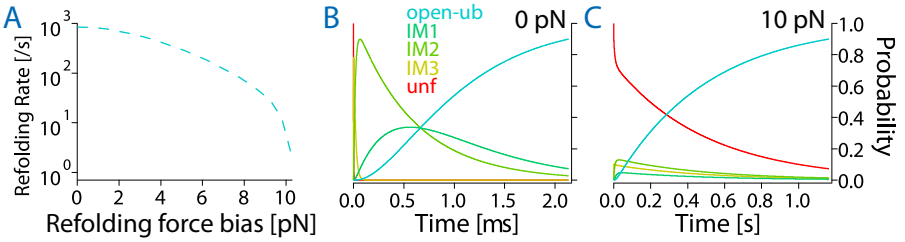

Figure 5.7: (A) Force dependence of overall folding rate $k^{overall}_{unf \curvearrowright open\text{-}ub}$. (B) Evolution of state populations at 0 pN starting from the $P_{unf}(t = 0) = 1$. States are colored as in Figure 5.3. (C) Same data as in (B) but at 10 pN. All data was calculated numerically by using the transition rates between the intermediate states as measured in passive-mode experiments (5.5). Calculation procedure is explained in Section 3.6.

Figure 5.7A displays the dependence of the overall folding rate, $k^{overall}_{unf \curvearrowright open\text{-}ub}$, of the GR-LBD on the applied force bias. The force dependence becomes drastically steeper at higher forces as different processes on the folding pathway become limiting.

At low forces folding proceeds rapidly from *unf* to *IM2* and the limiting steps in folding are the slower transitions $IM2 \rightarrow IM1$ and $IM1 \rightarrow$ *open-ub* ($k_{IM2 \rightarrow IM1}, k_{IM1 \rightarrow open\text{-}ub} \ll k_{unf \rightarrow IM3}, k_{IM3 \rightarrow IM2}$, compare Table 5.3). This can be seen also in the population evolution in Figure 5.7B. The states *unf* (red) and *IM3* (yellow) are immediately depopulated into *IM2* (lime) and *IM1* (green), which then relatively slowly transform into the *open-ub*. Hence, in this force region the force dependence of $k^{overall}_{unf \curvearrowright open\text{-}ub}$ resembles that of $k_{IM2 \rightarrow IM1}$, which is determined by the contour length difference with the transition state $\Delta L^{T}_{IM2 \rightarrow IM1}$.

At high forces the overall refolding process is limited by fast unfolding of the intermediate states back to the *unf* state before proceeding to the folded *open-ub* state. that implies the protein stays in the *unf* state most of the time before it eventually ends up folded (compare Figure 5.7C). Thus, the force dependence at higher forces resembles the shift in equilibrium from the *unf* to the *IM1* state. As the difference in contour length between these states is much higher than $\Delta L^{T}_{IM2 \rightarrow IM1}$, the force dependence of $k^{overall}_{unf \curvearrowright open\text{-}ub}$ also increases.

FOLDING ON A MILLISECOND TIMESCALE The result of these calculations as presented in Figure 5.7A shows that on the basis of the kinetic folding network measured under force, the GR-LBD should fold on the millisecond timescale at 0 pN.

5.5 DECREASE OF REFOLDING RATES AT LOW FORCES

The passive-mode experiments around 10 pN indicated that the GR-LBD refolds fast even in the presence of relatively high mechanical forces (Section 5.3). Since folding rates increase exponentially with decreasing force, one would expect fast overall folding rates in the absence of force. This is also expected from the extrapolation of the kinetic folding network, which yields an overall folding rate in the millisecond range at zero-force (as calculated in Section 5.4).

FORCE-JUMP METHOD TO MEASURE LOW FORCE FOLDING RATES To test the extrapolation of the overall refolding rate $k^{overall}_{unf \curvearrowright open\text{-}ub}$, an indirect method was used as described in Section 2.6.3, similar to the one used in Section 4.9. Refolding near zero force is challenging to measure directly in single-molecule mechanical experiments, since measurable signal depends on the application of force. Another limitation on the investigation of refolding at low forces in passive-mode is the slow unfolding rate of GR-LBD at these forces, which would require impracticably long observation times. To overcome these limitations, a force-jump assay was employed in which the forces on the protein were continuously switched between high and low forces.

An example is illustrated in Figure 5.8A, where a low force of 6 pN is applied for 200 ms alternating with a high force of 12 pN for 30 ms. During the low force phases, the protein was driven to refold, while during the high force phase it quickly and completely unfolded upon hormone dissociation (compare Section 5.3).

The force bias during the low force phase will also be called the refolding force bias, F_{ref}.

A zoom into the high force phase in Figure 5.8B shows such a complete unfolding event during the high force phase. At 12 pN the equilibrium of the *lid* fluctuations was shifted to show mainly the *open* (blue) state and shows only short dwell-times in the *closed* state. To do a state assignment (as described in Section 3.4) of the data similar to that of the passive-mode traces, the low force phases were removed so that only data taken at the same trap distance remains. It is important to note that the refolding events detected in these traces (at the blue dashed line) actually occurred during the low force phases, as the high force inhibits refolding. Hence, the signal of each high force phase served as a read-out of to what extent refolding occurred during the preceding low force phase.

Surprisingly, the intermediate states as found in Section 5.1 could not clearly be identified in these experiments, even though their lifetimes would have been measurable at these forces. The partially

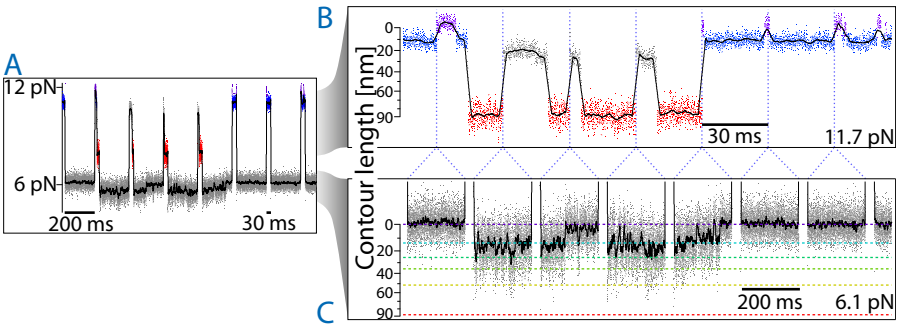

Figure 5.8: (A) Force vs. time trace taken while alternating between two trap distances in a stepwise manner to continuously switch between a high and a low force bias. High force phases are colored according their HMM state assignment, low force phases are shown in gray. The black line shows the data smoothed. (B) Contour length vs. time trace of the high force phases merged together. For better comparison to low force data the force axis was transformed into protein contour length as described in Section 3.1. The force bias shown is the force experienced by the *closed* state. Vertical blue dotted lines indicate where 200 ms of low force data was truncated. The trace is colored according to its HMM state assignment (as described in Section 3.4). The data colored in gray could not be classified unambiguously. (C) Zoom into the low force region, which shows refolding attempts after unfolding which eventually transitions to the bound state. For comparison, the colored dashed lines mark the contour length levels of the folding intermediates as shown in Figure 5.3.

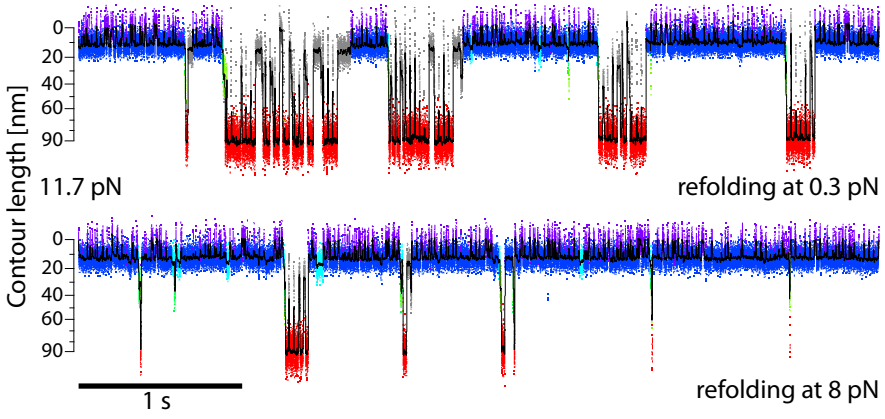

Figure 5.9: Merged high-force phases of contour length vs. time traces obtained in force-jump experiments, showing refolding at different forces. The refolding force bias F_{ref} during the corresponding low-force phases was set to 0.3 pN (upper trace) and 8 pN (lower trace). Coloring coding analogous to Figure 5.8B. DEX concentration was 200 µM.

folded structures occurring after the jumps to low force exhibited a broad range of contour lengths and an attempt to classify them into the intermediate states as before led to non-single-exponential lifetime distributions (as shown in Figure C.2B). The *open-closed* fluctuation on the other hand perfectly resembled the kinetics as measured in the passive-mode experiments before. This pattern can therefore be used as a hallmark of the correctly folded and hormone-bound native state.

SLOWER REFOLDING DESPITE LOWER FORCE BIAS The refolding kinetics at low force were obtained from the merged high force traces. Once the molecule was in an *unf* state (marked in red), the refolding kinetics could be calculated from the number of jumps to the low force necessary until refolding to the native state occurred (as described in Section 3.5). Figure 5.9 shows a direct comparison of the GR-LBD refolding at two different refolding force biases of $F_{ref} = 0.3\,\mathrm{pN}$ (top) and $F_{ref} = 8\,\mathrm{pN}$ (bottom). Refolding at zero-force was significantly slower than refolding in the presence of 8 pN of force, in contrast to the predictions from simple models.

Through systematic variation of the trap distance in the low force phase, the refolding-&-binding kinetics at different F_{ref} were probed. The overall rate $k_{FB} = k^{overall}_{unf \curvearrowright closed}$ for folding starting from the *unf* state including subsequent hormone binding was evaluated as described in Section 3.5. The evaluation of k_{FB} was chosen rather than the overall rate for folding up to the hormone-unbound *open-ub* state, $k^{overall}_{unf \curvearrowright open\text{-}ub}$, due to the uncertain classification of the *open-ub* state in force-jump traces (as described in Section C.2). The distinct pattern of *open-closed* fluctuation served as a well-defined readout for correct folding into a binding-competent native state.

The obtained data is plotted as blue circles in Figure 5.10. To extend the data to higher forces ($> 9\,\mathrm{pN}$), k_{FB} was additionally computed from passive-mode traces as shown in Figure 5.4. The times it took after each complete unfolding until the next *closed* state occurrence were analyzed to calculate k_{FB}. These data were appended as blue squares in Figure 5.10.

At forces higher than 8 pN, k_{FB} showed the steep decrease generally predicted by simple models of force-dependent protein folding [21]. Since force puts an energy penalty on the folding process it slows folding down as visualized in Figure 5.4.

Off-pathway intermediate states need to unfold again for the protein to proceed to the native state. Hence they are also called misfolded states.

OFF-PATHWAY MISFOLDED STATES The decrease in k_{FB} towards lower forces is less intuitive. A roll-over of refolding kinetics towards low forces or denaturant conditions can be explained by an increased occurrence of off-pathway misfolded intermediates [17].

If these misfolded intermediates are more compact than the transition state on the folding pathway, increasing force will depopulate

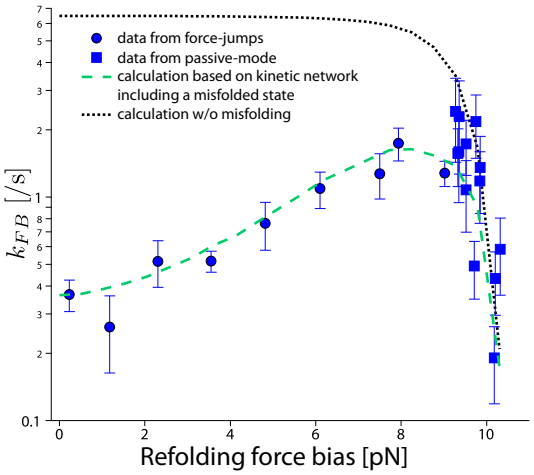

Figure 5.10: Force dependence of the overall folding-&-binding rates k_{FB}. The force-jump experiment data (blue circles) from 28 traces of 9 different molecules was binned into 9 equidistant force bins, averaging the force. The error bars reflect SEM. Squares show the overall transition rates from *unf* to *closed* as obtained from passive-mode traces as presented in Section 5.3. The black dotted line shows the expected folding-&-binding rates k_{FB} computed as described in Section 5.4 but including the DEX binding transition. The dashed line shows the analogous calculation including the possibility of misfolding branching from the *IM1* state as shown in the state model in Figure 5.12.

the misfolded state more than it slows down productive folding and lead to the measured force dependence.

Could the misfolded state be identified in the traces directly? The states populated after the refolding attempts did not exhibit well-defined contour length. Moreover, their lifetime distributions were not single-exponential (Figure C.2B). From this it can be concluded that rather than a single, well-defined misfolded state, an ensemble of misfolded states was populated at low forces.

MISFOLDING MUST OCCUR BEFORE FOLDING TO *open-ub* Could the reduction of k_{FB} be an effect of a reduced DEX binding rate at low forces? The $k_{bind}^{0\,\mathrm{pN}}$ was measured in another force-jump assay as described in Section 4.9 and did not show a significant decrease at zero-force, which is evidence that the misfolding must occur on the folding pathway from the *unf* to the *open-ub* state.

The population probability evolution of the intermediate states at zero-force (as shown in Figure 5.7B) can be used as an additional check. If the deviation from the on-pathway folding model were to occur after folding into the *open-ub* state, then after 10 ms the probability for detecting any folding intermediate earlier on the folding pathway would be less than 1×10^{-5} (ref. Figure C.4). But even 200 ms after the jumps to zero-force (compare upper trace in Figure 5.9) in

about 50% of the cases the protein was in a structure, less folded than the *open-ub* state. This supports the case that misfolding must occur earlier on the folding pathway.

The expected rate for k_{FB} without any off-pathway intermediates (black dotted line in Figure 5.10) settles to the force independent binding rate for $c(DEX) = 200\,\mu M$ at low forces. Note that as k_{FB} is not limited by DEX binding but rather a misfold on the folding pathway to *open-ub*, k_{FB} should be compared to the expected fast overall folding rate $k^{overall}_{unf \curvearrowright open\text{-}ub}$ of $\approx 1000\,/s$ at zero-force (as shown in Figure 5.7A). This accentuates the drastic effect of k_{FB} being reduced due to misfolding.

A more quantitative analysis of the effect of misfolding including the development of a state model is given in the next section.

5.6 MODEL OF MISFOLDING

For the force-jump traces in which the refolding force bias F_{ref} was above 0 pN, refolding could be followed directly by monitoring the length contraction during the low force phases (Figure 5.8C). Although the worse force resolution at low applied forces precluded an explicit state assignment, the average properties of the misfolded states could be assessed by averaging the time traces obtained during the low force phases. Figure 5.11 shows an average contour length vs. time trace of all low force phases for a molecule at the same F_{ref} in which the protein had been completely unfolded in the preceding high force phases. The force bias of $F_{ref} \approx 6\,pN$ was chosen because this bias the experiment had enough force resolution and also exhibited the drastic effect of misfolding on the refolding rate (compare Section C.3).

The trace in Figure 5.11 clearly shows that the protein contracted rapidly ($< 10\,ms$) to $L < 20\,nm$ but even after 200 ms it was stuck in misfolded states, on average exhibiting a contour length of $\approx 14\,nm$ longer than the native length. The black dashed line in Figure 5.11 shows the expected time-dependent contour length evolution based on the kinetics of the on-pathway intermediates (as determined in Section 5.3, the description of the detailed computation procedure is given in Section 3.6.3). After 200 ms, folding and DEX binding should have proceeded significantly further, had there been no misfolded states.

FINDING THE KINETIC MODEL ACCOUNTING FOR MISFOLDING

To model the force dependence of k_{FB}, this rate was numerically calculated from the kinetic folding network. This calculation was similar to that of the black dotted line in Figure 5.10 but included the possibility of misfolding (details described in Section 3.6.2). For simplicity, the model uses just a single misfolded state originating from one of the on-pathway intermediates to represent the average properties of

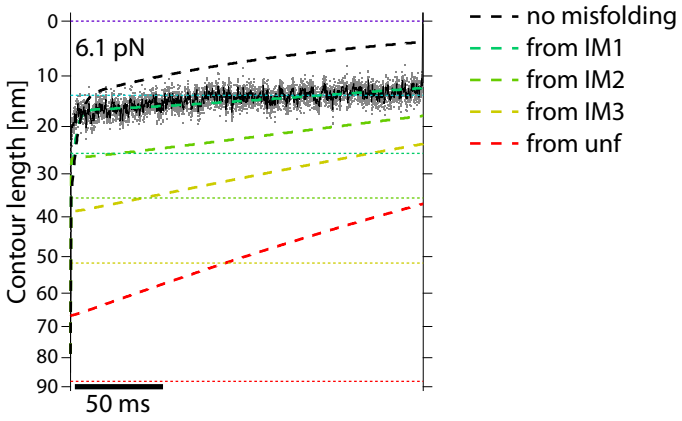

Figure 5.11: Average contour length evolution for refolding in the presence of a force bias of $F_{ref} = 6.1\,\mathrm{pN}$. To obtain this trace, 54 low force phases from 1 experiment that start with the protein in the *unf* state were overlaid and averaged. The dashed colored lines show the calculations of different models, each assuming misfolding branching off a different on-pathway intermediate. Dotted colored lines mark contour length levels of the respective on-pathway folding intermediates

the misfolded states. To this end, an additional state was introduced into the kinetic folding network describing an off-pathway misfolded structure with an additional length contraction ΔL_{mf} and free energy ΔG^0_{mf} branching off from one of the on-pathway states *unf*, *IM3*, *IM2*, or *IM1*. The exchange between the on-pathway and the misfolded state were modeled to be equilibrated.

For each scenario, the kinetic equations of the folding network were solved numerically as before, calculating k_{FB} for different forces. With each of the models, the force dependence of k_{FB} shown in Figure 5.10 could be reproduced, albeit with different parameters for ΔL_{mf} and ΔG^0_{mf} (see Figure C.5). The low force length contraction data in Figure 5.11 puts an additional constraint on the best model for the misfolded intermediate. In a second step, the same numerical calculations were used to obtain the contour length vs. time evolution of the folding network with the respective intermediates (dashed colored lines in Figure 5.11, as described in Section 3.6.3). Only the model assuming that the intermediate misfolding branches off *IM1* described the low force refolding data.

The additional length contraction by the misfolded part was $\Delta L_{mf} = 9.2 \pm 0.6\,\mathrm{nm}$. Consequently the misfolded structure exhibits a protein contour length of $L_{mf} = 16.4 \pm 2.0\,\mathrm{nm}$, which is just a bit longer than the *open-ub* state (compare Table 5.1). This could possibly be an explanation for the slight deviations of *open-ub* lifetimes from a single-exponential distribution measured in passive-mode experiments around 10 pN (Section C.1). L_{mf} is shorter than the position of the transition state for *IM1*→*open-ub* (compare Table 5.3), which was

the limiting folding transition at zero-force (compare Section 5.4). Increasing the force hence depopulates the off-pathway misfolded state more than it slows down the folding transition.

The associated free energy of misfolding was $\Delta G^0_{mf} = 7.8 \pm 0.5\,k_BT$. This energy leads to a reduction in $k^{overall}_{unf \curvearrowright open\text{-}ub}$ by a factor of $\approx 10^3$ (Figure C.3). The full folding pathway including the misfolding species is depicted in Figure 5.12

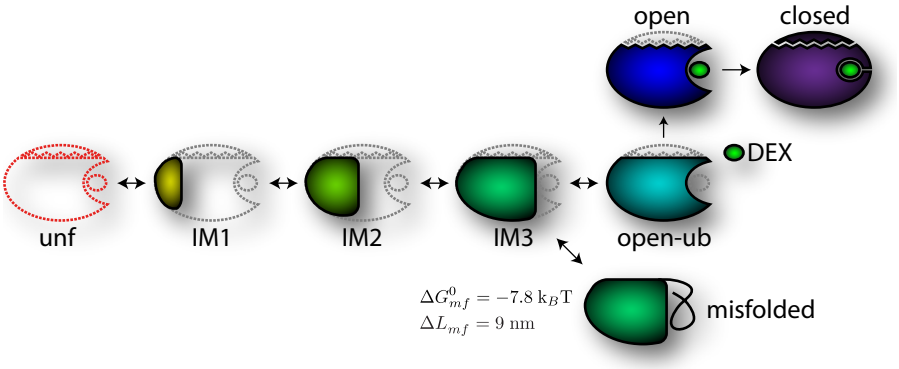

Figure 5.12: State model of GR-LBD folding pathway including an off-pathway misfolded state branching off *IM1*.

5.7 DISCUSSION OF APO-GR-LBD FOLDING AND STABILITY

Expression of soluble and functional GR-LBD has always been problematic, owing to its strong tendency to aggregate under bulk conditions [117, 215]. Due to aggregation, refolding of denatured GR-LBD *in vitro* has not been achieved despite stabilizing mutations and the presence of hormones [128]. Moreover, apo-GR-LBD appeared to be particularly unstable in ensemble measurements, exhibiting unfolding and aggregation already below room temperature [113, 128]. This observation supported the idea that GR-LBD needs assistance from chaperones to mature into its high-affinity hormone-binding state [23, 39, 176].

APO-GR-LBD IS A FOLDING-COMPETENT AND STABLE PROTEIN

In contrast, this single-molecule study shows refolding and hormone binding of single, isolated GR-LBD molecules occurs readily without the assistance from chaperones. Surprisingly, refolding is possible even in the absence of hormones. The GR-LBD in its unbound *open-ub* state exhibits a folding free energy of 41 k_BT (24 kcal/mol), making it a remarkably stable protein.

Folding of GR-LBD to the *open-ub* state was hormone independent and proceeded through at least 3 on-pathway intermediates, each of which added 8 – 13 k_BT of stability (Table 5.2). All these intermedi-

ates formed quickly with zero-force rates between 10^3 /s and 10^6 /s (Table 5.3).

It is important to note that with an increasing number of states, a clear separation becomes challenging and it cannot be excluded that even more intermediates were populated, leading to an even rougher energy landscape than the one depicted in Figure 5.6. It can be speculated that the multitude of intermediate states along the folding pathway reflects the receptors conformational plasticity which is needed so that it could adopt different conformations to allow interaction with a multitude of different ligands [209, 232, 254], co-factors [23, 117, 173, 188] and chaperones.

POSSIBLE EXPLANATION FOR GR-LBD AGGREGATION Why then is apo-GR-LBD so aggregation-prone in bulk? So far the structure of apo-GR-LBD had not been solved, but it is thought to be dynamic [15]. Here, the native state of the apo-GR-LBD was found to be the *apo* state (Section 4.8). It is similar to the *open-ub* state, where everything is stably folded except the *lid* that comprises the N-terminal 33 amino acid residues. At zero-force this *lid* weekly attaches to the residual structure with a free energy of $4\,k_BT$ in the *apo* state. It can be hypothesized that the *lid* plays an important role in bulk aggregation and may need protection by chaperones. Consistent with this view is the important role that has been attributed to the N-terminal region of GR-LBD for its interaction with Hsp70 [113].

The state with the lowest free energy is referred to as the native state.

MISFOLDING SLOWS DOWN FOLDING AT ZERO-FORCE The fast folding kinetics found for GR-LBD at forces around 10 pN under equilibrium conditions (ref. Section 5.4) suggested a folding rate from the completely unfolded to the binding-competent *open-ub* state at zero-force of $k^{overall}_{unf \curvearrowright open\text{-}ub} = 1000$ /s (Figure 5.7A). However, the force-jump experiments revealed that misfolded intermediates,populated at low force reduced the overall folding rate to less than 1 /s (Figure C.3).

A similar effect has been reported for Hsp90 [102], human neuronal calcium sensor-1 (NSC-1) [89] and Calmodulin (CaM) [227]. In contrast to the simpler proteins NSC-1 and CaM where the misfolded state could be directly detected in equilibrium traces, the nature of the misfolded state was more elusive in the case of GR-LBD. While a drastic effect on folding was evident, an identification of a single well-defined misfolded state was not possible. Instead the multi-exponential lifetimes of the intermediates formed at low forces (Figure C.2) indicated that the misfolded species constituted a broad ensemble of states. With their lengths often indistinguishable from those of the on-pathway intermediates, an unambiguous assignment of the regions involved was impossible. A key aspect of misfolded structures was that they branch off the folding pathway from one of the later folding intermediates, likely *IM1*, where 70% of the peptide

chain is already folded. It is hence likely only a small portion of the poly-peptide chain misfolds. Even though those misfolds were dynamic and did not prevent proper folding altogether, they may initiate further aggregation, as has been observed in bulk experiments due to the exposure of interactive potentially hydrophobic elements [128].

6

CHAPERONE INTERACTIONS WITH THE GR-LBD

In the following chapter the influence of the Hsp70/Hsp90 chaperone system on the GR-LBD function was investigated. Section 6.1 reviews the current knowledge of the chaperone systems interacting with the GR. Section 6.2 presents the drastic impact of the Hsp70 system on the GR-LBD, whereas Section 6.3 shows the influence of only the co-chaperone Hsp40. The direct interaction between Hsp90 and the GR-LBD will be the topic of Section 6.4 followed by the influence of the Complete Chaperone System (CCS) on the native receptor in Section 6.5. Section 6.6 focuses on the recovery of the unfolded GR-LBD to its functional, hormone binding state by the Hsp90 system. A schematic summary of the chaperone interaction pathway as measured in the present work, including the major chaperone-induced GR-LBD conformations will be given in Section 6.7. The results from this chapter will be summarized and discussed. Promising preliminary results, using new measurement techniques will be presented in Section 6.8.

6.1 INTRODUCTION OF THE GR MATURATION PATHWAY

The GR strictly depends on the Hsp90 molecular chaperone for *in-vivo* function [174, 243]. Hsp90 is thought to stabilize and activate the receptor for ligand binding, but why it is required and how it fulfills this function remains unclear.

The dependence of the GR-LBD on Hsp90 is discussed in more detail in Section 1.3.

Early reconstitution experiments [176] established a minimal chaperone system for the GR maturation pathway, including Hsp40, Hsp70, Hsp90, Hsp70/Hsp90 Organizing Protein (HOP) and p23 [52, 62, 115]. It was shown that Hsp40 and Hsp70 prepare the receptor for the interaction with Hsp90 [94, 148, 220] and HOP acts as an adaptor protein that binds Hsp70 and Hsp90 to link this complex to the Hsp90 cycle [38]. Finally, Hsp90 becomes directly associated with the GR-LBD, stabilized by the ATP-dependent association of Hsp90 with the second co-chaperone p23, which binds to the closed state of Hsp90 [53, 68]. This has previously been hypothesized to promote and stabilize a conformational change establishing high affinity hormone binding [39].

This chaperone complex not only assists in maturation of the GR, but also prevents its degradation and mediates other receptor activities, such as nuclear localization and DNA binding [253]. For

TPR domains are found in many proteins and are generally considered protein interaction sites [82].

instance via its Tetratricopeptide Repeat (TPR) binding site Hsp90 is thought to mediate the additional regulation of GR activity by the TPR-domain-containing immunophilins FKBP52 and FKBP51 [12, 190].

This intricate regulatory network highlights the demand of sophisticated investigations to unravel all details of Hsp90 interaction with the GR.

6.1.1 *Function of the Hsp70 chaperone system*

The Hsp70 system is a central component of the cellular protein surveillance network [136]. It is involved in a variety of protein-folding processes, mainly in preventing misfolding or aggregation by binding to unfolded hydrophobic peptide parts.

Hsp70 interactions are highly versatile as the chaperone recognizes a general motif of five hydrophobic amino acids, flanked by positively charged amino acids [193], which occurs on average every 30-40 residues in almost all proteins [136]. Such motifs are mostly found in the hydrophobic core of natively folded proteins and are only exposed before *de novo* folding or upon denaturation.

VERSATILE HIGH AFFINITY BINDING BY HSP70 Despite the versatility of its interaction, Hsp70 achieves high affinities to its relatively unspecific substrates by a sophisticated mechanical mechanism, consuming energy by ATP hydrolysis [136]. Its substrate binding domain (SBD) contains a lid that can literally cover the substrate binding site preventing substrate dissociation. The SBD is mechanically coupled to a nucleotide binding site (NBD) that induces opening of the lid in the ATP-bound state and closing in the Adenosine Diphosphate (ADP) or nucleotide-free state [131]. The intrinsic ATP hydrolysis rates of Hsp70 are low (10^{-4} – 10^{-3}/s) but are stimulated by substrate binding (up to 1 /s) [160]. Thus, in the presence of ATP, substrates likely encounter ATP-Hsp70 with its high association rates ($k_+^{ATP} \approx 0.5\,/\mathrm{s}/\mu\mathrm{M}$) [80, 208], induce ATP hydrolysis and are then tightly bound with low dissociation rates ($k_-^{ADP} \approx 5 \times 10^{-4}\,/\mathrm{s}/\mu\mathrm{M}$) [195, 235].

ROLE OF CO-CHAPERONE HSP40 This mechanism is further supported by the action of Hsp40 that binds to similar motifs as Hsp70. When the Hsp40-associated substrate binds to Hsp70, the J-domain of Hsp40 stimulates the ATPase activity of Hsp70 by a factor of up to >1000-fold [123]. This further elevates the effect described before and consequently drastically increases substrate affinity. In contrast to Hsp70, Hsp40 does not require a specific orientation of the backbone. This allows Hsp40 to scan and associate to hydrophobic protein surfaces and subsequently target Hsp70 to these or neighboring hy-

drophobic patches [194].

One of the Hsp70 system's functions is also to prepare and facilitate client delivery to Hsp90 [94, 113, 220]. For GR, the interaction with Hsp70 – which precedes binding to Hsp90 – appears to play an important role in maturation [210]. In a recent study Hsp70 at physiological concentrations was found to stall productive folding of a client; this effect was reversed by Hsp90 [146]. However, if or why this process is necessary for maturation of a functional client-Hsp90 complex remains an open question.

The meaning of the vague common wording "Hsp70 delivers the client to Hsp90." often remained promiscuous.

6.1.2 *Function of the Hsp90 chaperone system*

The interfaces for Hsp90 interaction are less hydrophobic and more charged than Hsp70 binding sites [77, 107, 113, 146, 251]. This is consistent with the Hsp90 acting downstream of Hsp70 on the folding path. While Hsp70 binds to very hydrophobic, aggregation-prone short peptide stretches, Hsp90 preferentially binds to late folding intermediates where most of these sites are already buried in the hydrophobic core of the client [107, 185]

The mechanism of Hsp90 function, recently reviewed by Schopf *et al.* [210], is more complex and thus less exhaustively understood, leaving still some disagreements in the field, underlining the need for additional detailed investigations.

Information not cited in this part can be found in this review [210].

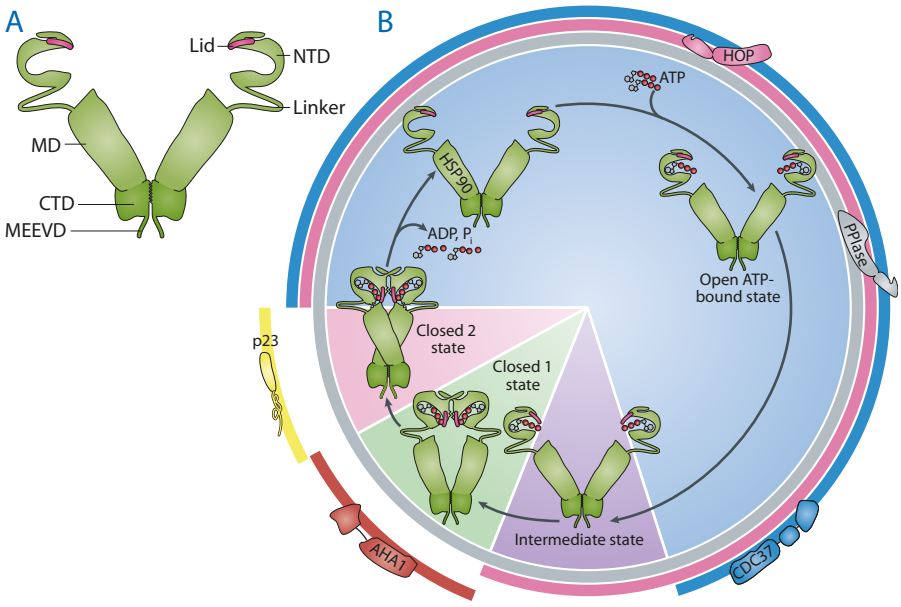

Figure 6.1: (A) Schematic representation of the domain organization of the Hsp90 dimer. (B) The HSP90 conformational cycle and the action of co-chaperones in different parts of the cycle. Adapted from [210].

HSP90 CONFORMATIONAL CYCLE Hsp90 functions as a homodimer (as shown in Figure 6.1A). The monomer consists of an amino-terminal domain (NTD) that mediates binding to and hydrolysis of ATP; the middle domain (MD), also necessary for ATP hydrolysis and client binding; and the carboxy-terminal domain (CTD), responsible for dimerization. In absence of nucleotide, Hsp90 is thought to exist in a V-shaped open conformation.

Hsp90 is a highly flexible molecule adopting distinct conformations during its functional cycle (Figure 6.1B). ATP binding leads to closing of the 'lid' located in the NTD (intermediate state), followed by an interaction of the NTDs (closed 1 state) and twisting of the monomers (closed 2 state). ATP hydrolysis finally leads back to the open conformation. The ATP turnover is slow, in human Hsp90 about one ATP per 10 minutes [95]. The dynamics of these conformations are regulated by a variety of co-chaperones [210].

HSP70-HSP90 CLIENT TRANSFER BY CO-CHAPERONE HOP HOP is suggested to act as an adaptor to facilitate client transfer from Hsp70 to Hsp90 by binding simultaneously to both of them [251]. HOP contains three Tetratricopeptide Repeat (TPR) domains. The central one was found to bind to Hsp90 and the N-terminal one to Hsp70 [38]. Additionally HOP stabilizes Hsp90 in the open conformation, thus inhibiting ATPase activity.

A study by Southworth and Agard [223] claimed that HOP induced an alternative Hsp90 open state poised for client loading by Hsp70 and subsequent ATP hydrolysis. In a study by Kirschke *et al.* [113] ATP hydrolysis by Hsp90 was shown to be required for the transfer from the Hsp70 to the Hsp90 system and to trigger the dissociation of the HOP-Hsp70 complex, likely through a coupling of the two chaperones' ATP cycles [106, 113]. The model by Schopf *et al.* [210] suggests that dissociation of the HOP-Hsp70 complex happens upon binding of ATP and the co-chaperones PPIase and p23, yielding the closed conformation, and that ATP hydrolysis leads to release of active GR-LBD [128].

GR-LBD ASSOCIATED WITH HSP90 DIMER Both GR-LBD and Hsp90 binding sites of this interaction were recently reviewed in [185]. After binding of the client, e.g. the GR-LBD, to Hsp90, the Hsp70 binding motifs are described to be buried in the core of a semi-folded state.

Structural analysis of Hsp90 in complex with GR-LBD by Lorenz *et al.* [128] suggested that the chaperone adopts a closed conformation upon client binding. Concomitantly, a decreased ATPase activity and deceleration of the Hsp90 conformational cycle was measured, which prolongs the dwell-time of the GR in Hsp90 complexes. In their experiments, Hsp90 without other co-chaperones could associate with two

GR-LBD molecules, binding to the opposite faces of Hsp90. Binding of p23 displaced one GR-LBD from the Hsp90 dimer.

Note that in these studies, the binding of DEX-bound GR-LBD to Hsp90 was probed. There was no evidence that this association pathway forms the same complex conformation as an unliganded GR-LBD, prepared by the Hsp70 system.

ROLE OF CO-CHAPERONE P23 p23 is a co-chaperone thought to act at a late stage of the Hsp90 cycle. It binds primarily to ATP-bound Hsp90 [39]. By binding in a groove between the dimerized NTDs, it stabilizes the closed 2 conformation (Figure 6.1B). It inhibits Hsp90's ATPase activity, thus slowing down the chaperone cycle, which supports the maturation of GRs by stabilizing the complex [68].

RELEASE OF GR The GR is thought to remain in a semi-folded, but hormone-binding-competent state, protected by Hsp90 until it binds hormone and may be released [176, 185].

Release from Hsp90 was first linked to hormone binding by GR-LBD [179]. However, *in-vitro* experiments showed an interaction of Hsp90 with a hormone-bound GR-LBD [128], supporting the idea of Hsp90 playing an additional role in nuclear import of GR-LBD [59, 67, 70, 128]. Thus Schopf *et al.* [210] suggest that GR-LBD remains bound to the Hsp90 complex upon hormone binding and release is only triggered by ATP hydrolysis. A model by Kirschke *et al.* [113] suggests binding of DEX triggers the release of GR-LBD.

Many ideas about the role of chaperones in GR maturation and structural binding motifs have been revealed. However, much remains to be learned about transitional assembly states, kinetic properties and the concrete influence on the GR-LBD conformation in particular that form the basis for why and how the support by chaperones works.

6.1.3 *A reconstruction of the chaperone cycle using GR-LBD F-DEX binding*

In a recent publication by Kirschke *et al.* [113], the minimal chaperone system cycle (Figure 6.2) was reconstructed from the view of GR-LBD by monitoring the F-DEX binding capabilities of GR-LBD in the presence of the different chaperone systems.

They found that Hsp70 only in combination with Hsp40 and ATP completely inhibited F-DEX binding to GR-LBD. From results by HDX-MS they concluded this happened due to partial unfolding of the GR-LBD. In presence of Hsp90 including its co-chaperones HOP and p23, the hormone binding capabilities could be fully recovered. The release of the GR-LBD-Hsp90 complex from Hsp70 was triggered

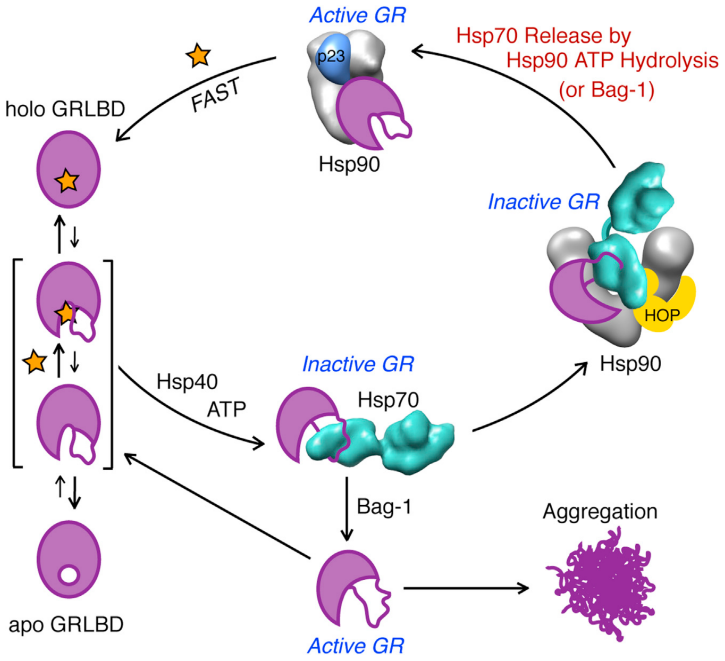

Figure 6.2: GR-LBD chaperone cycle adapted from [113].

by ATP hydrolysis. The release of GR-LBD could also be induced by the Hsp70 nucleotide exchange factor Bag-1 which resulted in aggregation of the GR-LBD. This aggregation could be prevented even by a hydrolysis-incompetent Hsp90 mutant.

The experiments presented in the following part of this work aimed to reconstruct these interactions by monitoring the conformational dynamics of a single GR-LBD molecule subjected to the chaperone systems. With the knowledge accumulated in Chapter 4 and Chapter 5 a more detailed understanding of the impact on GR-LBD function induced by the chaperones was sought at the single-molecule level.

This detailed understanding is key to answer questions about the exact roles of the chaperones like:

- How does Hsp70 inhibit DEX binding to the GR-LBD?
- How does it prepare the GR-LBD for interaction with Hsp90?
- Does this preparation actually induce the formation of a particular Hsp90 complex?
- Are there certain GR-LBD conditions affecting the Hsp70 interaction?
- How does Hsp90 protect the GR-LBD from aggregation?
- Are there different conformations of the GR-LBD-Hsp90 complex implying alternative functions?

6.2 INTERACTION OF THE HSP70 SYSTEM WITH THE GR-LBD

All measurements with Hsp70 included ATP if not stated otherwise.

6.2.1 *Hsp70-induced unfolding of the GR-LBD*

The application of force allowed the observation of the native *open-closed* fluctuations of the GR-LBD *lid* (as described in Section 4.2) and to monitor the dissociation and rebinding of DEX on a measurable timescale (as described in Chapter 4). Consequently the influence of the Hsp70 system on that conformational cycle could be investigated. To study the interaction of the Hsp70 system with the GR-LBD, passive-mode experiments were conducted. A force-bias of around 9 pN was applied on the DEX-bound GR-LBD with the chaperones Hsp40 and Hsp70 in solution.

The combination of Hsp70, including ATP and its co-chaperone Hsp40 will further also be referred to as the Hsp70 system.

Figure 6.3A displays a force vs. time trace in the presence of 180 µM DEX, 600 nM Hsp40, 2 µM Hsp70 and ATP. At the beginning the GR-LBD exhibited the fluctuations between the *lid open* (blue) and *closed* (purple) state as observed in absence chaperones. At some point the fluctuations stopped at the protein contour length of the *open-ub* state (marked in cyan) similarly to the behavior observed for a hormone dissociation event (compare Section 4.3). However, in this case, instead of a subsequent rebinding, the GR-LBD step-wise unfolded (gray part) until it ended up in the completely unfolded *unf* state (red). This complete unfolding (gray part), induced by the Hsp70 system will be henceforth referred to as *H7unfolding*.

The *H7unfolding* showed a variety of different patterns so it was not possible to classify intermediate states thus far. The time τ_{H7unf} from the end of the native *lid* fluctuations until the GR-LBD remained in the *unf* state (gray part) was approximately

$$\tau_{H7unf} = 7\,/\mathrm{s}$$

as averaged from 12 unfolding events.

After the *H7unfolding*, the GR-LBD remained in the unfolded conformation without exhibiting any refolding attempts as observed in the absence of chaperones at these forces (compare to Figure 5.1). Even the subsequent relaxation to zero force did not lead to any structure formation of the unfolded protein (Figure 6.3B). The subsequent stretch-and-relax cycles exhibited smooth force vs. extension traces following a WLC with the protein contour length of the completely unfolded peptide chain (compare to Figure 4.2). This shape of the force vs. extension trace will further be referred to as *Hsp70-folding-blocked* (short *H7blocked*) traces.

These results imply that the Hsp70 system including Hsp40 and ATP completely unfolded the GR-LBD and inhibited any re-formation of tertiary structure.

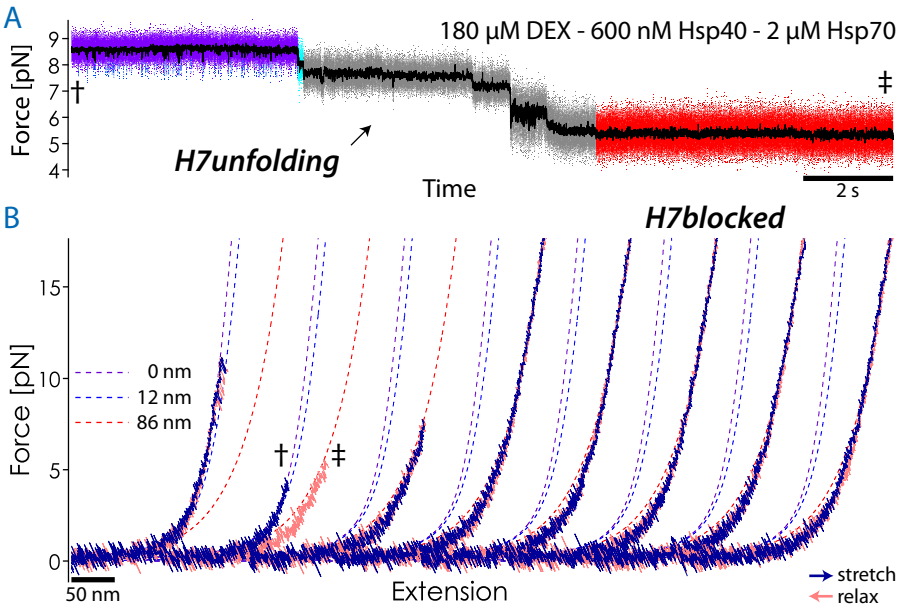

Figure 6.3: (A) Force vs. time trace of passive-mode experiment demonstrating an *H7unfolding* event (color coding as in Figure 5.1, gray: data not assigned). ‡ marks the switch to the stretch vs. relax cycles. (B) Consecutive stretch-and-relax cycles of the same molecule exhibiting *H7blocked* traces after the passive-mode trace (A) (presentation analogous to Figure 4.2). † marks the switch to passive-mode, ‡ marks the switch back to the stretch vs. relax cycles.

Also, lower concentrations of Hsp70 were tested qualitatively. The results are given in Section C.6.

HSP70 INTERACTS AFTER HORMONE DISSOCIATION Does Hsp70 interact with the DEX-bound GR-LBD and possibly trigger hormone dissociation? The *lid* opening and closing rates before the unfolding event in the presence of the Hsp70 chaperone system are plotted in Figure 6.4A. They do not show any difference to the rates measured in Section 4.2 (shown in light gray) indicating that neither Hsp40, nor Hsp70 interfered with this transition.

To determine whether Hsp70 increased the hormone dissociation rate by interaction with a DEX-bound state, the total dwell-times in the *open* state before the *H7unfolding* – $\tau^{open}_{till H7unf}$ – were analyzed (compare Section 4.4). Figure 6.4B shows an integrated histogram of the total dwell-times $\tau^{open}_{till H7unf}$ spent in the *open* state until the *H7unfolding* event. The dwell-times follow a single-exponential distribution. This suggests that the underlying process leading to the unfolding was the same each time. The inverse of the average $\tau^{open}_{till H7unf}$ yields a rate of $k = 1.7(+1-0.6)/\mathrm{s}$ which is in good agreement with the spontaneous DEX dissociation rate from the *open* state $k^{open}_{diss} = 3/\mathrm{s}$ (compare Figure 4.8B). that implies that none of the chaperone interactions increased the hormone dissociation rate.

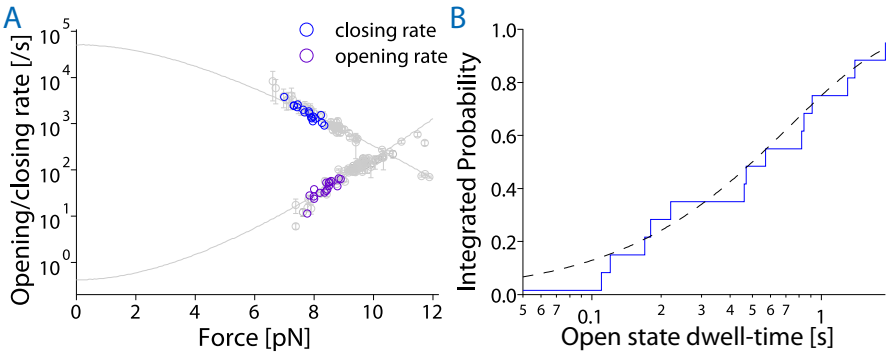

Figure 6.4: (A) Comparison of *lid* fluctuation rates with and without Hsp70 in solution. Colored data was taken from 4 molecules with 2 µM Hsp40 and 8 µM Hsp70 in solution. As a comparison the data without chaperones is displayed in light gray (compare Figure 4.4). (B) Integrated histogram of dwell-times in the *open* state before *H7unfolding*, $\tau^{open}_{till H7unf}$. The dashed line is a single-exponential fit.

Based on these results it can be concluded that the Hsp40/Hsp70 chaperone system does not interact with the DEX-bound GR-LBD; the unfolding process happened only after the self-contained spontaneous dissociation of the hormone.

HSP70 INTERACTION REQUIRES HSP40 To test whether Hsp70 requires its co-chaperone Hsp40 and ATP for the interaction with the

GR-LBD, the passive-mode experiments were repeated, leaving out each of these components.

Figure 6.5 displays a passive-mode trace without the co-chaperone Hsp40, and with only Hsp70 and ATP in solution. The traces exhibited the native DEX rebinding behavior as observed in Section 4.3 (compare Figure 4.5). Despite the three-fold higher (compared to **??**) Hsp70 concentration of 6 µM and a lower DEX concentration of 20 µM to increase the time of the hormone-unbound (cyan) phases, the effect of unfolding by Hsp70 could not be observed as demonstrated by the multiple rebindings shown in Figure 6.5. The DEX dissociation and rebinding rates agree with the ones measured in Section 4.3.

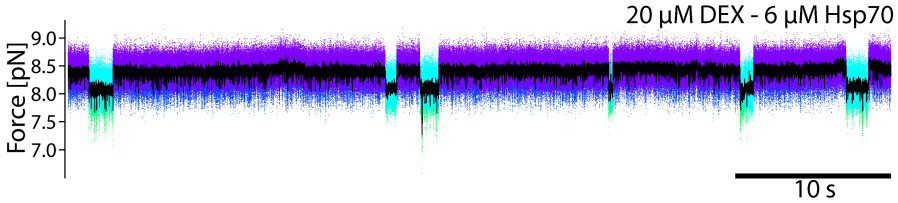

Figure 6.5: Force vs. time trace of a passive-mode experiment with 20 µM DEX and 6 µM Hsp70 and ATP in solution. Data presentation analogous to Figure 4.5.

HSP70 INTERACTION REQUIRES ATP Measurements with 600 nM Hsp40 and 2 µM Hsp70 but no ATP in solution did not differ from the traces in the presence of only Hsp40, as presented in Section 6.3 (data not shown).

This implies that the interaction of Hsp70 with the GR-LBD, as demonstrated in Figure 6.3 requires the presence of the co-chaperone Hsp40 and ATP.

The fact that all three components were necessary to observe the effect highlights the specificity of the interaction.

6.2.2 *Hsp70 induces unfolding also at zero-force*

Does the Hsp70 system completely unfold the unbound GR-LBD also in the absence of force? Due to the closing of the *lid*, the dissociation of DEX is slowed down to the timescale of 30 min in the absence of force (Section 4.10). To probe the interaction of the Hsp70 system with the DEX-unbound GR-LBD at zero-force, the protein was pre-incubated with the Hsp70 system at a low DEX concentration before the experiment (as described in Section 2.7). Figure 6.6 shows the first force vs. extension trace after the tether formation in the optical trap. The kink in the trace at 0 nm extension indicates the contact of the beads, implying this pulling trace shows the first application of force to the molecule.

In contrast to the native unfolding pattern of the GR-LBD (compare Figure 4.1), the force vs. extension trace exhibited a smooth curve along the protein contour length of the completely unfolded GR-LBD (red dashed line in Figure 6.6), similar to the *H7blocked* traces. The purple dashed line corresponds to a WLC fit of a completely folded GR-LBD and consequently the stretching of a 365 nm DNA-tether.

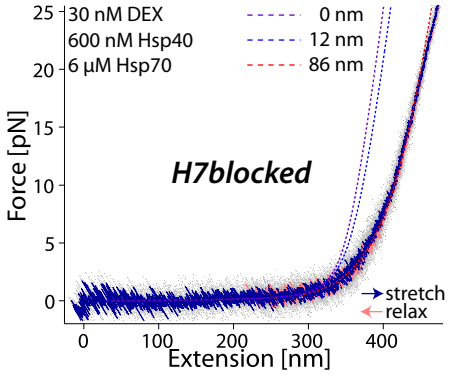

Figure 6.6: First stretch-and-relax cycle after tether formation and preceding incubation at 3 nM DEX, 6 µM Hsp70 and 600 nM Hsp40 exhibiting *H7blocked* traces. Presentation analogous to Figure 4.1. The WLC fit with $Lprot = 0$ (purple dashed line) corresponds to stretching of a DNA tether with contour length of 365 nm.

Different concentrations of Hsp70 and DEX were tested. Table 6.1 shows a summary of different conditions. The outcome is given as how many out of the total amount of protein tethers exhibited the *H7blocked* shape during the first application of force. Only tethers that exhibited at some point either a proper GR-LBD unfolding pattern or a *H7blocked* trace were considered. In the case of 2 µM Hsp70 and 20 nM DEX the patterns were problematic to distinguish from unspecific tethers as they mostly exhibited some residual structure but became *H7blocked*-like in subsequent pulls.

The major uncertainty of this method is that there was no evidence that the *H7blocked* traces were folding-competent GR-LBD molecules. To this end a microfluidics setup could be utilized as proposed in Section 7.2.

However, in contrast to these data, without Hsp70 at low DEX concentration no traces matching the one showed in Figure 6.6 could be observed. Hence these results were significant. They demonstrate that Hsp70 unfolds the apo-GR-LBD even in the absence of force.

6.2.3 *GR-LBD recovery into the native conformation*

Is the GR-LBD capable of refolding back and binding DEX after the *H7unfolding*? In the next set of experiments, the reversibility of the Hsp70 interaction was investigated.

c(HSP70)	[µM]	6	6	8	2	2	-	-
c(DEX)	[µM]	0.03	0.3	20	0.02	2	0.01	0.03
OUTCOME		5/6	4/8	0/6	$5^{?}$/7	1/7	0/5	0/9

Table 6.1: Number of tethers showing a *H7blocked* trace as displayed in Figure 6.6 in relation to all protein tethers in dependence of Hsp70 and DEX concentration. Hsp40 concentration was always 600 nM. $^{?}$ - *not completely smooth, ambiguous outcome.*

To this end, after an *H7unfolding* (as shown in Figure 6.3A), the force was reduced and the GR-LBD was kept at zero-force. To get a read-out for the protein state, stretch-and-relax cycle were performed intermittently, to monitor to what extent the protein had refolded (as described in Section 2.7).

An example of force vs. extension traces from such consecutive pulls after an *H7unfolding* is shown in Figure 6.7. The first traces typically showed a smooth WLC pattern with the protein contour length of the completely unfolded protein (*H7blocked*) as already shown in Figure 6.3B. In this example the first 15 cycles (that is ≈ 100 s) showed no transitions to lower contour length i.e. no gain in structure. At some point the traces typically started to show fast equilibrium fluctuations with a contraction of $30 - 40$ nm from the unfolded conformation (2nd to 5th trace in Figure 6.7). In some cases (roughly 10%) the traces reverted to the completely unfolded *H7blocked* shape. Eventually the proteins could recover into the folded and DEX-bound native conformation indicated by the distinctive *open-closed* fluctuations (as seen in the last trace in Figure 6.7).

Before this recovery, the stretch-and-relax traces showed heterogeneous patterns. that indicated various possible pathways for the recovery from the *H7blocked* back to the native state.

The times it took from the *H7unfolding* until the GR-LBD had refolded into the native and DEX-bound state in the presence of Hsp70 $\tau_{recover}^{Hsp70}$ were analyzed and plotted in Figure 6.8 as an integrated histogram. The average time for recovery was

$$\tau_{recover}^{Hsp70} = 340 \pm 110\,\text{s}$$

(error estimated by $\frac{1}{\sqrt{N}}$).

The times for recovery were measured at two DEX concentrations differing by two orders of magnitude. The single-exponential distribution of the measured $\tau_{recover}^{Hsp70}$ indicate that binding of DEX was not limiting at these concentrations. It also supports the assumption that the protein system was always in the same state after the *H7unfolding*.

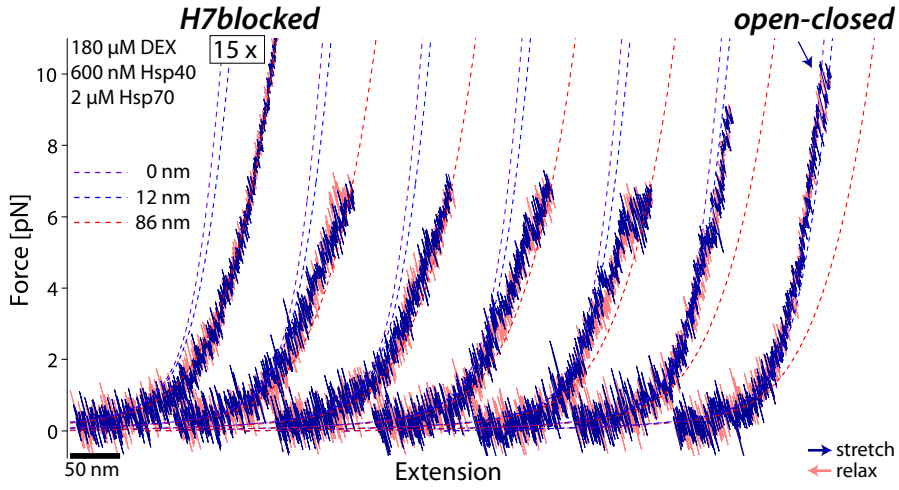

Figure 6.7: Example of consecutive stretch and relax cycles of GR-LBD after an *H7unfolding* event. Presentation analogous to Figure 6.3B. Before each cycle there was a waiting time of 6 s at 0 pN to allow the protein to refold before applying the stretching. The first 15 stretches exhibited the same *H7blocked* appearance and thus are represented as one cycle here. The last cycle represents native *open-closed* fluctuations.

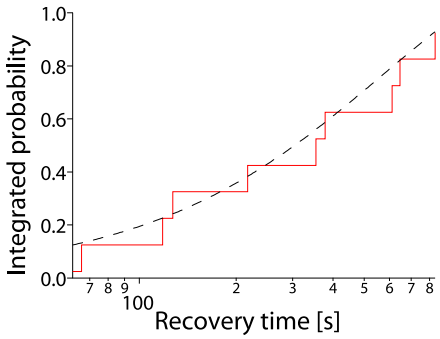

Figure 6.8: Integrated histogram of times $\tau_{recover}^{Hsp70}$ until the GR-LBD was found in the native, hormone-bound state again after *H7unfolding*. Data was combined from 4 molecules at 200 µM and 3 molecules at 2 µM DEX. Dashed line is a single-exponential fit.

6.3 GR-LBD INTERACTION WITH THE SOLE HSP40

As demonstrated in Section 6.2.1, the interaction of Hsp70 with the GR-LBD required the presence of Hsp40 in solution. Is there an interaction of Hsp40 alone with the GR-LBD? To answer this question, passive-mode experiments were conducted as before, monitoring the DEX-rebinding behavior in the presence of 600 nM Hsp40.

Figure 6.9 displays an example trace of a DEX-rebinding event from such an experiment. During some of the DEX-unbound phases, a new state (orange) occurred with a protein contour length between the *open-ub* and *IM1* state (compare Table 5.1). This state was not observed within the traces in the absence of chaperones. This Hsp40-induced state will be henceforth referred to as the *H4* state.

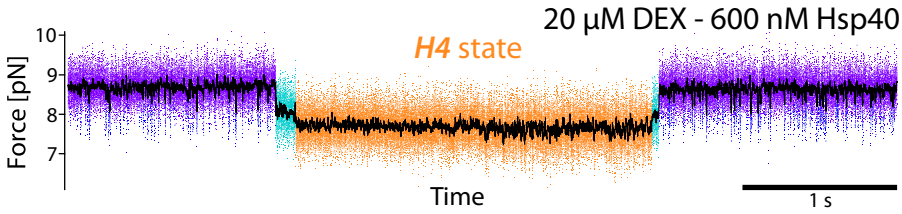

Figure 6.9: The *H4* state: Force vs. time trace of a DEX rebinding event in the presence of 600 nM Hsp40. Data presentation analogous to Figure 4.5. The new state induced by Hsp40 (*H4* state) is colored in orange.

The protein contour length of the *H4* state was measured to be

$$L_{prot} = 21 \pm 2\,\text{nm}.$$

A possible structural interpretation of this state is given in Section 6.7.1

The 7 ± 2 nm gain in protein contour length additional to the *open-ub* state corresponds to an unfolding of roughly further 24 ± 6 amino acid residues.

Such as in the case together with Hsp70, Hsp40 alone did not show any influence on neither the kinetics of the *open-closed* fluctuation, nor the DEX dissociation rates (data not shown).

The *H4* state was observed at different DEX concentrations of 20, 60 and 200 µM and Hsp40 concentrations of 200 nM, 600 nM and 2 µM, but was only analyzed qualitatively thus far. At 200 nM it appeared to be less prominent and at 2 µM in most cases (roughly 90%) the GR-LBD seemed to be trapped in that state until it was unfolded by stretch-and-relax cycles up to 15 pN. After this unfolding the GR-LBD was able to refold into the native conformation.

Is the occurrence of the *H4* state force-dependent? Is the *H4* state capable of hormone binding? What are the on- and off-rates of Hsp40 binding to the GR-LBD? To answer these questions and determine the kinetics and energy of this interaction, more experiments would be required, systematically varying force, DEX and Hsp40 concentration.

6.4 GR-LBD INTERACTION WITH THE SOLE HSP90

As discussed in Section 1.3 it is still an ongoing debate whether Hsp90 serves only for GR maturation or stays associated with the hormone-bound receptor [128].

Is there direct interaction between Hsp90 and the hormone-bound GR-LBD? To gain insight into the direct interaction between the GR-LBD and Heat shock protein 90 (Hsp90), the *open-closed* state fluctuations were monitored in the presence of 600 nM Hsp90 (including ATP). Figure 6.10 displays a force vs. time trace of these fluctuations. Additionally to the interruptions by DEX rebinding events (cyan), a new state could be observed (labeled in brown). It exhibits an intermediate length between the *open* and *closed* state and stalls the fluctuations. This Hsp90-induced state will henceforth be referred to as the *H9* state.

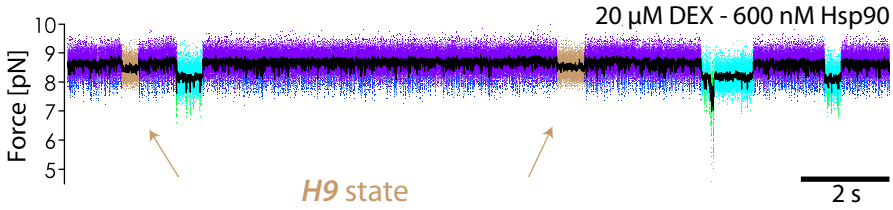

Figure 6.10: Demonstration of the *H9* state. Force vs. time trace of *lid* fluctuation in the presence of 600 nM Hsp90 and ATP. Data presentation analogous to Figure 4.5. Additionally to the DEX rebinding events (cyan), a new state appeared (*H9* state, brown) with a protein contour length between the *open* (blue) and *closed* state.

The *H9* state exhibited an average protein contour length of

$$L_{prot}^{H9} = 4.7 \pm 0.3\,\text{nm}.$$

6 traces from 3 different molecules were analyzed. The on-rates of the *H9* state followed a single-exponential behavior, but it should be noted that only traces clearly showing an occurrence of the *H9* state were analyzed. Some traces under the same conditions appeared to show only 1 or none of these events on a timescale of 60 s. Thus it cannot be excluded that there is some underlying bimodal behavior. The analyzed traces yielded average on- and off-rates for the *H9* state of

$$k_{on}^{H9} = 0.24 \pm 0.04\,/\text{s}, k_{off}^{H9} = 5 \pm 1\,/\text{s}.$$

The zero-force free energy difference from the *closed* to the *H9* state was calculated as described in Section 3.4.1 and yields

$$\Delta G_{closed \to H9}^{0} = 6.5 \pm 0.2\,k_B T.$$

Assuming that this would be the only interaction between the GR-LBD and Hsp90, in the absence of force Hsp90 would be bound with a probability of $P_{Hsp90bound} = e^{-6.5} = 1.5 \times 10^{-3}$ at 600 nM. This results in an affinity of 400 µM. Comparing this with the affinities of

0.8 µM for Hsp90 in the presence of ATP measured with analytical ultracentrifugation [128] leads to the conclusion that the *H9* state does not resemble the only interaction between Hsp90 and the GR-LBD.

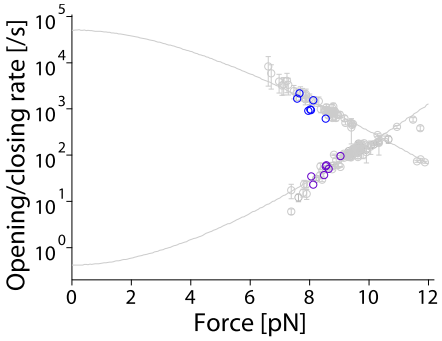

Figure 6.11: Comparison of *lid* fluctuation rates with and without Hsp90. Colored data was taken from 2 molecules with 2 µM Hsp90 in solution. Underlied in gray is the data without chaperones (compare 4.4).

NO FURTHER INFLUENCE ON BINDING AND *lid* FLUCTUATIONS

To test whether Hsp90 additionally influences the transitions between the *open* and *closed* state, the kinetics of the *lid* fluctuations in the presence of 2 µM Hsp90 were analyzed (Figure 6.11). The rates did not show a significant difference to the ones in the absence of chaperones (displayed in gray).

The rates of DEX binding and dissociation did not show a significant difference at 600 nM (3 molecules measured) and 2 µM (1 molecule measured) Hsp90.

6.5 THE ACTION OF THE COMPLETE CHAPERONE SYSTEM (CCS)

Hsp90 and its co-chaperones, p23 and HOP will also be referred to as the Hsp90 system.

In this section the combined interaction of the Hsp70 and Hsp90 chaperone system – namely Hsp40, Hsp70, Hsp90, p23, HOP, and ATP – on GR-LBD was investigated. These chaperones will be further referred to as the Complete Chaperone System (CCS).

The same concentration of Hsp40 and Hsp70 as in Section 6.2.1 were used, adding 2 µM of the other three chaperones. The GR-LBD was kept under a force of $\approx 9pN$ to monitor the native *open-closed* fluctuations. Figure 6.12A displays an example trace of such an experiment. The GR-LBD exhibited a similar behavior as in the case of only Hsp40 and Hsp70. After a phase, observing the native DEX-bound *lid* kinetics (purple/blue) the GR-LBD transitions to the completely unfolded state (*H7unfolding*, gray part).

During the *lid* fluctuations before the *H7unfolding* the Hsp90-induced *H9* state could be also observed (data not shown) as described in Section 6.4.

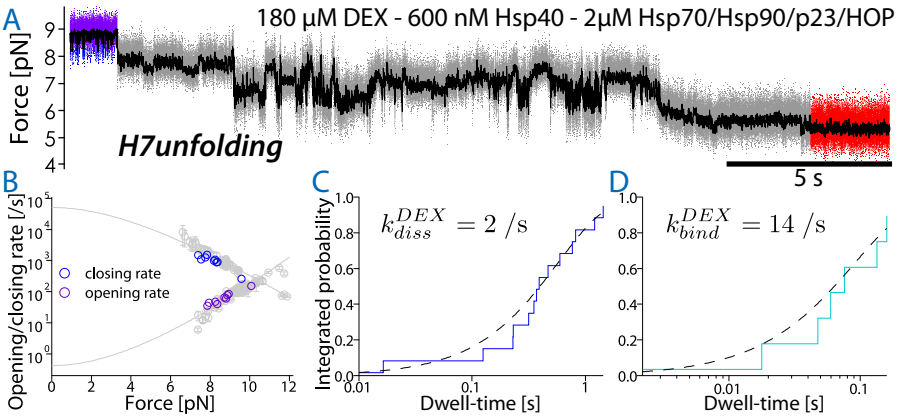

Figure 6.12: (A) Force vs. time trace of an *H7unfolding* in the presence of the CCS (Color coding as in Figure 6.3). (B) Comparison of *lid* fluctuation rates with and without the CCS in solution. Colored data was taken from 3 molecules with 600 nM Hsp40 and 2 µM Hsp70,Hsp90, p23 and HOP in solution. Data without chaperones is displayed in gray (compare 4.4). (C) Integrated histogram of dwell-times in the *open* state before the *H7unfolding* or DEX rebinding event. (D) Integrated histogram of dwell-times in the *open-ub* state at DEX-rebinding events before the *H7unfolding*. Dashed lines are single-exponential fits. 8 traces from 5 different molecules were analyzed.

ADDITIONAL CHAPERONES INFLUENCED THE *h7unfolding* The *H7unfolding* transitions qualitatively differed from the case of the Hsp70 system alone (compare Figure 6.12A and Figure 6.3A). A variety of heterogeneous unfolding pathways could be observed. In general, the unfolding included more back and forth transitions in the presence of the CCS. In the end GR-LBD mostly still ended up in the completely unfolded state, exhibiting the *H7blocked* shape in subsequent stretch-and-relax cycles (as shown in Figure 6.3A).

The time for the *H7unfolding* process (gray part in Figure 6.12A) in the presence of the CCS – τ_{H7unf}^{CCS} – until the GR-LBD remained in the unfolded state was approximately

$$\tau_{H7unf}^{CCS} \approx 25\,\text{s}$$

as averaged from 7 unfolding traces. This time was about 3.5-fold longer than τ_{H7unf} in the absence of the Hsp90 system (Section 6.2.1). Consequently the Hsp90 system already interferes with the Hsp70 interaction. In roughly half of the cases in the presence of the CCS the GR-LBD did not completely remain in the fully unfolded state, still exhibiting some conformational fluctuations.

lid FLUCTUATIONS AND DEX REBINDING NOT ALTERED To test whether the conformational dynamics of the native protein was altered in the presence of the 5 chaperones, the *open-closed* fluctuations and the kinetics of DEX rebinding – that occurred before the

H7unfolding – were analyzed (as displayed in Figure 6.12B-D). The kinetics of the *lid* fluctuations exhibited no difference to the chaperone-free case. Also, the rate for DEX dissociation from the *open* state agreed with the rate in the absence of chaperones (as presented in Section 4.4).

As Hsp70 only interacts with the DEX-unbound receptor, DEX rebinding competes with the *H7unfolding*. In the analyzed 8 traces, a total of 7 DEX rebinding events could be observed before the *H7unfolding*. This indicates that under the given conditions (2 µM Hsp70) the rate for Hsp70 attack on the *open-ub* state ($k_{Hsp70}^{open\text{-}ub}$) is about the same as the rate for DEX rebinding ($k_{Hsp70}^{open\text{-}ub} \approx 7\,/\mathrm{s}$ at 200 µM DEX). This agrees well with the fact that for the rebinding events that successfully competed with the Hsp70 attack, a rate of 14 /s was measured (Figure 6.12D) which is the sum of the competing processes.

These findings confirm that both *lid* fluctuations and DEX dissociation and rebinding before the *H7unfolding* remain unaffected by the presence of the CCS.

6.6 RECOVERY IN THE PRESENCE OF THE COMPLETE CHAPERONE SYSTEM

In the following, the influence of the Hsp90 system on the recovery of the GR-LBD after an *H7unfolding* was investigated similarly to Section 6.2. In comparison to the case with the Hsp70 system only (compare Figure 6.3B), the force vs. extension traces after the *H7unfolding* remain *H7blocked*-like for a shorter period of time, already showing fluctuations to more compact states after a couple of cycles.

A drastic effect was the change in recovery pathway, induced by the Hsp90 system. The force vs. extension traces reproducibly exhibited two new distinct stable states with almost native protein contour length. Those "pre-recovery" states occur directly before the final transition to the native, hormone-bound state and are described in the following sections 6.6.1 and 6.6.2.

The average time for the recovery from the fully unfolded, outstretched *H7blocked* state into one of the pre-recovery states in the presence of the CCS was

$$\tau_{recover}^{CCS} = 110 \pm 30\,\mathrm{s}$$

(error estimated by $\frac{1}{\sqrt{N}}$). This is about 3-fold shorter than the $\tau_{recover}^{Hsp70}$ in the absence of the Hsp90 system (compare Section 6.2.3). The majority of the traces were measured at 2 µM Hsp90, p23 and HOP, but all of the mentioned effects could be reproduced also using 600 nM of the Hsp90 system.

Consequently, the Hsp90 system promotes the recovery of the GR-LBD after the *H7unfolding* back to its native state. The following sec-

tions present the qualitative differences of this recovery, induced by the Hsp90 system.

6.6.1 *Recovery via a new stable state (state A)*

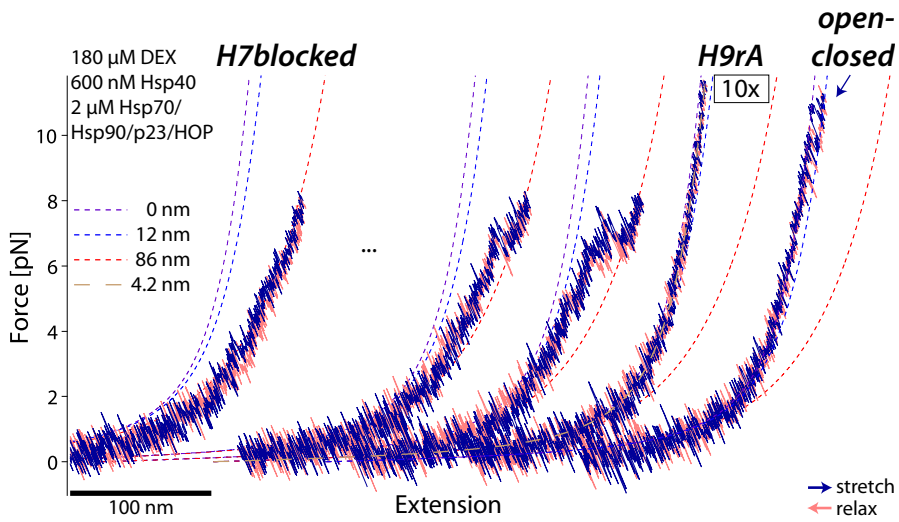

Figure 6.13: The "pre-recovery" state *H9rA*: Example of consecutive stretch-and-relax cycles of GR-LBD after an *H7unfolding* before it recovered to the native state in the presence of the CCS. Presentation analogous to Figure 6.3B. Before each cycle there was a waiting time of 2 s at 0 pN. At the position of the three black dots, 20 cycles were removed that showed traces similar to the ones in the 2nd and 3rd cycle. The second to last cycle represents 10 cycles exhibiting indistinguishable traces (*H9rA* state).

The Hsp90 system induced a new stable state of the GR-LBD, after an *H7unfolding* that directly transitions into the native hormone-bound state. Due to its direct transition into the native state it will be also referred to as a "pre-recovery" state.

Figure 6.13 displays an example of consecutive stretch-and-relax cycles after an *H7unfolding*, in the presence of the Hsp90 system. Before finally ending up in the native conformation (last cycle in Figure 6.13) the GR-LBD reached a state with a protein contour length between the *open* and *closed* state that did not unfold any longer below 12 pN (demonstrated in the second to last cycle in Figure 6.13). This state will henceforth be referred to as the *Hsp90 recovery state A* (short *H9rA* state). After 10 cycles without any further unfolding, the *H9rA* state directly transitioned into the native conformation, exhibiting the distinct *lid* fluctuations (last cycle in Figure 6.13). Such a direct transition, without a preceding unfolding, indicates that most of the structure had already mostly native conformation.

The unfolding forces of the H9rA *state were even higher, as probed in Section 6.8.1).*

The *H9rA* state exhibited an average protein contour length of

$$L_{prot}^{H9rA} = 4.2 \pm 1.0\,\text{nm}.$$

This contour length agrees well with the one of the Hsp90-induced *H9* state, described in Section 6.4.

The average time spent in the *H9rA* state before the final transition to the native state was

$$\tau_{H9rA} = 40 \pm 15\,\text{s}.$$

This recovery pathway was observed in 6 out of 12 cases after an *H7unfolding*, in the presence of the Hsp90 system.

6.6.2 *Recovery via fluctuating states (state B and C)*

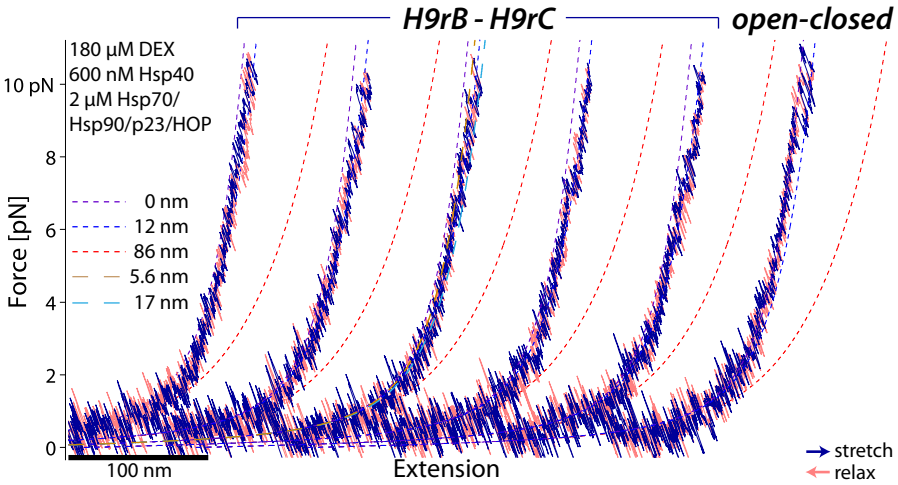

Figure 6.14: The "pre-recovery" states *H9rB* and *H9rC*: Example of stretch-and-relax cycles that show the GR-LBD after it had been unfolded by Hsp70 and before it recovered back to the native state in the presence of the CCS. Presentation analogous to Figure 6.3B. Here only the last two cycles displayed are consecutive cycles.

Figure 6.14 shows examples of stretch-and-relax cycles exhibiting another pre-recovery state that occurred in the other 6 out of 12 cases in the presence of the Hsp90 system after an *H7unfolding*.

After the *H7unfolding* the GR-LBD initially exhibited similar recovery attempts as before (first three cycles in Figure 6.13). Then it took on a conformation with a similar contour length as the *H9rA* state but exhibiting fluctuations to another conformation with slightly longer contour length (first 5 cycles in Figure 6.14). These fluctuations appeared similar to the native *lid* fluctuations (last cycle) but shifted to increased contour length and lower forces. These two conformations will henceforth be referred to as *Hsp90 recovery* state *B* and *C* (short *H9rB* and *H9rC* state).

Again after a certain time the GR-LBD directly transitioned into the native conformation, exhibiting the *open-closed lid* fluctuations (the last two displayed cycles were consecutive cycles). For 2 molecules,

An example trace of this switching and a detailed analysis of the kinetic properties of the fluctuations will be described in Section 6.8.1.

the switching from the *H9rB-H9rC* fluctuations to the native *open-closed* fluctuations was observed directly in passive-mode traces (described as preliminary data in Section 6.8.1).

The average contour length of the *H9rB* and *H9rC* states were

$$L_{prot}^{H9rB} = 5.6 \pm 0.6\,\text{nm}, L_{prot}^{H9rC} = 17.3 \pm 0.7\,\text{nm},$$

and consequently the contour length difference between them was

$$\Delta L_{prot}^{H9rB-H9rC} = 11.7 \pm 0.6\,\text{nm}.$$

The L_{prot} of the *H9rB* roughly agrees with the one of the *H9rA* pre-recovery state described before in Section 6.6.1. Hence it could resemble a structurally similar conformation.

The average time exhibiting the *H9rA-H9rB* state fluctuations before the final transition to the native state was

$$\tau_{H9rB/C} = 100 \pm 40\,\text{s}.$$

6.7 DISCUSSION OF GR-LBD-CHAPERONE INTERACTIONS

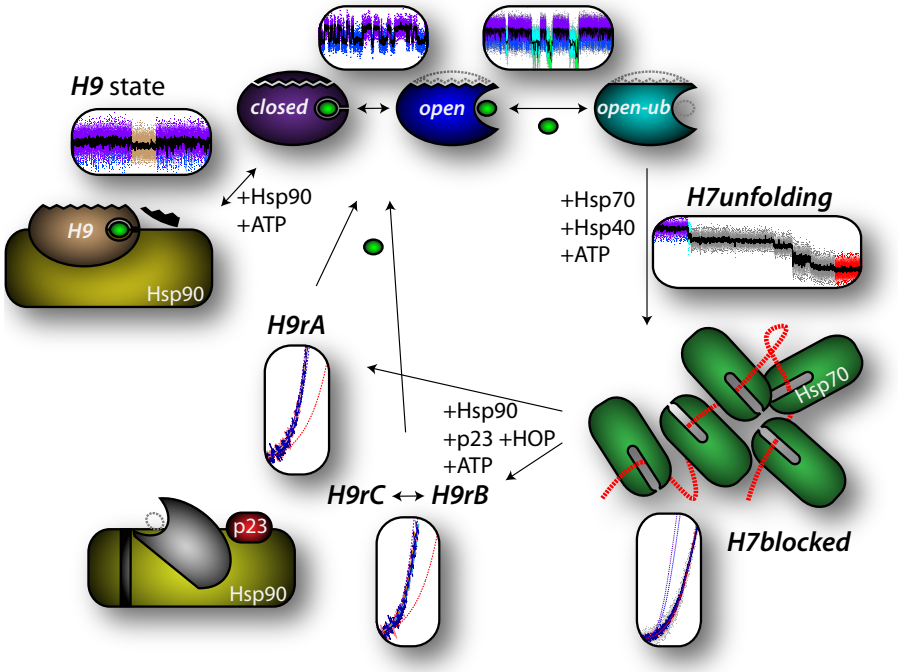

Figure 6.15: Schematic summary of the GR-LBD-chaperone interaction pathway as measured using single-molecule force-spectroscopy. The data included within the black frames illustrate the single-molecule mechanical readout for the interactions. The details are discussed in this section.

Some single-molecule research on chaperone function investigated the conformational dynamics of the chaperones ([102, 131]). In the

present work the perspective was reversed and additional insights were gained by monitoring conformational dynamics of a substrate, observing chaperone function in action.

The detailed mechanical characterization of the GR-LBD's conformational dynamics upon hormone binding and release in Chapter 4 were successfully used to perform an in-depth analysis of the interaction of the chaperone machinery with the GR-LBD. Unprecedented details of chaperone action from the perspective of a substrate's mechanics were revealed. The chaperone interactions could be mechanically triggered, their dependence on certain substrate conditions were probed and the alteration of the GR-LBD's conformation observed.

Figure 6.15 illustrates a schematic summary of the chaperone interaction pathway as measured in the present work, including the major chaperone-induced GR-LBD conformations.

6.7.1 *GR-LBD interaction with the Hsp70 system*

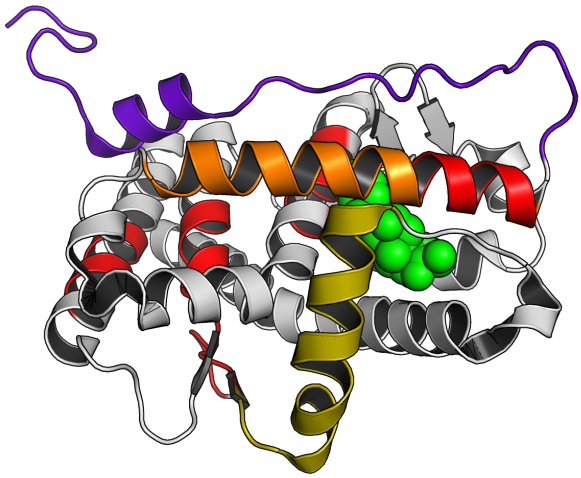

Figure 6.16: GR-LBD structure (pdb 1M2Z [24]). The *lid* is highlighted in purple, possible opening by Hsp40 in orange (N-terminal) and yellow (C-terminal) and Hsp70 binding sites predicted by LIMBO [242] in red.

Foldases are a particular kind of molecular chaperones that assist the folding of proteins in an ATP-dependent manner.

HSP70 UNFOLDS THE APO-GR-LBD AND BLOCKS REFOLDING The function of Hsp70 is widely seen as foldase [66, 111, 125, 172, 211]. The results presented in the present work demonstrate that the Hsp70 system does not act as a foldase at the molecular level.

In Section 6.2 it was presented that the Hsp70 system completely unfolds the GR-LBD (*H7unfolding*) after spontaneous dissociation of DEX and fully inhibits any refolding attempts (*H7blocked* state), as illustrated in the right part of Figure 6.15. The specificity of this interaction was proven by the fact that all components, Hsp40, Hsp70 and ATP were essential for the effect.

These results confirmed the effects of F-DEX binding inhibition observed by Kirschke *et al.* [113] including the dependence on ATP and Hsp40. Additionally they yield a more elaborate picture of the mechanistic details of interaction. The data taken in this work suggest that the inactivation by Hsp70 is due to annihilation of the tertiary structure of the GR-LBD.

Such an Hsp70-inflicted folding block was indirectly measured recently for luciferase and the GR-LBD using chemical or thermal denaturation and luciferase or F-DEX binding activity to report for refolding [146]. Here additionally the driven unfolding of the apo-GR-LBD was revealed and the conformation of the *H7blocked* state directly observed as an unfolded polypeptide chain.

The heterogeneity of *H7unfolding* patterns and recovery pathways as well as the thorough inhibition of any structure formation by the GR-LBD in the presence of Hsp70 indicated that there was more than one Hsp70 molecule interacting with the GR-LBD. The interaction of Hsp70 with the unfolded GR-LBD peptide could be pictured as proposed by Kellner *et al.* [110] for the DnaK interaction with rhodanese (see Figure 6.17). The sequence of the GR-LBD offers at least 5 DnaK binding sites (red in Figure 6.16) predicted by LIMBO [242]. Those binding sites are also equally distributed along the GR-LBD sequence, which might allow full coverage of the unfolded peptide.

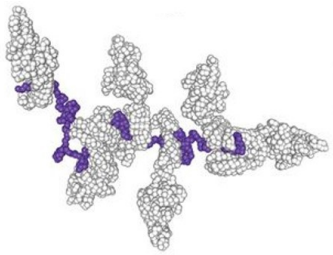

Figure 6.17: Representative structures from molecular dynamics (MD) simulations of rhodanese (purple) bound by 7 DnaK molecules (white) to all possible DnaK binding sites in the rhodanese sequence predicted by LIMBO [242]. Taken from [110].

Kirschke *et al.* [113] proposed that Hsp70 would induce only local unfolding, concluding from limited proteolysis and Hydrogen Deuterium Exchange coupled with Mass Spectrometry (HDX-MS) that exhibited only three limited GR-LBD regions showing increased solvent accessibility (with the most extensive increase on helix 3, residues 564-573). The picture presented here could explain that result in a different way: Hsp70 molecules completely cover the unfolded peptide, protecting them from proteolysis and HDX.

INTERACTION OF HSP40 ALONE Hsp40 alone resulted in stabilization of an additional 24 amino acid residues unfolded structure. A structural interpretation could possibly be the unfolding of helix 3

(orange in Figure 6.16) succeeding the N-terminal *lid* (purple) or opening of the C-terminal helix 12 (yellow). To precisely answer this question, further measurements are required as described in Section 7.2.3. In both cases the interaction of Hsp40 would free one of the 5 possible Hsp70 binding sites (red). The binding sites at the C-terminus and in helix 3 above the hormone binding pocket right behind the N-terminal *lid* could be good candidates as interaction site for the first Hsp70 attack.

Binding sites were predicted for the bacterial Hsp70 homolog DnaK by the LIMBO algorithm [242].

This direct interaction indicates how Hsp40 prepares the GR-LBD for Hsp70 binding. This finding is in agreement with the general mechanism of J-domain co-chaperones, transiently interacting with Hsp70 substrates to prime them for Hsp70 interaction as described in Section 6.1.1 [134, 194].

HSP70 DOES NOT INTERACT WITH DEX-BOUND RECEPTOR Analysis of the *open* state dwell-time before *H7unfolding* (Section 6.2.1) indicated that the presence of the Hsp70 system did not increase DEX dissociation. Based on the results presented in the present work, Hsp70 interacts exclusively with the hormone-unbound receptor. The 2-folds increase in F-DEX dissociation seen by Kirschke *et al.* [113] could not be confirmed for the unlabeled DEX used in this study.

Hsp40 association is needed to prime the client for Hsp70 interaction [134, 194].

The interaction of the Hsp70 system exclusively with the hormone-unbound receptor is in line with the fact that Hsp40 shows interaction only starting from the unbound *open-ub* state.

As the Hsp70 system does not interact with the DEX-bound receptor, it is not surprising that having a certain concentration of DEX in solution, despite the presence of the Hsp70 system, the GR-LBD ends up in the bound state after a certain equilibration time at zero-force (as observed in Section 6.2.3).

HSP70 EQUILIBRIUM IN THE ABSENCE OF FORCE AND HORMONE The application of force increases the DEX dissociation rate by opening the binding *lid* and also energetically favors the unfolded state, consequently shifting the equilibrium to the *H7blocked* state. But does the unbound GR-LBD end up in the *H7blocked* state also in equilibrium at zero-force? This is a question of free energy differences. The 41 k_BT folding free energy of the *open-ub* state need to be compared with the total free energy of Hsp70 molecules binding. Due to the sophisticated mechanism of Hsp70 binding to its substrates [160], involving ATP hydrolysis [240] and co-chaperone interaction [123], so-called ultra-affinities [47] of around $K_d^{substrate} = 0.2\,\text{nM}$ [258] can be reached. Thus, at an Hsp70 concentration of 6 µM, the binding free energy can be estimated as $\Delta G_{binding} = k_BT \cdot \ln(\frac{6\,\mu\text{M}}{0.2\,\text{nM}}) \approx 10\,k_BT$ per Hsp70 molecule. Thus, a binding of 4-5 Hsp70 molecules to the binding sites predicted in the unfolded GR-LBD sequence would be the energetically favored conformation at the given concentration.

Due to the rough energy landscape (elaborated in Section 5.3) the 41 k_BT folding free energy stored in the *open-ub* state does not need to be overcome at once. As it splits into parts of roughly 10 k_BT per folding intermediate, a stepwise attachment of several Hsp70 molecules becomes more likely.

The experiments presented in Section 6.2.2 at a minimum DEX concentration and preincubation with Hsp70 indicated the GR-LBD molecules already being unfolded before the first application of force. This observation confirmed the theoretical considerations. These findings do not connote that the *H7blocked* GR-LBD at zero-force is in the same outstretched conformation as under force, which is unlikely due to its entropy. However, as most of the energy of the tertiary structure is lost, residual parts might remain compact at zero-force but unravel already at very low forces.

A quantitative analysis of *H7unfoling* at zero-force was problematic for two reasons.

1. The time of incubation with Hsp70 could not be controlled as the start of an experiment depends on the formation of a tether.

2. Evidence of whether a stretched tether comprises a functional protein depends on measuring the fingerprint of the GR-LBD, which was not possible in this assay.

To examine the exact time of *H7unfolding* of the unbound GR-LBD at zero-force and calculate interaction free energies, a microfluidics setup integrated in the optical trap (as demonstrated in Section 6.8.2) could be used as proposed in Section 7.2.

The results presented in Section 6.2.2 indicate a half-maximal inhibitory concentration (IC_{50}) in the order of magnitude around 2 µM Hsp70, which is in agreement to the findings by Kirschke *et al.* [113]. A concentration of 2 µM DEX already shifts the zero-force equilibrium to the folded hormone-bound state.

THE PHYSIOLOGICAL REASON OF THE HSP70 INTERACTION What is the reasoning behind the mechanism of Hsp70-induced unfolding of the GR-LBD? Hsp70 is widely known to refold misfolded and aggregated proteins [134, 146]. In particular the unbound GR-LBD, has previously been shown to be prone to aggregation in ensemble studies [128]. Also in this work, the decrease in refolding rate due to misfolding was observed (Section 5.5). Additional to these fast forming misfolds, the protein showed an unprecedented occurrence of highly stable and partially irreversible heterogeneous misfolds that could not be systematically characterized (Section A.4), some of which might possibly be prevented by Hsp70.

Such irreversible misfolding, possibly due to oxygen damage or aggregation is sometimes called dying of the protein.

In this single-molecule assay the decrease of refolding rate at zero-force to $\approx 1/\mathrm{s}$ did not prevent proper refolding overall. However,

in-vivo it might lead to an increased tendency to aggregate. Hsp70 might act similarly as the observed chaperoning by force to prevent these fast forming misfolded structures.

The data presented in this work demonstrate that the role of Hsp70 is not only to refold misfolded conformations, but unfolds even the correctly folded unbound GR-LBD, possibly to avoid aggregation.

A possible source for aggregation was discovered to be the N-terminal *lid*, which in the hormone-unbound case is only weakly structured and consequently needs protection by chaperones. Thus, Hsp70 needs to cover the GR-LBD after hormone dissociation until it finally associates with the Hsp90 complex or rebinds hormone.

In case, the GR-LBD cannot be recovered, Hsp70 has the role to target the GR-LBD for proteasomal degradation [104, 226, 261].

Hsp70 might also have an additional regulatory role by stalling the GR-LBD in an inactive conformation. Without Hsp90 it has been shown to decrease the percentage of properly folded protein at physiological concentrations [146].

A further hypothesis is that the GR-LBD needs to be actively prepared by Hsp70 for the formation of a distinct functional complex with Hsp90 [94, 223].

6.7.2 *GR-LBD interaction with the Hsp90 system*

In Section 6.4 Hsp90 was observed to directly interact with the DEX-bound conformation of native GR-LBD as illustrated in the upper left part of Figure 6.15. This interaction resulted in short interruptions of the *lid* fluctuations by the *H9* state, in which half of the *lid* appeared unfolded.

These interactions of Hsp90 with the *lid* would be too weak to explain the affinity to the GR-LBD measured by Lorenz *et al.* [128]. Hence, Hsp90 likely interacts also with other structural parts of the GR-LBD The extended nature of GR-LBD binding sites in Hsp90 suggests that Hsp90 forms various low-energy contatcs with the GR-LBD [185].

From electron microscopy (EM), Small-angle X-ray scattering (SAXS) and Nuclear magnetic resonance spectroscopy (NMR) data, Lorenz *et al.* [128] inferred a structural model for a GR-LBD-Hsp90-p23 complex, depicted in Figure 6.18. In this structural model, Hsp90 does not have direct contacts with the GR-LBD N-terminal *lid*. This could explain why the *lid* fluctuations are mostly unaffected [185]. The main stabilization would only be detected further down on the unfolding pathway.

The interruptions to the *open-closed lid* fluctuations, the newly identified *H9* state, might reflect a conformation that resembles the native *open* state with half of the N-terminal *lid* attached to Hsp90, stabilized by roughly $5\,k_BT$. This view would be consistent with mutagenesis

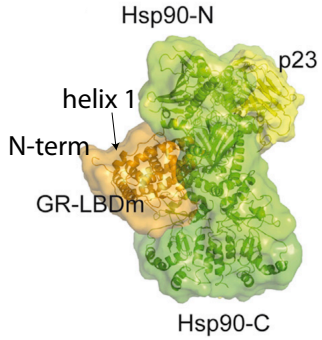

Figure 6.18: Structural model for GR-LBD (orange) in complex with Hsp90 (green) and p23 (lime). It was generated by docking the GR-LBD onto the crystal structure of Hsp90 (PDB 2CG9) using EM, SAXS, and NMR data for the binding interfaces. Adapted from [128].

studies that have identified amino acids at the end of the N-terminal *lid* to be required for proper GR-LBD/Hsp90 complex assembly [79, 108, 260].

The contour length of the *H9* state agrees with the one of the *H9rA* state found along the recovery pathway in the presence of the complete chaperone system (Section 6.6.1). However, in the latter case the dwell-times in that state were much longer. It possibly still resembles a similar Hsp90 binding mode just stabilized by p23. To address this question, passive-mode experiments should be performed, using different combinations and concentrations of Hsp90, p23 and HOP.

Thus far, the results presented in this work rather indicate that without preparation by the Hsp70 system binding of GR-LBD to Hsp90 leads to a different complex conformation. It has been proposed, as the binding surface for Hsp90 extends over the entire LBD, it requires partially or locally unfolded regions of the GR-LBD [23]. Mutagenesis studies have demonstrated residues, buried in the folded structure, to be required for Hsp90 binding [44].

6.7.3 *Maturation of the GR-LBD – the idle state*

In presence of the Complete Chaperone System, consisting of Hsp70, Hsp40, HOP,Hsp90 and p23, new stable configurations of the GR-LBD were detected (as depicted in the lower left part of Figure 6.15).

After the unfolding induced by Hsp70, and exclusively in presence of the Hsp90 system, the GR-LBD adopted either the *H9rA* conformation or a fluctuation between the *H9rB* and *H9rC* states. In these conformations likely most of the native contacts were already formed, as they could directly exchange into the native bound conformation without exhibiting detectable unfolding. They appeared to be significantly more stable than the hormone-unbound *open-ub* state.

Preliminary data presented in Section 6.8.1 show unfolding forces of recovery states higher even than the ones of DEX-bound GR-LBD.

Additionally, the Hsp90 chaperone system accelerated the process for recovery after the *H7unfolding* by a factor of 3. The time to reach one of the stable pre-recovery states after the *H7unfolding* was roughly 100 s.

In a recent study by Morán Luengo *et al.* [146], the authors also showed Hsp90 to resolve an Hsp70-imposed folding deadlock, suggesting this to be the key role of Hsp90 in protein folding. The results described in the present work additionally reveal explicit stable client conformations that are adopted exclusively in presence of Hsp90, suggesting a more sophisticated role of Hsp90. In the same study Morán Luengo *et al.* [146], using luciferase as a client protein, elaborated that the chaperones act within the first seconds of the folding pathway, preventing misfolding, but that the rate-limiting step of the reaction is the chaperone-free folding of the client. The data described in the present work yielded a minutes timescale for the recovery into the native state from the *H7blocked* state opposed to an intrinsic folding rate of the GR-LBD on the seconds timescale despite misfolding. This also indicates a possibly different role of Hsp90 in maturation of the GR-LBD as in the case of the slowly folding luciferase. Kirschke *et al.* [113] have observed a lag phase for hormone-binding recovery by the Hsp90 system after inhibition by Hsp70 of about 10 min. This time is in the same order of magnitude and might reflect the time required for the client transfer.

RELEVANCE OF THE HSP90-INDUCED PRE-RECOVERY STATES

There are different possible interpretations for these Hsp90-induced pre-recovery states. They might be Hsp90-associated hormone-unbound or already hormone-bound but still need Hsp90 to dissociate before becoming native. Lorenz *et al.* [128] also proposed a state in which the Hsp70 complex is still associated additionally to Hsp90. The states could also reflect different conformations or nucleotide and co-chaperone binding status of Hsp90 [124, 210, 223].

What are these states and what is their relevance for the physiological pathway of GR maturation? Preliminary data (presented in Section 6.8.1) indicated that at least one of these conformations could be adopted also in the absence of hormone. Hence, this state could be a candidate for resembling the default idle – activation-upon-binding – conformation of the unbound receptor as it resides in the cytosol, associated and protected by Hsp90 and p23, waiting to bind hormone and being transported into the nucleus [113, 176, 185]. The co-chaperones are needed to maintain this idle conformation [198].

It is still an open question, why the unbound GR needs to be associated with Hsp90 for *in-vivo* function. Hence, providing evidence for a hormone-unbound GR-LBD state stabilized by Hsp90 which possibly protects especially the weakly attached N-terminal *lid* from aggregation or to inhibit Hsp70-induced unfolding and keeps the receptor in

a hormone-binding-competent state could shed light on this question. This protection of the unbound receptor might resemble the mechanism that often times was referred with the misleading term "opening of the binding pocket" by Hsp90 [181]. Such a stabilization could also be achieved by promoting a conformational change in the residual GR-LBD conformation as proposed by Fang *et al.* [61].

OPENING OF THE BINDING POCKET BY HSP90 Kirschke *et al.* [113] measured a 2-fold increase in DEX binding rate to GR-LBD in the presence of all chaperones, from which they concluded an open binding pocket of GR-LBD associated to Hsp90. Considering the insights from the present work, the open binding pocket could actually be the N-terminal *lid* interacting with Hsp90. The experiments in Section 4.9 showed slightly decreased binding rates of DEX and F-DEX by a factor of 2 and 4 respectively due to some interaction of the weakly structured *lid* with the residual structure (Section 4.8) at zero-force. This is in agreement with the hypothesis of an increased binding rate upon Hsp90 interaction. This effect might increase with the rest of the full length GR continuing at the N-terminus of the LBD.

EVIDENCE FOR THE HSP90-INDUCED IDLE CONFORMATION To provide evidence that such a Hsp90-induced stable state could be adopted in the absence of hormones, but resembles a hormone-binding-competent conformation, the GR-LBD molecule should be probed in a setup that allows for switching solution conditions during the measurement. Preliminary data presented in Section 6.8.3, using a microfluidics setup built into the optical trap already yielded first evidence for the binding capability of such a state.

The long ongoing discussion, whether Hsp90 dissociates from the GR-LBD upon hormone binding might be solved by a model that suggests two different complex conformations: The idle conformation in which the unbound GR-LBD is associated with Hsp90 in a partially unfolded state. This conformation might need preparation by the Hsp70 system. The hormone-bound complex on the other side might involve the GR-LBD in a native like conformation.

6.8 PRELIMINARY RESULTS – INVESTIGATION OF THE IDLE STATE

6.8.1 *Characterization of CCS pre-recovery states*

KINETIC PROPERTIES OF THE *h9rb-h9rc* FLUCTUATIONS In Section 6.6.2 fluctuations between the *H9rB* and *H9rC* states after the *H7unfolding* of the GR-LBD were observed right before the recovery back to the native state. They were induced by the presence of the Hsp90 system. To characterize these fluctuations in more detail, passive-mode measurements were used. To this end, after the char-

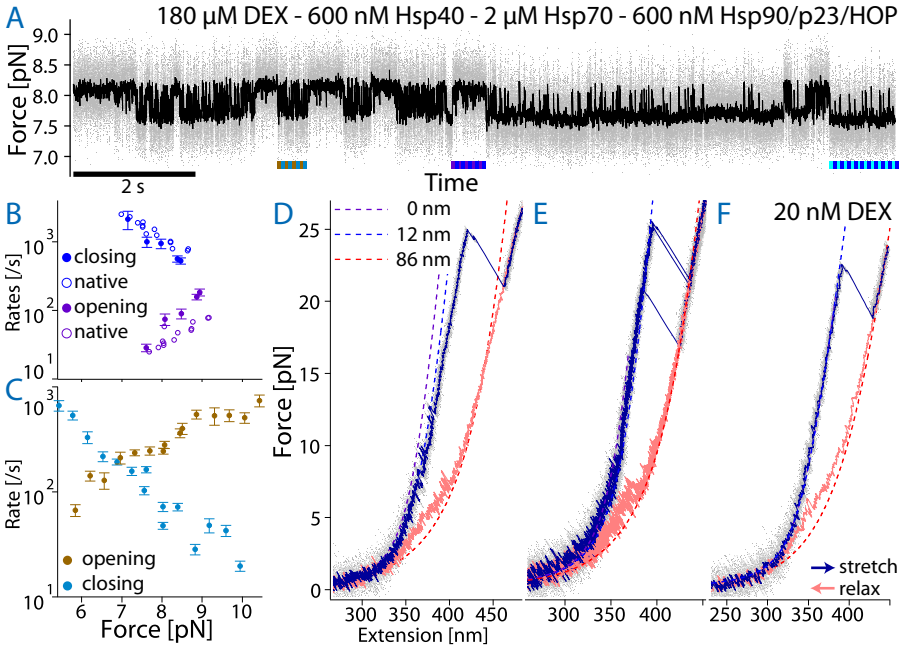

Figure 6.19: Probing the CCS recovery states. (A) Passive-mode trace of the *H9rB-H9rC* fluctuations as discussed in Section 6.6.2 after it had recovered from the *H7unfolding*. The colored bars mark kinetically different fluctuation phases. (B) Opening and closing rates (filled dots) of fluctuations marked by the purple/blue bar in (A) compared to rates of the native *open-closed* fluctuations (empty circles) measured for the same molecule before the *H7unfolding*. (C) Opening (brown) and closing (light blue) rates of fluctuations marked by the brown/light blue bar in (A). (D) Stretch-and-relax trace presented as in Figure 4.1, unfolding the GR-LBD from the *H9rC* state. (E) Overlay of 3 unfolding traces of GR-LBD after recovery into the *H9rA* state. (F) Similar unfolding as in (E) but at low DEX concentration.

acteristic pattern of the *H9rB-H9rC* fluctuations was observed in the stretch-and-relax cycles (as presented in Figure 6.14), the protein was kept at constant forces varying around 7 pN, analyzing fluctuation kinetics as described in Section 4.2.

At the beginning, one kinetic behavior was predominant, but at some point a switching between at least 3 different kinetic behaviors could be observed as highlighted by the colored bars in the trace of Figure 6.19A. One of these (purple/blue bar) interestingly agrees quite well with the kinetics of the native *open-closed lid* fluctuations (comparison of the two is displayed in Figure 6.19B). Note that the protein contour length of these fluctuations is slightly increased (5.6 – 17.3 nm, as described in Section 6.6.2) compared to the native *lid* fluctuations (0 – 12 nm).

The predominant kinetic behaviors throughout the *H9rB-H9rC* fluctuations were the ones marked by the brown/light blue bar. The force-dependent opening and closing rates of these are given in Figure 6.19C. The rates were measured for 2 independent molecules so far. Once determined, they serve as a hallmark for this certain Hsp90-induced pre-recovery pathway. The switching of these kinetic behaviors might indicate different conformations of the associated chaperone complex.

HIGH UNFOLDING FORCES OF PRE-RECOVERY STATES To test the stability of the Hsp90-induced pre-recovery states described in Section 6.6, the GR-LBD was stretched to higher forces at the point when the appeared to have reached one of these states after an *H7unfolding*. An inherent problem of this method is that after unfolding it cannot be proven that the state was actually a pre-recovery state, capable to exchange into the native state.

Figure 6.14D shows an unfolding of the GR-LBD at 25 pN after exhibiting the characteristic *H9rB-H9rC* fluctuations, pulled with a relative trap velocity of 500 nm/s. Figure 6.14E shows an overlay of 3 unfoldings of the putative *H9rA* state (as described in Section 6.6.1), each between 20 – 25 pN. These forces are much higher than the average unfolding force of even the hormone-bound GR-LBD (16 pN, compare Section 4.1).

TESTING RECOVERY IN THE ABSENCE OF HORMONES Could one of the stable pre-recovery states be the hormone-free GR-LBD-Hsp90 complex, as it is thought to be the idle configuration found in the cytosol [113]? To test this hypothesis, the recovery after the *H7unfolding* in the presence of the CCS (as in Section 6.6) was investigated at very low concentration of 20 nM DEX. Even in the absence of hormones, a state was observed that could resemble the *H9rA*. Figure 6.14F shows an unfolding of such a state at around 23 pN, which is drastically higher than the average unfolding force of the unbound GR-LBD of

10 pN (compare Section A.2). Such an event was measured for 2 independent molecules so far. This state could be a candidate for a hormone-free state of the GR-LBD stabilized and protected by Hsp90.

Still, in this measurement there was no evidence that this state was actually competent of hormone binding. To prove this hypothesis and reproduce the complete chaperone cycle, a microfluidics setup could be used.

6.8.2 *Switching Hsp70 conditions using microfluidics*

The following measurements were performed to test the microfluidics setup described in Section 2.8 and compare different chaperone conditions back to back. The interaction of the Hsp70 system in the absence of any hormones in solution could be observed, with subsequent recovery of the GR-LBD under chaperone-free conditions, into its native, DEX rebinding state. This *H7unfolding*-recovery cycle could be observed up to 4 times with the same molecule. Evidence for full GR-LBD functionality can be seen in the traces observing *lid* fluctuations, repeated DEX rebinding events and refolding with native kinetics.

Figure 6.20 shows part of such an experiment. In the first measurement channel (DEX channel), there was a concentration of 20 µM DEX without any chaperones. In passive-mode experiments around 10 pN, the native behavior of the GR-LBD could be observed, exhibiting the native *lid* fluctuations, DEX rebinding and partial unfolding during hormone-unbound phases as shown in the first (highlighted in blue) part of Figure 6.20A (compare to Figure 4.5).

In the second measurement channel (chaperone channel), there was no DEX in solution, 6 µM of Hsp70 and 600 nM of Hsp40. During the transfer to the other measurement channel (highlighted in red), the force was reduced to avoid any unfolding happening during the transfer. Subsequently the force was increased again and the native *lid* fluctuations could be observed again until the *H7unfolding* (compare to Figure 6.3A). The GR-LBD remained in the *H7blocked* state.

Figure 6.20B shows subsequent stretch-and-relax cycles before and after the transfer back to the DEX channel with a waiting time at 0 pN before each stretch of 6 s. Still in the chaperone channel the force vs. extension traces exhibited the *H7blocked* shape (as in Figure 6.3B). This shape of the traces remained until the transfer back to the first measurement channel after about 70 s (highlighted in blue). During the waiting time at 0 pN between two cycles the molecule was transferred back into the DEX channel. After 4 stretch-and-relax cycles, the GR-LBD had recovered back into the native DEX-bound state.

Figure 6.20C shows a subsequent passive-mode trace again exhibiting the native, DEX rebinding GR-LBD and another transfer to the chaperone channel (red) followed by a *H7unfolding*.

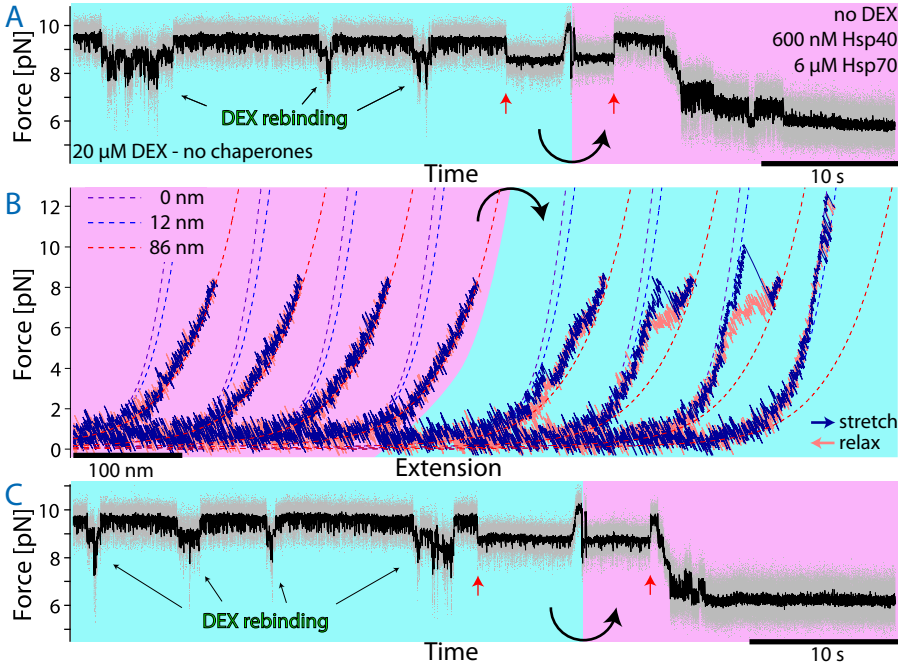

Figure 6.20: Hsp70 interaction with GR-LBD probed using a microfluidics system. (A) Passive-mode trace before and after the transfer from the DEX to the chaperone channel. Background color indicate the current measurement channel. Red arrows mark the point where force was decreased during the transfer. (B) Consecutive stretch (blue) and relax (pink) cycles following (A) at the time of transfer from the chaperone (red) back to the DEX channel (blue). In the chaperone channel the traces exhibited the *H7blocked* appearance. Presentation as in Figure 6.3B. Waiting time between cycles: 6 s. (C) Similar trace as in (A) subsequent to (B).

6.8.3 *Evidence for binding capability of hormone-free CCS recovery state*

In Section 6.6 an exclusive pathway for GR-LBD recovery after *H7unfolding* was found, induced by the Hsp90 system. It resulted in pre-recovery states with almost native protein contour length, appearing immediately before the transition to the native, DEX-bound state. Preliminary data, presented in Section 6.8.1, showed high unfolding forces of these states possibly even before binding hormone. These results indicated a highly stable, Hsp90-associated, hormone-free state of the GR-LBD after an *H7unfolding*.

To provide evidence that this stable state could be adopted in the absence of hormones, but resembles a functional conformation, capable of binding DEX, an approach using a microfluidics system was started. To this end, a DEX-bound GR-LBD was brought into a measurement channel without DEX in solution, and 6 µM of Hsp70, 600 nM of Hsp40 and 2 µM of Hsp90, p23 and HOP in solution. After the *H7unfolding* as described in Section 6.5, the molecule was kept at 0 pN with stretch-and-relax cycles after each 6 s to check the folding status of the GR-LBD.

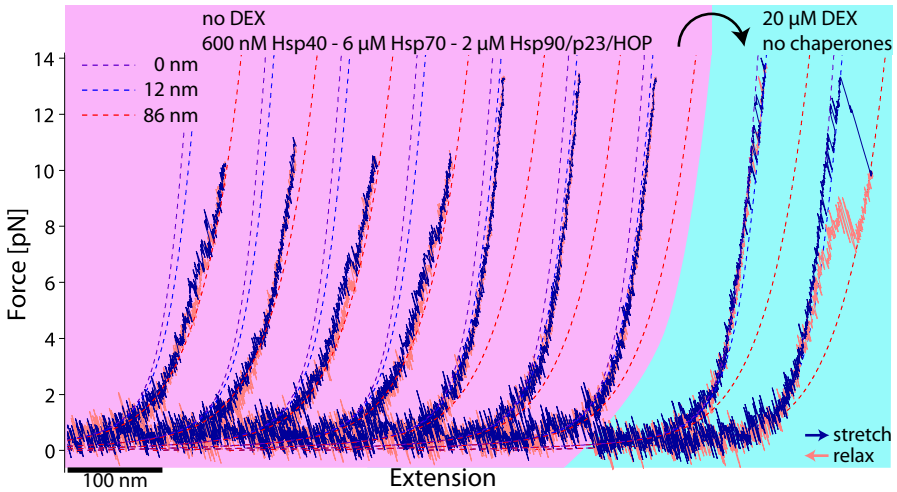

Figure 6.21: Recovery into a hormone-free but stable state by the CCS including evidence of this state binding hormone. Presentation as in Figure 6.20B. Displayed traces show consecutive stretch vs. relax cycles with a waiting time of 6 s between each cycle.

The GR-LBD showed mostly unfolded force vs. extension traces as displayed in the first 4 cycles in Figure 6.21. Around 60 s after the *H7unfolding* the stretch-and-relax cycles exhibited smooth traces without unfolding up to 13.3 pN and a protein contour length of 21 ± 1 nm (5th–7th cycle). These traces appeared to resemble a stable hormone-free Hsp90-induced pre-recovery state (compare Section 6.8.1).

At this point the protein was transferred to another measurement channel containing 20 µM DEX and no chaperones, while being kept at 0 pN (highlighted in blue). After an additional waiting time of 10 s

at 0 pN, the protein was stretched again and directly exhibited the native, DEX-bound *lid* fluctuation pattern.

The fact that there was no unfolding between the stably folded pre-recovery state and the native GR-LBD pattern suggests that this state was already capable of hormone binding without major structural rearrangements. Tt is therefore a good candidate to be the Hsp90-associated, hormone-unbound GR-LBD idle state that is readily capable of hormone binding and stabilized by Hsp90.

7 CONCLUSION AND OUTLOOK

This chapter summarizes the contributions of this work to understand the GR function and chaperone interactions (Section 7.1) and proposes ideas to address further open questions (Section 7.2).

7.1 CONCLUSION

The GR exhibits a complex functional pathway that relies on the interaction with many different ligands, co-factors and chaperones and subtle conformational rearrangements. that is one of the reasons, why many details about its function remained elusive. The experiments presented in this work shed light on questions that have been unanswered so far by using novel methods investigating the GR-LBD on a single-molecule level.

By excluding ensemble effects like aggregation, the investigations at the single-molecule level allowed to study the full folding energy landscape of the GR-LBD, its possible conformations and their stability. The application of force to the molecule allowed to modulate the timescales of processes such as hormone dissociation to specifically observe different configurations. By direct observation of the GR-LBD conformational trajectory, single hormone-binding events could be monitored as well as interactions linked to certain conditions of the investigated protein.

Innovative force-jump experiments revealed intrinsic folding defects of the GR-LBD, but also showed that it still folds on a seconds timescale without the assistance of chaperones. For the first time, the apo-conformation of the GR-LBD could be directly observed. The hormone-unbound GR-LBD could be identified as a stable protein, in contrast to current knowledge.

The mechanical single-molecule assay used in this work provides a direct readout for hormone binding together with primary structure information about the conformational changes involved. The so far enigmatic pathway of hormone binding into the buried GR-LBD binding pocket was revealed. The scenario of the protein folding around the hormone could be excluded. A new key structural *lid* element was identified that is tightly linked to hormone binding and dissociation. New experiments were developed to definitely localize this *lid* to the N-terminal helix 1. This was unexpected as it has no direct contact to the hormone. Complementing our findings with the existing literature, the determined mechanism is confirmed to be the

relevant binding pathway also in the absence of force. The instability of the N-terminal *lid* in the hormone-unbound case also gives a new explanation for the GR-LBD's strong tendency to aggregate and the need for chaperone interaction.

This detailed knowledge about the GR-LBD dynamics allowed the direct observation of chaperone function in action. The unfolding of a protein by a chaperone was directly observed for the first time in a single-molecule study. Comparing the GR-LBD behavior with and without chaperones, details about the interaction could be revealed; such as the role of Hsp40 and hormone dissociation for Hsp70 interaction. By sophisticated measurements including a multi-component chaperone system and the controlled application of force, different states of GR-LBD-Hsp90 complexes could be directly detected. These observations could finally end the ongoing debate about the role of Hsp90 in client regulation.

Due to the involvement of several players, the reconstruction of the full chaperone interaction cycle demands new measurement approaches. The implementation of a microfluidics system is yielding promising results and opens new horizons to study these complex interactions on a single-molecule level.

7.2 OPEN QUESTIONS AND OUTLOOK

Every answer opens new questions. Having established the observation of GR-LBD conformational dynamics, many new questions can be addressed. In particular the use of a microfluidics system to investigate the assembly of the GR-LBD-chaperone complex seems promising.

7.2.1 *Interaction of the complete chaperone system*

COMPLEX ASSEMBLY AT ZERO-FORCE In Section 6.2.2 Hsp70 was observed to unfold the hormone-unbound GR-LBD at zero-force in equilibrium. Hsp90 was found to recover this unfolded GR-LBD into a stable state (Section 6.6), possibly even in the absence of hormones (Section 6.8.1). It would be interesting to observe this whole process happening at equilibrium in the absence of force. To this end, the GR-LBD could be pre-incubated in the absence of hormones and in the presence of varying concentrations of Hsp70 and Hsp90 including co-chaperones (starting with 6 µM Hsp70 and 2 µM Hsp90). The trace upon first stretching of a tether should now exhibit the properties of the Hsp90-stabilized states. By further stretching the tether, the unfolding forces of the complexed GR-LBD can be examined. The comparison with subsequent traces, exhibiting the *H7blocked* shape after the unfolding, could serve as a sanity check.

This experiment would provide evidence that these specific Hsp90-complexes assemble at zero-force, in the absence of hormones and in equilibrium. This experiment would also allow a more efficient investigation of the GR-LBD-chaperone complexes as they would be pre-assembled before the measurement. The microfluidics system would allow to subsequently transfer these complexes into an environment containing DEX to probe the hormone-binding capabilities.

DIFFERENT COMPLEX CONFORMATIONS In Section 6.6 different conformations of GR-LBD were induced by the presence of Hsp90. To probe their different characteristics, the components influencing the Hsp90 conformation should be systematically varied such as the concentrations of p23, HOP and ATP.

SEQUENCE OF COMPLEX ASSEMBLY The microfluidics system also allows to probe the sequence of possible complex formations. Do the chaperones form a different complex with the GR-LBD if they can pre-assemble in solution, in comparison to a stepwise association of each single chaperone?

7.2.2 *Interaction of the Hsp90 system*

To better quantify the direct interaction of the Hsp90 system with the hormone-bound GR-LBD, the *H9so* state, interrupting the native *open-closed* fluctuations, has to be observed under systematic variation of Hsp90 concentration.

The interaction of Hsp90 alone showed only a minor influence on the *lid open-closed* fluctuations. To observe and quantify the whole stabilization by this interaction, the free energy of all folding intermediate states of the GR-LBD must be explored in the presence of Hsp90.

Along this line also the influence of p23, HOP and DEX on the interaction should be investigated. An interesting question would be, whether the Hsp90-stabilized states found after the unfolding by Hsp70 could be adopted also without the preceding Hsp70 interaction. Would the GR-LBD-Hsp90 complex possibly also assemble after unfolding of the GR-LBD by force?

7.2.3 *Interaction of the Hsp70 system*

HSP70 ZERO-FORCE INTERACTION A rather qualitative investigation of Hsp70 unfolding the GR-LBD at zero-force was performed in Section 6.2.2, lacking a readout for functional hormone-bound GR-LBD before and after the interaction.

To examine the kinetics of Hsp70 unfolding the unbound GR-LBD at zero-force and calculate the free energy of the interaction, the mi-

crofluidics system integrated in the optical trap (as demonstrated in Section 6.8.2) can be used.

To this end, a functional GR-LBD can be triggered to dissociate DEX in the absence of Hsp70, subsequently relaxed to zero-force and brought into Hsp70-containing buffer conditions. Stretching of the molecule after a defined waiting time τ_w would yield information about the concentration dependent Hsp70 association rate to the hormone-unbound GR-LBD at zero-force. Variation of τ_w can shed light on the intermediate states of Hsp70-induced unfolding at zero-force. The dependence of these intermediate states on the concentration of Hsp40 and Hsp70 can yield additional detailed information about the process.

The other way round in the absence of chaperones also the dissociation rate at zero-force can be investigated in the absence or presence of DEX. These measurements would also allow the computation of values as stoichiometry and interaction free energy.

THE HSP40 INTERACTION Hsp40 was found to induce a state, slightly more unfolded than the *open-ub* state (Section 6.3), but an exact structural interpretation of this interaction is still missing. Candidates for the interpretation are the unfolding of helix 3 or helix 12. A loop mutation similar to the one used in Section 4.6.3 could be used to address this question but includes the effort of mutagenesis, expression and purification of the protein which might be even not stable.

Similar to the measurements in Section 4.6.1, the combined interaction of Hsp40 and the TIF2 peptide that is known to interact with helix 12, could help with the structural interpretation.

It is also unclear, whether Hsp40 interacts also with other intermediates further down on the unfolding pathway. How many Hsp40 molecules are involved in the Hsp70-induced unfolding? Observing the state fluctuations between all intermediate states of the GR-LBD and measure the folding free energies in dependence on Hsp40 concentration could answer this question.

To investigate the kinetics and free energy of the Hsp40 interaction, the *H4* state (Section 6.3) should be quantified under systematic variation of Hsp40 concentration.

7.2.4 *Function of the GR alone*

The N-terminal helix 1 of the GR-LBD was found to play a key role in hormone binding. As the full length GR continues from this terminus, it will be interesting to study the influence of the other receptor parts on the GR-LBD dynamics.

Such as for the DEX-bound GR-LBD, the stability and conformational dynamics of the LBD, binding different ligands, e.g. the antagonist Mifepristone can be investigated.

The presented measurements can also be used to further study the influence of co-regulatory proteins, such as TIF2 (see Section 4.6.1), on the conformation and hormone binding of the GR-LBD.

Altogether, optical tweezers, particularly including a microfluidics system, allow to answer a plethora of detailed questions about the function and interaction of proteins and will certainly contribute to complete the picture of GR-LBD function and chaperone interaction.

Part IV

APPENDIX

A

ADDITIONAL CHARACTERISTICS OF GR-LBD

This chapter describes further results that characterize the GR-LBD. Section A.1 describes the force dependent unfolding rates of the DEX-bound *open* state. Section A.2 illustrates the unfolding pattern of the apo-GR-LBD, measured in stretch-and-relax cycles. Section A.3 contains the kinetic properties for hormone-binding of another GR-LBD variant that was used in other studies. Section A.4 illustrates various heterogeneous misfoldings of the GR-LBD that were not investigated quantitatively due to their strong variability, but demonstrate the complex nature of the GR-LBD. Section A.5 demonstrates the occurrence of a folded, but *lid*-closing-incompetent GR-LBD state. Section A.6 describes a kinetic switch in the *lid* fluctuations of the native GR-LBD and a possible explanation by proline isomerisation.

A.1 FORCE DEPENDENT UNFOLDING RATE OF DEX-BOUND GR-LBD

In Section 4.1 the unfolding of the DEX-bound GR-LBD by constantly increasing the force on the molecule in stretch-and-relax cycles was described. Using a method described by Oberbarnscheidt *et al.* [162], the force-dependent unfolding rates can be calculated from the obtained force vs. extension traces.

Figure A.1A shows an overlay of some example force vs. extension traces, exhibiting unfolding of the DEX-bound GR-LBD. The unfolding occurs at forces, significantly higher than the force range of the *open-closed* fluctuations (as discussed in Section 4.2). Consequently the transition resembles unfolding of the *open* state. Using the number of unfolding events in a certain force range and dividing it by the time, the molecule spent in this force range in total, yields an unfolding rate at this force (as described in [162]).

Figure A.1B displays the force-dependent unfolding rates of the *open* state, $k_{open\rightarrow unf}(F)$. The extrapolations of three independent experiments yielded an average unfolding rate of the *open* state at zero-force:

$$k^{0\,\mathrm{pN}}_{open\rightarrow unf} = 0.1 \pm 0.5\,/\mathrm{s},$$

and a contour length difference to the transition state of

$$\Delta L^{T}_{open\rightarrow unf} = 2.2 \pm 0.2\,\mathrm{nm}.$$

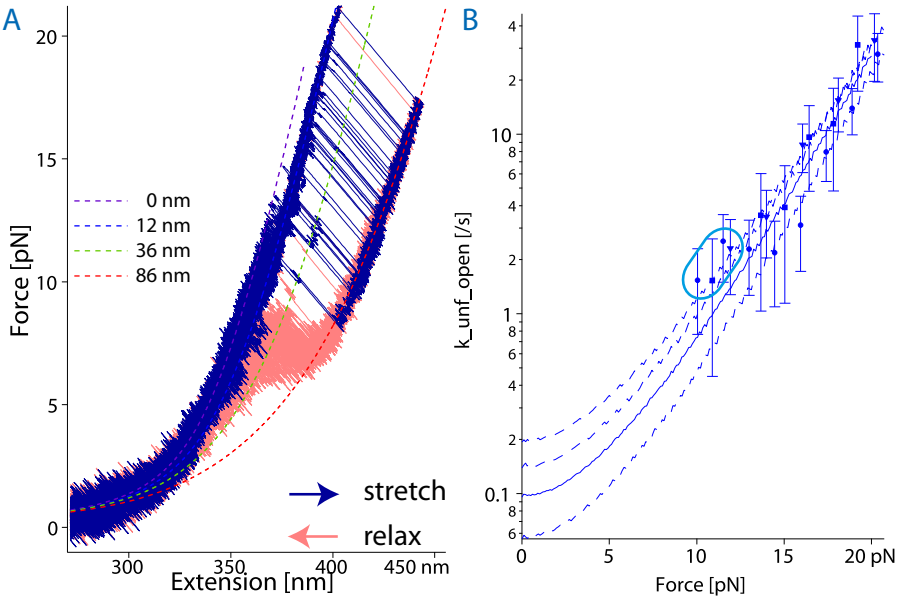

Figure A.1: Analysis of the force-dependent unfolding rates of DEX-bound GR-LBD. (A) Overlay of force vs. extension traces at 200 µM DEX, showing the DEX-bound GR-LBD unfolding. The dashed lines are fits based on the WLC model. (B) Force-dependent unfolding rates of the *open* state combined from 3 independent experiments. The dashed lines are extrapolations based on a model described in Section 3.4.2. The solid line is an average extrapolation. The cyan circle highlights slight deviations of the rates from the fit.

At forces around 12 pN (highlighted by cyan circle), the rates slightly deviate from the fits displayed. This is possibly due to mixing of the unfolding events with the dissociation of DEX from the *open* state during the stretch that occurs with a rate of $k_{diss}^{open} = 3\,/\mathrm{s}$, independently of force.

Note that the rates for unfolding of the *open* state at around 10 pN were roughly an order of magnitude smaller than the dissociation of DEX from the *open* state. Hence, the dominant pathway of unfolding around these forces is unbinding of DEX and subsequent unfolding of the *open-ub* state.

A.2 UNFOLDING PATTERN OF HORMONE UNBOUND GR-LBD

In Section 4.1, the unfolding pattern of the DEX-bound GR-LBD in stretch-and-relax cycles was discussed.

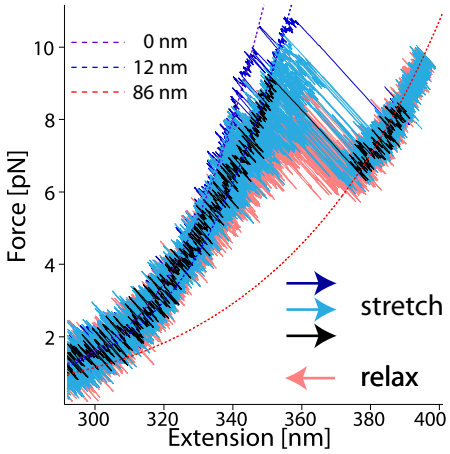

Figure A.2: Example force vs. extension traces of unbound unfolding, at a DEX concentration of 30 nM. The blue traces shows the first unfolding, exhibiting the *open-closed* fluctuations around 10 pN, indicating unfolding of a DEX-bound state. The black trace was the subsequent unfolding. The cyan traces occurred later.

Figure A.2 displays and overlay of the prominent unfolding pattern at a DEX concentration of 30 nM. The first unfolding (blue) trace still shows the DEX-bound unfolding pattern, exhibiting the *open-closed* fluctuations. Subsequent traces do not exhibit these fluctuations but roughly follow the WLC fit with a contour length of the *open* state and unfold below 10 pN. These traces are considered to show the unfolding of the DEX-unbound *open-ub* state.

At a constant pulling velocity of 500 nm/s, the unbound GR-LBD exhibited an average unfolding force of roughly

$$F_{open\text{-}ub}^{unf} = 10\,\mathrm{pN}.$$

Below 5 pN, the unbound GR-LBD transitions to a contour length resembling the *closed* state (purple dashed line). This is consistent

	GR-LBD$_{6x}$	GR-LBD
$k^{0\,\mathrm{pN}}_{open\to closed}[/\mathrm{s}]$	$9 \pm 3 \times 10^4$	$4.8 \pm 0.5 \times 10^4$
$k^{0\,\mathrm{pN}}_{closed\to open}[/\mathrm{s}]$	1.3 ± 0.5	0.4 ± 0.1
$\Delta G^0_{lid}[k_BT]$	11.2 ± 0.5	11.6 ± 0.3
$k_{bind}[/\mathrm{s}/\mu\mathrm{M}]$	0.080 ± 0.008	0.033 ± 0.003
$k^{open}_{diss}[/\mathrm{s}]$	0.80 ± 0.08	3.0 ± 0.2
$k^{eff}_{diss}(0\,\mathrm{pN})[/\mathrm{s}]$	$1.1(+0.8-0.5) \times 10^{-5}$	$3 \pm 2 \times 10^{-5}$
$K^{closed-open\text{-}ub}_{d,eff}[\mathrm{nM}]$	$0.1(+0.1-0.5) \times 10^{-5}$	0.8 ± 0.5

Table A.1: Comparison of *lid*, and DEX-binding kinetics of GR-LBD$_{6x}$ with the GR-LBD

with the attachment of the *lid* in the unbound state below these forces as discussed in Section 4.8.

A detailed analysis of hormone-unbound GR-LBD folding and unfolding is done using passive-mode measurements, presented in Chapter 5.

A.3 KINETICS OF ANOTHER VARIANT GR$_{6x}$

A second variant GR-LBD$_{6x}$ with 6 stabilizing mutations (sequence given in Section B.1), used in a previous study by Lorenz *et al.* [128], was analyzed to check the influence of the mutations on the native hormone-binding and *lid* kinetics.

The measurements and analysis were done similarly as described in Chapter 4.

Table A.1 compares the rates for *lid* opening and closing and DEX-binding and dissociation of the GR-LBD$_{6x}$ variant with the GR-LBD. The *lid* appears slightly destabilized in the GR-LBD$_{6x}$ variant, but the hormone is bound more tightly in the *open* state, exhibiting a slower k^{open}_{diss} and faster k_{bind}. This results in a 8-fold higher effective affinity to the *open-ub* state, which could explain the lower tendency to aggregate [128].

A comparison of the DEX binding and dissociation rates was not possible, as the ensemble rates were only measured for the fluorescently labeled F-DEX

A.4 HETEROGENEOUS MISFOLDING BEHAVIOR OF THE GR-LBD

Several examples of partial purification from recombinant sources have noted the difficult nature of the GR [4, 33, 164]. Also, the expression, purification and biophysical characterization of only the GR-LBD have proven to be problematic due to the putatively low

intrinsic stability and poor solubility [23, 215]. SHR LBDs in general, are inherently unstable and extensive mutagenesis was required to enhance expression and crystallization [253]. However, without bound hormone, the GR-LBD displayed a very unstable nature, exhibiting unfolding and aggregation already at very low temperatures even despite stabilizing mutations [113, 117, 128]. Hence, it was not amenable to structural investigations [69]. Folding studies using ensemble methods have been difficult due to solubility issues and refolding into its native configuration could not be achieved [139].

Also, in the single-molecule measurements using optical tweezers, there were several difficulties investigating the GR-LBD. This section describes various types of misfoldings that were hard to be quantified due to their heterogeneity.

A.4.1 *Reversible misfolding during passive-mode*

One type of misfolding, was the change of the hormone-unbound folding fluctuation kinetics during the passive-mode experiments. Figure A.3 shows an example of such misfolding behavior during the passive-mode experiments. The trace needs to be compared with the traces displayed in Figure 5.1 and Figure 5.4. Reversible misfolding (highlighted in green) alternating with native GR-LBD behavior was observed

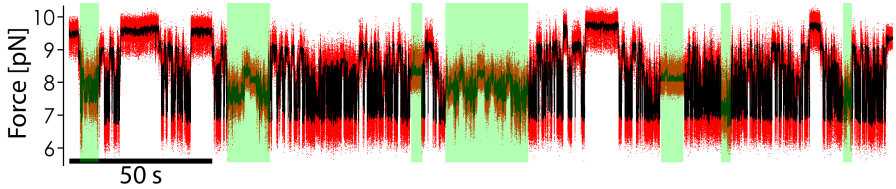

Figure A.3: Example force vs. time trace of reversible misfolding. The phases were the kinetics deviated from the reproducible folding kinetics are highlighted in green.

A.4.2 *Irreversible misfolding*

In roughly 50% of the experiments, the measurement ended, as the protein – that exhibited native behavior at the beginning of the experiment – started to show only non-native behavior.

Figure A.4A demonstrates the switch of a GR-LBD from a native folding behavior during a passive-mode experiment (compare to Chapter 5) to a misfolded structure (highlighted in green).

Figure A.4B illustrates example traces obtained by performing stretch-and-relax cycles after the molecule started to misfold. Only the stretching part of each cycle is displayed. The protein adopts a variety of different contour lengths. Many of these misfolded states were signif-

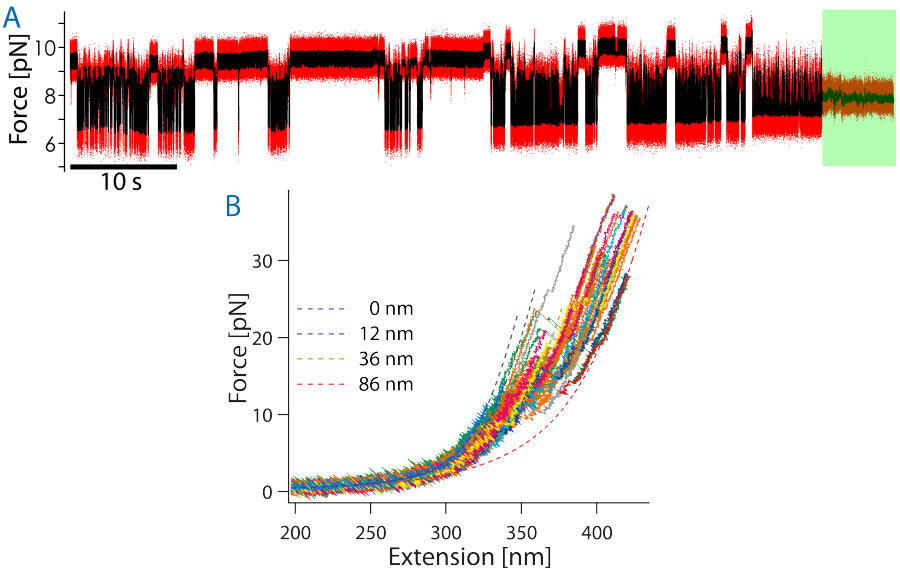

Figure A.4: (A) Force vs. time trace of a passive-mode experiment. The force was stepwise increased during the experiment. The switch to a misfolded protein structure is highlighted in green. (B) Overlay of stretch-and-relax cycles after the beginning of misfolding by the GR-LBD. The force vs. extension traces are colored differently to highlight the heterogeneity of unfolding patterns. Dashed lines illustrate the WLC model for protein contour lengths of the native protein states.

icantly more stable than the native state and could not be unfolded, even applying forces of up to 40 pN. These misfoldings appeared to be irreversible.

These misfoldings appeared to be dependent on the time the protein was kept unfolded for. This suggests some kind of modification on amino acid residues that were otherwise protected inside the folded protein structure. A hypothetical explanation is the association of some structural part with other proteins, possibly other GR-LBD molecules in close proximity, for example also attached to the bead surface.

A.4.3 *Small peptide domain involved in misfolding*

In roughly 20% of the cases, a protein, exhibiting the misfolding behavior described in Section A.4.2, could recover into its native folding behavior. Interestingly, the unfolding of a short peptide part (with a contour length increase of $\Delta L \approx 8\,\text{nm}$) was reproducibly observed in the last stretch before the GR-LBD folded back into its native state.

Figure A.5 displays an example of a force vs. extension trace, exhibiting such an unfolding. The trace shows the unfolding of a non-native misfolded structure. The last unfolding transition around $F = 17\,\text{pN}$ is the unfolding of a structure, where only 8 nm (this cor-

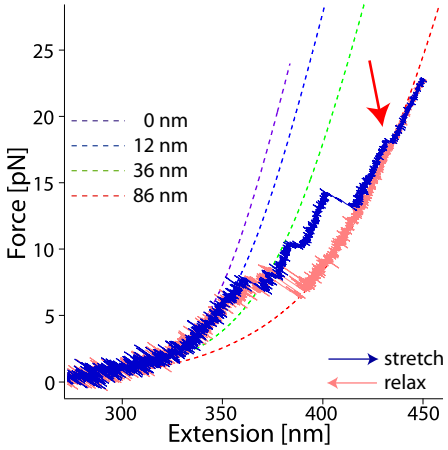

Figure A.5: Example of a short peptide part unfolding after a period of GR-LBD misfolding. The red arrow highlights the unfolding event of the short peptide part.

relates to roughly 22 amino acid residues) were folded. Due to the small length change, this transition has only a very weak force dependence, which explains the difficulties of resolving this misfolded structure by the application of force.

However, such a small peptide-domain, exhibiting such a high energy barrier for unfolding that it can inhibit proper refolding of the GR-LBD again suggests interactions with a third molecule from solution.

Qualitatively all these types of misfolding seemed to show some dependence on the assay conditions like contamination of the solution with dirt particles, the amount of applied protein, the quality of scavenger system and the laser power. The latter two suggest that oxidation of certain amino acid residues could play a role for the misfolding behavior (as described in Section B.5). The use of a new oxygen scavenger system, PCD + PCA (as described in Section B.5) generally decreased the amount of heterogeneous misfoldings. However, as the occurrence of these misfoldings varied from day to day and between the molecules, a quantification was difficult.

The hypothesis of misfolding due to proline isomerisation, was tested by the addition of 2 µM proline isomerase SlyD [269]. Preliminary data suggests that this had no influence on these misfoldings (data not shown). Another hypothesis suggested the association of other GR-LBD molecules from solution, but preliminary experiments, using 6 µM in solution did not show a drastic effect (data not shown) on the misfolding behavior.

Also the presence of the Hsp70 or Hsp90 chaperone system did not resolve these misfoldings.

A.5 A FOLDED *lid*-CLOSING-INCOMPETENT STATE

During the experiments to measure the rebinding of DEX (as described in Section 4.3), an apparently *lid*-closing-incompetent state occurred, when omitting DTT in the experiments.

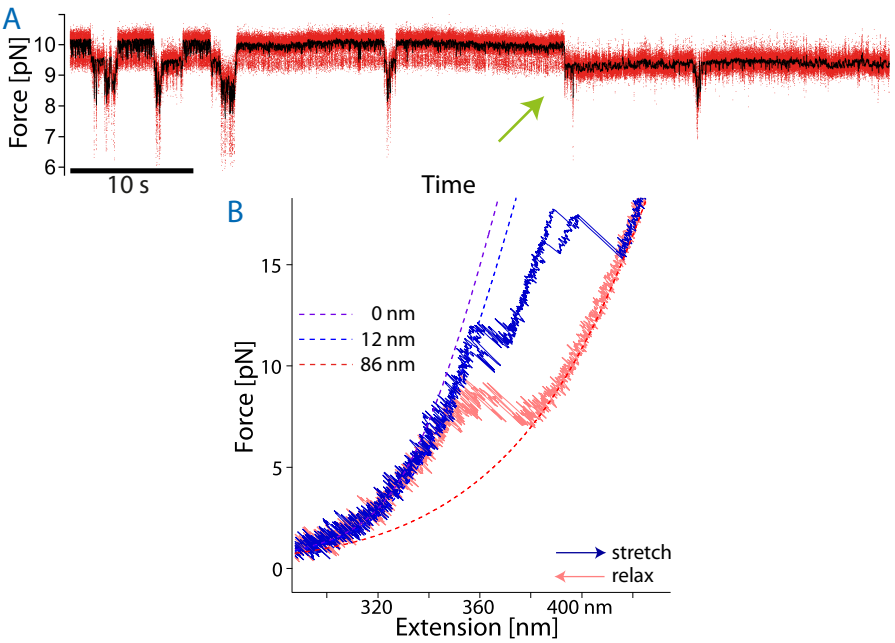

Figure A.6: Example traces illustrating the *lid*-closing-competent state in the absence of DTT. (A) Passive-mode experiment, illustrating the native *lid* fluctuations including 4 DEX-rebinding events (compare to Figure 4.6). The green arrow marks the point where the *lid* remains open. (B) Overlay of two stretch-and-relax cycles after the traces shown in (A). They exhibit the fingerprint of the *lid*-closing-incompetent state.

Figure A.6A illustrates the occurrence of such a *lid*-closing-incompetent state during a passive-mode experiment. After the native *open-closed lid* fluctuations, including 4 DEX-rebinding events (compare to Figure 4.6), the GR-LBD transitions into a state with the contour length of roughly the *closed* or *open-ub* state, but does not show closing of the *lid* any more (green arrow). This state will be henceforth referred to as the *lid*-closing-incompetent state (short *incompetent* state).

The application of subsequent stretch-and-relax cycles exhibit a characteristic unfolding pattern of the *incompetent* state, as described by Figure A.6B. After unfolding of the protein several times, the GR-LBD eventually switches back to the native state on a timescale of roughly 1 min. This indicates that switching to this *incompetent* is a reversible modification.

The occurrence of the *incompetent* state appeared to exhibit some dependence on the performance of the oxygen scavenger system, but

was difficult to quantify, as it strongly varied between the experiments.

INHIBITION OF THE *incompetent* STATE BY DTT DTT serves as a reducing agent, commonly used in protein biochemistry to counteract sulfhydryl oxidation [78]. The use of 1 mM DTT inhibited the occurrence of the *incompetent* state.

A reducing agent – also called a reductant or reducer – is a compound that donates an electron to another chemical species in a redox-chemical reaction.

Oxidation has shown to be a cause for malfunction of biological systems in general, and the oxidation of sulfhydryl (SH) groups of cystein residues are the most prominent modulations in proteins, caused by oxidation. [92, 204, 225].

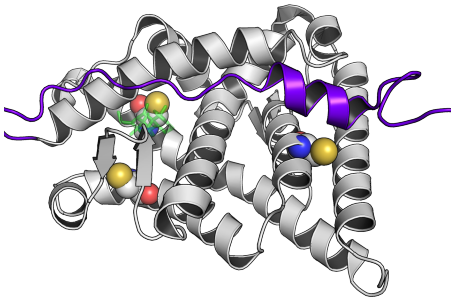

Figure A.7: Illustration of cystein residues in the GR-LBD structure (pdb:1M2Z), prone to aggregation. Cystein residues are displayed as spheres, SH-groups are colored in yellow, oxygen in red, nitrogen in blue. DEX is displayed as transparent green sticks. The *lid* is colored in purple.

incompetent STATE CAUSED BY CYSTEIN OXIDATION So one hypothesis is that the *incompetent*-state is caused by reversible oxidation of SH groups of cystein residues. Figure A.7 shows the structure of the GR-LBD with 3 cystein residues highlighted (sphere representation) that are possibly related to the *incompetent* state. Residue C665 is positioned directly underneath the N-terminal *lid* (colored in purple) and residues C643, C736 are flanking the DEX-binding site and could get solvent exposed in the DEX-unbound state. It is unclear, whether the *incompetent* state is hormone-bound.

A study reported the inhibition of GR ligand-binding by nitric oxide – that has been reported to react with -SH groups – which further supports the hypothesis [72].

Interestingly, using 1 mM of the sulfhydryl reductant TCEP [78], did not inhibit the *incompetent* state (data not shown). It can be hypothesized that TCEP, due to its bulky nature does not reduce intramolecular sulfides as easily as DTT.

A.6 SWITCHING OF *lid* KINETICS DUE TO PROLINE ISOMERISATION

During the native *open-closed lid* fluctuations (as described in Section 4.2), a temporary switch of the closing kinetics occurred.

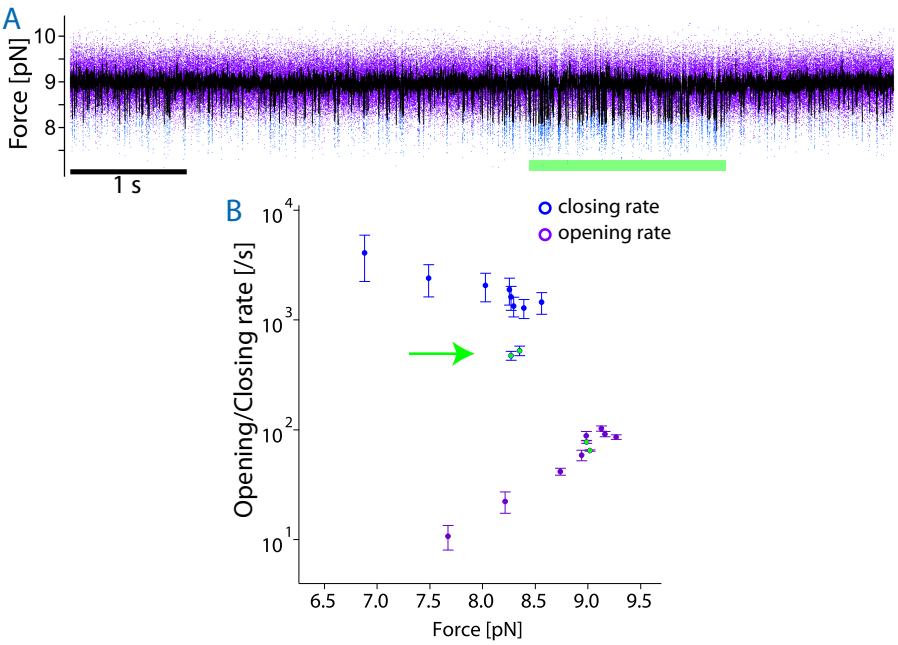

Figure A.8: (A) Example passive-mode trace, exhibiting a kinetic switch in the *open* (blue)-*closed* (purple) fluctuations. In a period of roughly 2 s, the lifetime of the blue *open* state increases (highlighted by the green bar). (B) Comparison of opening (purple) and closing (blue) rates during the period of altered kinetics with the rates measured for the same molecule but in other parts of the trace and at different forces. The rates during the period of altered kinetics are highlighted by green dots.

Figure A.8A shows the trace of a passive-mode experiment, exhibiting a period of altered *open-closed* kinetics (highlighted by the green bar). During these phases the lifetime of the *open* state increases.

These changed kinetics were existent during roughly 5% of the fluctuations.

Figure A.8B displays an analysis of the *lid* opening and closing rates during the period of altered kinetics in comparison to the kinetics, exhibited during the rest of the experiment (compare to Section 4.2). The closing rate during the period of altered kinetics reduces by a factor of 3, while the opening rate appears unaffected. This change in the closing rate results in a decrease of the energy stored in the *closed lid*, ΔG_{lid}, by 1 k_BT under these conditions.

DEX dissociation from the *open* state, k_{diss}^{open}, remains unaffected. Hence, the effective dissociation rate, k_{diss}^{eff}, is decreased during the period of altered *open-closed* kinetics.

EXPLANATION BY PROLINE ISOMERISATION The switch between these two kinetics occurred on the timescale of several seconds. Due to this timescale it can be hypothesized that this switch is a result of a proline isomerisation that occurs on this timescale and has been found to induce switching of protein folding kinetics [191].

There are 10 prolines present in the GR-LBD structure, as illustrated in Figure A.9, 4 of which are present in the *lid*. In the native structure they are all in the energetically favored trans-configuration. In an unfolded peptide chain they have a chance of 1:6 to occur in the cis-configuration [191]. This suggests that upon opening of the N-terminal *lid*, a proline isomerises into the cis-configuration and thus hampers the closing of the *lid*. The proline P553 – located at the kink between the *lid* and the subsequent helix (on the left side in Figure A.9) – would be an intuitive candidate for causing this kinetic switch in the closing kinetics of the *lid*.

Whether there is a physiological significance of this switch for GR function, can be only hypothesized.

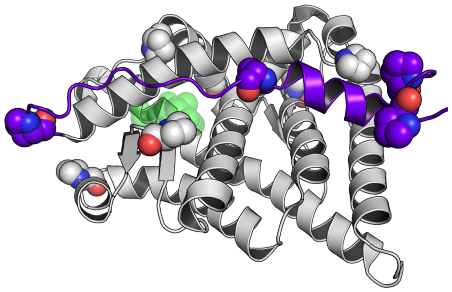

Figure A.9: Prolines in the structure of GR-LBD (pdb:1M2Z), highlighted by sphere representation. Oxygen is colored in red, nitrogen in blue. The N-terminal *lid* and the prolines present in the *lid* are colored in purple. DEX is colored in green.

B

MEASUREMENT PREPARATION

In this chapter, details are given about the measured protein constructs (B.1), chaperones (B.2), peptides (B.3), buffer conditions (B.4) and the newly used oxygen scavenger system (B.5). Section B.6 describes the azide oligo attachment and the preparation of the trap assay is described in Section B.7.

B.1 GR-LBD CONSTRUCTS

The expression and purification of the given protein constructs was done by D. Rutz according the following protocol [196].

PROTEIN EXPRESSION AND PURIFICATION Human GR-LBD variants (aa 527-777) were expressed at 18°C overnight in ZYM-5052 autoinduction media supplied with 500 µM DEX (Sigma-Aldrich, St. Louis, USA) [230]. Cells were harvested by centrifugation for 15 min at 7000 rpm and 4°C (Beckman Avanti J-26 XP, Beckman Coulter, Brea, California) and washed with ice-cold PBS. Cells were resuspended in Ni-A buffer (50 mM Tris, 2 M Urea, 100 mM NaCl, 5 mM $MgCl_2$, 10 mM Imidazole, 2 mM β-mercaptoethanol, 50 µM DEX, pH 7.9) supplemented with DNaseI (Roche, Basel, Swiss) and Protease Inhibitor HP (Serva electrophoresis GmbH, Heidelberg, Germany). Cell suspension was lysed by sonication (Bandelin Sonoplus UW2200, Bandelin electronic, Berlin Germany) or french press (Constant Systems Limited, Low March, UK) and centrifuged for 1 hour at 20 000 rpm and 4°C. Cleared lysate was applied onto a Ni-column (5 ml FF,GE Healthcare, Chalfont St. Giles, Great Britain), pre-equilibrated in Ni-B buffer (50 mM Tris, 500 mM NaCl, 10 mM Imidazole, 10% Glycerol, 2 mM β-mercaptoethanol, 50 µM DEX pH 7.9). The column was then gradient-equilibrated in NiB buffer and His6-Halo-GR-LBD was eluted with Ni-C buffer (50 mM Tris, 500 mM NaCl, 350 mM Imidazole, 10% Glycerol, 2 mM β-mercaptoethanol, 50 µM DEX pH 7.9). IMAC-Buffers for the purification of apo-GR-LBD were supplied with 2 mM ATP to prevent binding of E. coli GroE and DnaK. GR-protein containing fractions were pooled, supplemented with His6-tagged TEV protease and dialyzed against 50 mM Tris, 100 mM NaCl, 10% Glycerol, 2 mM β-mercaptoethanol, 0.5% CHAPS, 50 µM DEX pH 7.9 overnight. Then, digested protein was passed through a Ni-column to remove Halo-tag-Fusion and TEV protease. The flow through was concentrated and loaded onto a gel filtration column (Superdex 200,

16/60 pg, GE Healthcare, Chalfont St. Giles, Great Britain) equilibrated in GR-storage buffer (25 mM Tris, 100 mM NaCl, 10% Glycerol, 2 mM DTT, 50 µM DEX pH 7.9). GR-proteins were snap-frozen and analyzed by SDS-PAGE.

PROTEIN SEQUENCES The sequences of the used protein constructs are given below. Terminal cyteins (sequence highlighted as bold) were introduced for the attachment of DNA-oligos (procedure given in Section B.6). To prevent attachment of the DNA-oligos to another site, the cystein at position 638 was mutated. The F602S mutation is a commonly used stabilizing mutation. These mutations are also discussed in [23]. The single point mutations and loop insertion are highlighted in red.

N-SACK-GR-LBD F602S/C638D-KCL-C (GR-LBD):

SACKQLTPTLVSLLEVIEPEVLYAGYDSSVPDSTWRIMTTLNMLGGRQVIAAVKW-
AKAIPGFRNLHLDDQMTLLQYSWMSLMAFALGWRSYRQSSANLLCFAPDLIINEQ-
RMTLPDMYDQCKHMLYVSSELHRLQVSYEEYLCMKTLLLLSSVPKDGLKSQELFD-
EIRMTYIKELGKAIVKREGNSSQNWQRFYQLTKLLDSMHEVVENLLNYCFQTFLD-
KTMSIEFPEMLAEIITNQIPKYSNGNIKKLLFHQK**CL**

N-SACK-GR-LBD F602S/A605V/C638D/V702A/E705G/M752T-KCL-C (GR-LBD$_{6x}$):

SACKQLTPTLVSLLEVIEPEVLYAGYDSSVPDSTWRIMTTLNMLGGRQVIAAVKW-
AKAIPGFRNLHLDDQMTLLQYSWMSLMVFALGWRSYRQSSANLLCFAPDLIINEQ-
RKTLPDMYDQCKHMLYVSSELHRLQVSYEEYLCMKTLLLLSSVPKDGLKSQELFD-
EIRMTYIKELGKAIAKRGGNSSQNWQRFYQLTKLLDSMHEVVENLLNYCFQTFLD-
KTMSIEFPETLAEIITNQIPKYSNGNIKKLLFHQK**CL**

N-SACK-GR-LBD S551-GGSGGSGGSGG-V522/F602S/C638D-KCL-C (GR-LBD^{N-loop}):

SACKQLTPTLVSLLEVIEPEVLYAGYDSSGGSGGSGGSGGVPDSTWRIMTTLNML-
GGRQVIAAVKWAKAIPGFRNLHLDDQMTLLQYSWMSLMAFALGWRSYRQSSANLL-
CFAPDLIINEQRMTLPDMYDQCKHMLYVSSELHRLQVSYEEYLCMKTLLLLSSVP-
KDGLKSQELFDEIRMTYIKELGKAIVKREGNSSQNWQRFYQLTKLLDSMHEVVEN-
LLNYCFQTFLDKTMSIEFPEMLAEIITNQIPKYSNGNIKKLLFHQK**CL**

B.2 CHAPERONES

Protein expression and purification. Human Hsp90β, Hsp40 (yeast homologue Ydj1), human Hsp70, HOP and p23 were expressed and purified from E. coli.

Following previous studies, yeast Hsp40 homologue Ydj1 was used in combination with human Hsp70 ([52, 113, 196])

To avoid contamination and aggregates, all chaperones were diluted to roughly 40 µM, centrifuged for 30 min at 17 000 g at 4°C prior to all measurements.

If not stated differently, Hsp70 and Hsp90 were always used in presence of 3 mM ATP and 2 mM MgCl2 (ATP snap-frozen and stored at -80°C after preparation).

B.2.1 *Expression and purification of Hsp70 and Hsp40*

Hsp70 and Ydj1 (Hsp40) were expressed and purified by Ulrike Majdic, using the following protocol. Buffer solutions *Buffer A* and *Buffer B* are described in the PhD thesis of Schmid [207]. The sequences of the proteins, cloning vectors, cell cultures and final concentrations are given below.

6 × 0.5 liter of LBo-Media containing Kanamycin were inoculated with an overnight culture to an initial OD600 of 0.2. After incubation at 37°C and OD600 of 0.6 – 0.8 was reached, gene expression was induced by addition of 1 mM IPTG. The cells were incubated at 30°C over night. Cells were harvested by centrifugation and resuspended in *Buffer A* containing DNase I and AEBSF (Roth). After cell disruption and centrifugation, the cleared and filtrated lysate was loaded on a HisTrap HF (1ml, GE) column. The column was washed with 20x of the column size with *Buffer A*. To get rid of further unspecific bound proteins, 20x of the column size were washed with 6% *Buffer B*. Elution of the protein was performed by step gradient to 100% *Buffer B*. The protein containing fractions were pooled and diluted 1:5 with ice-cold ddH2O. SUMO-protease was added and the mixture dialysed against SEC buffer at 4°C over night. Followed affinity chromatography was used to remove remaining undigested proteins, SUMO-tags and His-tagged SUMO-protease. The flow through was collected, concentrated and loaded on gel filtration column equilibrated with SEC-running-buffer. Size exclusion chromatography was performed and purity of the protein was checked by SDS-PAGE. Fractions that contained pure protein were pooled, concentrated and frozen in liquid nitrogen. The protein was stored at -80°C.

YDJ1 (HSP40) plasmid was a generous gift from the Buchner lab, cloned in pET-SUMO via BamHI and XhoI, expressed in BL21 (DE3), final concentration 43 µM

```
SL*XILFTLRRRYTMGSSHHHHHHSSGLVPRGSHMSDSEVNQEAKPEVKPEVKPE-
THINLKVSDGSSEIFFKIKKTTPLRRLMEAFAKRQGKEMDSLRFLYDGIRIQADQ-
TPEDLDMEDNDIIEAHREQIGGSMVKETKFYDILGVPVTATDVEIKKAYRKCALK-
YHPDKNPSEEAAEKFKEASAAYEILSDPEKRDIYDQFGEDGLSGAGGAGGFPGGG-
FGFGDDIFSQFFGAGGAQRPRGPQRGKDIKHEISASLEELYKGRTAKLALNKQIL-
CKECEGRGGKKGAVKKCTSCNGQGIKFVTRQMGPMIQRFQTECDVCHGTGDIIDP-
KDRCKSCNGKKVENERKILEVHVEPGMKDGQRIVFKGEADQAPDVIPGDVVFIVS-
ERPHKSFKRDGDDLVYEAEIDLLTAIAGGEFALEHVSGDWLKVGIVPGEVIAPGM-
RKVIEGKGMPIPKYGGYGNLIIKFTIKFPENHFTSEENLKKLEEILPPRIVPAIP-
KKATVDECVLADFDPAKYNRTRASRGGANYDSDEEEQGGEGVQCASQ**LEHHHH-
HH*DPA
```

HSP70 NATURAL VARIANT VAR029053 (E110D) (Uniprot PoDMV8[1]), Gene HSPA1A, cloned in pET-SUMO via BamHI and XhoI, expressed in BL21 (DE3), final concentration 25 µM

```
MAKAAAIGIDLGTTYSCVGVFQHGKVEIIANDQGNRTTPSYVAFTDTERLIGDAA-
KNQVALNPQNTVFDAKRLIGRKFGDPVVQSDMKHWPFQVINDGDKPKVQVSYKGD-
TKAFYPEEISSMVLTKMKEIAEAYLGYPVTNAVITVPAYFNDSQRQATKDAGVIA-
GLNVLRIINEPTAAAIAYGLDRTGKGERNVLIFDLGGGTFDVSILTIDDGIFEVK-
ATAGDTHLGGEDFDNRLVNHFVEEFKRKHKKDISQNKRAVRRLRTACERAKRTLS-
SSTQASLEIDSLFEGIDFYTSITRARFEELCSDLFRSTLEPVEKALRDAKLDKAQ-
IHDLVLVGGSTRIPKVQKLLQDFFNGRDLNKSINPDEAVAYGAAVQAAILMGDKS-
ENVQDLLLLDVAPLSLGLETAGGVMTALIKRNSTIPTKQTQIFTTYSDNQPGVLI-
QVYEGERAMTKDNNLLGRFELSGIPPAPRGVPQIEVTFDIDANGILNVTATDKST-
GKANKITITNDKGRLSKEEIERMVQEAEKYKAEDEVQRERVSAKNALESYAFNMK-
SAVEDEGLKGKISEADKKKVLDKCQEVISWLDANTLAEKDEFEHKRKELEQVCNP-
IISGLYQGAGGPGPGGFGAQGPKGGSGSGPTIEEVD
```

B.2.2 *Expression and purification of Hsp90*

Human Hsp90β was a generous gift from the Buchner lab. It was expressed an purified by D. Rutz according to the following protocol that can be found in [196]. The sequence of the protein, cloning vectors, cell cultures and final concentrations are given below. It was stored at -80°C in 6 µl aliquots at a concentration of 150 µM.

Human Hsp90β were expressed at 37°C for 4 h with 1 mM IPTG. Cells were harvested by centrifugation for 20 min at 6000 rpm and 4°C (Beckman Avanti J-26 XP, Beckman Coulter, Brea, California) and resuspended in Ni-A buffer (40 mM KPi, 150 mM KCl, 6 mM Imidazol, pH 7.5) supplemented with DNaseI (Roche, Basel, Swiss) and Protease Inhibitor HP (Serva electrophoresis GmbH, Heidelberg, Germany). Cell suspension was lysed by french press (Constant Systems Limited, Low March, UK) and centrifuged for 35 min at 20 000 rpm and 4°C. The cleared lysate was loaded on a Ni-column (5 ml FF,GE Healthcare, Chalfont St. Giles, Great Britain) and eluted with 300 ml imidazole. Fractions containing the target protein were pooled and diluted to 150 ml with ResQA buffer (40 mM Hepes, 20 mM KCl, 1 mM EDTA, 1 mM DTT pH 7.5) to lower the salt concentration that would prevent the protein from binding the anion-exchange column. The protein was then loaded on the ResQ column (6 ml, GE Healthcare, Chalfont St. Giles, Great Britain) equilibrated in ResQA buffer. After loading, the column was washed with 10 CV ResQA buffer and eluted using a gradient from 0-50% ResQB buffer (40 mM Hepes, 1 M KCl, 1 mM EDTA, 1 mM DTT pH 7.5). Protein-containing fractions were pooled, concentrated and loaded on a Superdex 16/60 200 pg gel-filtration column (GE Healthcare, Chalfont St. Giles, Great

1 http://www.uniprot.org/uniprot/P0DMV8

Britain). Purity of the protein charge was controlled by SDS-PAGE and the protein was frozen in liquid nitrogen.

HUMAN HSP90β cloned in pET28, expressed in BL21 (DE3), final concentration 180 µM

```
MPEEVHHGEEEVETFAFQAEIAQLMSLIINTFYSNKEIFLRELISNASDALDKIR-
YESLTDPSKLDSGKELKIDIIPNPQERTLTLVDTGIGMTKADLINNLGTIAKSGT-
KAFMEALQAGADISMIGQFGVGFYSAYLVAEKVVVITKHNDDEQYAWESSAGGSF-
TVRADHGEPIGRGTKVILHLKEDQTEYLEERRVKEVVKKHSQFIGYPITLYLEKE-
REKEISDDEAEEEKGEKEEEDKDDEEKPKIEDVGSDEEDDSGKDKKKKTKKIKEK-
YIDQEELNKTKPIWTRNPDDITQEEYGEFYKSLTNDWEDHLAVKHFSVEGQLEFR-
ALLFIPRRAPFDLFENKKKKNNIKLYVRRVFIMDSCDELIPEYLNFIRGVVDSED-
LPLNISREMLQQSKILKVIRKNIVKKCLELFSELAEDKENYKKFYEAFSKNLKLG-
IHEDSTNRRRLSELLRYHTSQSGDEMTSLSEYVSRMKETQKSIYYITGESKEQVA-
NSAFVERVRKRGFEVVYMTEPIDEYCVQQLKEFDGKSLVSVTKEGLELPEDEEEK-
KKMEESKAKFENLCKLMKEILDKKVEKVTISNRLVSSPCCIVTSTYGWTANMERI-
MKAQALRDNSTMGYMMAKKHLEINPDHPIVETLRQKAEADKNDKAVKDLVVLLFE-
TALLSSGFSLEDPQTHSNRIYRMIKLGLGIDEDEVAAEEPNAAVPDEIPPLEGDE-
DASRMEEVD
```

B.2.3 *Expression and purification of HOP and p23*

Human co-chaperones HOP and p23 were generous gifts from the Buchner lab. They were expressed an purified by D. Rutz according to the following protocol (see [196]). They were stored at -80°C in 7 µl aliquots at a concentration of 300 µM (HOP) and 5 µl aliquots at a concentration of 450 µM (p23).

Human co-chaperones HOP and p23 were expressed tag-free in E. coli. Purification was conducted via a combination of anion-exchange, hydroxyapatite (HAT) and gel-filtration chromatography. Cells were harvested, disrupted and the lysate cleared as mentioned for the other proteins. The lysate was loaded on a self-packed Q-Sepharose column (GE Healthcare, Chalfont St. Giles, Great Britain) and eluted via a linear gradient from 0 – 600 mM KCl. The fractions containing the target protein were diluted to 150 ml in HAT low-salt buffer (10 mM KPi, pH 7.0) and subsequently applied to the self-packed HAT-column (GE Healthcare, Chalfont St. Giles, Great Britain). Protein elution was reached by applying a linear gradient of 0-100% HAT high-salt buffer (400 mM KPi, pH 7.0). Desired protein fractions were combined and loaded on a Superdex 16/60 75 or 200 pg gel-filtration column (GE Healthcare, Chalfont St. Giles, Great Britain). Protein purity was assessed by SDS-PAGE analysis.

B.3 PEPTIDES

B.3.1 *Peptide fragments comprising GR-LBD sequence*

The synthesis of peptide fragments, comprising the N-terminal and C-terminal of the GR-LBD sequence was ordered from Genscript[2]. The sequences and properties of the ordered peptides were:

NT22AA_NOTERM N-TERMINAL PEPTIDE (*Npep*) 2.4 kDa, extinction coefficient = 3000, PI = 3.5, purity (HPLC) 30%, aliquots of 10×0.9 mg
`TLVSLLEVIEPEVLYAGYDSSV`

CT25AA C-TERMINAL PEPTIDE 2.88 kDa, extinction coefficient = 1500, PI = 8.8, purity (HPLC) 98%, aliquots of 10×0.9 mg
`PEMLAEIITNQIPKYSNGNIKKLLF`

The net peptide content was roughly 70% of the gross weight for both peptides. The *Npep* could only be purified to 30% purity measured by HPLC. The residual contaminations were smaller peptide fragments. The problems in purification were attributed to the high hydrophobicity of the peptide.

The *Npep* was diluted by adding 250 µl of 3% ammonia water (30% ammonia water was filtered twice, using filters with 200 nm pore size and diluted in doubly distilled water). This resulted in a net peptide concentration of 300 µM.

In the measurements using 10 µM of *Npep*, the measurement solution contained 0.1 % residual ammonia water. This increased the pH to pH 10. Roughly 50 mM HCl were used to adjust the pH of the measurement solution to pH 7.5.

As a control measurement, the GR-LBD was measured without the peptide, but 0.1 % ammonia water in solution. There was no detectable effect on the *lid* fluctuations.

For the measurements using 2 µM *Npep* in solution, the measurement solution contained only 0.02 % ammonia water and the pH was not monitored. For a quantitative analysis of peptide binding rates, these measurements should be repeated using similar conditions for all peptide concentrations. During the time of writing the present work, another purification of *Npep* arrived, exhibiting a purity of 58% that can be used for further measurements.

The C-terminal peptide was diluted in 200 µM doubly distilled water, which yielded a stock concentration of 1 mM.

The diluted peptides were stored in aliquots at -20°C.

2 https://www.genscript.com/

B.3.2 *Peptide fragment comprising TIF2 binding site*

The peptide fragment comprising the GR-LBD binding site of the Transcriptional Intermediary Factor 2 (TIF2) co-activator protein was a generous gift from the Buchner lab. The sequence is given below.

This peptide fragment was also used for the crystallization of GR-LBD, pdb 1M2Z [24]

TIF2 PEPTIDE `KENALLRYLLDKDD`

The peptide was resuspended 40 mM HEPES, 150 mM NaCl to result in a concentration of 3 mM and the pH was adjusted to pH 7.5.

B.4 BUFFER CONDITIONS

All measurements were performed at 23°C in the presence of 40 mM HEPES, 150 mM NaCl and 1 mM DTT at pH 7.5 with the addition of 0 – 200 µM Dexamethasone (DEX, Sigma D1756). An oxygen scavenger system was added consisting of 1 mM protocatechuic acid (PCA, Sigma 08992-50MG) and 0.2 U/mL protocatechuate-3,4-dioxygenase (PCD, ordered from OYCeu) as described in Section B.5.

The following buffers were used:

- P^-: 40 mM HEPES, 150 mM NaCl at pH 7.5
- P_{50}: P^- including 50 µM DEX
- P_{GR}: P^- including 50 µM DEX and 0.5% CHAPS

The GR-LBD was stored in P_{GR}, including 1 mM TCEP.

DEX was resuspended in DMSO at a concentration of 40 mM and stored at -20°C in 10 µl aliquots. DEX was soluble up to 270 µM in the measurement buffer (data not shown).

DTT was resuspended in doubly distilled water and stored at 1 M concentration in 10 µl aliquots at -20°C. These were diluted 1:10 in P^- on the day of the measurement.

B.5 OXYGEN SCAVENGER SYSTEM

The high laser intensity necessary for the creation of the optical traps can cause photodamage to the biological system [127, 145, 157]. The exact mechanism for this process is still unknown, but it is suggested that it happens due to the excitation of molecular oxygen into reactive oxidative species (ROS). For *in-vitro* optical tweezers experiments this mainly results in DNA tether rupturing and proteins to deviate from their native behavior and misfolding [122]. Thus oxygen scavenger systems are used to eliminate oxygen molecules in solution. The most commonly used system is the glucose oxydase and catalase system (GODCAT) [216].

In the present work, an alternative oxygen scavenger system was used, as it resulted in a more stable behavior of the GR-LBD, exhibiting less heterogeneous misfolding behavior as described in Section A.4 and less ruptures of DNA tethers.

In the present work, 1 mM protocatechuic acid (PCA, Sigma 08992-50MG) and 0.2 $\frac{U}{ml}$ protocatechuate-3,4-dioxygenase (PCD, ordered from OYCeu, catalog number 46852004) was used. PCD is an enzyme that catalyzes the conversion of PCA to β-carboxy-cis, cis-muconic acid in one step, resulting in the consumption of 1 mole of O2 and the production of two protons per mole of PCA converted [2].

STUDIES DEMONSTRATING THE ADVANTAGES OF THE PCD OXYGEN SCAVENGER SYSTEM A study by Senavirathne *et al.* [216] demonstrated a widespread nuclease contamination in commonly used oxygen-scavenging systems. The PCD, ordered from OYCeu (catalog number 46852004) was shown to be free of nuclease contamination. The authors show drastic decrease in the photobleaching rate of Cy3, using 10 nM of PCD.

Another study by Aitken *et al.* [2] also compared the stability of fluorescent dyes in single-molecule fluorescence experiments using the GODCAT and PCD systems. They also demonstrate an increased dye stability, using 50 nM PCD and 2.5 mM PCA, compared to standardized GODCAT concentrations. Interestingly, the PCD system proceeded to a fivefold lower steady-state oxygen concentration (3.0 ± 1.5 µM).

Landry *et al.* [122] compared different oxygen scavenger systems on the lifetime of DNA tethers in optical tweezers experiments. They found the highest lifetime using the 10 nM of PCD and 100 mM PCA, exhibiting a more than 2-fold increase compared to the GODCAT system.

Enzymatic activity is commonly expressed in Units U. One unit will oxidize 1 µmole *of PCA to 3-carboxy-cis,cis-muconate per min at pH 7.5 at 37 °C.*

USED CONCENTRATION The PCD was shipped as solutions with a given enzymatic activity of 130 $\frac{U}{ml}$ and a given activity per protein mass 3.9 $\frac{U}{mg}$ in an unknown buffer. The company OYCeu did not answer questions about the buffer conditions. PCD was stored at -20°C with the addition of same amounts of glycerol (50%) in 10 µl aliquots 65 $\frac{U}{ml}$.

The molecular weight (MW) of PCD was given as 420 kDa [216], 600 kD [27] and 700 kD (Sigma[3]). With a MW of 600 kDa, the 0.2 $\frac{U}{ml}$ used in this work translate into a concentration of 90 nM.

PCA (Sigma 08992-50MG) was diluted in KET buffer (50mM KCl 1mM EDTA 100mM Tris pH8) to a concentration of 60 mM.

ACIDIFICATION Due to the production of two protons per mole of PCA converted, the scavenger system acidifies the solution. Hence, for higher concentrations of the scavenger system, NaOH needs to

3 https://www.sigmaaldrich.com/catalog/product/sigma/p8279

be added to maintain the pH without increasing the concentration of the buffer (for a PCA/PCD concentration of 10 mM and 1.3 U/mL 16.7 mM NaOH).

B.6 AZIDE OLIGO ATTACHMENT

This section describes the attachment of the short (34 bp) oligo-nucleotides (DNA-oligos) to the cystein residues, introduced at the protein termini. The principles of this assay were described before [35]. A maleimide modification on the DNA-oligos covalently binds to the cystein residues. In the present work, instead of using maleimide modified DNA-oligos, Dibenzylcyclooctyne-Maleimide (DBCO-Maleimide, Jena Bioscience, Cat. No. CLK-A108-25) molecules were used to bind to the cystein residues. DNA-oligos with an azide modification at the 3'-end (IBA GmbH) could then bind to the DBCO ("click chemistry"). A general protocol for this attachment can be found in the wiki[4].

The advantage of this attachment is that the maleimide-modified DNA-oligos contain also a fraction of oligo-dimers that in the optical tweezers assay compete with the formation of protein tethers.

A specific attachment procedure that worked well for the GR-LBD is described here and can be found in the wiki[5].

COMPONENTS

DBCO-MALEIMIDE freshly prepared or stored in 2 µl DMSO aliquots, $c = 20$ mM, extinction at 309nm =12000/M/cm, extinction at 280nm = 13000/M/cm

PROTEIN F602S 50µl c=76 µM (in 40mM HEPES, 150mM NaCl, pH7.5, 50µM DEX, 0.5% CHAPS, 1mM TCEP), extincton at 280nm = 45380/M/cm, MW=29.6 kDa

AZIDE OLIGOS 100 µM Aliquots 25 µl Aliquots -80°C

MALEIMIDE-ATTACHMENT Maleimide-DBCO was diluted to 1mM in P^- to avoid high DMSO concentration exposure of the Protein (1:20 in HEPES)

A 5-fold molar excess of Maleimide-DBCO was added to the Protein:

50 µl F602S (3.8nmol) + 20 µl diluted Maleimide-DBCO (20nmol) and was incubated for 2 h at room temperature or 6 h on ice.

PURIFICATION To get rid of excess DBCO-maleimide, centrifugal filters (Amicon Ultra 0.5 mL, Sigma) with a MWCO of 3 kDa were used. The attachment solution was diluted to 500 µl in GR-buffer

4 https://wiki.tum.de/display/biophysics/Azide+Oligos+Attachment
5 https://wiki.tum.de/display/biophysics/Thomas+GR

and centrifuged until 100 µl (10min at 17000g at 4°C) were left. This procedure was repeated 3 times, while the last time the solution was concentrated to 50 µl. Finally, the concentration was determined using the nanodrop. DBCO absorbs at 309nm with 12000/M/cm and 1.089 times more at 280nm which needed to be substracted to get the real protein concentration.

AZIDE OLIGO ATTACHMENT Now a 1.4-fold molar excess of azide oligos was added and left on a shaker at 4°C over night. E.g.: 50 µl F602S+DBCO (50 µM, 2.4 nmol) + 35 µl azide oligos (3.5 nmol).

This solution was then loaded onto a Yarra SEC 3000 HPLC column, flushing the column with 1 ml/min P_{GR}. Figure B.1 shows an HPLC chromatogram of a successful attachment reaction. The first peak corresponds to the protein with 2 oligos attached. The second peak corresponds to the protein with 1 oligo attached and the last peak is caused by oligo monomers. The different fractions were collected and the concentration of DNA measured at the nanodrop. The MW of an oligo monomer is 11 kDa, therefore the construct concentration in μM is calculated by dividing the measured value $\frac{ng}{\mu l}$ by 22. Typical construct concentrations were 0.5 µM.

The absorption of the protein is usually negligible in comparison to the DNA absorption.

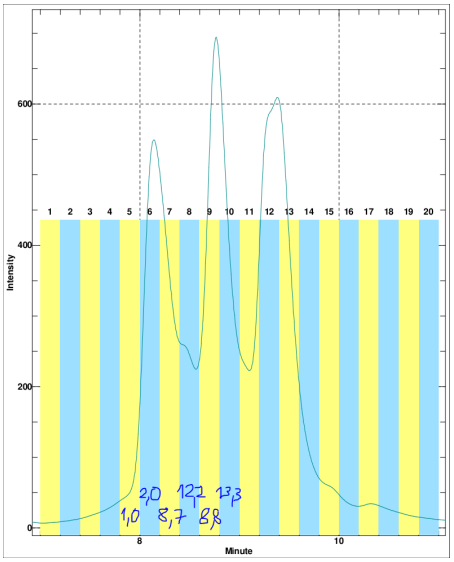

Figure B.1: Chromatogram of a successful GR-LBD-oligo attachment. It displays the absorption at 260 nm wavelength (a.u.) against the time after running through a Yarra SEC 3000 HPLC column. The green and yellow background displays different fractions. The written numbers are measurements of the DNA concentration in the different fractions in $\frac{ng}{\mu l}$. There is an offset of 23 seconds between the chromatogram and the fractions due to the tubing from the detection to the fraction collector.

The correct fraction was stored at -80°C in 3 µl aliquots. This construct is further referred to as the PO construct.

B.7 PREPARATION OF THE OPTICAL TWEEZERS ASSAY

The next part describes the procedure of assay preparation at the day of the experiment.

To measure with low residual DEX in the final solution, buffers were used without DEX for any further dilution.

B.7.1 *Handle attachment*

On the day of the measurement, the DNA handles were hybridized to the PO construct.

1. PO was thawed on ice.
2. POH: 2 µl PO (at 0.2 µM) + 0.5 µl DNA handles (490 ng/µl) (on ice for 30 min)
3. POH was diluted in 100 µl P_{GR}
4. The POH could be reused for 2-3 days, stored on ice.

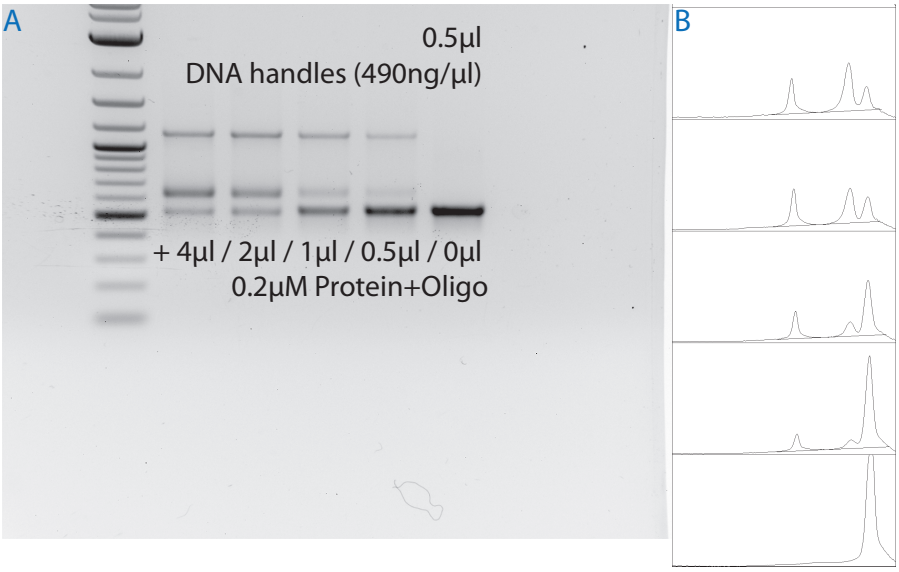

Figure B.2: (A) Agarose gel of different POH attachments. The left lane shows a 2-log DNA ladder. The other lanes show different ratios used for DNA handle attachments. The lowest band shows DNA handle monomers (550 base pairs). The middle band is the PO construct with 1 DNA handle attached. The upper band is the POH construct. (B) Analysis of the different lanes using ImageJ (upper panel displays left lane).

To evaluate the best ratio of the amount of DNA handles to the amount of PO, different ratios were tested and the result monitored using agarose gel electrophoresis. An example gel is displayed in Figure B.2A. It was analyzed using ImageJ (Figure B.2B) to determine

the best ratio of POH construct (upper band in (A) and left peak in (B)) to DNA-handle monomers.

B.7.2 *Incubation of POH with beads*

In the next step, the diluted POH was incubated with the streptavidin functionalized beads (SA) (BANG labs CS01N/11971). They have a concentration of around $2 \times 10^7 \frac{N_{beads}}{\mu l}$.

Adding too little POH results in rare tether formation. Adding too much POH results in more unspecific tethers, not exhibiting the protein fingerprint. Adding even more results in less tether formation again. With a good ratio a single protein tether for every 50-80% of the bead pairs could be achieved. The good ratio depends also on the properties of the functionalized beads.

The concentration and binding capacity of the latest bead stock can be found in the wiki[6]. The amount of DNA handles binding to a bead is determined by a protocol developed by Ulrike Majdic. Commercial streptavidin beads usually have a higher binding capacity than the self-made anti-dig (AD) beads (usually about 20000 vs. 2000 handles per bead).

1. POH': POH was diluted in P_{50} 1:10 – 1:700 (depending on the bead stock)
   2 µl POH + 100 µl P_{50})
2. SA/40: The streptavidin bead stock was diluted 1:40 in P^-
   0.5 µl SA + 20 µl P^-
3. S: 15 µl POH' + 5 µl SA/40 (mixed gently, incubated on ice for 20 min)
4. AD/100: The anti-dig functionalized bead stock was diluted 1:100 in P^-
   0.5 µl AD + 50 µl P^-

B.7.3 *Final solution*

In the final solution all necessary components were added to 100 µl P^- and mixed gently.

For a measurement at 200 µM DEX, the following final solution was used:

- F: 95 µl P^- + 0.5 µl DEX (40 µM) + 1.7 µl PCA (60 mM) + 1 µl AD/100 + 1 µl DTT (100 mM) + 0.3 µl PCD (65 $\frac{U}{ml}$)

The sample chambers were made by two 170 µm-thick coverslips (Carl Roth), attached with Parafilm (Bemis Company). The surface

6 https://wiki.tum.de/display/biophysics/Beads

was passivated by incubation for 5 min with 10 mg/ml BSA (Sigma-Aldrich) to prevent beads from sticking to the surface. The chambers were flushed with 100 µl P^- before addition of the final solution F and sealing with vacuum grease.

Note that the PO ($\approx$ 0.5 µM) was finally diluted by a factor of 5×10^4 in the final solution, resulting in a protein concentration in the final solution below 10 pM. The residual DEX concentration $c(DEX) <$ 1 nM, if DEX was omitted in the buffers for dilution.

C

SUPPLEMENTAL FIGURES

This chapter is a collection of supplemental figures to further illustrate details of certain analysis methods described in the main part.

C.1 DWELL-TIME DISTRIBUTIONS AFTER HMM STATE ASSIGNMENT

In this work, a HMM analysis was used to assign raw data points to discrete folding states (as described in Section 3.4 and [229]).

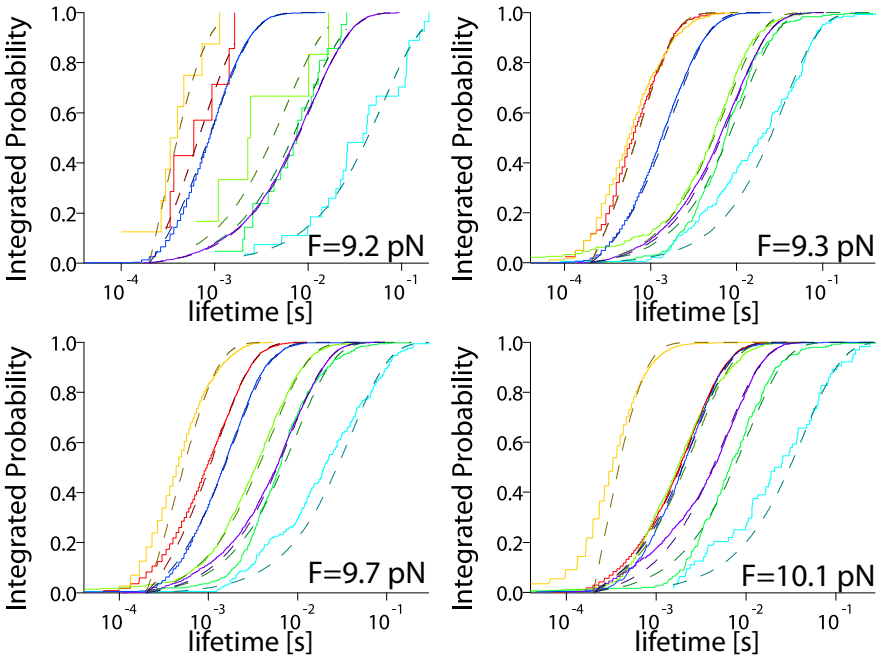

Figure C.1: Integrated lifetime histograms of the seven states *closed* (purple), *open* (blue), *open-ub* (cyan), *IM1* (green), *IM2* (lime), *IM3* (yellow) and *unf* (red) at 4 different force biases taken from the traces shown in Figure 5.4. The dashed lines are single-exponential fits. The *open-ub* state repeatedly shows some slight deviations from the single-exponential behavior indicating it could be convoluted with a different short lived state with similar contour length.

The number of states and their initial emission probabilities were determined by fitting gaussians to the force histogram of the evaluated trace. A minimal number of states was chosen accounting for all peaks in the force histogram and resulting in a single-exponential lifetime distribution. The transition probability matrix was adjusted manually to result in an optimal single-exponential lifetime distribu-

tions and kept constant for different molecules at similar trap distance. A single-exponential distribution is a hallmark of lifetimes with an underlying Poisson process and also serves as further evidence for correct state assignments.

Figure C.1 shows an example of such lifetime distributions at 4 different force biases. Only the *open-ub* state partially showed some slight deviations from the single-exponential behavior indicating it might be convoluted with a different short lived state with similar contour length. The lifetime of that state is negligible compared to the *open-ub* state. Thus this minor misclassification does not have an influence neither on the calculation of the *open-ub* state energy, nor on the hormone binding rate. It might be an indication for an off-pathway misfolded structure that becomes more relevant at zero-force as discussed in Section 5.6.

C.2 STATE ASSIGNMENT DURING FORCE-JUMP EXPERIMENTS

A force jump assay was employed to monitor refolding at forces close to zero as described in Section 5.5.

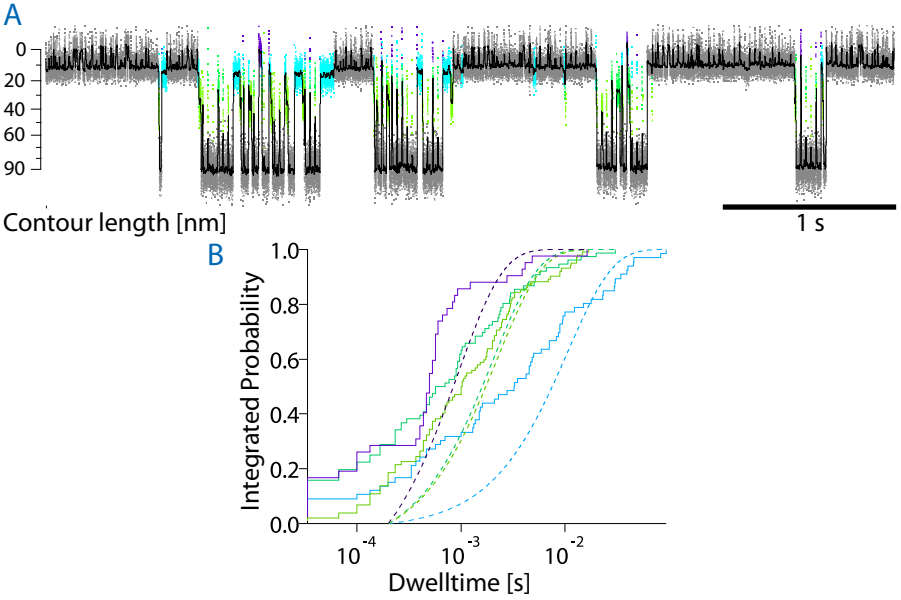

Figure C.2: (A) Merged high-force phases of contour length vs. time traces, obtained in force-jump experiments as shown in Figure 5.9 (F_{ref} = 0.3 pN during the low force phase and Force bias F = 11.7 pN during the high force phase). The colored parts are intermediate states assigned by an HMM analysis using the same model as for the passive-mode traces (Figure 5.3). (B) Integrated lifetime histogram of the colored parts shown in (A). Dashed lines show exponential fits. The lifetimes are not single-exponential distribution.

Figure C.2A displays a merge of the high force phases of such an experiment that reports on the extent of refolding during the low force phases. Similarly to the passive-mode experiments, the merged high force traces can be analyzed with the HMM algorithm as described in Section 3.4 to classify the states present in the high force phase as described in Section 3.5. As unfolding of the native state does not occur in the low force phase, its dwell-times can be treated as in passive-mode traces because of the memoryless property of the underlying Poisson process.

The intermediate states as found in Section 5.1 could not be identified in these experiments, even though their lifetimes would have been within the limits of the experimental setup. The partially folded structures occurring after the jumps to low force exhibited a broad range of contour lengths and an attempt to classify them into the intermediate states as before led to non-single-exponential lifetime distributions (as shown in Section C.2).

The attempt to classify refolding intermediates failed due to heterogeneity of states. The intermediates show an undefined variety of contour lengths, some even as short as the *closed* state. Also the distribution of lifetimes is not single-exponential. This is most likely due to mixing of on-pathway intermediate states with a variety of misfolded states as discussed in Section 5.5.

C.3 IMPACT OF MISFOLDING ON FOLDING RATE

Knowledge of the folding energy landscape and the kinetic folding network discussed in Section 5.3, allows the calculation of the overall time it takes for the protein to fold from the *unf* state to the *open-ub* state at different force biases.

The time evolution of the state population probabilities, starting from the *unf* state, was numerically computed using the transition rates between the intermediates as shown in Figure 5.5. The details of the procedure for the computation of this evolution are specified in Section 3.6. From the probability that folding had proceeded from the *unf* to the *open-ub* state after a certain time, the overall folding rate $k^{overall}_{unf \curvearrowright open\text{-}ub}$ was derived as described in Section 3.6.1. Note that $k^{overall}_{unf \curvearrowright open\text{-}ub}$ reflects the rate at which the *open-ub* state is reached for the first time. It does not account for unfolding transitions from *open-ub*.

A similar calculation was done that included the possibility of an off-pathway misfolded state (details described in Section 3.6.2) branching off the *IM1* state as depicted in Figure 5.12.

Figure C.3 shows a comparison of the force-dependent overall folding rate $k^{overall}_{unf \curvearrowright open\text{-}ub}$ of the GR-LBD. It illustrates the effect of misfolding on $k^{overall}_{unf \curvearrowright open\text{-}ub}$, which is decreased by 3 orders of magnitude at

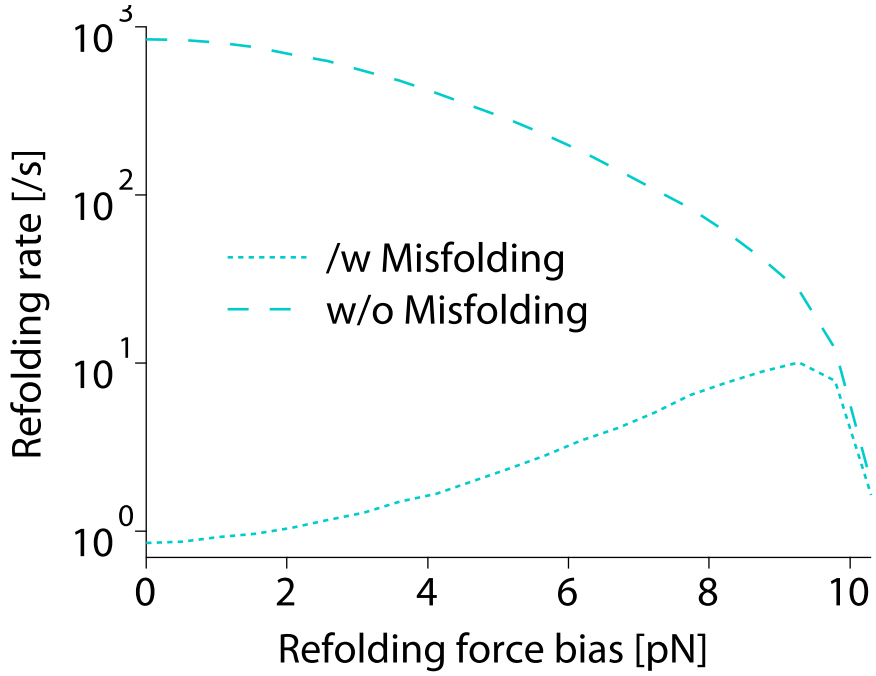

Figure C.3: Comparison of the numerically calculated, force-dependent $k^{overall}_{unf \curvearrowright open\text{-}ub}$ with (dashed) and without (dotted) misfolding.

zero-force. It also demonstrates the effect of misfolding already at 6 pN, decreasing the $k^{overall}_{unf \curvearrowright open\text{-}ub}$ by 2 orders of magnitude.

Note, there is a slight difference between $k^{overall}_{unf \curvearrowright open\text{-}ub}$ and the folding-&-binding rate k_{FB} at zero-force, even though the binding of DEX is not the limiting step ($k_{bind} = 7/s$). This is due to the measurement of k_{FB}, using the outcome after a waiting time of 200 ms. As this time is in the same order of magnitude of the time it takes for a hormone to bind, k_{FB} slightly deviates. This effect is considered in the model analysis of k_{FB}.

C.4 ATTRIBUTING IMPAIRED FOLDING TO IMPAIRED BINDING

The decrease of the folding-&-binding rate k_{FB} at zero-force was discussed in Section 5.5. This decrease was modeled by an off-pathway misfolded state branching off the *IM1* state. Could the reduction of k_{FB} be an effect of a reduced DEX binding rate rather than misfolding at low forces?

If the deviation from the on-pathway folding model were to occur after folding into the *open-ub* state, then the folding would have proceeded significantly faster than measured in the force-jump experiments 8Figure C.2A), as demonstrated in the following.

The population probability evolution of the intermediate states starting from the *unf* state at zero-force can be used to check the expected extent of refolding after a certain waiting time.

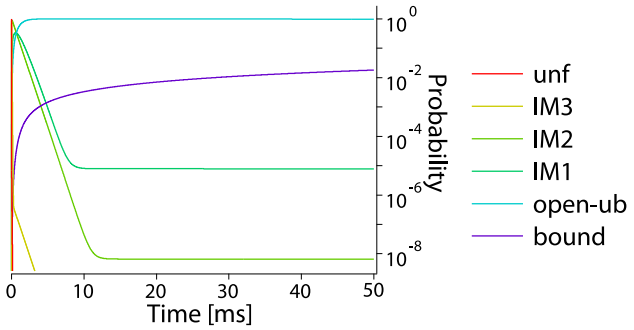

Figure C.4: Evolution of state populations at 0 pN, starting from $P_{unf}(t = 0) = 1$ (as in Figure 5.7B). All data was calculated numerically by using the transition rates between the intermediate states as measured in passive-mode experiments (Section 5.3).

Figure C.4 shows the state population probability evolution at zero-force, starting from the *unf* state assuming folding without misfolding (based on the kinetic folding network as discussed in Section 5.3 and computed as described in Section 3.6). After 10 ms the probability for detecting any folding intermediate earlier on the folding pathway would be less than 1×10^{-5}. The force-jump traces (as displayed in Figure C.2A) exhibit that even 200 ms after the jumps to zero-force, in about 50% of the cases the protein was in a structure, less folded – i.e. exhibiting longer protein contour lengths – than the *open-ub* state.

Could the *open-ub* state be overlooked in these traces due to limited time resolution? At the Force bias of $F = 11.7$ pN used during the high force phase of the force-jump experiments, the *open-ub* state experiences a force of $F_{open\text{-}ub} = 11$ pN. At these forces, the *open-ub* state unfolds with a rate of $k_{ubf \to IM1} \lesssim 100$ /s. Hence, its average lifetime is roughly 30 times longer than the time resolution in the force-jump experiments (300 µs, given by the hydrodynamics of the beads, as discussed in Section 3.5).

This serves as further evidence that misfolding must occur earlier on the folding pathway.

The actual probability of 50% of the putative *open-ub* state after 200 ms at 0 pN correlates with an $k^{overall}_{unf \curvearrowright open\text{-}ub} = 3$ /s. These rate is in good agreement with the $k^{overall}_{unf \curvearrowright open\text{-}ub}(0\,\text{pN}) = 0.8$ /s (Figure C.3), based on the model for misfolding branching off the *IM1* state (as discussed in Section 5.6).

Assuming that another 50% of these states were actually misclassified misfolded states, results in $k^{overall}_{unf \curvearrowright \text{open-ub}} =$ 1.6 /s, which agrees even better.

C.5 DIFFERENT MISFOLDING MODELS FOR THE FORCE DEPENDENT k_{FB}

In Section 5.5, a decrease in the overall folding-&-binding rate k_{FB} was measured. To model the force dependence of k_{FB}, this rate was numerically calculated from the kinetic folding network (as discussed in

Section 5.3), including the possibility of misfolding (details described in Section 3.6.2).

For simplicity, this model uses just a single misfolded state originating from one of the on-pathway intermediates. To this end, an additional state was introduced into the kinetic folding network describing an off-pathway misfolded structure with an additional length contraction ΔL_{mf} and free energy ΔG^0_{mf} branching off from one of the on-pathway states *unf*, *IM3*, *IM2*, or *IM1* (as depicted in Figure 5.3). The exchange between the on-pathway and the misfolded state were modeled to be equilibrated.

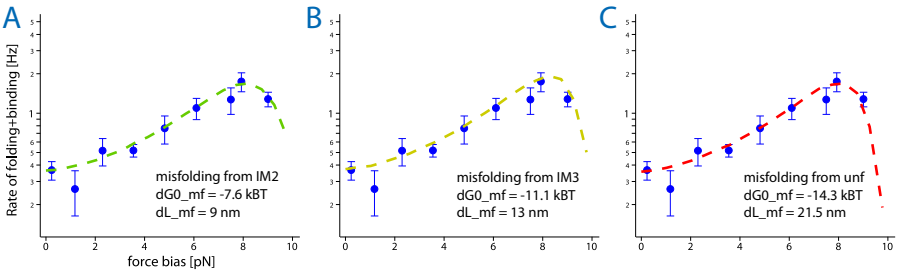

Figure C.5: Force dependence of the overall folding-&-binding rates k_{FB} (blue circles), fitted (dashed lines), based on different models for misfolding branching off the (A) *IM2*, (B) *IM2* or (C) *unf* state.

For each scenario, the kinetic equations of the folding network were solved numerically, calculating k_{FB} for different forces. Figure C.5A-C shows the results based on the different models. With each of the models, the force dependence of k_{FB} shown in Figure 5.10 could be reproduced, albeit with different parameters for ΔL_{mf} and ΔG^0_{mf}.

C.6 INDUCED UNFOLDING AT LOWER HSP70 CONCENTRATIONS

In Section 6.2.1, the unfolding of GR-LBD, induced by Hsp70 (*H7unfolding*), was demonstrated in the presence of 180 µM DEX, 600 nM Hsp40, 2 µM Hsp70 and ATP. After the *H7unfolding*, the GR-LBD remained in the unfolded conformation, even at zero-force (*H7blocked* state).

Also lower concentrations of Hsp70 were tested qualitatively. A constant concentration of 2 µM Hsp40 was used.

At 500 nM 3 of 5 molecules exhibited complete *H7unfolding* and 1 of 3 exhibited some *H7blocked* traces. At 100 nM, 1 of 2 molecules exhibited slow *H7unfolding* (as demonstrated in Figure C.6) and 1 of 2 molecules exhibited at least a few *H7blocked* traces.

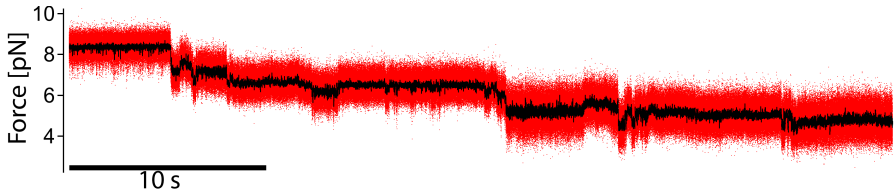

Figure C.6: Force vs. time trace of a passive-mode experiment, applying a force bias of around 8.5 pN in presence of 20 µM DEX, 2 µM Hsp40, 100 nM Hsp70 and ATP. During the first 5 s, the native *open-closed* fluctuations were observed. The contour length at the end of the trace correlates with the *unf* state of GR-LBD, measured through a subsequent stretch and relax cycle (data not shown).

BIBLIOGRAPHY

[1] Dostert A. and Heinzel T. «Negative Glucocorticoid Receptor Response Elements and their Role in Glucocorticoid Action.» In: *Current Pharmaceutical Design* 10.23 (Sept. 2004), pp. 2807–2816. ISSN: 13816128. DOI: 10.2174/1381612043383601. URL: http://www.eurekaselect.com/openurl/content.php?genre=article%7B%5C&%7Dissn=1381-6128%7B%5C&%7Dvolume=10%7B%5C&%7Dissue=23%7B%5C&%7Dspage=2807 (cit. on p. 8).

[2] Colin Echeverría Aitken *et al.* «An Oxygen Scavenging System for Improvement of Dye Stability in Single-Molecule Fluorescence Experiments.» In: *Biophysical Journal* 94.5 (2008), pp. 1826–1835. ISSN: 00063495. DOI: 10.1529/biophysj.107.117689. URL: http://linkinghub.elsevier.com/retrieve/pii/S0006349508706210 (cit. on p. 166).

[3] Maruf M U Ali *et al.* «Crystal structure of an Hsp90–nucleotide–p23/Sba1 closed chaperone complex.» In: *Nature* 440.7087 (Apr. 2006), pp. 1013–1017. ISSN: 0028-0836. DOI: 10.1038/nature04716. URL: http://www.nature.com/articles/nature04716 (cit. on p. 14).

[4] Emad S Alnemri *et al.* «Characterization and purification of a functional rat glucocorticoid receptor overexpressed in a baculovirus system.» In: *The Journal of biological chemistry* 266.6 (Feb. 1991), pp. 3925–36. ISSN: 0021-9258. URL: http://www.ncbi.nlm.nih.gov/pubmed/1995640 (cit. on pp. 13, 150).

[5] Sara Alvira *et al.* «Structural characterization of the substrate transfer mechanism in Hsp70/Hsp90 folding machinery mediated by Hop.» In: *Nature communications* 5 (2014), p. 5484. ISSN: 2041-1723. DOI: 10.1038/ncomms6484. URL: http://www.ncbi.nlm.nih.gov/pubmed/25407331 (cit. on p. 16).

[6] Svante Arrhenius. «Über die Reaktionsgeschwindigkeit bei der Inversion von Rohrzucker durch Säuren.» In: *Zeitschrift für Physikalische Chemie* 4U.1 (Jan. 1889). ISSN: 2196-7156. DOI: 10.1515/zpch-1889-0416. URL: http://www.degruyter.com/view/j/zpch.1889.4.issue-1/zpch-1889-0416/zpch-1889-0416.xml (cit. on p. 41).

[7] A. Ashkin. «Acceleration and Trapping of Particles by Radiation Pressure.» In: *Physical Review Letters* 24.4 (1970), pp. 156–159. ISSN: 00319007. DOI: 10.1103/PhysRevLett.24.156 (cit. on p. 22).

[8] A. Ashkin. «Forces of a single-beam gradient laser trap on a dielectric sphere in the ray optics regime.» In: *Biophysical Journal* 61.2 (1992), pp. 569–582. ISSN: 00063495. DOI: 10.1016/S0006-3495(92)81860-X. URL: http://dx.doi.org/10.1016/S0006-3495(92)81860-X (cit. on p. 22).

[9] A. Ashkin *et al.* «Observation of a single-beam gradient force optical trap for dielectric particles.» In: *Optics Letters* 11.5 (1986), p. 288. ISSN: 0146-9592. DOI: 10.1364/OL.11.000288. arXiv: 1411.1912. URL: https://www.osapublishing.org/abstract.cfm?URI=ol-11-5-288 (cit. on p. 22).

[10] A. Ashkin *et al.* «Optical trapping and manipulation of single cells using infrared laser beams.» In: *Nature* 330.6150 (Dec. 1987), pp. 769–771. ISSN: 0028-0836. DOI: 10.1038/330769a0. URL: http://www.nature.com/doifinder/10.1038/330769a0 (cit. on p. 22).

[11] A Ashkin and J. Dziedzic. «Optical trapping and manipulation of viruses and bacteria.» In: *Science* 235.4795 (1987), pp. 1517–1520. ISSN: 0036-8075. DOI: 10.1126/science.3547653. URL: http://www.sciencemag.org/cgi/doi/10.1126/science.3547653 (cit. on p. 22).

[12] Victoria A. Assimon *et al.* «Specific Binding of Tetratricopeptide Repeat Proteins to Heat Shock Protein 70 (Hsp70) and Heat Shock Protein 90 (Hsp90) Is Regulated by Affinity and Phosphorylation.» In: *Biochemistry* 54.48 (2015), pp. 7120–7131. ISSN: 15204995. DOI: 10.1021/acs.biochem.5b00801. arXiv: 15334406 (cit. on p. 104).

[13] M. Atakhorrami *et al.* «Twin optical traps for two-particle cross-correlation measurements: Eliminating cross-talk.» In: *Review of Scientific Instruments* 79.4 (Apr. 2008), p. 043103. ISSN: 0034-6748. DOI: 10.1063/1.2898407. URL: http://aip.scitation.org/doi/10.1063/1.2898407 (cit. on p. 24).

[14] Emira Ayroldi *et al.* «Mechanisms of the anti-inflammatory effects of glucocorticoids: genomic and nongenomic interference with MAPK signaling pathways.» In: *The FASEB Journal* 26.12 (Dec. 2012), pp. 4805–4820. ISSN: 0892-6638. DOI: 10.1096/fj.12-216382. URL: http://www.fasebj.org/doi/10.1096/fj.12-216382 (cit. on p. 8).

[15] David L. Bain *et al.* «Nuclear Receptor Structure: Implications for Function.» In: *Annual Review of Physiology* 69.1 (2007), pp. 201–220. ISSN: 0066-4278. DOI: 10.1146/annurev.physiol.69.031905.160308. URL: http://www.annualreviews.org/doi/10.1146/annurev.physiol.69.031905.160308 (cit. on pp. 10, 101).

[16] David Balchin *et al.* «In vivo aspects of protein folding and quality control.» In: *Science* 353.6294 (2016). ISSN: 10959203. DOI: 10.1126/science.aac4354 (cit. on p. 5).

[17] R L Baldwin. «On-pathway versus off-pathway folding intermediates.» In: *Folding & design* 1.1 (1996), R1–R8. ISSN: 13590278. DOI: 10.1016/S1359-0278(96)00003-X (cit. on pp. 50, 96).

[18] CHRISTOPH M. BAMBERGER *et al.* «Molecular Determinants of Glucocorticoid Receptor Function and Tissue Sensitivity to Glucocorticoids.» In: 17.3 (2013), pp. 245–261. URL: http://press.endocrine.org/doi/abs/10.1210/edrv-17-3-245 (cit. on p. 7).

[19] P J Barnes. «Therapeutic strategies for allergic diseases.» In: *Nature* 402.6760 Suppl (Nov. 1999), B31–8. ISSN: 0028-0836. URL: http://www.ncbi.nlm.nih.gov/pubmed/10586893 (cit. on p. 6).

[20] Daniela Bauer *et al.* «Nucleotides regulate the mechanical hierarchy between subdomains of the nucleotide binding domain of the Hsp70 chaperone DnaK.» In: *Proceedings of the National Academy of Sciences* 112.33 (2015), pp. 10389–10394. ISSN: 0027-8424. DOI: 10.1073/pnas.1504625112. URL: http://www.pnas.org/lookup/doi/10.1073/pnas.1504625112 (cit. on p. 72).

[21] G. Bell. «Models for the specific adhesion of cells to cells.» In: *Science* 200.4342 (1978), pp. 618–627. ISSN: 0036-8075. DOI: 10.1126/science.347575. arXiv: arXiv:1011.1669v3. URL: http://www.sciencemag.org/cgi/doi/10.1126/science.347575 (cit. on p. 96).

[22] Simon C. Biddie *et al.* «Dynamic regulation of glucocorticoid signalling in health and disease.» In: *Rheumatology* 51.3 (2012), pp. 403–412. ISSN: 14620324. DOI: 10.1093/rheumatology/ker215. arXiv: NIHMS150003 (cit. on p. 6).

[23] Randy K. Bledsoe *et al.* «Structure and Function of the Glucocorticoid Receptor Ligand Binding Domain.» In: *Vitamins and Hormones* 68 (2004), pp. 49–91. ISSN: 00836729. DOI: 10.1016/S0083-6729(04)68002-2 (cit. on pp. 4, 6, 8–13, 68, 69, 75, 100, 101, 129, 151, 160).

[24] Randy K Bledsoe *et al.* «Crystal structure of the glucocorticoid receptor ligand binding domain reveals a novel mode of receptor dimerization and coactivator recognition.» In: *Cell* 110.1 (July 2002), pp. 93–105. ISSN: 0092-8674. DOI: 10.1016/S0092-8674(02)00817-6. URL: http://www.ncbi.nlm.nih.gov/pubmed/12151000 (cit. on pp. 9–11, 13, 68, 69, 78, 79, 124, 165).

[25] William Bourguet *et al.* «Nuclear receptor ligand-binding domains: three-dimensional structures, molecular interactions and pharmacological implications.» In: *Trends in Pharmacological Sciences* 21.10 (Oct. 2000), pp. 381–388. ISSN: 01656147. DOI: 10.1016/S0165-6147(00)01548-0. URL: http://linkinghub.elsevier.com/retrieve/pii/S0165614700015480 (cit. on p. 9).

[26] Emery H Bresnick *et al.* «Evidence That the 90-kDa Heat Shock Protein Is Necessary for the Steroid Binding Conformation of the L Cell Glucocorticoid Receptor *.» In: 264.9 (1989), pp. 4992–4997 (cit. on p. 16).

[27] C. Kent Brown *et al.* «Biophysical Analyses of Designed and Selected Mutants of Protocatechuate 3,4-Dioxygenase.» In: *Annual Review of Microbiology* 58.1 (Oct. 2004), pp. 555–585. ISSN: 0066-4227. DOI: 10.1146/annurev.micro.57.030502.090927. URL: http://www.annualreviews.org/doi/10.1146/annurev.micro.57.030502.090927 (cit. on p. 166).

[28] Melanie Brunnbauer *et al.* «Regulation of a heterodimeric kinesin-2 through an unprocessive motor domain that is turned processive by its partner.» In: *Proceedings of the National Academy of Sciences of the United States of America* 107.23 (2010), pp. 10460–10465. ISSN: 0027-8424. DOI: 10.1073/pnas.1005177107 (cit. on p. 22).

[29] Joseph D. Bryngelson *et al.* «Funnels, pathways, and the energy landscape of protein folding: A synthesis.» In: *Proteins: Structure, Function, and Bioinformatics* 21.3 (1995), pp. 167–195. ISSN: 10970134. DOI: 10.1002/prot.340210302. arXiv: 9411008 [chem-ph] (cit. on pp. 40, 41).

[30] Johannes Buchner and Jing Li. «Structure, Function and Regulation of the Hsp90 Machinery.» In: *Biomedical Journal* 36.3 (2013), p. 106. ISSN: 2319-4170. DOI: 10.4103/2319-4170.113230. URL: http://biomedj.cgu.edu.tw/pdfs/2013/36/3/images/BiomedJ%7B%5C_%7D2013%7B%5C_%7D36%7B%5C_%7D3%7B%5C_%7D106%7B%5C_%7D113230.pdf (cit. on p. 16).

[31] Bernd Bukau *et al.* «Molecular Chaperones and Protein Quality Control.» In: *Cell* 125.3 (2006), pp. 443–451. ISSN: 00928674. DOI: 10.1016/j.cell.2006.04.014. URL: http://dx.doi.org/10.1016/j.cell.2006.04.014 (cit. on p. 5).

[32] John M. Busillo and John A. Cidlowski. «The five Rs of glucocorticoid action during inflammation: ready, reinforce, repress, resolve, and restore.» In: *Trends in Endocrinology & Metabolism* 24.3 (Mar. 2013), pp. 109–119. ISSN: 10432760. DOI: 10.1016/j.tem.2012.11.005. URL: http://linkinghub.elsevier.com/retrieve/pii/S1043276012002159 (cit. on p. 8).

[33] C A Caamaño *et al.* «The functional relevance of the heteromeric structure of corticosteroid receptors.» In: *Annals of the New York Academy of Sciences* 746 (Nov. 1994), 68–77, discussion 77–8, 131–3. ISSN: 0077-8923. URL: http://www.ncbi.nlm.nih.gov/pubmed/7825922 (cit. on pp. 13, 150).

[34] Giovanni Cappello *et al.* «Myosin V stepping mechanism.» In: *Proceedings of the National Academy of Sciences of the United States of America* 104.39 (2007), pp. 15328–15333. ISSN: 0027-8424. DOI: 10.1073/pnas.0706653104 (cit. on pp. 22, 79).

[35] Ciro Cecconi *et al.* «Protein-DNA chimeras for single molecule mechanical folding studies with the optical tweezers.» In: *European Biophysics Journal* 37.6 (2008), pp. 729–738. DOI: 10.1007/s00249-007-0247-y.Protein-DNA (cit. on pp. 24, 167).

[36] G. Cecconi *et al.* «Direct Observation of the Three-State Folding of a Single Protein Molecule.» In: *Science* 309.5743 (Sept. 2005), pp. 2057–2060. ISSN: 0036-8075. DOI: 10.1126/science.1116702. URL: http://www.sciencemag.org/cgi/doi/10.1126/science.1116702 (cit. on p. 22).

[37] P. K. Chakraborti *et al.* «Creation of "super" glucocorticoid receptors by point mutations in the steroid binding domain.» In: *Journal of Biological Chemistry* 266.33 (1991), pp. 22075–22078. ISSN: 00219258 (cit. on p. 75).

[38] Shiying Chen and David F. Smith. «Hop as an adaptor in the heat shock protein 70 (Hsp70) and Hsp90 chaperone machinery.» In: *Journal of Biological Chemistry* 273.52 (Dec. 1998), pp. 35194–35200. ISSN: 00219258. DOI: 10.1074/jbc.273.52.35194. URL: http://www.jbc.org/lookup/doi/10.1074/jbc.273.52.35194 (cit. on pp. 16, 103, 106).

[39] Joyce Cheung and David F Smith. «Molecular Chaperone Interactions with Steroid Receptors: an Update.» In: *Molecular Endocrinology* 14.7 (July 2000), pp. 939–946. ISSN: 0888-8809. DOI: 10.1210/mend.14.7.0489. URL: https://academic.oup.com/mend/article-lookup/doi/10.1210/mend.14.7.0489 (cit. on pp. 7, 16, 100, 103, 107).

[40] Sabine Chourbaji and Peter Gass. «Glucocorticoid receptor transgenic mice as models for depression.» In: *Brain Research Reviews* 57.2 (2008), pp. 554–560. ISSN: 01650173. DOI: 10.1016/j.brainresrev.2007.04.008 (cit. on p. 6).

[41] T. N. Collingwood *et al.* «Nuclear receptors: Coactivators, corepressors and chromatin remodeling in the control of transcription.» In: *Journal of Molecular Endocrinology* 23.3 (1999), pp. 255–275. ISSN: 09525041. DOI: 10.1677/jme.0.0230255 (cit. on p. 8).

[42] Péter Csermely *et al.* «The 90-kDa Molecular Chaperone Family: Structure, Function, and Clinical Applications. A Comprehensive Review.» In: *Pharmacology & Therapeutics* 79.2 (1998), pp. 129–168. ISSN: 01637258. DOI: 10.1016/S0163-7258(98)00013-8 (cit. on p. 5).

[43] K Dahlman-Wright *et al.* «Structural characterization of a minimal functional transactivation domain from the human glucocorticoid receptor.» In: *Proceedings of the National Academy of Sciences of the United States of America* 92.5 (1995), pp. 1699–703. ISSN: 0027-8424. DOI: 10.1073/pnas.92.5.1699. URL: http://www.pubmedcentral.nih.gov/articlerender.fcgi?artid=42587%7B%5C&%7Dtool=pmcentrez%7B%5C&%7Drendertype=abstract (cit. on p. 5).

[44] F C Dalman *et al.* «Localization of the 90-kDa heat shock protein-binding site within the hormone-binding domain of the glucocorticoid receptor by peptide competition.» In: *The Journal of biological chemistry* 266.6 (Feb. 1991), pp. 3482–90. ISSN: 0021-9258. DOI: 1995612. URL: http://www.ncbi.nlm.nih.gov/pubmed/1995612 (cit. on pp. 12, 129).

[45] Beatrice D Darimont *et al.* «Structure and specificity of nuclear receptor-coactivator interactions.» In: *Genes & development* 12.21 (Nov. 1998), pp. 3343–56. ISSN: 0890-9369. URL: http://www.ncbi.nlm.nih.gov/pubmed/9808622%20http://www.pubmedcentral.nih.gov/articlerender.fcgi?artid=PMC317236 (cit. on p. 11).

[46] Karolien De Bosscher and Guy Haegeman. «Minireview: Latest Perspectives on Antiinflammatory Actions of Glucocorticoids.» In: *Molecular Endocrinology* 23.3 (2009), pp. 281–291. ISSN: 0888-8809. DOI: 10.1210/me.2008-0283. URL: https://academic.oup.com/mend/article-lookup/doi/10.1210/me.2008-0283 (cit. on p. 8).

[47] Paolo De Los Rios and Alessandro Barducci. «Hsp70 chaperones are non-equilibrium machines that achieve ultra-affinity by energy consumption.» In: *eLife* 2014.3 (2014), pp. 1–10. ISSN: 2050084X. DOI: 10.7554/eLife.02218.001 (cit. on p. 126).

[48] Marc Denis *et al. Requirement of hormone for thermal conversion of the glucocorticoid receptor to a DNA-binding state*. 1988. DOI: 10.1038/333686a0 (cit. on p. 8).

[49] A. A Deniz *et al.* «Single-molecule biophysics: at the interface of biology, physics and chemistry.» In: *Journal of The Royal Society Interface* 5.18 (2008), pp. 15–45. ISSN: 1742-5689. DOI: 10.1098/rsif.2007.1021. URL: http://rsif.royalsocietypublishing.org/cgi/doi/10.1098/rsif.2007.1021 (cit. on p. 21).

[50] Hendrik Dietz and Matthias Rief. «Protein structure by mechanical triangulation.» In: *Proceedings of the National Academy of Sciences of the United States of America* 103.5 (Jan. 2006), pp. 1244–7. ISSN: 0027-8424. DOI: 10.1073/pnas.0509217103. URL: http://www.pubmedcentral.nih.gov/articlerender.fcgi?artid=1360557%7B%5C&%7Dtool=pmcentrez%7B%5C&%7Drendertype=abstract (cit. on pp. 40, 72).

[51] Ken A Dill and Justin L MacCallum. «The Protein-Folding Problem, 50 Years On.» In: *Science* 338.6110 (Nov. 2012), pp. 1042–1046. ISSN: 0036-8075. DOI: 10.1126/science.1219021. URL: http://www.ncbi.nlm.nih.gov/pubmed/23180855%20http://www.sciencemag.org/cgi/doi/10.1126/science.1219021 (cit. on pp. 3, 40).

[52] K. D. Dittmar. «The Role of DnaJ-like Proteins in Glucocorticoid Receptor hsp90 Heterocomplex Assembly by the Reconstituted hsp90 p60 hsp70 Foldosome Complex.» In: *Journal of Biological Chemistry* 273.13 (1998), pp. 7358–7366. ISSN: 00219258. DOI: 10.1074/jbc.273.13.7358. URL: http://www.jbc.org/cgi/doi/10.1074/jbc.273.13.7358 (cit. on pp. 103, 160).

[53] Kurt D. Dittmar *et al.* «Folding of the Glucocorticoid Receptor by the Heat Shock Protein (hsp) 90-based Chaperone Machinery.» In: *Journal of Biological Chemistry* 272.34 (Aug. 1997), pp. 21213–21220. ISSN: 0021-9258. DOI: 10.1074/jbc.272.34.21213. URL: http://www.jbc.org/cgi/doi/10.1074/jbc.272.34.21213%20http://www.jbc.org/lookup/doi/10.1074/jbc.272.34.21213 (cit. on p. 103).

[54] D Eric Dollins *et al.* «Structures of GRP94-Nucleotide Complexes Reveal Mechanistic Differences between the hsp90 Chaperones.» In: *Molecular Cell* 28.1 (Oct. 2007), pp. 41–56. ISSN: 10972765. DOI: 10.1016/j.molcel.2007.08.024. URL: http://linkinghub.elsevier.com/retrieve/pii/S1097276507005941 (cit. on p. 14).

[55] Diane D. Dong *et al.* «Functional analysis of the LXXLL motifs of the human glucocorticoid receptor: Association with altered ligand affinity.» In: *Journal of Steroid Biochemistry and Molecular Biology* 101.2-3 (2006), pp. 106–117. ISSN: 09600760. DOI: 10.1016/j.jsbmb.2006.06.010 (cit. on p. 78).

[56] Petras Dzeja and Andre Terzic. «Adenylate Kinase and AMP Signaling Networks: Metabolic Monitoring, Signal Communication and Body Energy Sensing.» In: *International Journal of Molecular Sciences* 10.4 (Apr. 2009), pp. 1729–1772. ISSN: 1422-0067. DOI: 10.3390/ijms10041729. URL: http://www.mdpi.com/1422-0067/10/4/1729 (cit. on p. 4).

[57] Pablo C. Echeverria and D. Picard Didier. «Molecular chaperones, essential partners of steroid hormone receptors for activity and mobility.» In: *Biochimica et Biophysica Acta - Molecular Cell Research* 1803.6 (2010), pp. 641–649. ISSN: 01674889. DOI: 10.1016/j.bbamcr.2009.11.012. URL: http://dx.doi.org/10.1016/j.bbamcr.2009.11.012 (cit. on p. 16).

[58] Pablo C. Echeverría *et al.* «An Interaction Network Predicted from Public Data as a Discovery Tool: Application to the Hsp90 Molecular Chaperone Machine.» In: *PLoS ONE* 6.10 (Oct. 2011). Ed. by Sue Cotterill, e26044. ISSN: 1932-6203. DOI: 10.1371/journal.pone.0026044. URL: http://dx.plos.org/10.1371/journal.pone.0026044 (cit. on p. 14).

[59] Cem Elbi *et al.* «Molecular chaperones function as steroid receptor nuclear mobility factors.» In: *Proceedings of the National Academy of Sciences of the United States of America* 101.9 (2004), pp. 2876–2881. ISSN: 0027-8424. DOI: 10.1073/pnas.0400116101 (cit. on pp. 8, 107).

[60] S. Walter Englander and Leland Mayne. «The nature of protein folding pathways.» In: *Proceedings of the National Academy of Sciences* 111.45 (2014), pp. 15873–15880. ISSN: 0027-8424. DOI: 10.1073/pnas.1411798111. URL: http://www.pnas.org/lookup/doi/10.1073/pnas.1411798111 (cit. on p. 40).

[61] L Fang *et al.* «Unliganded and hormone-bound glucocorticoid receptors interact with distinct hydrophobic sites in the Hsp90 C-terminal domain.» In: *Proceedings of the National Academy of Sciences* 103.49 (Dec. 2006), pp. 18487–18492. ISSN: 0027-8424. DOI: 10.1073/pnas.0609163103. URL: http://www.pnas.org/cgi/doi/10.1073/pnas.0609163103 (cit. on p. 131).

[62] Sara J. Felts and David O. Toft. «p23, a simple protein with complex activities.» In: *Cell Stress & Chaperones* 8.2 (2003), p. 108. ISSN: 1355-8145. DOI: 10.1379/1466-1268(2003)008<0108:PASPWC>2.0.CO;2. URL: http://cest.allenpress.com/perlserv/?request=get-abstract%7B%5C&%7Ddoi=10.1379%7B%5C%%7D2F1466-1268(2003)008%7B%5C%%7D3C0108%7B%5C%%7D3APASPWC%7B%5C%%7D3E2.0.CO%7B%5C%%7D3B2 (cit. on p. 103).

[63] Daniel L. Floyd *et al.* «Analysis of kinetic intermediates in single-particle dwell-Time distributions.» In: *Biophysical Journal* 99.2 (2010), pp. 360–366. ISSN: 15420086. DOI: 10.1016/j.bpj.2010.04.049. URL: http://dx.doi.org/10.1016/j.bpj.2010.04.049 (cit. on p. 41).

[64] Hans Frauenfelder *et al.* «The energy landscapes and motions of proteins.» In: *Science (New York, N.Y.)* 254.5038 (Dec. 1991), pp. 1598–603. ISSN: 0036-8075. URL: http://www.ncbi.nlm.nih.gov/pubmed/1749933 (cit. on pp. 40, 41).

[65] L. P. Freedman and B. F. Luisi. «On the mechanism of DNA binding by nuclear hormone receptors: A structural and functional perspective.» In: *Journal of Cellular Biochemistry* 51.2 (1993), pp. 140–150. ISSN: 07302312. DOI: 10.1002/jcb.240510205. URL: http://www.ncbi.nlm.nih.gov/pubmed/8440748 (cit. on p. 5).

[66] B C Freeman and R I Morimoto. «The human cytosolic molecular chaperones hsp90, hsp70 (hsc70) and hdj-1 have distinct roles in recognition of a non-native protein and protein refolding.» In: *The EMBO journal* 15.12 (June 1996), pp. 2969–79. ISSN: 0261-4189. URL: http://www.ncbi.nlm.nih.gov/pubmed/8670798%20http://www.pubmedcentral.nih.gov/articlerender.fcgi?artid=PMC450238 (cit. on p. 124).

[67] B. C. Freeman. «Disassembly of Transcriptional Regulatory Complexes by Molecular Chaperones.» In: *Science* 296.5576 (2002), pp. 2232–2235. ISSN: 00368075. DOI: 10.1126/science.1073051. URL: http://www.sciencemag.org/cgi/doi/10.1126/science.1073051 (cit. on p. 107).

[68] Brian C. Freeman *et al.* «The p23 molecular chaperones act at a late step in intracellular receptor action to differentially affect ligand efficacies.» In: *Genes and Development* 14.4 (2000), pp. 422–434. ISSN: 08909369. DOI: 10.1101/gad.14.4.422 (cit. on pp. 8, 103, 107).

[69] Lee Frego and Walter Davidson. «Conformational changes of the glucocorticoid receptor ligand binding domain induced by ligand and cofactor binding, and the location of cofactor binding sites determined by hydrogen/deuterium exchange mass spectrometry.» In: *Protein science : a publication of the Protein Society* 15.4 (Apr. 2006), pp. 722–730. ISSN: 0961-8368. DOI: 10.1110/ps.051781406. URL: http://www.ncbi.nlm.nih.gov/pubmed/16600964%20http://www.pubmedcentral.nih.gov/articlerender.fcgi?artid=PMC2242475 (cit. on pp. 10, 11, 13, 68, 78, 151).

[70] Mario D. Galigniana *et al.* «Evidence that the Peptidylprolyl Isomerase Domain of the hsp90-binding Immunophilin FKBP52 is Involved in Both Dynein Interaction and Glucocorticoid Receptor Movement to the Nucleus.» In: *Journal of Biological Chemistry* 276.18 (2001), pp. 14884–14889. ISSN: 00219258. DOI: 10.1074/jbc.M010809200 (cit. on p. 107).

[71] Mario D Galigniana *et al.* «Heat Shock Protein 90-Dependent (Geldanamycin-Inhibited) Movement of the Glucocorticoid Receptor through the Cytoplasm to the Nucleus Requires Intact Cytoskeleton.» In: *Molecular Endocrinology* 12.12 (Dec. 1998), pp. 1903–1913. ISSN: 0888-8809. DOI: 10.1210/mend.12.12.0204. URL: https://academic.oup.com/mend/article-lookup/doi/10.1210/mend.12.12.0204 (cit. on p. 8).

[72] Mario D Galigniana *et al.* «Inhibition of Glucocorticoid Receptor Binding by Nitric Oxide.» In: *Molecular Pharmacology* 55.2 (Feb. 1999), pp. 317–323. ISSN: 0026-895X. DOI: 10.1124/mol.55.2.317. URL: http://molpharm.aspetjournals.org/lookup/doi/10.1124/mol.55.2.317 (cit. on p. 155).

[73] JÉRÔME GALON *et al.* «Gene profiling reveals unknown enhancing and suppressive actions of glucocorticoids on immune cells.» In: *The FASEB Journal* 16.1 (Jan. 2002), pp. 61–71. ISSN: 0892-6638. DOI: 10.1096/fj.01-0245com. URL: http://www.fasebj.org/doi/10.1096/fj.01-0245com (cit. on p. 6).

[74] Helen Garside *et al.* «Glucocorticoid ligands specify different interactions with NF-κB by allosteric effects on the glucocorticoid receptor DNA binding domain.» In: *Journal of Biological Chemistry* 279.48 (2004), pp. 50050–50059. ISSN: 00219258. DOI: 10.1074/jbc.M407309200 (cit. on p. 8).

[75] J Christof M Gebhardt *et al.* «Full distance-resolved folding energy landscape of one single protein molecule.» In: *Proceedings of the National Academy of Sciences of the United States of America* 107.5 (Feb. 2010), pp. 2013–8. ISSN: 1091-6490. DOI: 10.1073/pnas.0909854107. URL: http://www.pubmedcentral.nih.gov/articlerender.fcgi?artid=2836620%7B%5C&%7Dtool=pmcentrez%7B%5C&%7Drendertype=abstract (cit. on pp. 45, 46).

[76] Arvin C Gee and John A Katzenellenbogen. «Probing Conformational Changes in the Estrogen Receptor: Evidence for a Partially Unfolded Intermediate Facilitating Ligand Binding and Release.» In: *Molecular Endocrinology* 15.3 (Mar. 2001), pp. 421–428. ISSN: 0888-8809. DOI: 10.1210/mend.15.3.0602. URL: https://academic.oup.com/mend/article-lookup/doi/10.1210/mend.15.3.0602 (cit. on pp. 11, 79).

[77] Olivier Genest *et al.* «Heat shock protein 90 from Escherichia coli collaborates with the DnaK chaperone system in client protein remodeling.» In: *Proceedings of the National Academy of Sciences* 108.20 (May 2011), pp. 8206–8211. ISSN: 0027-8424. DOI: 10.1073/pnas.1104703108. URL: http://www.pnas.org/cgi/doi/10.1073/pnas.1104703108 (cit. on p. 105).

[78] Elise Burmeister Getz *et al.* «A Comparison between the Sulfhydryl Reductants Tris(2-carboxyethyl)phosphine and Dithiothreitol for Use in Protein Biochemistry.» In: *Analytical Biochemistry* 273.1 (Aug. 1999), pp. 73–80. ISSN: 00032697. DOI: 10.1006/abio.1999.4203. URL: http://linkinghub.elsevier.com/retrieve/pii/S0003269799942033 (cit. on p. 155).

[79] Georgia Giannoukos *et al.* «The seven amino acids (547-553) of rat glucocorticoid receptor required for steroid and Hsp90 binding contain a functionally independent LXXLL motif that is critical for steroid binding.» In: *Journal of Biological Chemistry* 274.51 (1999), pp. 36527–36536. ISSN: 00219258. DOI: 10.1074/jbc.274.51.36527 (cit. on pp. 78, 129).

[80] Serge M. Gisler *et al.* «Catapult mechanism renders the chaperone action of hsp70 unidirectional.» In: *Journal of Molecular Biology* 279.4 (June 1998), pp. 833–840. ISSN: 00222836. DOI: 10.1006/jmbi.1998.1815. URL: http://linkinghub.elsevier.com/retrieve/pii/S0022283698918150 (cit. on p. 104).

[81] C K Glass and M G Rosenfeld. «The coregulator exchange in transcriptional functions of nuclear receptors.» In: *Genes & development* 14.2 (Jan. 2000), pp. 121–41. ISSN: 0890-9369. URL: http://www.ncbi.nlm.nih.gov/pubmed/10652267 (cit. on p. 4).

[82] M Goebl and M Yanagida. «The TPR snap helix: a novel protein repeat motif from mitosis to transcription.» In: *Trends in biochemical sciences* 16.5 (May 1991), pp. 173–7. ISSN: 0968-0004. URL: http://www.ncbi.nlm.nih.gov/pubmed/1882418 (cit. on p. 103).

[83] Marco Grison. «Single-molecule cohesion and adhesion in muscle cells.» PhD thesis. Technische Universität München, 2017 (cit. on pp. 25, 39).

[84] Marco Grison *et al.* «α-Actinin/titin interaction: A dynamic and mechanically stable cluster of bonds in the muscle Z-disk.» In: *Proceedings of the National Academy of Sciences* 114.5 (Jan. 2017), pp. 1015–1020. ISSN: 0027-8424. DOI: 10.1073/pnas.1612681114. URL: http://www.ncbi.nlm.nih.gov/pubmed/28096424%20http://www.pubmedcentral.nih.gov/articlerender.fcgi?artid=PMC5293040%20http://www.pnas.org/lookup/doi/10.1073/pnas.1612681114 (cit. on pp. 28, 47, 70, 90).

[85] Yann von Hansen *et al.* «Auto- and cross-power spectral analysis of dual trap optical tweezer experiments using Bayesian inference.» In: *The Review of scientific instruments* 83.9 (Sept. 2012), p. 095116. ISSN: 1089-7623. DOI: 10.1063/1.4753917. URL: http://www.ncbi.nlm.nih.gov/pubmed/23020428 (cit. on p. 23).

[86] F Hartl. «Molecular Chaperones in the Cytosol: from Nascent Chainto Folded Protein.» In: *Science* 295.5561 (2002), p. 1852. ISSN: 00368075. DOI: 10.1126/science.1068408 (cit. on p. 5).

[87] Yuanzheng He *et al.* «Structures and mechanism for the design of highly potent glucocorticoids.» In: *Cell Research* 24.6 (2014), pp. 713–726. ISSN: 17487838. DOI: 10.1038/cr.2014.52. URL: http://dx.doi.org/10.1038/cr.2014.52 (cit. on p. 10).

[88] David M Heery *et al.* «A signature motif in transcriptional co-activators mediates binding to nuclear receptors.» In: *Nature* 387.6634 (June 1997), pp. 733–736. ISSN: 0028-0836. DOI: 10.1038/42750. URL: http://www.nature.com/articles/42750 (cit. on p. 11).

[89] P. O. Heidarsson *et al.* «Direct single-molecule observation of calcium-dependent misfolding in human neuronal calcium sensor-1.» In: *Proceedings of the National Academy of Sciences* 111.36 (2014), pp. 13069–13074. ISSN: 0027-8424. DOI: 10.1073/pnas.1401065111. URL: http://www.pnas.org/cgi/doi/10.1073/pnas.1401065111 (cit. on p. 101).

[90] Marjet D. Heitzer *et al.* «Glucocorticoid receptor physiology.» In: *Reviews in Endocrine and Metabolic Disorders* 8.4 (2007), pp. 321–330. ISSN: 13899155. DOI: 10.1007/s11154-007-9059-8 (cit. on pp. 4, 6).

[91] Katherine Henzler-Wildman and Dorothee Kern. «Dynamic personalities of proteins.» In: *Nature* 450.7172 (2007), pp. 964–972. ISSN: 14764687. DOI: 10.1038/nature06522 (cit. on pp. 21, 41).

[92] S. Hepp and M. Müller. «Sulfhydryl oxidation: A potential strategy to achieve neuroprotection during severe hypoxia?» In: *Neuroscience* 152.4 (Apr. 2008), pp. 903–912. ISSN: 03064522. DOI: 10.1016/j.neuroscience.2008.01.029. URL: http://linkinghub.elsevier.com/retrieve/pii/S0306452208001437 (cit. on p. 155).

[93] Ola Hermanson *et al.* «Nuclear receptor coregulators: Multiple modes of modification.» In: *Trends in Endocrinology and Metabolism* 13.2 (2002), pp. 55–60. ISSN: 10432760. DOI: 10.1016/S1043-2760(01)00527-6 (cit. on p. 8).

[94] MP Hernández *et al.* «HSP40 binding is the first step in the HSP90 chaperoning pathway for the progesterone receptor.» In: *Journal of Biological Chemistry* 277.14 (2002), pp. 11873–11881. ISSN: 0021-9258. DOI: 10.1074/jbc.M111445200. URL: http://www.ncbi.nlm.nih.gov/pubmed/11809754%7B%5C%%7D5Cnhttp://www.jbc.org/content/277/14/11873.short (cit. on pp. 103, 105, 128).

[95] Martin Hessling *et al.* «Dissection of the ATP-induced conformational cycle of the molecular chaperone Hsp90.» In: *Nature Structural and Molecular Biology* 16.3 (2009), pp. 287–293. ISSN: 15459993. DOI: 10.1038/nsmb.1565 (cit. on pp. 14, 106).

[96] Adam B. Hittelman *et al.* «Differential regulation of glucocorticoid receptor transcriptional activation via AF-1-associated proteins.» In: *EMBO Journal* 18.19 (1999), pp. 5380–5388. ISSN: 02614189. DOI: 10.1093/emboj/18.19.5380 (cit. on p. 5).

[97] J Howard *et al.* «Mapping the HSP9O Binding Region of the Glucocorticoid Receptor.» In: *Jbc* 265.20 (1990), pp. 11928–35 (cit. on pp. 5, 12, 13).

[98] Megan L Hughes and Lorna Dougan. «The physics of pulling polyproteins: a review of single molecule force spectroscopy using the AFM to study protein unfolding.» In: *Reports on Progress in Physics* 79.7 (July 2016), p. 076601. ISSN: 0034-4885. DOI: 10.1088/0034-4885/79/7/076601. URL: http://stacks.iop.org/0034-4885/79/i=7/a=076601?key=crossref.5ec78f1fb85396e30d3e8d0b23b64877 (cit. on p. 22).

[99] International Human Genome Sequencing Consortium. «Finishing the euchromatic sequence of the human genome.» In: *Nature* 431.7011 (Oct. 2004), pp. 931–945. ISSN: 0028-0836. DOI: 10.1038/nature03001. URL: http://www.nature.com/doifinder/10.1038/nature03001 (cit. on p. 3).

[100] Peer B Jacobson *et al.* «Hepatic glucocorticoid receptor antagonism is sufficient to reduce elevated hepatic glucose output and improve glucose control in animal models of type 2 diabetes.» In: *The Journal of pharmacology and experimental therapeutics* 314.1 (2005), pp. 191–200. ISSN: 0022-3565. DOI: 10.1124/jpet.104.081257. URL: http://www.ncbi.nlm.nih.gov/pubmed/15784656 (cit. on p. 6).

[101] Markus Jahn. «Heat Shock Protein 90 Studied At The Single Molecule Level.» PhD thesis. Technische Universität München, 2016. URL: https://mediatum.ub.tum.de/1304142 (cit. on p. 39).

[102] Markus Jahn *et al.* «Folding and assembly of the large molecular machine Hsp90 studied in single-molecule experiments.» In: *Proceedings of the National Academy of Sciences* 113.5 (2016), pp. 1232–1237. ISSN: 0027-8424. DOI: 10.1073/pnas.1518827113. URL: http://www.pnas.org/lookup/doi/10.1073/pnas.1518827113 (cit. on pp. 14, 101, 123).

[103] Ursula Jakob *et al.* «Structural organization of procaryotic and eucaryotic Hsp90. Influence of divalent cations on structure and function.» In: *The Journal of biological chemistry* 270.24 (June 1995), pp. 14412–9. ISSN: 0021-9258. DOI: 10.1074/jbc.270.24.14412. URL: http://www.ncbi.nlm.nih.gov/pubmed/7782303 (cit. on p. 15).

[104] J L Johnson and D O Toft. «Binding of p23 and hsp90 during assembly with the progesterone receptor.» In: *Molecular Endocrinology* 9.6 (June 1995), pp. 670–678. ISSN: 0888-8809. DOI: 10.1210/mend.9.6.8592513. URL: https://academic.oup.com/mend/article-lookup/doi/10.1210/mend.9.6.8592513 (cit. on p. 128).

[105] Mahita Kadmiel and John A. Cidlowski. «Glucocorticoid receptor signaling in health and disease.» In: *Trends in Pharmacological Sciences* 34.9 (2013), pp. 518–530. ISSN: 01656147. DOI: 10.1016/j.tips.2013.07.003. arXiv: NIHMS150003. URL: http://dx.doi.org/10.1016/j.tips.2013.07.003 (cit. on pp. 6–8).

[106] G. Elif Karagöz and Stefan G D Rüdiger. «Hsp90 interaction with clients.» In: *Trends in Biochemical Sciences* 40.2 (2015), pp. 117–125. ISSN: 13624326. DOI: 10.1016/j.tibs.2014.12.002 (cit. on pp. 15, 16, 106).

[107] G. Elif Karagöz *et al.* «Hsp90-tau complex reveals molecular basis for specificity in chaperone action.» In: *Cell* 156.5 (2014), pp. 963–974. ISSN: 00928674. DOI: 10.1016/j.cell.2014.01.037. arXiv: NIHMS150003 (cit. on pp. 15, 105).

[108] Sunil Kaul *et al.* «Mutations at Positions 547–553 of Rat Glucocorticoid Receptors Reveal That hsp90 Binding Requires the Presence, but Not Defined Composition, of a Seven-amino Acid Sequence at the Amino Terminus of the Ligand Binding Domain.» In: *Journal of Biological Chemistry* 277.39 (Sept. 2002), pp. 36223–36232. ISSN: 0021-9258. DOI: 10.1074/jbc.M206748200. URL: http://www.jbc.org/lookup/doi/10.1074/jbc.M206748200 (cit. on pp. 12, 129).

[109] Björn Kauppi *et al.* «The three-dimensional structures of antagonistic and agonistic forms of the glucocorticoid receptor ligand-binding domain: RU-486 induces a transconformation that leads to active antagonism.» In: *Journal of Biological Chemistry* 278.25 (2003), pp. 22748–22754. ISSN: 00219258. DOI: 10.1074/jbc.M212711200 (cit. on pp. 10, 11).

[110] Ruth Kellner *et al.* «Single-molecule spectroscopy reveals chaperone-mediated expansion of substrate protein.» In: *Proceedings of the National Academy of Sciences* 111.37 (2014), pp. 13355–13360. ISSN: 0027-8424. DOI: 10.1073/pnas.1407086111. URL: http://www.pnas.org/lookup/doi/10.1073/pnas.1407086111 (cit. on p. 125).

[111] Pawel Kermer *et al.* «BAG1 is Neuroprotective in In Vivo and In Vitro Models of Parkinson's Disease.» In: *Journal of Molecular Neuroscience* 55.3 (Mar. 2015), pp. 587–595. ISSN: 0895-8696. DOI: 10.1007/s12031-014-0396-2. URL: http://link.springer.com/10.1007/s12031-014-0396-2 (cit. on p. 124).

[112] Yujin E. Kim *et al.* «Molecular Chaperone Functions in Protein Folding and Proteostasis.» In: *Annual Review of Biochemistry* 82.1 (June 2013), pp. 323–355. ISSN: 0066-4154. DOI: 10.1146/annurev-biochem-060208-092442. URL: http://www.annualreviews.org/doi/10.1146/annurev-biochem-060208-092442 (cit. on p. 15).

[113] Elaine Kirschke *et al.* «Glucocorticoid Receptor Function Regulated by Coordinated Action of the Hsp90 and Hsp70 Chaperone Cycles.» In: *Cell* 157.7 (2014), pp. 1685–1697. ISSN: 00928674. DOI: 10.1016/j.cell.2014.04.038. URL: http://linkinghub.elsevier.com/retrieve/pii/S0092867414006540 (cit. on pp. 13, 15, 59, 65, 74, 83, 100, 101, 105–108, 125–127, 130, 131, 133, 151, 160).

[114] John Koren *et al.* «Chaperone signalling complexes in Alzheimer's disease.» In: *Journal of Cellular and Molecular Medicine* 13.4 (2009), pp. 619–630. ISSN: 15821838. DOI: 10.1111/j.1582-4934.2008.00557.x (cit. on p. 5).

[115] Hiroshi Kosano *et al.* «The Assembly of Progesterone Receptor-hsp90 Complexes Using Purified Proteins.» In: *Journal of Biological Chemistry* 273.49 (Dec. 1998), pp. 32973–32979. ISSN: 0021-9258. DOI: 10.1074/jbc.273.49.32973. URL: http://www.jbc.org/lookup/doi/10.1074/jbc.273.49.32973 (cit. on p. 103).

[116] Lukasz P. Kozlowski. «Proteome- pI : proteome isoelectric point database.» In: *Nucleic Acids Research* 45.D1 (Jan. 2017), pp. D1112–D1116. ISSN: 0305-1048. DOI: 10.1093/nar/gkw978. URL: https://academic.oup.com/nar/article-lookup/doi/10.1093/nar/gkw978 (cit. on p. 14).

[117] Rachel R. Kroe *et al.* «Agonist versus antagonist induce distinct thermodynamic modes of co-factor binding to the glucocorticoid receptor.» In: *Biophysical Chemistry* 128.2-3 (2007), pp. 156–164. ISSN: 03014622. DOI: 10.1016/j.bpc.2007.03.013 (cit. on pp. 13, 68, 79, 100, 101, 151).

[118] Raj Kumar and E.Brad Thompson. «The structure of the nuclear hormone receptors.» In: *Steroids* 64.5 (1999), pp. 310–319. ISSN: 0039128X. DOI: 10.1016/S0039-128X(99)00014-8 (cit. on p. 4).

[119] R F Laan *et al.* «Glucocorticosteroids in the management of rheumatoid arthritis.» In: *Rheumatology (Oxford, England)* 38.1 (Jan. 1999), pp. 6–12. ISSN: 1462-0324. URL: http://www.ncbi.nlm.nih.gov/pubmed/10334676 (cit. on p. 6).

[120] Keith J. Laidler and M. Christine King. «Development of transition-state theory.» In: *The Journal of Physical Chemistry* 87.15 (July 1983), pp. 2657–2664. ISSN: 0022-3654. DOI: 10.1021/j100238a002. URL: http://pubs.acs.org/doi/abs/10.1021/j100238a002 (cit. on p. 41).

[121] Katja A Lamia *et al.* «Glucocorticoid Receptor.» In: *Nature* 480.7378 (2011), pp. 552–556. ISSN: 0028-0836. DOI: 10.1038/nature10700. URL: http://dx.doi.org/10.1038/nature10700 (cit. on p. 5).

[122] Markita P. Landry *et al.* «Characterization of photoactivated singlet oxygen damage in single-molecule optical trap experiments.» In: *Biophysical Journal* 97.8 (2009), pp. 2128–2136. ISSN: 00063495. DOI: 10.1016/j.bpj.2009.07.048. URL: http://dx.doi.org/10.1016/j.bpj.2009.07.048 (cit. on pp. 165, 166).

[123] T. Laufen *et al.* «Mechanism of regulation of Hsp70 chaperones by DnaJ cochaperones.» In: *Proceedings of the National Academy of Sciences* 96.10 (1999), pp. 5452–5457. ISSN: 0027-8424. DOI: 10.1073/pnas.96.10.5452. URL: http://www.pnas.org/cgi/doi/10.1073/pnas.96.10.5452 (cit. on pp. 104, 126).

[124] Jing Li *et al.* «The Hsp90 chaperone machinery: Conformational dynamics and regulation by co-chaperones.» In: *Biochimica et Biophysica Acta - Molecular Cell Research* 1823.3 (2012), pp. 624–635. ISSN: 01674889. DOI: 10.1016/j.bbamcr.2011.09.003. URL: http://dx.doi.org/10.1016/j.bbamcr.2011.09.003 (cit. on pp. 21, 130).

[125] J. Liman *et al.* «Interaction of BAG1 and Hsp70 Mediates Neuroprotectivity and Increases Chaperone Activity.» In: *Molecular and Cellular Biology* 25.9 (May 2005), pp. 3715–3725. ISSN: 0270-7306. DOI: 10.1128/MCB.25.9.3715-3725.2005. URL: http://mcb.asm.org/cgi/doi/10.1128/MCB.25.9.3715-3725.2005 (cit. on p. 124).

[126] Shu-qun Liu *et al.* «Protein Folding, Binding and Energy Landscape: A Synthesis.» In: *Protein Engineering*. InTech, Feb. 2012, pp. 207–252. ISBN: 978-953-51-0037-9. DOI: 10.5772/30440. URL: http://www.intechopen.com/books/protein-engineering/protein-folding-binding-and-energy-landscape-a-synthesis (cit. on pp. 3, 40, 41).

[127] Y. Liu *et al.* «Physiological monitoring of optically trapped cells: assessing the effects of confinement by 1064-nm laser tweezers using microfluorometry.» In: *Biophysical Journal* 71.4 (Oct. 1996), pp. 2158–2167. ISSN: 00063495. DOI: 10.1016/S0006-3495(96)79417-1. URL: http://linkinghub.elsevier.com/retrieve/pii/S0006349596794171 (cit. on p. 165).

[128] Oliver Robin Lorenz *et al.* «Modulation of the Hsp90 Chaperone Cycle by a Stringent Client Protein.» In: *Molecular Cell* 53.6 (Mar. 2014), pp. 941–953. ISSN: 10972765. DOI: 10.1016/j.molcel.2014.02.003. URL: http://linkinghub.elsevier.com/retrieve/pii/S1097276514001178 (cit. on pp. 12, 13, 15, 16, 21, 56, 65, 74, 83, 100, 102, 106, 107, 117, 118, 127–130, 150, 151).

[129] Bf F Luisi *et al. Crystallographic analysis of the interaction of the glucocorticoid receptor with DNA*. 1991. DOI: 10.1038/352497a0. URL: http://dx.doi.org/10.1038/352497a0%7B%5C%%7D5Cnhttp://www.nature.com/nature/journal/v352/n6335/abs/352497a0.html (cit. on p. 5).

[130] Wenjie Luo *et al.* «Heat shock protein 90 in neurodegenerative diseases.» In: *Molecular Neurodegeneration* 5.1 (Sept. 2010), p. 24. ISSN: 1750-1326. DOI: 10.1186/1750-1326-5-24. URL: http://www.nature.com/doifinder/10.1038/nrc1716%20http://molecularneurodegeneration.biomedcentral.com/articles/10.1186/1750-1326-5-24 (cit. on p. 14).

[131] Soumit Sankar Mandal *et al.* «Nanomechanics of the substrate binding domain of Hsp70 determine its allosteric ATP-induced conformational change.» In: *Proceedings of the National Academy of Sciences* 114.23 (2017), pp. 6040–6045. ISSN: 0027-8424. DOI: 10.1073/pnas.1619843114. URL: http://www.pnas.org/lookup/doi/10.1073/pnas.1619843114 (cit. on pp. 21, 104, 123).

[132] Klemens Marischler. *BASICS Endokrinologie*. Elsevier Verlag, 2014. ISBN: 9783437292668. URL: https://www.elsevier.com/books/basics-endokrinologie/marischler/978-3-437-42267-6 (cit. on pp. 6, 83).

[133] John F. Marko and Eric D. Siggia. «Stretching DNA.» In: *Macromolecules* 28.26 (1995), pp. 8759–8770. ISSN: 15205835. DOI: 10.1021/ma00130a008 (cit. on p. 40).

[134] M. P. Mayer and B. Bukau. «Hsp70 chaperones: Cellular functions and molecular mechanism.» In: *Cellular and Molecular Life Sciences* 62.6 (Mar. 2005), pp. 670–684. ISSN: 1420-682X. DOI: 10.1007/s00018-004-4464-6. arXiv: arXiv:1011.1669v3. URL: http://link.springer.com/10.1007/s00018-004-4464-6 (cit. on pp. 5, 126, 127).

[135] Matthias P Mayer. «Gymnastics of Molecular Chaperones.» In: *Molecular Cell* 39.3 (Aug. 2010), pp. 321–331. ISSN: 10972765. DOI: 10.1016/j.molcel.2010.07.012. URL: http://dx.doi.org/10.1016/j.molcel.2010.07.012%20http://linkinghub.elsevier.com/retrieve/pii/S1097276510005344 (cit. on p. 5).

[136] Matthias P. Mayer. «Hsp70 chaperone dynamics and molecular mechanism.» In: *Trends in Biochemical Sciences* 38.10 (Oct. 2013), pp. 507–514. ISSN: 09680004. DOI: 10.1016/j.tibs.2013.08.001. URL: http://linkinghub.elsevier.com/retrieve/pii/S0968000413001321 (cit. on p. 104).

[137] Iain J. McEwan *et al.* «Mechanism of gene expression by the glucocorticoid receptor: Role of protein-protein interactions.» In: *BioEssays* 19.2 (1997), pp. 153–160. ISSN: 0265-9247. DOI: 10.1002/bies.950190210. URL: http://dx.doi.org/10.1002/bies.950190210 (cit. on p. 9).

[138] Lorraine I McKay and John a Cidlowski. «Molecular Control of Immune / Inflammatory Responses : Interactions Between Nuclear Factor- kB and Steroid Receptor-Signaling Pathways.» In: *Endocrine Reviews* 20.4 (1999), pp. 435–459. ISSN: 0163-769X. DOI: 10.1210/edrv.20.4.0375 (cit. on p. 8).

[139] Stephen H Mclaughlin and Sophie E Jackson. «Folding and stability of the ligand-binding domain of the glucocorticoid receptor.» In: *Protein Science* 11.8 (2002), pp. 1926–1936. DOI: 10.1110/ps.5000102.served. URL: http://www.ncbi.nlm.nih.gov/entrez/query.fcgi?cmd=Retrieve%7B%5C&%7Ddb=PubMed%7B%5C&%7Ddopt=Citation%7B%5C&%7Dlist%7B%5C_%7Duids=12142447 (cit. on pp. 13, 151).

[140] James G Mcnally *et al.* «Regulatory Sites in Living Cells The Glucocorticoid Receptor : Rapid Exchange with Regulatory Sites in Living Cells.» In: 1262.2000 (2009), pp. 1262–1266. DOI: 10.1126/science.287.5456.1262 (cit. on p. 8).

[141] Alexander Mehlich. «Transition paths of protein-folding probed with optical tweezers.» PhD thesis. Technische Universität München, 2017. URL: https://mediatum.ub.tum.de/1398063 (cit. on p. 39).

[142] Haydyn D.T. Mertens and Dmitri I. Svergun. «Structural characterization of proteins and complexes using small-angle X-ray solution scattering.» In: *Journal of Structural Biology* 172.1 (Oct. 2010), pp. 128–141. ISSN: 10478477. DOI: 10.1016/j.jsb.2010.06.012. URL: http://linkinghub.elsevier.com/retrieve/pii/S1047847710001905 (cit. on p. 21).

[143] Helen Miller *et al.* «Single-molecule techniques in biophysics: A review of the progress in methods and applications.» In: *Reports on Progress in Physics* 81.2 (2018). ISSN: 00344885. DOI: 10.1088/1361-6633/aa8a02 (cit. on p. 21).

[144] Jeffrey R Moffitt *et al.* «Differential detection of dual traps improves the spatial resolution of optical tweezers.» In: *Proceedings of the National Academy of Sciences of the United States of America* 103.24 (June 2006), pp. 9006–11. ISSN: 0027-8424. DOI: 10.1073/pnas.0603342103. URL: http://www.pubmedcentral.nih.gov/articlerender.fcgi?artid=1482556%7B%5C&%7Dtool=pmcentrez%7B%5C&%7Drendertype=abstract (cit. on p. 22).

[145] Samarendra Kumar Mohanty *et al.* «Generation of ROS in cells on exposure to CW and pulsed near-infrared laser tweezers.» In: *Photochem. Photobiol. Sci.* 5.1 (2006), pp. 134–139. ISSN: 1474-905X. DOI: 10.1039/B506061C. URL: http://xlink.rsc.org/?DOI=B506061C (cit. on p. 165).

[146] Tania Morán Luengo *et al.* «Hsp90 Breaks the Deadlock of the Hsp70 Chaperone System.» In: *Molecular Cell* 70.3 (May 2018), 545–552.e9. ISSN: 10972765. DOI: 10.1016/j.molcel.2018.03.028. URL: http://linkinghub.elsevier.com/retrieve/pii/S1097276518302314 (cit. on pp. 105, 125, 127, 128, 130).

[147] Dino Moras and Hinrich Gronemeyer. «The nuclear receptor ligand-binding domain: structure and function.» In: *Current Opinion in Cell Biology* 10.3 (June 1998), pp. 384–391. ISSN: 09550674. DOI: 10.1016/S0955-0674(98)80015-X. URL: http://linkinghub.elsevier.com/retrieve/pii/S095506749880015X (cit. on p. 9).

[148] Yoshihiro Morishima *et al.* «Stepwise assembly of a glucocorticoid receptor??hsp90 heterocomplex resolves two sequential ATP-dependent events involving first hsp70 and then hsp90 in opening of the steroid binding pocket.» In: *Journal of Biological Chemistry* 275.24 (2000), pp. 18054–18060. ISSN: 00219258. DOI: 10.1074/jbc.M000434200 (cit. on pp. 16, 103).

[149] Nigel Morrison and John Eisman. «Role of the negative glucocorticoid regulatory element in glucocorticoid repression of the human osteocalcin promoter.» In: *Journal of Bone and Mineral Research* 8.8 (Dec. 2009), pp. 969–975. ISSN: 08840431. DOI: 10.1002/jbmr.5650080810. URL: http://doi.wiley.com/10.1002/jbmr.5650080810 (cit. on p. 8).

[150] M Mücke and F X Schmid. «Folding mechanism of ribonuclease T1 in the absence of the disulfide bonds.» In: *Biochemistry* 33.48 (Dec. 1994), pp. 14608–19. ISSN: 0006-2960. URL: http://www.ncbi.nlm.nih.gov/pubmed/7981223 (cit. on p. 28).

[151] Leif Mummenbrauer. «Fluorescence Spectroscopy of Dexamethasone Binding to the Glucocorticoid Receptor.» In: (2015) (cit. on p. 83).

[152] Kazuyoshi Murata and Matthias Wolf. «Cryo-electron microscopy for structural analysis of dynamic biological macromolecules.» In: *Biochimica et Biophysica Acta (BBA) - General Subjects* 1862.2 (Feb. 2018), pp. 324–334. ISSN: 03044165. DOI: 10.1016/j.bbagen.2017.07.020. URL: http://linkinghub.elsevier.com/retrieve/pii/S0304416517302374 (cit. on p. 21).

[153] Sua Myong *et al.* «Bridging Conformational Dynamics and Function Using Single-Molecule Spectroscopy.» In: *Structure* 14.4 (2006), pp. 633–643. ISSN: 09692126. DOI: 10.1016/j.str.2006.02.005 (cit. on p. 21).

[154] Debra F Nathan and Susan Lindquist. «Mutational analysis of Hsp90 function: interactions with a steroid receptor and a protein kinase.» In: *Molecular and cellular biology* 15.7 (July 1995), pp. 3917–25. ISSN: 0270-7306. URL: http://www.ncbi.nlm.nih.gov/pubmed/7791797%20http://www.pubmedcentral.nih.gov/articlerender.fcgi?artid=PMC230631 (cit. on p. 15).

[155] Len Neckers. «Heat shock protein 90: The cancer chaperone.» In: *Journal of Biosciences* 32.3 (2007), pp. 517–530. ISSN: 02505991. DOI: 10.1007/s12038-007-0051-y (cit. on pp. 5, 14).

[156] T Nemoto *et al.* «The transformed glucocorticoid receptor has a lower steroid-binding affinity than the nontransformed receptor.» In: *Biochemistry* 29.7 (Feb. 1990), pp. 1880–6. ISSN: 0006-2960. URL: http://www.ncbi.nlm.nih.gov/pubmed/2184891 (cit. on p. 16).

[157] Keir C. Neuman *et al.* «Characterization of Photodamage to Escherichia coli in Optical Traps.» In: *Biophysical Journal* 77.5 (Nov. 1999), pp. 2856–2863. ISSN: 00063495. DOI: 10.1016/S0006-3495(99)77117-1. URL: http://linkinghub.elsevier.com/retrieve/pii/S0006349599771171 (cit. on p. 165).

[158] Keir C Neuman and Attila Nagy. «Single-molecule force spectroscopy: optical tweezers, magnetic tweezers and atomic force microscopy.» In: *Nature Methods* 5.6 (June 2008), pp. 491–505. ISSN: 1548-7091. DOI: 10.1038/nmeth.1218. URL: http://www.nature.com/articles/nmeth.1218 (cit. on p. 22).

[159] Antonio a R Neves *et al.* «Electromagnetic forces for an arbitrary optical trapping of a spherical dielectric.» In: *Optics Express* 14.26 (2006), p. 13101. ISSN: 1094-4087. DOI: 10.1364/OE.14.013101. arXiv: 0610068 [physics]. URL: http://www.scopus.com/inward/record.url?eid=2-s2.0-33845794335%7B%5C&%7DpartnerID=tZOtx3y1%7B%5C%%7D5Cnhttps://www.osapublishing.org/oe/abstract.cfm?uri=oe-14-26-13101 (cit. on p. 23).

[160] Basile Nguyen *et al.* «Thermodynamic Bounds on the Ultra- and Infra-affinity of Hsp70 for Its Substrates.» In: *Biophysical Journal* 113.2 (2017), pp. 362–370. ISSN: 15420086. DOI: 10.1016/j.bpj.2017.06.010. arXiv: 1702.01649. URL: http://dx.doi.org/10.1016/j.bpj.2017.06.010 (cit. on pp. 104, 126).

[161] Robert H. Oakley and John A. Cidlowski. «Cellular processing of the glucocorticoid receptor gene and protein: New mechanisms for generating tissue-specific actions of glucocorticoids.» In: *Journal of Biological Chemistry* 286.5 (2011), pp. 3177–3184. ISSN: 00219258. DOI: 10.1074/jbc.R110.179325 (cit. on pp. 6, 8).

[162] Leoni Oberbarnscheidt *et al.* «Direct and model free calculation of force-dependent dissociation rates from force spectroscopic data.» In: *Biophysical journal* 97.9 (Nov. 2009), pp. L19–21. ISSN: 1542-0086. DOI: 10.1016/j.bpj.2009.08.015. URL: http://www.pubmedcentral.nih.gov/articlerender.fcgi?artid=2770607%7B%5C&%7Dtool=pmcentrez%7B%5C&%7Drendertype=abstract (cit. on pp. 27, 56, 70, 147).

[163] Wolfgang M.J. Obermann *et al.* «In Vivo Function of Hsp90 Is Dependent on ATP Binding and ATP Hydrolysis.» In: *The Journal of Cell Biology* 143.4 (Nov. 1998), pp. 901–910. ISSN: 0021-9525. DOI: 10.1083/jcb.143.4.901. URL: http://www.jcb.org/lookup/doi/10.1083/jcb.143.4.901 (cit. on p. 14).

[164] Y Ohara-Nemoto *et al.* «The steroid-binding properties of recombinant glucocorticoid receptor: a putative role for heat shock protein hsp90.» In: *The Journal of steroid biochemistry and molecular biology* 37.4 (Nov. 1990), pp. 481–90. ISSN: 0960-0760. URL: http://www.ncbi.nlm.nih.gov/pubmed/2278831 (cit. on pp. 13, 150).

[165] Jerrold M. Olefsky. «Nuclear Receptor Minireview Series.» In: *Journal of Biological Chemistry* 276.40 (2001), pp. 36863–36864. ISSN: 00219258. DOI: 10.1074/jbc.R100047200 (cit. on p. 4).

[166] John P. Overington *et al.* «How many drug targets are there?» In: *Nature Reviews Drug Discovery* 5.12 (2006), pp. 993–996. ISSN: 14741776. DOI: 10.1038/nrd2199. arXiv: NIHMS150003 (cit. on p. 4).

[167] B. Panaretou. «ATP binding and hydrolysis are essential to the function of the Hsp90 molecular chaperone invivo.» In: *The EMBO Journal* 17.16 (Aug. 1998), pp. 4829–4836. ISSN: 14602075. DOI: 10.1093/emboj/17.16.4829. URL: http://www.ncbi.nlm.nih.gov/pubmed/9817749%20http://www.pubmedcentral.nih.gov/articlerender.fcgi?artid=PMC2132952%20http://emboj.embopress.org/cgi/doi/10.1093/emboj/17.16.4829 (cit. on p. 14).

[168] Pdr. *PDR Lab Advisor: A comprehensive point-of-care guide for over 600 lab tests*. PHYSICIANS DESK REFERENCE, 2006. ISBN: 9781563636271. URL: https://www.strandbooks.com/medical-reference/pdr-lab-advisor-a-comprehensive-point-of-care-guide-for-over-600-lab-tests (cit. on p. 83).

[169] Benjamin Pelz. «Enzyme mechanics studied by single molecule force spectroscopy.» PhD thesis. Technische Universität München, 2014. URL: https://mediatum.ub.tum.de/1232877 (cit. on pp. 23, 39).

[170] Benjamin Pelz *et al.* «Subnanometre enzyme mechanics probed by single-molecule force spectroscopy.» In: *Nature Communications* 7 (2016), p. 10848. ISSN: 2041-1723. DOI: 10.1038/ncomms10848. URL: http://www.nature.com/doifinder/10.1038/ncomms10848 (cit. on pp. 21, 22).

[171] Benjamin Pelz *et al.* «Subnanometre enzyme mechanics probed by single-molecule force spectroscopy.» In: *Nature Communications* 7 (Feb. 2016), p. 10848. ISSN: 2041-1723. DOI: 10.1038/ncomms10848. URL: http://www.nature.com/doifinder/10.1038/ncomms10848 (cit. on p. 79).

[172] Judit Perales-Calvo *et al.* «The force-dependent mechanism of DnaK-mediated mechanical folding.» In: *Science Advances* 4.2 (Feb. 2018), eaaq0243. ISSN: 2375-2548. DOI: 10.1126/sciadv.aaq0243. URL: http://advances.sciencemag.org/lookup/doi/10.1126/sciadv.aaq0243 (cit. on p. 124).

[173] Samuel J. Pfaff and Robert J. Fletterick. «Hormone binding and co-regulator binding to the glucocorticoid receptor are allosterically coupled.» In: *Journal of Biological Chemistry* 285.20 (2010), pp. 15256–15267. ISSN: 00219258. DOI: 10.1074/jbc.M110.108118 (cit. on pp. 5, 65, 68, 70, 78, 81–83, 101).

[174] D Picard *et al. Reduced levels of hsp90 compromise steroid receptor action in vivo.* 1990. DOI: 10.1038/348166a0 (cit. on pp. 7, 16, 103).

[175] Nicholas F. Polizzi *et al.* «Mean First-Passage Times in Biology.» In: *Israel Journal of Chemistry* 56.9-10 (Oct. 2016), pp. 816–824. ISSN: 00212148. DOI: 10.1002/ijch.201600040. arXiv: 15334406. URL: http://doi.wiley.com/10.1002/ijch.201600040 (cit. on pp. 44, 49, 93).

[176] W B Pratt *et al.* «Chaperoning of glucocorticoid receptors.» In: *Handbook of experimental pharmacology* 172 (2006), pp. 111–38. ISSN: 0171-2004. URL: http://www.ncbi.nlm.nih.gov/pubmed/16610357 (cit. on pp. 13, 16, 100, 103, 107, 130).

[177] William B. Pratt and David O. Toft. «Regulation of Signaling Protein Function and Trafficking by the hsp90/hsp70-Based Chaperone Machinery.» In: *Experimental Biology and Medicine* 228.2 (Feb. 2003), pp. 111–133. ISSN: 1535-3702. DOI: 10.1177/153537020322800201. URL: http://journals.sagepub.com/doi/10.1177/153537020322800201 (cit. on pp. 15, 16).

[178] William B Pratt and Kurt D Dittmar. «Studies with Purified Chaperones Advance the Understanding of the Mechanism of Glucocorticoid Receptor–hsp90 Heterocomplex Assembly.» In: *Trends in Endocrinology & Metabolism* 9.6 (1998), pp. 244–252. ISSN: 10432760. DOI: 10.1016/S1043-2760(98)00059-9. URL: http://www.sciencedirect.com/science/article/pii/S1043276098000599 (cit. on p. 7).

[179] William B Pratt and David O Toft. «Steroid receptor interactions with heat shock protein and immunophilin chaperones.» In: *Endocr Rev* 18.3 (1997), pp. 306–360. ISSN: 0163-769X. DOI: 10.1210/edrv.18.3.0303. URL: http://www.ncbi.nlm.nih.gov/entrez/query.fcgi?cmd=Retrieve%7B%5C&%7Ddb=PubMed%7B%5C&%7Ddopt=Citation%7B%5C&%7Dlist%7B%5C_%7Duids=9183567 (cit. on pp. 7, 16, 107).

[180] William B Pratt *et al.* «Role of molecular chaperones in steroid receptor action.» In: *Essays In Biochemistry* 40 (June 2004), pp. 41–58. ISSN: 0071-1365. DOI: 10.1042/bse0400041. URL: http://essays.biochemistry.org/lookup/doi/10.1042/bse0400041 (cit. on p. 16).

[181] William B Pratt *et al.* «The Hsp90 Chaperone Machinery Regulates Signaling by Modulating Ligand Binding Clefts.» In: *Journal of Biological Chemistry* 283.34 (Aug. 2008), pp. 22885–22889. ISSN: 0021-9258. DOI: 10.1074/jbc.R800023200. URL: http://www.jbc.org/lookup/doi/10.1074/jbc.R800023200 (cit. on pp. 16, 83, 131).

[182] Florian Joachim Raabe and Dietmar Spengler. «Epigenetic risk factors in PTSD and depression.» In: *Frontiers in Psychiatry* 4.AUG (2013), pp. 1–17. ISSN: 16640640. DOI: 10.3389/fpsyt.2013.00080 (cit. on p. 6).

[183] L.R. Rabiner. «A tutorial on hidden Markov models and selected applications in speech recognition.» In: *Proceedings of the IEEE* 77.2 (1989), pp. 257–286. ISSN: 00189219. DOI: 10.1109/5.18626. arXiv: arXiv:1011.1669v3. URL: http://ieeexplore.ieee.org/ielx5/5/698/00018626.pdf?tp=%7B%5C&%7Darnumber=18626%7B%5C&%7Disnumber=698%7B%5C%%7D5Cnhttp://ieeexplore.ieee.org/xpls/abs%7B%5C_%7Dall.jsp?arnumber=18626%7B%5C&%7Dtag=1%7B%5C%%7D0Ahttp://ieeexplore.ieee.org/document/18626/ (cit. on p. 43).

[184] Martina Radli and Stefan G.D. Rüdiger. «Picky Hsp90—Every Game with Another Mate.» In: *Molecular Cell* 67.6 (2017), pp. 899–900. ISSN: 10974164. DOI: 10.1016/j.molcel.2017.09.013 (cit. on p. 15).

[185] Martina Radli and Stefan G.D. Rüdiger. «Dancing with the Diva: Hsp90-Client Interactions.» In: *Journal of Molecular Biology* (May 2018), #pagerange#. ISSN: 00222836. DOI: 10.1016/j.jmb.2018.05.026. URL: https://doi.org/10.1016/j.jmb.2018.05.026%20http://linkinghub.elsevier.com/retrieve/pii/S0022283618304509 (cit. on pp. 12, 14, 16, 105–107, 128, 130).

[186] Mona Radwan *et al.* «When proteostasis goes bad: Protein aggregation in the cell.» In: *IUBMB Life* 69.2 (2017), pp. 49–54. ISSN: 15216551. DOI: 10.1002/iub.1597 (cit. on p. 5).

[187] K. Renner *et al.* «A Conceptual View on Glucocorticoid-Induced Apoptosis, Cell Cycle Arrest and Glucocorticoid Resistance in Lymphoblastic Leukemia.» In: *Current Molecular Medicine* 3.8 (Dec. 2003), pp. 707–717. ISSN: 15665240. DOI: 10.2174/1566524033479357. URL: http://www.eurekaselect.com/openurl/content.php?genre=article%7B%5C&%7Dissn=1566-5240%7B%5C&%7Dvolume=3%7B%5C&%7Dissue=8%7B%5C&%7Dspage=707 (cit. on p. 6).

[188] D. Ricketson *et al.* «A Conformational Switch in the Ligand-binding Domain Regulates the Dependence of the Glucocorticoid Receptor on Hsp90.» In: *Journal of Molecular Biology* 368.3 (2007), pp. 729–741. ISSN: 00222836. DOI: 10.1016/j.jmb.2007.02.057 (cit. on pp. 16, 83, 101).

[189] Matthias Rief *et al.* «Reversible unfolding of individual titin immunoglobulin domains by AFM.» In: *Science* 276.5315 (1997), pp. 1109–1112. ISSN: 00368075. DOI: 10.1126/science.276.5315.1109. arXiv: arXiv:1011.1669v3 (cit. on p. 40).

[190] Daniel L Riggs *et al.* «The Hsp90-binding peptidylprolyl isomerase FKBP52 potentiates glucocorticoid signaling in vivo.» In: *The EMBO journal* 22.5 (2003), pp. 1158–67. ISSN: 0261-4189. DOI: 10.1093/emboj/cdg108. URL: http://www.pubmedcentral.nih.gov/articlerender.fcgi?artid=150341%7B%5C&%7Dtool=pmcentrez%7B%5C&%7Drendertype=abstract (cit. on p. 104).

[191] Lorenz Rognoni. «lorenz e . rognoni MOLECULAR MECHANISM OF THE MECHANOSENSOR FILAMIN.» PhD thesis. Technische Universität München, 2014 (cit. on pp. 39, 157).

[192] Alina Röhl *et al.* «The chaperone Hsp90: changing partners for demanding clients.» In: *Trends in Biochemical Sciences* 38.5 (May 2013), pp. 253–262. ISSN: 09680004. DOI: 10.1016/j.tibs.2013.02.003. URL: http://linkinghub.elsevier.com/retrieve/pii/S0968000413000248 (cit. on p. 15).

[193] Stefan Rüdiger *et al.* «Substrate specificity of the DnaK chaperone determined by screening cellulose-bound peptide libraries.» In: *EMBO Journal* 16.7 (1997), pp. 1501–1507. ISSN: 02614189. DOI: 10.1093/emboj/16.7.1501 (cit. on p. 104).

[194] Stefan Rüdiger *et al.* «Its substrate specificity characterizes the DnaJ co-chaperone as a scanning factor for the DnaK chaperone.» In: *EMBO Journal* 20.5 (2001), pp. 1042–1050. ISSN: 02614189. DOI: 10.1093/emboj/20.5.1042 (cit. on pp. 105, 126).

[195] Rick Russell *et al.* «Kinetic Characterization of the ATPase Cycle of the DnaK Molecular Chaperone †.» In: *Biochemistry* 37.2 (Jan. 1998), pp. 596–607. ISSN: 0006-2960. DOI: 10.1021/bi972025p. URL: http://pubs.acs.org/doi/abs/10.1021/bi972025p (cit. on p. 104).

[196] Daniel Andreas Rutz *et al.* «A switch point in the molecular chaperone Hsp90 responding to client interaction.» In: *Nature Communications* 9.1 (2018), p. 1472. ISSN: 2041-1723. DOI: 10.1038/s41467-018-03946-x. URL: http://www.nature.com/articles/s41467-018-03946-x (cit. on pp. 16, 159, 160, 162, 163).

[197] Maria A. Sacta *et al.* «Glucocorticoid Signaling: An Update from a Genomic Perspective.» In: *Annual Review of Physiology* 78.1 (2016), pp. 155–180. ISSN: 0066-4278. DOI: 10.1146/annurev-physiol-021115-105323. arXiv: 9605103 [cs]. URL: http://www.annualreviews.org/doi/10.1146/annurev-physiol-021115-105323 (cit. on pp. 6, 7).

[198] Priyanka Sahasrabudhe *et al.* «The Plasticity of the Hsp90 Co-chaperone System.» In: *Molecular Cell* 67.6 (Sept. 2017), 947–961.e5. ISSN: 10972765. DOI: 10.1016/j.molcel.2017.08.004. URL: http://dx.doi.org/10.1016/j.molcel.2017.08.004%20http://linkinghub.elsevier.com/retrieve/pii/S1097276517305786 (cit. on p. 130).

[199] Helen Saibil. «Chaperone machines for protein folding, unfolding and disaggregation.» In: *Nature Reviews Molecular Cell Biology* 14.10 (2013), pp. 630–642. ISSN: 14710072. DOI: 10.1038/nrm3658. URL: http://dx.doi.org/10.1038/nrm3658 (cit. on pp. 5, 15).

[200] D. D. Sakai *et al.* «Hormone-mediated repression: a negative glucocorticoid response element from the bovine prolactin gene.» In: *Genes & development* 2.9 (1988), pp. 1144–1154. ISSN: 08909369. DOI: 10.1101/gad.2.9.1144 (cit. on p. 8).

[201] E. R. Sanchez *et al.* «Relationship of the 90-kDa murine heat shock protein to the untransformed and transformed states of the L cell glucocorticoid receptor.» In: *Journal of Biological Chemistry* 262.15 (1987), pp. 6986–6991. ISSN: 00219258 (cit. on p. 16).

[202] J G Savory *et al.* «Glucocorticoid receptor homodimers and glucocorticoid-mineralocorticoid receptor heterodimers form in the cytoplasm through alternative dimerization interfaces.» In: *Molecular and cellular biology* 21.3 (2001), pp. 781–93. ISSN: 0270-7306. DOI: 10.1128/MCB.21.3.781-793.2001. URL: http://www.pubmedcentral.nih.gov/articlerender.fcgi?artid=86670%7B%5C&%7Dtool=pmcentrez%7B%5C&%7Drendertype=abstract (cit. on p. 7).

[203] R I Scheinman *et al.* «Characterization of mechanisms involved in transrepression of NF-kappa B by activated glucocorticoid receptors.» In: *Molecular and Cellular Biology* 15.2 (1995), pp. 943–953. ISSN: 0270-7306. DOI: 10.1128/MCB.15.2.943. URL: http://mcb.asm.org/lookup/doi/10.1128/MCB.15.2.943 (cit. on p. 8).

[204] David Schilter. «Thiol oxidation: A slippery slope.» In: *Nature Reviews Chemistry* 1.2 (Jan. 2017), p. 0013. ISSN: 2397-3358. DOI: 10.1038/s41570-016-0013. URL: http://www.nature.com/articles/s41570-016-0013 (cit. on p. 155).

[205] M Schlierf *et al.* «Direct observation of active protein folding using lock-in force spectroscopy.» In: *Biophys J* 93.11 (2007), pp. 3989–3998. ISSN: 1542-0086. DOI: 10.1529/biophysj.107.114397. URL: http://www.ncbi.nlm.nih.gov/pubmed/17704164 (cit. on pp. 42, 45).

[206] Manfred Schliwa and Günther Woehlke. «Molecular motors.» In: *Nature* 422.6933 (Apr. 2003), pp. 759–765. ISSN: 0028-0836. DOI: 10.1038/nature01601. URL: http://www.nature.com/doifinder/10.1038/nature01601 (cit. on p. 3).

[207] Andreas B Schmid. «The adaptor protein Sti1/Hop connects the Hsp70 and Hsp90 chaperone cycle.» Dissertation. Technical University Munich, 2009. URL: http://mediatum.ub.tum.de/node?id=815015 (cit. on p. 161).

[208] D Schmid *et al.* «Kinetics of molecular chaperone action.» In: *Science (New York, N.Y.)* 263.5149 (Feb. 1994), pp. 971–3. ISSN: 0036-8075. URL: http://www.ncbi.nlm.nih.gov/pubmed/8310296 (cit. on p. 104).

[209] Guillaume A. Schoch *et al.* «Molecular Switch in the Glucocorticoid Receptor: Active and Passive Antagonist Conformations.» In: *Journal of Molecular Biology* 395.3 (Jan. 2010), pp. 568–577. ISSN: 00222836. DOI: 10.1016/j.jmb.2009.11.011. URL: http://linkinghub.elsevier.com/retrieve/pii/S0022283609013886 (cit. on pp. 9, 10, 12, 68, 78, 101).

[210] Florian H. Schopf *et al.* «The HSP90 chaperone machinery.» In: *Nature Reviews Molecular Cell Biology* 18.6 (2017), pp. 345–360. ISSN: 14710080. DOI: 10.1038/nrm.2017.20. URL: http://dx.doi.org/10.1038/nrm.2017.20 (cit. on pp. 14, 16, 105–107, 130).

[211] H Schröder *et al.* «DnaK, DnaJ and GrpE form a cellular chaperone machinery capable of repairing heat-induced protein damage.» In: *The EMBO journal* 12.11 (Nov. 1993), pp. 4137–44. ISSN: 0261-4189. URL: http://www.ncbi.nlm.nih.gov/pubmed/7900997%20http://www.pubmedcentral.nih.gov/articlerender.fcgi?artid=PMC413706 (cit. on p. 124).

[212] Benjamin Schuler *et al.* «Probing the free-energy surface for protein folding with single-molecule fluorescence spectroscopy.» In: *October* (2002), pp. 743–748. ISSN: 00280836. DOI: 10.1038/nature01062.1. (cit. on p. 45).

[213] Ingo Schwaiger *et al.* «The folding pathway of a fast-folding immunoglobulin domain revealed by single-molecule mechanical experiments.» In: *EMBO reports* 6.1 (Jan. 2005), pp. 46–51. ISSN: 1469-221X. DOI: 10.1038/sj.embor.7400317. URL: http://www.nature.com/doifinder/10.1038/sj.embor.7400317 (cit. on p. 28).

[214] Kathryn a Scott *et al.* «The folding of spectrin domains I: wild-type domains have the same stability but very different kinetic properties.» In: *Journal of molecular biology* 344.1 (Dec. 2004), pp. 195–205. ISSN: 0022-2836. DOI: 10.1016/j.jmb.2004.09.037. URL: http://www.ncbi.nlm.nih.gov/pubmed/15504411 (cit. on p. 28).

[215] Tobias Seitz *et al.* «Enhancing the Stability and Solubility of the Glucocorticoid Receptor Ligand-Binding Domain by High-Throughput Library Screening.» In: *Journal of Molecular Biology* 403.4 (2010), pp. 562–577. ISSN: 00222836. DOI: 10.1016/j.jmb.2010.08.048. URL: http://dx.doi.org/10.1016/j.jmb.2010.08.048 (cit. on pp. 13, 79, 100, 151).

[216] Gayan Senavirathne *et al.* «Widespread nuclease contamination in commonly used oxygen-scavenging systems.» In: *Nature Methods* 12.10 (2015), pp. 901–902. ISSN: 1548-7091. DOI: 10.1038/nmeth.3588. URL: http://www.nature.com/doifinder/10.1038/nmeth.3588 (cit. on pp. 165, 166).

[217] Yigong Shi. «A Glimpse of Structural Biology through X-Ray Crystallography.» In: *Cell* 159.5 (Nov. 2014), pp. 995–1014. ISSN: 00928674. DOI: 10.1016/j.cell.2014.10.051. URL: http://linkinghub.elsevier.com/retrieve/pii/S0092867414014238 (cit. on p. 21).

[218] Andrew K Shiau *et al.* «Structural Analysis of E. coli hsp90 Reveals Dramatic Nucleotide-Dependent Conformational Rearrangements.» In: *Cell* 127.2 (Oct. 2006), pp. 329–340. ISSN: 00928674. DOI: 10.1016/j.cell.2006.09.027. URL: http://linkinghub.elsevier.com/retrieve/pii/S009286740601275X (cit. on p. 14).

[219] D F Smith. «Dynamics of heat shock protein 90-progesterone receptor binding and the disactivation loop model for steroid receptor complexes.» In: *Molecular Endocrinology* 7.11 (Nov. 1993), pp. 1418–1429. ISSN: 0888-8809. DOI: 10.1210/mend.7.11.7906860. URL: https://academic.oup.com/mend/article-lookup/doi/10.1210/mend.7.11.7906860 (cit. on p. 16).

[220] D. F. Smith *et al.* «Assembly of progesterone receptor with heat shock proteins and receptor activation are ATP mediated events.» In: *Journal of Biological Chemistry* 267.2 (1992), pp. 1350–1356. ISSN: 00219258 (cit. on pp. 103, 105).

[221] David F Smith and David O Toft. «Minireview: The Intersection of Steroid Receptors with Molecular Chaperones: Observations and Questions.» In: *Molecular Endocrinology* 22.10 (Oct. 2008), pp. 2229–2240. ISSN: 0888-8809. DOI: 10.1210/me.2008-0089. URL: https://academic.oup.com/mend/article-lookup/doi/10.1210/me.2008-0089 (cit. on p. 16).

[222] Steven B Smith *et al.* «Overstretching B-DNA: The Elastic Response of Individual Double-Stranded and Single-Stranded DNA Molecules.» In: *Science* 271.5250 (Feb. 1996), pp. 795–799. ISSN: 0036-8075. DOI: 10.1126/science.271.5250.795. arXiv: arXiv:1011.1669v3. URL: http://www.sciencemag.org/cgi/doi/10.1126/science.271.5250.795 (cit. on p. 22).

[223] Daniel R. Southworth and David A. Agard. «Client-Loading Conformation of the Hsp90 Molecular Chaperone Revealed in the Cryo-EM Structure of the Human Hsp90:Hop Complex.» In: *Molecular Cell* 42.6 (June 2011), pp. 771–781. ISSN: 10972765. DOI: 10.1016/j.molcel.2011.04.023. URL: http://dx.doi.org/10.1016/j.molcel.2011.04.023%20http://linkinghub.elsevier.com/retrieve/pii/S1097276511003698 (cit. on pp. 106, 128, 130).

[224] T E Spencer *et al.* «Steroid receptor coactivator-1 is a histone acetyltransferase.» In: *Nature* 389.6647 (1997), pp. 194–198. ISSN: 0028-0836. DOI: 10.1038/38304 (cit. on p. 8).

[225] E. R. Stadtman and R. L. Levine. «Free radical-mediated oxidation of free amino acids and amino acid residues in proteins.» In: *Amino Acids* 25.3-4 (Dec. 2003), pp. 207–218. ISSN: 0939-4451. DOI: 10.1007/s00726-003-0011-2. URL: http://link.springer.com/10.1007/s00726-003-0011-2 (cit. on p. 155).

[226] Marta Stankiewicz *et al.* «CHIP participates in protein triage decisions by preferentially ubiquitinating Hsp70-bound substrates.» In: *FEBS Journal* 277.16 (Aug. 2010), pp. 3353–3367. ISSN: 1742464X. DOI: 10.1111/j.1742-4658.2010.07737.x. URL: http://doi.wiley.com/10.1111/j.1742-4658.2010.07737.x (cit. on p. 128).

[227] J. Stigler *et al.* «The Complex Folding Network of Single Calmodulin Molecules.» In: *Science* 334.6055 (Oct. 2011), pp. 512–516. ISSN: 0036-8075. DOI: 10.1126/science.1207598. arXiv: arXiv:1308.5367. URL: http://www.sciencemag.org/cgi/doi/10.1126/science.1207598 (cit. on pp. 22, 43, 101).

[228] Johannes Stigler. «Complex ligand-dependent folding of single proteins observed with optical tweezers.» PhD thesis. Technische Universität München, 2012 (cit. on p. 39).

[229] Johannes Stigler and Matthias Rief. «Hidden Markov analysis of trajectories in single-molecule experiments and the effects of missed events.» In: *ChemPhysChem* 13.4 (2012), pp. 1079–1086. ISSN: 14394235. DOI: 10.1002/cphc.201100814 (cit. on pp. 43, 173).

[230] F. William Studier. «Protein production by auto-induction in high-density shaking cultures.» In: *Protein Expression and Purification* 41.1 (May 2005), pp. 207–234. ISSN: 10465928. DOI: 10.1016/j.pep.2005.01.016. arXiv: NIHMS150003. URL: http://linkinghub.elsevier.com/retrieve/pii/S1046592805000264 (cit. on p. 159).

[231] Toshihiko Sugiki *et al.* «Modern Technologies of Solution Nuclear Magnetic Resonance Spectroscopy for Three-dimensional Structure Determination of Proteins Open Avenues for Life Scientists.» In: *Computational and Structural Biotechnology Journal* 15 (2017), pp. 328–339. ISSN: 20010370. DOI: 10.1016/j.csbj.2017.04.001. URL: http://linkinghub.elsevier.com/retrieve/pii/S2001037017300053 (cit. on p. 21).

[232] K. Suino-Powell *et al.* «Doubling the Size of the Glucocorticoid Receptor Ligand Binding Pocket by Deacylcortivazol.» In: *Molecular and Cellular Biology* 28.6 (2008), pp. 1915–1923. ISSN: 0270-7306. DOI: 10.1128/MCB.01541-07. URL: http://mcb.asm.org/cgi/doi/10.1128/MCB.01541-07 (cit. on p. 101).

[233] K Svoboda and S M Block. «Biological applications of optical forces.» In: *Annual review of biophysics and biomolecular structure* 23 (Jan. 1994), pp. 247–85. ISSN: 1056-8700. DOI: 10.1146/annurev.bb.23.060194.001335. URL: http://www.ncbi.nlm.nih.gov/pubmed/7919782 (cit. on p. 23).

[234] Mikko Taipale *et al.* «Quantitative Analysis of Hsp90-Client Interactions Reveals Principles of Substrate Recognition.» In: *Cell* 150.5 (Aug. 2012), pp. 987–1001. ISSN: 00928674. DOI: 10.1016/j.cell.2012.06.047. URL: http://linkinghub.elsevier.com/retrieve/pii/S0092867412009373 (cit. on pp. 15, 16).

[235] H Theyssen *et al.* «The second step of ATP binding to DnaK induces peptide release.» In: *Journal of molecular biology* 263.5 (Nov. 1996), pp. 657–70. ISSN: 0022-2836. DOI: 10.1006/jmbi.1996.0606. URL: http://www.ncbi.nlm.nih.gov/pubmed/8947566 (cit. on p. 104).

[236] J. W. Thornton. «Evolution of vertebrate steroid receptors from an ancestral estrogen receptor by ligand exploitation and serial genome expansions.» In: *Proceedings of the National Academy of Sciences* 98.10 (2001), pp. 5671–5676. ISSN: 0027-8424. DOI: 10.1073/pnas.091553298. URL: http://www.pnas.org/cgi/doi/10.1073/pnas.091553298 (cit. on p. 10).

[237] Tsvi Tlusty *et al.* «Optical Gradient Forces of Strongly Localized Fields.» In: *Physical Review Letters* 81.8 (1998), pp. 1738–1741. ISSN: 0031-9007. DOI: 10.1103/PhysRevLett.81.1738. URL: http://link.aps.org/doi/10.1103/PhysRevLett.81.1738 (cit. on p. 23).

[238] Simon F. Tolić-Nørrelykke *et al.* «Calibration of optical tweezers with positional detection in the back focal plane.» In: *Review of Scientific Instruments* 77.10 (Oct. 2006), p. 103101. ISSN: 0034-6748. DOI: 10.1063/1.2356852. URL: http://link.aip.org/link/RSINAK/v77/i10/p103101/s1%7B%5C&%7DAgg=doi%20http://aip.scitation.org/doi/10.1063/1.2356852 (cit. on p. 24).

[239] Joseph Torchia *et al.* «The transcriptional co-activator p/CIP binds CBP and mediates nuclear-receptor function.» In: *Nature* 387.6634 (June 1997), pp. 677–684. ISSN: 0028-0836. DOI: 10.1038/42652. URL: http://www.nature.com/articles/42652 (cit. on p. 11).

[240] Quang Hon Tran and Gottfried Unden. «Changes in the proton potential and the cellular energetics of Escherichia coli during growth by aerobic and anaerobic respiration or by fermentation.» In: *European Journal of Biochemistry* 251.1-2 (1998), pp. 538–543. ISSN: 00142956. DOI: 10.1046/j.1432-1327.1998.2510538.x (cit. on p. 126).

[241] Ming-jer Tsai and Bert W. O'Malley. «Molecular mechanisms of action of steroid / thyroid receptor superfamily members.» In: *Annual Review of Biochemestry* 63 (1994), pp. 451–486. ISSN: 0066-4154. DOI: 10.1146/annurev.bi.63.070194.002315 (cit. on p. 5).

[242] Joost Van Durme *et al.* «Accurate prediction of DnaK-peptide binding via homology modelling and experimental data.» In: *PLoS Computational Biology* 5.8 (2009). ISSN: 1553734X. DOI: 10.1371/journal.pcbi.1000475 (cit. on pp. 124–126).

[243] Sofie Vandevyver *et al.* «On the Trail of the Glucocorticoid Receptor: Into the Nucleus and Back.» In: *Traffic* 13.3 (2012), pp. 364–374. ISSN: 13989219. DOI: 10.1111/j.1600-0854.2011.01288.x (cit. on pp. 6, 8, 13, 16, 103).

[244] Sofie Vandevyver *et al.* «Comprehensive overview of the structure and regulation of the glucocorticoid receptor.» In: *Endocrine Reviews* 35.4 (2014), pp. 671–693. ISSN: 0163769X. DOI: 10.1210/er.2014-1010 (cit. on pp. 5, 6, 11).

[245] K. A. Verba *et al.* «Atomic structure of Hsp90-Cdc37-Cdk4 reveals that Hsp90 traps and stabilizes an unfolded kinase.» In: *Science* 352.6293 (June 2016), pp. 1542–1547. ISSN: 0036-8075. DOI: 10.1126/science.aaf5023. URL: http://www.sciencemag.org/cgi/doi/10.1126/science.aaf5023 (cit. on p. 15).

[246] David Wales. *Energy Landscapes: Applications to Clusters, Biomolecules and Glasses*. Ed. by Richard Saykally *et al.* University of Cambridge, 2003. ISBN: 0521814154 (cit. on p. 40).

[247] Stefan Walter and Johannes Buchner. «Molecular Chaperones – Cellular Machines for Protein Folding.» In: *Angewandte Chemie International Edition* 41 (2002), pp. 1098–1113. ISSN: 1433-7851. DOI: 10.1002/1521-3773(20020402)41:73.0.CO;2-9 (cit. on p. 5).

[248] M D Wang *et al.* «Stretching DNA with optical tweezers.» In: *Biophysical journal* 72.3 (Mar. 1997), pp. 1335–46. ISSN: 0006-3495. DOI: 10.1016/S0006-3495(97)78780-0. URL: http://www.pubmedcentral.nih.gov/articlerender.fcgi?artid=1184516%7B%5C&%7Dtool=pmcentrez%7B%5C&%7Drendertype=abstract (cit. on pp. 22, 39).

[249] M D Wang *et al.* «Force and velocity measured for single molecules of RNA-polymerase.» In: *Science* 282.October (1998), pp. 902–907 (cit. on p. 22).

[250] Zhulun Wang *et al.* «Structure and function of Nurr1 identifies a class of ligand-independent nuclear receptors.» In: *Nature* 423.6939 (May 2003), pp. 555–560. ISSN: 0028-0836. DOI: 10.1038/nature01645. URL: http://www.nature.com/articles/nature01667%20http://www.nature.com/articles/nature01645 (cit. on p. 11).

[251] Harald Wegele *et al.* «Substrate Transfer from the Chaperone Hsp70 to Hsp90.» In: *Journal of Molecular Biology* 356.3 (Feb. 2006), pp. 802–811. ISSN: 00222836. DOI: 10.1016/j.jmb.2005.12.008. URL: http://linkinghub.elsevier.com/retrieve/pii/S0022283605015688 (cit. on pp. 105, 106).

[252] Jimena Weibezahn *et al.* «Novel insights into the mechanism of chaperone-assisted protein disaggregation.» In: *Biological Chemistry* 386.8 (2005), pp. 739–744. ISSN: 14316730. DOI: 10.1515/BC.2005.086 (cit. on p. 5).

[253] Emily R. Weikum *et al.* «Glucocorticoid receptor control of transcription: Precision and plasticity via allostery.» In: *Nature Reviews Molecular Cell Biology* 18.3 (2017), pp. 159–174. ISSN: 14710080. DOI: 10.1038/nrm.2016.152. URL: http://dx.doi.org/10.1038/nrm.2016.152 (cit. on pp. 4, 6–8, 13, 103, 151).

[254] Emily R Weikum *et al.* «Structural Analysis of the Glucocorticoid Receptor Ligand-Binding Domain in Complex with Triamcinolone Acetonide and a Fragment of the Atypical Coregulator , Small Heterodimer Partner.» In: July (2017), pp. 12–21. ISSN: 15210111. DOI: 10.1124/mol.117.108506 (cit. on pp. 10, 101).

[255] Luke Whitesell and Susan L Lindquist. «HSP90 and the chaperoning of cancer.» In: *Nature Reviews Cancer* 5.10 (Sept. 2005), pp. 761–772. ISSN: 1474-175X. DOI: 10.1038/nrc1716. URL: http://www.nature.com/doifinder/10.1038/nrc1716 (cit. on p. 14).

[256] R H Williams *et al.* *Williams Textbook of endocrinology*. Saunders, 1985. ISBN: 9780721610825. URL: https://books.google.de/books?id=8TNsAAAAMAAJ (cit. on p. 6).

[257] Juliane Winkler *et al.* «Chaperone networks in protein disaggregation and prion propagation.» In: *Journal of Structural Biology* 179.2 (Aug. 2012), pp. 152–160. ISSN: 10478477. DOI: 10.1016/j.jsb.2012.05.002. URL: http://linkinghub.elsevier.com/retrieve/pii/S1047847712001384 (cit. on p. 15).

[258] Pernilla Wittung-Stafshede *et al.* «The J-domain of Hsp40 couples ATP hydrolysis to substrate capture in Hsp70.» In: *Biochemistry* 42.17 (2003), pp. 4937–4944. ISSN: 00062960. DOI: 10.1021/bi027333o (cit. on p. 126).

[259] Jean-Marie Wurtz *et al.* «A canonical structure for the ligand-binding domain of nuclear receptors.» In: *Nature Structural Biology* 3.1 (Jan. 1996), pp. 87–94. ISSN: 1072-8368. DOI: 10.1038/nsb0196-87. URL: http://www.nature.com/doifinder/10.1038/nsb0196-87 (cit. on p. 9).

[260] M Xu *et al.* «Binding of hsp90 to the glucocorticoid receptor requires a specific 7-amino acid sequence at the amino terminus of the hormone-binding domain.» In: *The Journal of biological chemistry* 273.22 (May 1998), pp. 13918–24. ISSN: 0021-9258. URL: http://www.ncbi.nlm.nih.gov/pubmed/9593740 (cit. on p. 129).

[261] W. Xu *et al.* «Chaperone-dependent E3 ubiquitin ligase CHIP mediates a degradative pathway for c-ErbB2/Neu.» In: *Proceedings of the National Academy of Sciences* 99.20 (Oct. 2002), pp. 12847–12852. ISSN: 0027-8424. DOI: 10.1073/pnas.202365899. URL: http://www.pnas.org/cgi/doi/10.1073/pnas.202365899 (cit. on p. 128).

[262] Li Quan Yang *et al.* «Protein dynamics and motions in relation to their functions: Several case studies and the underlying mechanisms.» In: *Journal of Biomolecular Structure and Dynamics* 32.3 (2014), pp. 372–393. ISSN: 07391102. DOI: 10.1080/07391102.2013.770372 (cit. on p. 21).

[263] Wei Yuan Yang and Martin Gruebele. «Folding at the speed limit.» In: *Nature* 423.6936 (May 2003), pp. 193–197. ISSN: 0028-0836. DOI: 10.1038/nature01609. URL: http://www.nature.com/articles/nature01609 (cit. on pp. 21, 45).

[264] Justin J. Yerbury *et al.* «Walking the tightrope: Proteostasis and neurodegenerative disease.» In: *Journal of Neurochemistry* 137.4 (2016), pp. 489–505. ISSN: 14714159. DOI: 10.1111/jnc.13575 (cit. on p. 5).

[265] Chunying Yu *et al.* «Cysteines 638 and 665 in the hormone binding domain of human glucocorticoid receptor define the specificity to glucocorticoids.» In: *Biochemistry* 34.43 (Oct. 1995), pp. 14163–14173. ISSN: 0006-2960. DOI: 10.1021/bi00043a022. URL: http://pubs.acs.org/doi/abs/10.1021/bi00043a022 (cit. on p. 75).

[266] Shimin Zhang *et al.* «Role of the C terminus of the glucocorticoid receptor in hormone binding and agonist/antagonist discrimination.» In: *Molecular Endocrinology* 10.1 (Jan. 1996), pp. 24–34. ISSN: 0888-8809. DOI: 10.1210/mend.10.1.8838142. URL: https://academic.oup.com/mend/article-lookup/doi/10.1210/mend.10.1.8838142 (cit. on p. 9).

[267] Fabian Benedikt Ziegler. «Einzelmolekülexperimente zum Einfluss von Knoten und makromolekularem Crowding auf die Faltung von Proteinen.» PhD thesis. Technische Universität München, 2015 (cit. on p. 39).

[268] Gabriel Zoldák *et al.* «The prolyl isomerase SlyD is a highly efficient enzyme but decelerates the conformational folding of a client protein.» In: *Journal of the American Chemical Society* 135.11 (2013), pp. 4372–4379. ISSN: 00027863. DOI: 10.1021/ja311775a (cit. on p. 28).

[269] Gabriel Zoldák *et al.* «The prolyl isomerase SlyD is a highly efficient enzyme but decelerates the conformational folding of a client protein.» In: *Journal of the American Chemical Society* 135.11 (2013), pp. 4372–4379. ISSN: 00027863. DOI: 10.1021/ja311775a (cit. on p. 153).

[270] Gabriel Žoldák *et al.* «Ultrafast folding kinetics and cooperativity of villin headpiece in single-molecule force spectroscopy.» In: *Proceedings of the National Academy of Sciences of the United States of America* 110.45 (2013), pp. 18156–61. ISSN: 1091-6490. DOI: 10.1073/pnas.1311495110. URL: http://www.pnas.org/content/110/45/18156.long (cit. on p. 22).

[271] R. Zwanzig *et al.* «Levinthal's paradox.» In: *Proceedings of the National Academy of Sciences* 89.1 (1992), pp. 20–22. ISSN: 0027-8424. DOI: 10.1073/pnas.89.1.20. URL: http://www.pnas.org/cgi/doi/10.1073/pnas.89.1.20 (cit. on p. 3).